Metal-Ligand Multiple Bonds

Nitrido and Fluoroimido Complexes of High-Valent Late Transition Metals

Inaugural-Dissertation
to obtain the academic degree
Doctor rerum naturalium (Dr. rer. nat.)

submitted to the Department of Biology, Chemistry, Pharmacy
of Freie Universität Berlin

by

TONY STÜKER

2021

The work for this dissertation was done in the time period from April 2016 to May 2021 under the supervision of Prof. Dr. Sebastian Hasenstab-Riedel at the Institute of Chemistry and Biochemistry of Freie Universität Berlin.

I hereby declare that the dissertation submitted is my own work. All direct or indirect sources used are acknowledged as references.

1st Referee:	Prof. Dr. Sebastian Hasenstab-Riedel
2nd Referee:	Prof. Dr. Martin Kaupp
Day of Disputation:	19 July 2021

Acknowledgements

Throughout the writing of this dissertation I have received a great deal of support and assistance.
I would first like to thank my supervisor, Prof. Dr. Sebastian Hasenstab-Riedel, for the opportunity to conduct my doctoral thesis in his group, for the interesting topic, for his support, and for his encouraging enthusiasm.
Next, I would like to thank Prof. Dr. Martin Kaupp for his time and effort to assess my work as a second referee. Thanks also to the other members of my committee for their time and effort.
I would like to express my sincere gratitude to Dr. habil. Helmut Beckers for proofreading all my manuscripts and whose office door was always open whenever I ran into a trouble spot or had a question about my research or writing. His patience during our countless discussions and insight have steered me through this work.
Thanks to Thomas Hohmann and Xia Xiya for their help while working under my supervision for their internship and Bachelor thesis, respectively.
Many thanks go to the entire working group for the very pleasant working atmosphere, for the many productive discussions and the general helpfulness of everyone. I will especially have fond memories of my colleagues and friends Dr. Li Lin and Dr. Frenio Redeker from the matrix-isolation subgroup.
Finally, I must express my gratitude to my beloved partner Dr. Rita Fernandes, who provided me with unfailing support, proofread this work and the continuous encouragement throughout my years of study. My appreciation also goes out to my dear parents Monika and Gert Stüker, and my dear brother Martin Stüker for their encouragement and support. This accomplishment would not have been possible without them.

Metal-Ligand Multiple Bonds

Nitrido and Fluoroimido Complexes of High-Valent Late Transition Metals

Tony Stüker

Abstract: High-valent group 8 and 9 transition metal complexes bearing nitrogen-metal multiple bonds, such as the fluoroimido difluorides $FNMF_2$, M = Co, Rh, the nitrido trifluorides NMF_3, M = Fe, Ru, Os, Rh, Ir, and the binary molecular iridium-nitride $Ir(N)_2$, have been investigated in a joint matrix-isolation infrared and a thorough quantum-chemical study. These novel molecules and their ^{15}N isotopologues were produced by the reaction of laser-ablated metals with NF_3 and N_2, and embedded in solid inert gas matrices. An uneven e^3 occupation of the metal centered, doubly degenerate HOMO of the group 9 NMF_3 (M = Rh, Ir) in the reference C_{3v} configurations leads to their observed Jahn–Teller distorted low-spin doublet ground state, while the even e^2 HOMO configuration for the group 8 metals suggests an undistorted high-spin $^3A_2$ ground state. However, the latter ground state was only confirmed for $NFeF_3$, while a pseudo-Jahn–Teller distorted low-spin structure of $NRuF_3$, and a magnetic bistability was observed for $NOsF_3$, which exists in two near-degenerate distorted low-spin and high-spin configurations. Since the reasons for their structural distortion is their electronic structure, this has been extensively investigated using multi-configurational calculations. The strongly bent F−N−M units in the group 9 fluoroimido complexes $FNMF_2$ (M = Co, Rh) follow from an unusual metal-nitrogen σ bond interaction between the M(d_{z^2}) and a N(p_z) orbital that is perpendicular to the N−F bond axis. Comparatively weak 3*d*-metal-nitrogen multiple bonds in $NFeF_3$ and $FNCoF_2$ were attributed to partial ligand oxidations and significant populations of their M−N σ^* and π^* antibonding orbitals. Spin-densities calculated for $FNCoF_2$ and $Ir(N)_2$ show a considerable nitrogen radical character because of spin-polarization and spin-delocalization, respectively. Hence, the fluoroimido and nitrido ligands in $FNCoF_2$, $NFeF_3$ and $Ir(N)_2$ must be considered as non-innocent.

Zusammenfassung: Hochvalente Gruppe 8 und 9 Übergangsmetallkomplexe, die Stickstoff-Metall Mehrfachbindungen tragen, wie die Fluoroimido-Difluorid $FNMF_2$, M = Co, Rh, die Nitrido-Trifluoride NMF_3, M = Fe, Ru, Os, Rh, Ir, und das binäre, molekulare Iridiumdinitrid $Ir(N)_2$, wurden in einer Matrix-Isolations Infrarotspektroskopischen, kombiniert mit einer gründlichen quantenchemischen Studie, untersucht. Diese neuartigen Moleküle und ihre ^{15}N-Isotopologe wurden durch die Reaktion von Laser-ablatierten Metallen mit NF_3 bzw. N_2 dargestellt und in festen Inertgasmatrizen eingebettet. Eine ungerade e^3-Besetzung des metallzentrierten, doppelt entarteten HOMO der Gruppe 9 NMF_3 (M = Rh, Ir) in den Referenz-C_{3v}-Konfigurationen führt zu ihrem beobachteten Jahn–Teller verzerrten, Low-Spin Dublett Grundzustand, während die gerade e^2 HOMO Konfiguration für die Metalle der Gruppe 8 einen unverzerrten High-Spin $^3A_2$ Grundzustand nahelegt. Der zuletzt Genannte wurde jedoch nur für $NFeF_3$ bestätigt, während für $NRuF_3$ eine pseudo-Jahn–Teller verzerrte Low-Spin Struktur, und für $NOsF_3$ eine magnetische Bistabilität beobachtet wurde, die in zwei nahezu entarteten, verzerrten Low-Spin- und High-Spin Konfigurationen existiert. Da der Grund für ihre strukturelle Verzerrung ihre elektronischen Struktur ist, wurde diese ausgiebig mit Multikonfigurationsrechnungen untersucht. Die stark gewinkelten F−N−M Einheiten in den Gruppe 9 Fluoroimido-Komplexen $FNMF_2$ (M = Co, Rh) ergeben sich aus einer ungewöhnlichen Metall-Stickstoff σ-Bindungswechselwirkung zwischen dem M(d_{z^2}) und einem N(p_z) Orbital, das senkrecht auf der N−F-Bindungsachse steht. Vergleichsweise schwache 3d-Metall-Stickstoff Mehrfachbindungen in $NFeF_3$ und $FNCoF_2$ wurden auf partielle Ligandenoxidationen und signifikante Populationen ihrer M−N σ^* und π^* antibindenden Orbitale zurückgeführt. Hervorgerufen von Spin-Polarisation bzw. Spin-Delokalisation zeigen die Spindichten von $FNCoF_2$ und $Ir(N)_2$ einen deutlichen Radikalcharacter am Stickstoff. Daher müssen die Fluoroimido- und Nitrido-Liganden in $FNCoF_2$, $NFeF_3$ und $Ir(N)_2$ als nicht-unschuldig angesehen werden.

List of Abbreviations

B3LYP Becke, 3-parameter, Lee–Yang–Parr

BO bond order

BP86 Becke–Perdew 1986

CASPT2 complete active-space second-order perturbation theory

CASSCF complete active space self-consistent field

CBS complete basis set

CC coupled-cluster

CCSD coupled-cluster singles doubles

CCSD(T) coupled-cluster singles, doubles and perturbative triples

CI configuration interaction

CISD configuration interaction singles doubles

DFT density functional theory

DKH Douglas-Kroll-Hess

DLPNO domain based local pair natural orbital

EBO effective bond order

ECP effective core potential

EN electronegativity

EPR electron paramagnetic resonance

EXAFS extended X-ray absorption fine structure

FCI full configuration interaction

FTIR Fourier-transform infrared

GGA generalized gradient approximation

HF Hartree-Fock

HOMO highest occupied molecular orbital

IR infrared

IRPD infrared photodissociation

KS Kohn-Sham

LCAO linear combination of atomic orbitals

LED light-emitting diode

LFS ligand field splitting

LFSE ligand field splitting energy

LIF laser-induced fluorescence

LUMO lowest unoccupied molecular orbital

MO molecular orbital

MP2 Møller-Plesset perturbation theory second order

MRCI multireference configuration interaction

MRPT multireference perturbation theory

NBO natural bond orbital

Nd:YAG neodymium-doped yttrium aluminum garnet

NEVPT2 n-electron valence state perturbation theory second order

NHC *N*-heterocyclic carbene

NPA natural population analysis

NR non-relativistic

NRVS nuclear resonant vibrational spectroscopy

OS oxidation state

PES potential energy surface

PO pseudo octahedral

PTD pseudo tetrahedral

QTAIM quantum theory of atoms in molecules

RR resonance Raman

SOMO singly occupied molecular orbital

SPL square planar

SPY square pyramidal

TBP trigonal bipyramidal

TG tetragonal

TISE time independent Schrödinger equation

TPL trigonal planar

UV/Vis ultraviolet-visible

XAS X-ray absorption spectroscopy

XRD X-ray diffraction

Z_{eff} effective core charge

ZORA zeroth order regular approximation

List of Ligand Abbrevations

Ad adamatyl

Cp* pentamethylcyclopentadiene

cyclam 1,4,8,11-tetraazacyclotetradecane

cyclam-ac 1,4,8,11-tetraazacyclotetradecane-1-acetate

dchypyb 1,2-dichloro-4,5-bis(2-hydroxybenzamido)benzene

Dipp 2,6-diisopropylphenyl

Dmp 2,6-dimesitylphenyl

dppe 1,2-bis(diphenylphosphino)ethane

Hind indazole

hmds bis(trimethylsilyl)amide

hypyb 1,2-bis(2-hydroxybenzamido)benzene

***i*PrPDBP** 2-[(2,6-diisopropyl-phenyl)imino]methyl-4,6-dibromophenol

LNO_2 2,6-bis(2-hydroxy-2,2-diphenylethyl)pyridine

Me methyl

3,5-Me_2Hpz 3,5-dimethylpyrazole

1-Mebzim 1-methylbenzimidazole

5-MeHpz 5-methylpyrazole

3,4,5-MeO-TPP *meso*-tetrakis(3,4,5-trimethoxy-phenyl)porphyrinate dianion

$MePy_2$tacn *N*-methyl-*N*,*N*-bis(2-picolyl)-1,4,7-triazacyclononane

Mes mesityl

3-MPA 3-mercaptopropionate dianion

MTPDPH 5-mesityl-1,9-(2,4,6-triphenylphenyl)dipyrromethene

NN_4 2,6-bis[1,1-di(aminomethyl)ethyl]pyridine

OEP octaethylporphyrinate dianion

OMPG *meso*-octamethyl-porphyrinogenate tetraanion

$P_3{}^B$ tris(*o*-diisopropylphosphinophenyl)borane

PDI pyridine diimine

Ph phenyl

PhB(CH_2P*i*Pr)$_2$ tris(diisopropylphosphino)borate

PhB(*t*BuIm)$_3$ phenyltris(1-tert-butylimidazol-2-ylidene)borate

PhB(MesIm)$_3$ phenyltris(1-mesityl-imidazol-2-ylidene)borate

phen 1,10-phenanthroline

PNP bis[2-(di-tert-butylphosphanyl)ethyl]amide

PNP′ bis[2-(di-tert-butylphosphanyl)ethenyl]amide

PNP^{Si} 3,9-di-tert-butyl-2,2,5,5,7,7,10,10-octamethyl-6-aza-3,9-diphospha-5,7-disilaundecan-6-ide

salen *N*,*N*′-bis(salicylidene)-o-cyclohexyldiamine dianion

salophen *N*,*N*′-bis(salicylidene)-o-phenylenediamine dianion

sap *N*-salicylidene-2-aminophenolat dianion

***t*Bu** *tert*-Butyl

TIMEN^{Mes} tris[2-(3-mesityl-imidazol-2-ylide-ne)ethyl]amine

TIMEN^{Xyl} tris[2-(3-xylyl-imidazol-2-ylide-ne)ethyl]amine

TMP *meso*-tetrakis(2,4,6-trimethylphenyl)-porphyrinatre dianion

Tol *p*-tolyl

TPP tetraphenylporphyrinate dianion

TRAP tetrapropylammonium perruthenate

TTPPP 5,10,15,20-tetrakis(2,4,6-triphenylphenyl)porphyrinato

Xyl Xylyl

Contents

1. Introduction 1
   1.1. The Nature of Metal-Ligand Multiple Bonds 2
   1.2. Oxidation States 4
   1.3. Matrix-Isolation Spectroscopy 6
   1.4. Computational Methods 11
   1.5. Nitrido Complexes of the Group 8 and Group 9 Transition Metals . . . 19
      1.5.1. Group 8 19
      1.5.2. Group 9 33
      1.5.3. Matrix-Isolation Works 40

2. Objectives 43

3. Outline 45
   3.1. Group 8 Nitrido Fluoride Complexes 46
   3.2. Group 9 Nitrido and Imido Complexes 49

4. Publications 53
   4.1. High-Spin Iron(VI), Low-Spin Ruthenium(VI), and Magnetically Bistable of Osmium(VI): Molecular Group 8 Nitrido Trifluorides NMF_3 53
   4.2. Fluoro Nitrenoid Complexes $FN{=}MF_2$ (M = Co, Rh, Ir): Electronic Structure Dichotomy and Formation of Nitrido Fluorides $N{\equiv}MF_3$ 63
   4.3. A Cornucopia of Iridium Nitrogen Compounds Produced from Laser-Ablated Iridium Atoms and Dinitrogen 71

5. Conclusion and Outlook 83
   5.1. Conclusion 83
   5.2. Outlook 84

6. References 85

7. List of Publications 103

A. Supporting Information of Publications 107
   A.1. High-Spin Iron(VI), Low-Spin Ruthenium(VI), and Magnetically Bistable of Osmium(VI): Molecular Group 8 Nitrido Trifluorides NMF_3 107
   A.2. Fluoro Nitrenoid Complexes $FN{=}MF_2$ (M = Co, Rh, Ir): Electronic Structure Dichotomy and Formation of Nitrido Fluorides $N{\equiv}MF_3$ 196

A.3. A Cornucopia of Iridium Nitrogen Compounds Produced from Laser-Ablated Iridium Atoms and Dinitrogen 233

1. Introduction

The metal-ligand multiple bonds represent an ubiquitous feature of early transition metals in high oxidation states (OSs).[1] The carbene ($M{=}CR_2$) and carbyne ($M{\equiv}CR$) complexes represent a significant class of organometallic chemistry where they play important roles in catalytic reactions, most prominently in alkene and alkyne metathesis.[2–6] Transition metal oxo complexes ($M{=}O$ or $M^{-}{\equiv}O^{+}$) are omnipresent in oxidation catalysis,[7] most notably in the oxygen evolving complex of photosystem II, responsible for catalyzing the oxidation of water to molecular oxygen in chloroplasts and cyanobacteria.[8,9] Due to their tendency to act as bridging ligands and their instability towards hydrolysis, comparatively few terminal sulphides ($M{=}S$) are known.[10] They are proposed as intermediates in the catalytic cycle of the petroleum desulfurization process.[11]

The focus of the this work is on the complexes carrying nitrido ($M{\equiv}N$) and imido ($M{=}NR$) moieties. Nitrido complexes of transition metals have been known for more than 170 years when the synthesis of OsO_3N^{-} was reported in 1847.[12] Only recently serious efforts have been made to develop their chemistry and to explore fundamental questions regarding their structure and bonding. The $M{\equiv}N$ moiety is isolobal to the $N{\equiv}N$ molecule and therefore comes as no surprise that nitrido complexes are subject of investigations surrounding dinitrogen coordination and activation, including the catalytic formation of ammonia in technology[13–22] and organic synthesis.[23–26] Quite recently, transition metal nitrides emerged as new class of potential anti-cancer and anti-tumor agents.[27–30] Other applications include the catalysis of triple-bond metathesis reactions of alkynes[31,32] and nitriles.[33] Nitrides are examined as potential model compounds in the Haber-Bosch process[34,35] and in the biological nitrogen fixation and activation in the nitrogenase enzyme.[36,37] The chemistry of the imides and nitrides has a lot in common, as they are both often found in the same catalytic cycles. Transition metal imido complexes participate in large number of reactions with direct involvement of the imido ligand, or as stabilizing spectator ligand.[38] Examples of the former type are aminations[39–44] and hydroaminations[45–53] of unsaturated substrates. An outstanding example for the latter type are metathesis reactions of unsaturated hydrocarbons catalyzed by imidocarbene complexes,[54,55] closely related to the above mentioned metathesis reactions of alkenes.

Despite the many applications of nitrido and imido complexes, the number of known late transition metal complexes lags behind that of early transition metals. This section deals with the nature of metal-ligand multiple bonds in general, and with the theoretical and experimental methods employed in this work. Furthermore, relevant examples of group 8 and group 9 nitrido complexes, as well as group 9 imido complexes are presented. Lastly, a brief overview of matrix-isolation works dealing with relevant nitrido complexes is given.

1.1. The Nature of Metal-Ligand Multiple Bonds

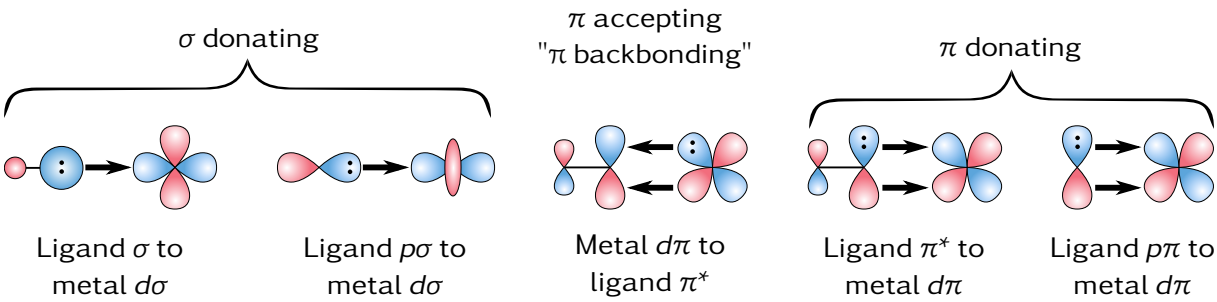

Figure 1.1. Illustration of a few examples of metal-ligand σ- and π-type orbital interactions.

In addition to the M−L σ bond, overlap between appropriate π-type ligand binding site orbitals and metal $d\pi$ orbitals must be invoked. While the metal-ligand σ bonding is usually ligand-to-metal donating, it is established to distinguish between metal-to-ligand (π accepting) and ligand-to-metal (π donating) π bonding (Figure 1.1). The former is known as π backbonding and normally occurs in transition metal complexes of low OSs. The excess charge at the metal center caused by the metal-ligand σ bond is compensated by ligands with empty π^* orbitals which act as π acceptor ligands. The resulting interaction between the filled metal $d\pi$ orbital and the low lying lowest unoccupied molecular orbital (LUMO) of the ligand leads to charge transfer from the metal center and a population of the ligands π^* molecular orbital (MO) and consequentially to a weakening of the corresponding π bond within the ligand. Typical π acceptor ligands are carbonyl (CO), nitrosyl (NO^+), cyanido (CN^-), and to a lesser extend also dinitrogen (N_2).

Ligand-to-metal π bonding is usually found in transition metal complexes of high OSs. It arises when a ligand non- or anti-bonding π-type orbital combines with an unoccupied metal d orbital of appropriate symmetry. The ligand donates electron density through the resulting M−L π bond. If the interacting ligand orbital is π^* antibonding, the π bond within the ligand is strengthened. Typical metal-to-ligand multiple bonds are found in oxo- (M=O or $M^-{\equiv}O^+$), nitrido- (M≡N), imido- (M=NR or $M^-{\equiv}N^+R$),

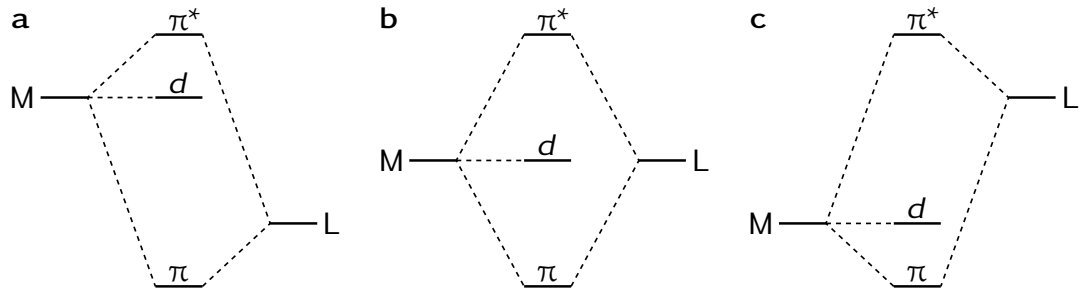

Figure 1.2. Simplified MO diagrams for symmetry-allowed metal-ligand π interactions with different relative energies of the interacting orbitals, including non-bonding metal centered d orbitals.

carbene- (M=CR_2) and carbyne- (M≡CR) complexes. Due to their higher electronegativity (EN) the π-type orbitals of nitrogen or oxygen ligands are usually lower in energy than the metal $d\pi$ orbitals (Figure 1.2, case **a**). It is thus the best way to describe them as closed shell N^{3-}, NR^{2-}, and O^{2-} anions. In contrast, the lower EN of carbon sometimes leads to cases **b** and **c** shown in Figure 1.2. In the latter case the carbyne ligands are best described as CR^{+}. The transition between these extremes depends on the relative energy of the interacting ligand and the metal orbitals. The average energy of the d orbitals decreases as we go from left to right across the transition metals and with increasing metal OS, and decreases in each group from top to bottom. The energy of the ligand based p orbitals decreases on moving from carbon to nitrogen to oxygen. The resulting M−L bonding and antibonding π MOs determine the ligand reactivity. The ligand reacts *nucleophilic* in case **a** in Figure 1.2 when the occupied π bonding orbitals are mostly localized on the ligand binding site while the π^* antibonding combinations have dominant metal d orbital character. As the energy difference between M(d) and L(p) decreases to case **b**, the M−L bonding becomes more covalent, whereas a *electrophilic* reactivity is expected in case **c** where the unoccupied π^* MO are mostly localized at the ligand.

In the formal ionic representation (Figure 1.2, case **a**) N^{3-}, NR^{2-}, O^{2-} and CR^{3-} are isoelectronic closed-shell anions able to form M≡L triple bonds with suitable metal centers.[1] This is most commonly assumed for terminal nitrido and oxo ligands, where these donor ligands lead to qualitatively similar metal orbital d splittings in the 4–6 coordinated complexes shown in Figure 1.3. This shows the influence of the coordination geometry on the d-orbital splitting and reveals that, for instance, four-fold symmetric (tetragonal (TG), C_{4v}) complexes become increasingly unstable when the d-electron count is larger than two. This leads to a population of π^*-antibonding MOs which reduces the formal bond order (BO) of the metal-ligand multiple bond. In this coordination geometry the BO remains unchanged for d^0, d^1 and d^2 low spin configurations and gradually decreases going from d^3 to d^6 from a triple to a single bond. The

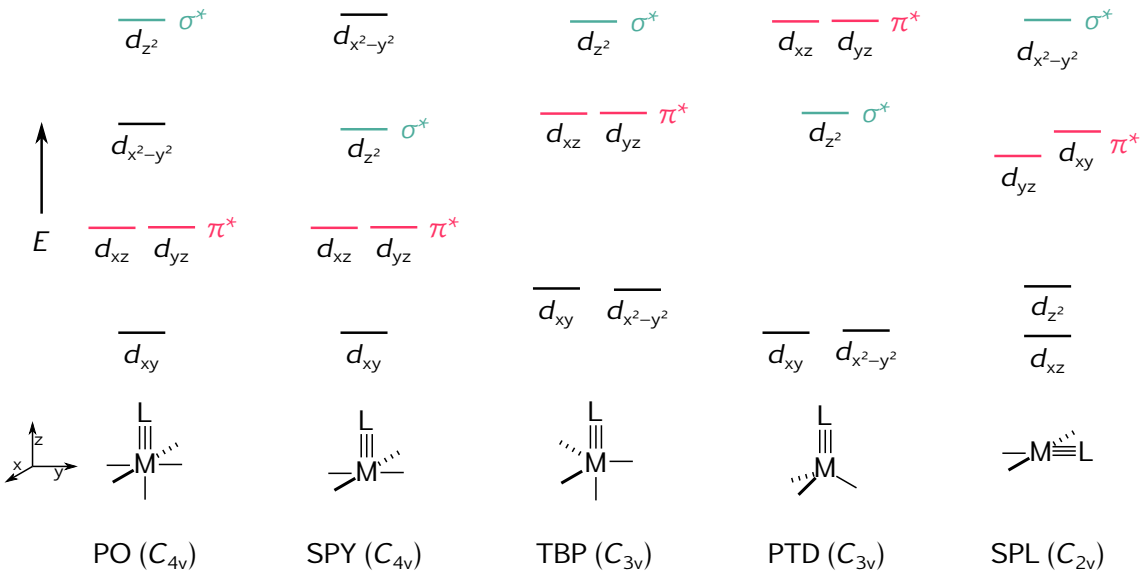

Figure 1.3. Qualitative *d*-orbital splittings for common coordination geometries of two-, three- and fourfold symmetric environments: pseudo octahedral (PO), square pyramidal (SPY), trigonal bipyramidal (TBP), pseudo tetrahedral (PTD) and square planar (SPL). The M≡L σ^* and π^*-antibonding orbitals are highlighted. Note that $d_{x^2-y^2}$ in C_{4v} symmetric coordinations is σ^*-antibonding with respect to ligands in the equatorial plane.

d-electron count of the metal center depends entirely on its position in the periodic table and its OS. The higher oxidation potential and a high *d*-electron count of late transition metals are the reasons for the lower stability of metal-ligand multiple bonds of these metal centers. In the case of oxo complexes, this led to the concept termed *oxo wall* and describes the rule that oxo ligands can not form multiple bonds to metals beyond group VIII in TG environments (PO and SPY coordination geometries).[56] The same is true for nitrogen and so it is also referred to as the *nitrido wall*.[24,57] In contrast, the presence of two instead of one non-bonding *d*-orbitals in trigonal and twofold symmetric geometries (Figure 1.3, C_{3v} and C_{2v}) allow metal-ligand multiple bonds with a higher *d*-electron count without overcoming, but instead *shifting* the oxo/nitrido wall further to the right.[58]

1.2. Oxidation States

The OS of an atom can be used to formally describe the electron count at an atom. A negative OS indicates increased electron count, and a positive OS decreased electron count with respect to the free, neutral atom. Deducted from the linear combination of atomic orbitals (LCAO) model, the bond's electrons are assigned to its main atomic contributor in heteronuclear, and equally in homonuclear bonds. The OS is the hypothetical charge that an atom would have if all heteronuclear bonds were purely

ionic. However, as a purely formal quantity it correlates poorly with the actual electron alignment or charge distribution. OSs are either positive, neutral or negative and are typically represented in integer values. Exceptions can exist when a (hypothetical) charge is shared between chemically equivalent atoms, such as the oxygen in the superoxid anion (O_2^-) which has the OS −0.5. In transition metal complexes the notation d^n describes the number of electrons n occupying d-type orbitals at the metal center. The OS of the metal center is the difference between n and the number of valence electrons of the neutral metal atom. The highest OS of an element within a chemical compound is generally limited by the number of its valence electrons. The activation of core electrons usually can only be overcome under extreme conditions, for example by applying high pressure.[59]

In practice, the assignment of OSs is often straightforward using the appropriate Lewis (resonance) structure of the compound and the EN values of the elements involved. The bond's electrons are assigned to the element with the higher EN. Problematic are compounds for which it is difficult or impossible to create a suitable Lewis structure *a priori*. In cases where the nature of the bond and therefore the electronic alignment is unclear and a satisfying Lewis structure can not be derived, experimental or theoretical methods can be used to assign an OS. Ambiguity may arise when quantum-chemical calculations results in bond polarities that contradict electron alignments suggested by their EN. In some cases the bond polarities depend on the theoretical method employed and may even differ for α and β spin orbitals in spin-unrestricted calculations.[60] The OSs assigned based on the bond multiplicity and EN without considering polarizations of covalent bonds are called *formal* OSs.[61,62] The highest known formal OS is IX, assigned to the iridiumtetroxide cation, $[IrO_4]^+$, experimentally observed in the gas-phase by infrared (IR) photodissociation spectroscopy.[63] Although IR spectroscopy cannot directly determine oxidation states, vibrational frequencies allow a variety of conclusions to be drawn about the properties of the bond in question. Especially supported by quantum-chemical predictions which are validated by experimentally measured parameters. Most of the experimental methods require theoretically calculated reference values. For example, the effective core charge (Z_{eff}) and thus the metal d^n configuration can be estimated using K-edge X-ray absorption spectroscopy (XAS) data of the ligands.[64–66] In Mößbauer spectroscopy, it is possible to observe a nearly linear relationship between OS and isomer shift if a series of complexes with similar geometric and electronic structure are used.[67] These *spectroscopic* OSs may differ from formal OSs.[62]

Transition metal OSs are limited by the redox stability of the ligands, since highly oxidized coordination centers are able to oxidize ligands by spontaneous self-reduction.[68] Predominantly closed-shell and redox-stable ligands that permit the evalua-

tion of the central atom's OS are called *innocent*.[61,69] Examples that are often considered innocent include F^-, Cl^- and O^{2-}, but also CO, CN^- or NH_3.[61] *Non-innocent* behavior arises when electrons cannot be unequivocally assigned to either the ligand or the central atom.[69] A well-known example of a compound with ambiguous oxidation state due to a non-innocent ligand is the "brown-ring" iron complex $[Fe(H_2O)_5NO]^{2+}$, for which Griffith et al.[70] in 1958 deducted a quartet electronic ground state and a $[Fe^{I}(H_2O)_5(^1NO^+)]^{2+}$ formulation. Due to the singly occupied π^*-MO of NO, it may also occur as anionic NO^-[71] or neutral NO.[72] In the most recent work from 2019 by Monsch and Klüfers[60] however, it was concluded that "there are no mandatory reasons to deprecate the $Fe^{I}(NO^+)$ formula in favor of the $Fe^{II}(NO^0)$ or the $Fe^{III}(NO^-)$ formulation". Non-innocent systems may be exploited as redox catalysts in which they participate in the catalytic cycle as electron reservoir, or in formation/breaking of substrate covalent bonds.[73] In these cases they are called *redox active* or *redox non-innocent*.[73–76]

1.3. Matrix-Isolation Spectroscopy

Temperature and concentration are important factors which can be tuned in order to control the rate of any chemical reaction. In chemical kinetics the empirical Arrhenius equation is a formula for the temperature dependence of chemical reaction rates. It states that any chemical reaction that has a reaction barrier can essentially be stopped if the temperature is low enough. In collision theory chemical reactions are rationalized as colliding particles which may lead to a chemical reaction if the collision energy is high enough to overcome the reaction barrier. A higher concentration of reaction partners leads to an increase of the collision rate which in turn leads to a higher reaction rate. This also applies to unimolecular reactions in which the internal energy of the particle needed to overcome the reaction barrier is provided by a collision with a bath particle of the same or different kind.

The matrix-isolation technique, pioneered in its modern form by George C. Pimentel in the 1950s, minimizes temperature and concentration effects and allows trapping reactive or otherwise unstable compounds.[77] This is done by co-depositing an inert host gas at very low temperatures, typically 4 K to 20 K, with a small amount of sample, usually in the 0.01 % to 1 % range, on a cryogenic matrix support in an evacuated chamber at about 1×10^{-6} mbar. The molecules trapped inside the solid, cryogenic matrix are surrounded by chemically inert molecules effectively preventing reaction inducing collisions with other particles. The most typical inert matrix host gases are Ne, Ar and N_2, but also Kr, Xe and CH_4. Reactive matrix hosts are also being used, such as F_2, if the direct formation of higher fluorides is desired.[78,79] The most inert, i.e.,

the least interacting matrix host, is Ne which also often produces highly transparent matrices, followed by Ar.

The most common way to investigate the isolated species is by vibrational or ultraviolet-visible (UV/Vis) spectroscopy, but also electron paramagnetic resonance (EPR) spectroscopy is very well suited for open-shell compounds. The spectroscopic data obtained from matrix-isolation experiments are often rightfully compared to gas-phase data and are often referred to as "pseudo gas-phase" data. An important effect caused by the low temperature and solid state of the matrix is the reduced number of degrees of freedom of the guest molecule by preventing rotational and translational motions. It reduces band broardening effects such as Collision and Doppler broadening as well as rotational transitions. It generally improves the quality of IR spectra and makes matrix-isolation IR spectra easier to interpret compared to spectra obtained using gas-phase experiments. In many cases, however, there are qualitative differences between matrix and gas-phase spectra. Their magnitude depends on the level and nature of the interactions between the guest and host. Especially transition metal ions and other suitable Lewis acids may coordinate matrix host molecules, even noble gas atoms. This can lead to noticeable spectroscopic band shifts and site-splittings with respect to the gas-phase absorption. *Matrix-site splittings*, i.e., IR band splittings observed under matrix-isolation conditions, can be caused by different orientations of the guest molecules inside the matrix cavity. For example, the IR spectrum of CO_2 embedded in Ar shows sharp bands of roughly the same intensity at $663.4\,cm^{-1}$ and $661.9\,cm^{-1}$ in the CO_2 bending region. Both are attributed to the bending mode (ν_2) of monomeric CO_2 in different orientations inside the host matrix.[80] *Matrix shifts* on the other hand are caused by electrostatic or chemical interactions between the matrix guest and the host and have been observed with any matrix gas. They range from rather weak van-der-Waals interactions with matrix shifts of less than $3\,cm^{-1}$ to the formation of complexes with noble gas atoms with significant matrix shifts, especially when symmetries are lifted, of more than $100\,cm^{-1}$.[81]

The workflow and instrumental requirements of a matrix-isolation experiment depend on the nature of the guest and the problem at hand. In any case, the guest must be deposited from the gas-phase seeded in excess host gas. The simplest case would be a pure gaseous sample which can be pre-mixed with matrix gas and directly be deposited on the matrix support. For this method, thermally stable samples that can be evaporated without decomposition can be used. For thermally less stable or highly reactive samples a u-tube can be used in front of the matrix chamber, in which the sample is placed into a stream of matrix host gas which carries the guest molecules with it into the matrix chamber and onto the matrix support. The vapor pressure of the sample is then controlled by adjusting the bath temperature around the u-tube. A Knudsen

cell consists of a quartz tube and a heating element in which a solid sample is exposed to a stream of matrix gas which carries the guest molecules to the matrix support.[82] These methods all have in common that the desired guest molecule is deposited directly, however, it is also possible to study reactions of the precursor molecules directly before or during deposition and to isolate the product molecules. To achieve this a number of methods are available. A gaseous sample can be passed through a heated tube prior deposition to trigger controlled (flash) pyrolysis reactions, or the matrix can be irradiated with visible or UV light to trigger photolysis reactions.[77] Another way is mixing different reactive gases which are allowed to react before or during deposition. For example, radicals, ionic species and excited atoms can be generated in a microwave discharge and co-deposited with a precursor diluted in matrix gas.[83] To react metal atoms with precursor molecules it is possible to evaporate the metal atoms thermally either by directly heating the metal using an electrically heated thin ribbon filament,[84] or by laser-ablation.[85] The latter method has the advantage that even electrically non-conductive material with very low vapor pressure, such as transition metal oxides[86] and alkali halides,[87] can be transferred to the gas-phase.

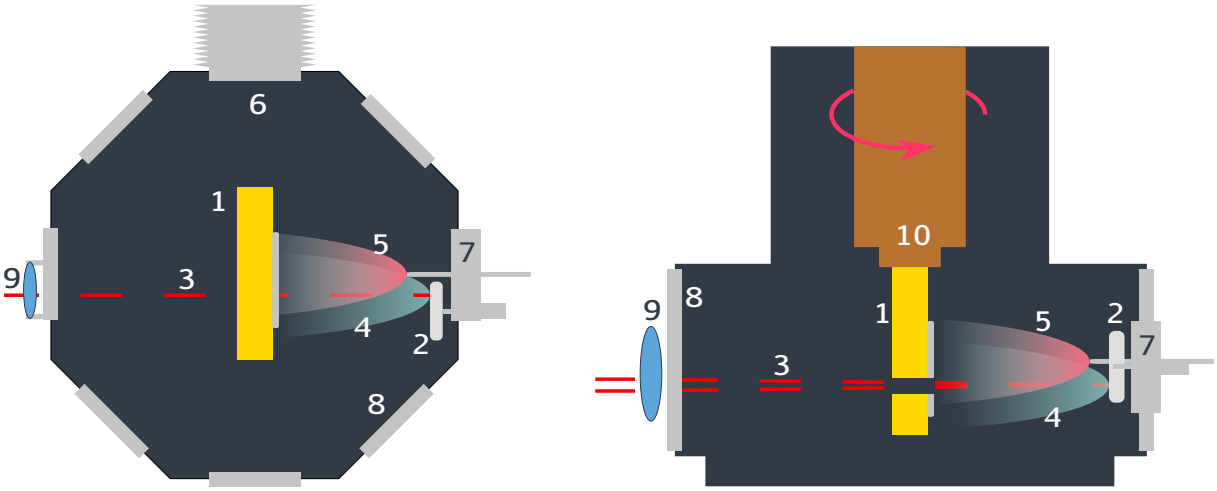

Figure 1.4. Top (left) and side view (right) of an illustration of a matrix chamber for co-depositing precursor gas mixed with laser-ablated material during the laser-ablation process. For measuring operation the matrix support is rotated 90° counterclockwise, for irradiation experiments 45° clockwise. 1 cold gold-plated copper matrix support with hole and matrix layer, 2 rotating laser ablation target, 3 pulsed IR laser, 4 plasma plume, 5 precursor gas, 6 CsI window to attached IR spectrometer, 7 gas nozzle and target motor assembly, 8 quartz windows, 9 focusing quartz lens, 10 closed-cycle helium cryostat & heating element assembly.

Figure 1.4 shows a drawing of an experimental setup that was used in this work. A neodymium-doped yttrium aluminum garnet (Nd:YAG) (λ = 1065 nm) laser pulse of about 10 ns (3) focused by a quartz lens (9) is guided through a hole in the matrix

support (1) and evaporates material from the rotating ablation target (2). The evaporation process at the surface of the ablation target induced by a pulsed nanosecond laser starts with the expulsion of electrons within femtoseconds. It proceeds by a Coulomb explosion of the cationic material left behind and is followed by thermal evaporation of target material under the influence of the pulse.[87] The vaporized target material in the plasma plume (4) is then mixed with precursor gas (5) inside the vacuum chamber and deposited on the cold gold-plated copper matrix support (1) until a sufficient amount of material is deposited. After about 60 min to 120 min when the deposition finished, the matrix support is rotated 90° and an IR spectrum can be recorded in reflection mode using a transfer optic assembly located in the sample compartment of the IR spectrometer and a CsI window (6) attached at the back of the matrix chamber. The high vacuum of 10^{-6} mbar to 10^{-5} mbar enables a controlled deposition rate and ensures thermal insulation of the matrix support held at 4 K to 20 K from the environment. Pumps able to create and maintain these pressures include turbomolecular and diffusion pumps. Both have in common that they transfer momentum to single gas particles in the direction of the outlet. The turbomolecular pump achieves this by rapidly spinning metal turbine blades. The diffusion pump does not contain any moving parts and uses a gas-jet of silicone oil vapor to direct gas particles to the exhaust. The latter is often found in matrix-isolation laboratories thanks to its low maintenance, robustness and longevity. Abrasive gases and sudden increases of pressure can degrade the silicon oil in diffusion pumps, but can destroy turbomolecular pumps.

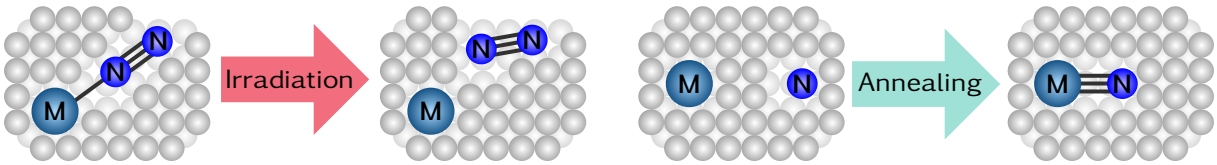

Figure 1.5. Illustration of guest reactions inside the matrix triggered by irradiation (left) and by annealing (right).

After the matrix has been deposited, irradiation and annealing experiments may be conducted. Irradiation experiments can be carried out either by unspecific broadband irradiation using, for example, a high-pressure mercury lamp, or selectively by using optical filters, laser light or light-emitting diode (LED) light with a narrow spectral range around $\lambda_{max} \pm 10$ nm. By using LED or monochromatic laser light it is possible to induce specific unimolecular photochemical reactions, such as rearrangements or dissociation reactions. The irradiation experiment shown in Figure 1.5 illustrates a dissociation reaction of a dinitrogen complex [M(N_2)] to M and N_2. It is worth pointing out that the matrix is exposed to radiation from the laser-ablation process, which could prevent the formation and buildup of photo-sensitive compounds. During irradiation

experiments diffusion effects are minimal and are usually not observed. In annealing experiments diffusion of lighter atoms through the softened matrix may occur. The right part of Figure 1.5 shows the formation of MN enabled by matrix annealing which initiates the diffusion of nitrogen atoms into the matrix cavity containing the metal atom. The annealing temperature is limited. As a rule of thumb, the maximum annealing temperature is approximately half of the freezing point of the matrix host gas. However, it is advisable to stay a little below that, depending on the host, evaporation can happen very suddenly because the temperature gradient within the matrix support and the solid matrix is often not precisely known. Spectroscopic data obtained in Ne are usually very close to those obtained in vacuum, since host guest interactions are very small and it offers a high transparency for all spectroscopic methods. Its low freezing point at 25 K and the resulting low maximum annealing temperature of about 10 K limits its applications in annealing experiments. The next suitable matrix host is Ar (freezing point: 84 K), which allows annealing temperatures of up to about 40 K. However, Ar matrices exhibit stronger host-guest interaction energies and a lower transparency.

Additionally, annealing and irradiation experiments are useful to assign species present in the matrix. As a result of the depletion or the enrichment of certain species, the spectrum looses or gains features. Furthermore, bands associated to the same species form a set of bands that show similar intensity ratios in different experiments. Even small band intensity changes can be made visible with the help of difference spectra. Here, the spectrum of the matrix before treatment is subtracted from the spectrum after treatment. In such a difference spectrum obtained in transmission mode, bands that lost intensity are pointing up, and new bands or bands that gained intensity are pointing down. Varying the host–guest concentration can also facilitate the assignment of unknown bands in the spectrum. When laser ablated atoms are allowed to react with precursor gas molecules, the concentration of the precursor in the matrix gas influences the distributions of different stoichiometries of the reaction products. The isotope effect is a very useful feature for the assignment of unknown bands in an IR spectrum. Isotopologues of precursor material often allow clear assignments of their bands based on their isotopic pattern and associated isotopic shifts, $\Delta\tilde{\nu} = \tilde{\nu} - \tilde{\nu}'$, or isotopic ratios $\left(\frac{\tilde{\nu}}{\tilde{\nu}'}\right)$, with $\tilde{\nu}$ as the band position of the isotopologue containing the most abundant isotope and $\tilde{\nu}'$ the band position of a different isotopologue in which at least one atom is substitutated by a different isotope. In contrast to computed absolute band positions, predicted isotopic ratios are often much more precise and therefore provide solid evidence for band assignments.

1.4. Computational Methods

What makes the chemistry of transition metal complexes so interesting is also what makes their quantum-chemical description difficult. The reliable prediction of transition metal complex properties is one of the most difficult tasks in quantum-chemistry.[88,89] This is, for the most part, because of the near degeneracies of their electronic states.[88]

To theoretically describe chemical bonding in transition metal compounds a number of electronic structure methods are available. For practical reasons, most commonly in electronic structure calculations a MO analysis is employed.[90] Valuable information about the electronic structure can be extracted from the electronic wave function, which makes it the central element for the analysis of the chemical bond. The total wave function of a quantum-mechanical system, such as a molecule, can be obtained by solving the time independent Schrödinger equation (TISE), which depends on electronic and nuclear coordinates.[91] Nuclei move much more slowly than electrons since they are much heavier. For this reason it is assumed within the Born Oppenheimer approximation that electrons are moving in a field of fixed nuclei. In this approximation the total wave function can be expressed as a product of the nuclear and electronic wave function, which depends on the nuclear coordinates only parametrically. Several approximations exist to solve the TISE, of which the Hartree-Fock (HF) method is the simplest. It is based on the expansion of the wave function in a single Slater determinant constructed from spin orbitals.

Wave Function Based Correlation Methods

In single-reference post-HF methods the HF wave function is the basis, or reference, of more sophisticated calculations in an attempt to recover what is called electron correlation energy. In the framework of the LCAO theory a basis set is composed of the spatial part of atomic orbitals, usually represented by orthogonal gaussian-type functions. The minimum number of functions equals the number of atomic orbitals, while the exact electronic wave function of the respective method is a linear combination of an infinite basis set, in practice only finite basis sets can be used. The number of spin orbitals in the Slater determinant is equal to twice the number of basis functions of the basis set. The full configuration interaction (FCI) approach uses a linear variational method which provides numerically exact solutions to the non-relativistic (NR)-TISE. In this method, all Slater determinants that can be generated by all possible electron excitations into all virtual orbitals are included in the variational space.

The correlation energy is the difference between the HF energy and the FCI energy using a complete basis set. The general term for methods which aim to approximate

that energy are called correlation methods, which can be divided further into single and multi-reference correlation methods. Figure 1.6 shows Pople's diagram which il-

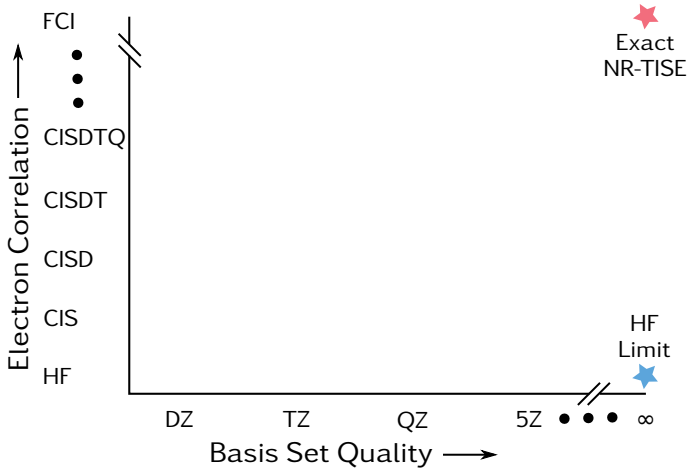

Figure 1.6. Pople's diagram showing the relationship between increasing configuration interaction (CI) excitation levels. The blue star marks the HF limit and the red star exact solution of the NR-TISE.

lustrates the relationship between basis sets and various correlation methods in computational chemistry.[92] While FCI is a conceptional simple method, the exponential dependence on the number of slater determinants limits its application to small systems. Truncated CI methods exist where, for instance, only single and double excitations are included (configuration interaction singles doubles (CISD)). However, there are significantly more efficient methods available, such as Møller-Plesset perturbation theory second order (MP2), where the electron correlation is treated as perturbation of the unperturbed reference wave function with one and two electron excitations. While this method is established and widely used since decades and available in virtually every quantum-chemistry software, it fails to address the rather large electron correlation often found in transition metal compounds.

The coupled-cluster (CC) method is conceptually similar to the FCI method and provides an exact solution to the NR-TISE, but instead of a linear, it follows an exponential expansion ansatz which comes with a number of advantages. The widely used "gold standard" of quantum-chemistry is coupled-cluster singles, doubles and perturbative triples (CCSD(T)). It involves a singles and doubles truncated CC ansatz with triple excitations approximated using perturbation theory.

Truncated CI, MP2 and CCSD(T) and all other methods which use one slater determinant (or reference function) are called single-reference correlation methods and are good approximations only when the reference state is properly described by a single slater determinant, i.e., only dynamic electron correlation needs to be considered. For transition metal compounds this approximation often breaks down and additionally

non-dynamic correlation becomes important when several electronic configurations have similar energies and considerable configuration mixing takes place. The suitability of the single-reference CCSD(T) ansatz for transition metal compounds can be gauged by the values of the T_1, D_1 and %TAE diagnostics.[93,94] The complete active space self-consistent field (CASSCF) method[95] allows one to perform an FCI calculation for a limited orbital space. This *active space* should consist of the most important orbitals and represents the most flexible part of the wave function, i.e., molecular orbitals that are expected to have occupations deviating from 0 and 2, or those that are involved in bond formation/breaking.

The primogenic effect describes the phenomenon and effects of the small and compact nature of the first row transition metal 3*d* orbitals.[96,97] The absence of radial nodes at $r \neq 0$ for shells of a given angular momentum quantum number l that are first occupied (1*s*, 2*p*, 3*d*, ...) leads to the compact nature of these orbitals. The consequence is that the size of the 3*d* orbitals of first row transition metals is actually comparable to those of the 3*s* and 3*p* orbitals. The electrostatic repulsion between the ligand and metal core orbitals prevents a relatively short bond from forming that would be required to maximize the overlap between the metal 3*d* and ligand orbitals. This leads to attenuated ligand–metal overlap and consequently to low excitation energies and considerable mixing of the ground state with excited states. As an example, in Figure 1.7 an active space for a NML_3 $3d^2$ (M = 3*d* metal), which includes the singly occupied, degenerate metal centered d_{xy} and $d_{x^2\text{-}y^2}$ type orbitals (3*e*), as well as the M−N bonding and anti-bonding σ type ($1a_1$, $2a_1$) and π type (2e, 4e) MOs. The green area marks the active space allowing the distribution of 8 valence electrons between all configurations that can be constructed from 8 molecular orbitals, or in short CASSCF(8,8). In this example, the three most contributing configurations contribute in total 75 % to the total electronic CASSCF wave function. The leading configuration determines the electronic state of $^3A_2$ and contributes 60 % to the total CASSCF wave function. The next two largest contributors shown in Figure 1.7 constitute double (10 %) and single excitations (5 %) from the M−N π bonding (2e) into the M−N anti-bonding π^* orbitals (4e). This form of electron correlation is commonly referred to as non-dynamical correlation. The dynamical electron correlation neglected by excluding the inactive and virtual orbitals can be recovered by taking the CASSCF wave function as a reference for subsequent multireference configuration interaction (MRCI)[98,99] or multireference perturbation theory (MRPT)[100] treatment. The latter in the form of complete active-space second-order perturbation theory (CASPT2)[89,101] or the more advanced n-electron valence state perturbation theory second order (NEVPT2)[102] which coincides with MP2 in the case of a HF reference (or single-reference) wave function.

Recent developments to reduce the computational cost and improve the accuracy

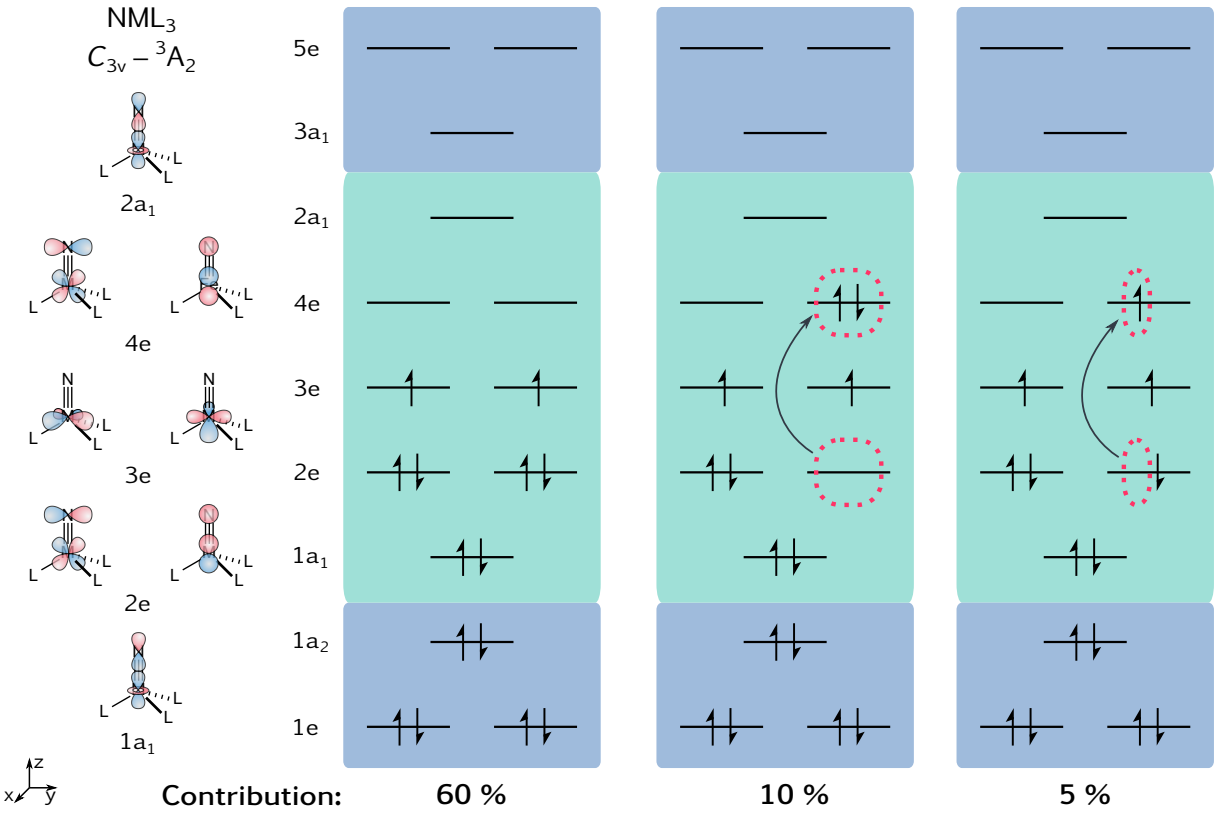

Figure 1.7. The three most contributing electronic configurations to the $^3A_2$ electronic ground state of a NML_3 complex in C_{3v} point group symmetry. The lower blue area contains the highest three MOs of the inactive orbitals ($1a_2$ and two components of 1e) and the top blue area contains the lowest three virtual MOs ($3a_1$ and two components of 5e). The green area contains the active space MOs: eight electrons in eight orbitals.

of wave function based correlation methods include explicitly correlated F12 theories (for example CCSD(T)-F12[103], CASPT2-F12[104] and MRCI-F12[104]) and the linear scaling domain based local pair natural orbital (DLPNO)-CCSD(T)[105] method. Nevertheless, the application of these high-level methods are still limited for geometry optimizations and normal mode analyses of transition metal complexes, in particular for systems larger than six heavy elements, i.e., elements of the second row and beyond.

Density Functional Theory

The HF and all post-HF methods have in common that all properties of the system are derived from the wave function. A different approach is density functional theory (DFT), where these are completely determined by the electron density of the system. The Hohenberg-Kohn[106] theorem is a proof that important properties such as the energy of a system depend directly on the electron density of the system and is

thus the basis for modern DFT. The single Slater determinant based Kohn-Sham (KS)-DFT framework[107] is the most wide-spread formalism and algorithmically very much alike the HF protocol. It is in fact so wide-spread that in quantum-chemistry KS-DFT is often simply referred to as DFT. Despite the similarities to HF, DFT is surprisingly accurate, even for some degree of static correlation. In fact, it is conceptionally accurate, however, for systems more complex than simple model systems the exchange–correlation term is unknown and its functional form needs to be approximated. For this purpose different families of exchange–correlation functionals exist with different levels of sophistication and reliance on empirical parameters.[108,109] The most common and almost universally applicable exchange–correlation functionals include the generalized gradient approximation (GGA) type Becke–Perdew 1986 (BP86),[110,111] and the hybrid type Becke, 3-parameter, Lee–Yang–Parr (B3LYP).[112–115] However, more sophisticated functionals exist,[116] including the long-range corrected family of functionals ωB97[117–119] and the highly parameterized M06[120–123] functionals. Among the latter, the specialized meta-GGA functional M06-L[120] is recommended for systems involving transition metals.[120]

The advantage offered by DFT is the relatively high accuracy with relatively low computational cost. However, unlike wave-function based methods, DFT cannot be systematically improved as it can be, for example, by switching from coupled-cluster singles doubles (CCSD) to CCSD(T). Instead, improvements can be achieved by choosing a more accurate exchange-correlation functional, informally classified in Jacob's ladder in which exchange-correlation functionals with similar capabilities are placed at the same rung.[108]

Relativistic Methods

Relativistic effects in the context of quantum-chemistry are all variances between values calculated by models that consider relativity and those which do not. By ignoring the finite speed of light in the NR-TISE, spin–orbit coupling and kinematic (or scalar) relativistic effects are completely neglected. The incorporation of relativistic effects in quantum-chemical calculations becomes more important as the nuclear charge number increases, making it a requirement for forth row elements and improves the accuracy of geometries and energetics involving elements from the third row.[124] The best relativistic method involves the explicit four-component solutions of the Dirac equation, however, even calculations of diatomic systems with a sufficiently large basis set are very expensive and require significant computational resources.[88,125] Approximations of this method involve the separation of scalar relativistic effects from those caused by spin–orbit coupling, or even removing the explicit consideration of rela-

tivistic effects entirely by using effective core potentials (ECPs).[126] Popular approximations to the Dirac equation used in this work are the Douglas-Kroll-Hess (DKH) Hamiltonian[127,128] and the zeroth order regular approximation (ZORA).[129,130]

Basis Sets

Basis sets are sets of functions which essentially all calculations use to express the unknown MOs by means of a set of known functions. While in principle any type of function might be chosen, in practice, the basis functions should fit the physical problem to be approached and be easy to use in computational algorithms. By weighing these requirements, Gaussian-type functions have emerged as the most used for molecular systems, mainly because they can be implemented most efficiently in computational code. In the LCAO framework, every MO is represented by a linear combination of a finite number of basis functions. For this, there must be at least as many basis functions as there are atomic orbitals of all involved atoms. These minimal basis sets are hardly used in practice because of their bad predictive quality. Split valence basis sets are used much more frequently, in which valence orbitals that are particularly relevant in chemistry are described by more than one basis function. Depending on the number of functions used to describe the valence orbitals, these basis sets are called valence double-, triple-, quadruple-ζ, and so on, basis sets. Functions that can be added to the basis set to improve the description of molecular systems include diffuse and polarization functions. The latter are integrated in most of the popular basis sets by default and the former can be added if systems are prone to dispersion effects, such as anions, or to gain accuracy in systems involving inter- and intramolecular non-covalent bonds.

A popular general purpose polarized split valence basis set, especially suitable for DFT calculations, is the def2 family of basis sets[131–134] of the Karlsruhe group of which the quadruple-ζ basis set def2-QZVP achieves near basis set limit accuracy for atomization energies at the DFT level of theory.[134] They are all-electron basis sets for elements H to Kr, and automatically load Stuttgart–Dresden ECPs for elements Rb to Rn.[133,135–138]

The quasi-standard for wave function based correlation methods is the correlation consistent family of basis sets which come with a number of useful features and variants. The standard variant follows the cc-pVnZ scheme (i.e.: correlation-consistent polarized n valence split, with n = D, T, Q, 5 for double-, triple-, quadruple- and 5-ζ qualities, respectively).[139–146] Popular variants incorporate relativistic effects in the form of ECPs (sufix "-PP")[133,138,147–153] or via the use of a DKH Hamiltonian (sufix "-DK"),[154] augmentations with diffuse functions to better satisfy the long-range part of the wave function of anions ("aug-" prefix), and core–valence correlation (cc-

pwCVnZ).[139,155,156] These basis sets are designed to systematically converge towards the complete basis set (CBS) limit with increasing cardinal number n. A large number of extrapolation schemes that can be used to estimate the CBS limit have been proposed.[157]

Wave Function Analysis

The wave function obtained by solving the electronic TISE determines all information that can be known from a quantum system. Unlike the electron density, which can be easily obtained from the wave function, the wave function itself does not have any physical meaning. A number of analytical methods have been developed to extract useful information from the wave function, such as magnetic properties, MO populations and compositions, as well as BOs and atomic charges. The latter is an important property to categorize reactive sites in molecules as electrophile (positive charge) or nucleophile (negative charge). The most commonly used approaches to assign charges to atoms are based on partitioning the electron density and distributing it to individual atoms based on the electrostatic potential, basis functions or topology. Established partition methods based on basis functions are the Mulliken[158] and the Löwdin[159] methods, which both best perform with small or medium sized basis sets but can lead to odd behavior, especially when used in conjunction with diffuse basis sets.[124] A more sophisticated method called natural bond orbital (NBO) analysis involves orbital transformations into a (localized) form which allows to analyze the wave function in terms of the classical Lewis structure concept of two-center electron pairs (bonds) and one-center electron pairs (lone pairs).[160]

Somewhat physically more justified is to analyze the electron density itself instead of the basis functions representing the wave function. The quantum theory of atoms in molecules (QTAIM) method of R. Bader[161–163] is probably the most accurate way to divide the molecular volume into atomic subspaces containing exactly one nucleus. In this framework, chemical bonding is defined based on the topology of the electron density with stationary points together with the gradient paths that connect and terminate at these points. Among these stationary points are maxima and saddle points. The former usually correspond to the position of the nuclei and are called attractors. One type of the latter is called bond critical points which are usually positioned between two attractors with one positive and two perpendicular negative second derivates. The electron density at a bond critical point (ρ_{bcp}) is associated with the bond strength and BO.[163] Based on the topology analysis, the total electron density can be assigned to attractors and its integration within each atomic basin gives atomic charges and electric moments.

From MO considerations the formal BO of a bond between two atoms is defined by Equation 1.

$$\mathrm{BO} = \frac{\text{number of bonding } e^- - \text{number of antibonding } e^-}{2} \tag{1}$$

It is a simple scheme to evaluate the number of electrons (e^-) shared between two atoms, which indicates the stability of the bond. An extension to that is the effective bond order (EBO) which allows fractional numbers and is obtained from natural occupations using the same formula.[164] The EBO is always smaller than the formal BO and the multiplicity of a bond is named according to the next larger integer value.[164]

Spin density profiles are obtained by subtracting the electron densities of the spin down (β) electrons from the one of the spin up (α) electrons obtained from spin-unrestricted calculations. They permit a simple, quick and visualizable probe of ligand non-innocence (see Section 1.2) in transition metal complexes in which positive or negative spin density at the ligand indicate spin delocalization or spin polarization, respectively.[69]

1.5. Nitrido Complexes of the Group 8 and Group 9 Transition Metals

A survey of selected known terminal nitrido complexes of the group 8 (iron, ruthenium and osmium) and group 9 (cobalt, rhodium and iridium) transition metals is presented. Additionally, selected terminal imido complexes are included for group 9 transition metals. The overview focuses on molecular complexes featuring metal–nitrogen multiple bonds for which experimental structural or vibrational data are available. In addition, a short overview of relevant matrix-isolation works in which the reaction products of laser-ablated transition metal atoms and dinitrogen, as well as nitrogen trifluoride were investigated is given.

1.5.1. Group 8

Transition metals of group 8 have 8 valence electrons and can reach oxidation states of up to VIII (Ru and Os). Os(VI) nitrido complexes in tetragonal structures with low-spin d^2 configurations avoid any population of antibonding π^* MOs (see Figure 1.3) and facilitate strong Os≡N triple bonds. Trigonal symmetric structures on the other hand, are able to accommodate up to four electrons in their non-bonding d-type MOs (Figure 1.3). Hence, the lowest OS needed to enable triple bonds for these structures is IV.

Iron Nitrido Complexes

The first terminal nitrido iron complex was reported by Wagner and Nakamoto[165] in 1988. The square planar porphyrin ligand based [(TPP)Fe^{V}N] complex (Figure 1.8 **A**) was produced by photolysis of the corresponding azide precursor and its resonance Raman (RR) spectrum was reported.[165] In 1989 the related complexes [(OEP)Fe^{V}N] and [(TMP)Fe^{V}N] were obtained by the same group using the same method.[166] Raman spectra of these complexes show Fe−N stretching frequencies at around 875 cm^{-1} as well as $^{14/15}$N isotopic shifts. The claimed OS of Fe(V) in the these complexes was questioned by Meyer et al.[168] in view of the non-innocent nature of the employed auxiliary ligands. However, a very recent report of the related [(TTPPP)Fe^{V}N] complex by Wang et al.[167] describes a Fe(V) center with a low-spin $(d_{xy})^2(d_{xz})^1(d_{yz})^0$ configuration (BO = 2.5) and an Fe−N stretching frequency of 876 cm^{-1} (RR), which supports the previously reported data for [(TPP)Fe^{V}N], [(OEP)Fe^{V}N] and [(TMP)Fe^{V}N].

About 10 years later, Meyer et al.[168] and shortly thereafter Grapperhaus et al.[169] presented the first cyclam ligand based pseudo octahedral nitrido complexes [(cyclam)(N$_3$)Fe^{V}N]$^+$ and [(cyclam-ac)Fe^{V}N]$^+$ (Figure 1.8 **B** and **C**), respectively, produced by

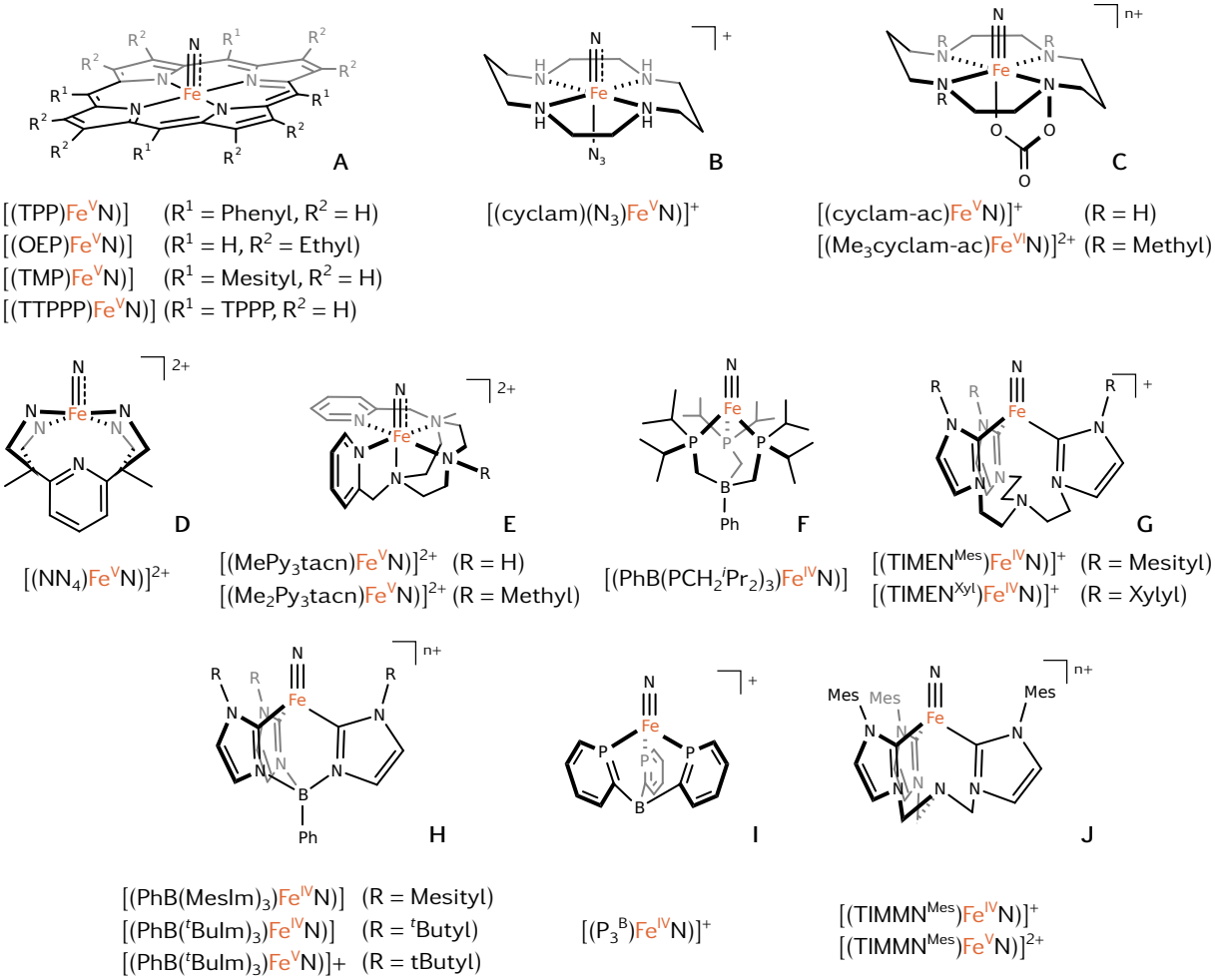

Figure 1.8. Selection of known iron nitrido complexes of tetragonal (**A**,[165–167] **B**,[168] **C**,[67,169] **D**,[170] **E**[171,172]) and trigonal symmetry (**F**,[173] **G**,[174] **H**,[15,175,176] **I**.[37] **J**[177])

photolysis of the corresponding azide in a frozen CH_3CN solution at 77 K to avoid dimerization. For these complexes, Fe(V) in d^3 high-spin configuration was found by Mößbauer and EPR spectroscopy, indicating the occupation pattern $(d_{xy})^1(d_{xz})^1(d_{yz})^1$ and a BO of 2. The Fe−N stretching mode was not reported, however, Fe−N stretching frequencies of 855 cm^{-1} and 864 cm^{-1} were later obtained for $[(cyclam\text{-}ac)Fe^{V}N]^+$ using infrared photodissociation (IRPD) spectroscopy[172] and nuclear resonant vibrational spectroscopy (NRVS),[178] respectively. The frequencies of these cationic complexes are somewhat lower than the RR frequencies obtained for the neutral Fe(V)-porphyrinato nitrido complexes (Table 1.1). The oxygenation of $[(cyclam\text{-}ac)Fe^{V}N]^+$ lead to an iron nitrosyl complex.[179]

Until the report of the dicationic complex $[(Me_3cyclam\text{-}ac)Fe^{VI}N]^{2+}$ by Berry et al.[67] in 2006 (Figure 1.8 **C**), the ferrate anion FeO_4^{2-} was the only known iron(VI) compound. Like the other cyclam-based complexes it was obtained by photolysis of the

corresponding azide, but *N*-methylation of the cyclam-ac ligand allowed the oxidation of the precursor to a stable Fe(IV)-azido complex prior photolysis. The Fe−N bond length of 157 pm was estimated by fitting extended X-ray absorption fine structure (EXAFS) data. Based on its Mößbauer spectrum and supported by DFT calculations the iron center adopts an OS of VI in a d^2 low-spin singlet configuration consistent with an occupation pattern of $(d_{xy})^2(d_{xz})^0(d_{yz})^0$ and a genuine Fe≡N triple bond, for which a computed Fe≡N stretching frequency of 1064 cm^{-1} (DFT) was reported.

Other tragonal dicationic nitrido iron complexes based on macrocyclic amine ligands, suchs as $[(NN_4)Fe^{V}N]^{2+}$[170] (Figure 1.8 **D**), $[(MePy_2tacn)Fe^{V}N]^{2+}$,[171] and $[(Me_2Py_2tacn)Fe^{V}N]^{2+}$[172] (Figure 1.8 **E**) have been published. The FeN stretching frequencies obtained by IRPD spectroscopy of the latter two complexes are reported to be 855 cm^{-1} and 867 cm^{-1},† as well as 866 cm^{-1}, respectively.[172] Thus, reported Fe−N stretching frequencies for tetragonal terminal Fe^{IV} and Fe^{V} nitrido complexes are within 855 cm^{-1} to 867 cm^{-1}, indicating comparable Fe−N bond strengths.

The Fe−N stretching frequency of the first reported trigonal symmetric pseudo tetrahedral complex $[(PhB(CH_2P\mathit{i}Pr_2)_3)Fe^{IV}N]$ (Figure 1.8 **F**), published by Betley and Peters[173] in 2004, was recorded in pentane at 1034 cm^{-1}, and is significantly higher than those assigned to the tetragonal symmetric complexes. The MO occupation pattern of $(d_{xy})^2(d_{x^2-y^2})^2(d_{yz})^0$ shows a low-spin d^4 configuration and accordingly a BO of 3. The short bond length of 153(2) pm obtained by fitting EXAFS data reflects the presence of an Fe≡N triple bond in accord with the observed Fe≡N vibrational frequency.[180] In contrast to all other iron nitrido complexes presented here, this complex was not prepared by photolysis of the corresponding azide, but from an iron chloride precursor and the *N*-atom transfer reagent Li(dbabh) (dbadh = 2,3:5,6-dibenzo-7-aza bicyclo[2.2.1]hepta-2,5-diene) by liberation of anthracene.

The first crystal structure obtained by X-ray diffraction (XRD) of a terminal iron nitrido complex was published in 2008 by Vogel et al.[174], which yielded bond distances of 152.6(2) pm and 152.7(3) pm for $[(TIMEN^{R})Fe^{IV}N]^{+}$ (R = Mesityl, Xylyl, see Figure 1.8 **G**). In the same year the crystal structure of $[(PhB(\mathit{t}BuIm)_3)Fe^{IV}N]$ with a Fe−N bond distance of 151.1(2) pm was reported (Figure 1.8 **H**).[175] It was later shown that this bond distance was influenced by coordinated solvent molecules and that the Fe−N bond distance in the solvent-free crystal structure is 153.2(5) pm.[181] The Fe−N stretching frequencies for these three complexes of 1008 cm^{-1}, 1008 cm^{-1} and 1029 cm^{-1} (RR), respectively, which combined with the short Fe≡N bond distances of about 153 pm indicate strong Fe≡N triple bonds. An in-depth experimental and computational study of $[(PhB(\mathit{t}BuIm)_3)Fe^{IV}N]$ by Bucinsky et al.[181] confirms a singlet ground state and a d^4 configuration with a $(d_{xy})^2(d_{x^2-y^2})^2(d_{yz})^0$ occupation pattern,

†Signals split due to coupling between the FeN stretching and ligand vibrational modes.

which supports previous results of Betley and Peters[173] on $[(PhB(CH_2PiPr_2)_3)Fe^{IV}N]$. These complexes have shown to undergo nitrogen atom transfer reactions with CO and C≡N*t*Bu, leading to the formation of new N−C bonds.[182] A rather short Fe−N bond distance of 150.9(2) pm has been determined by XRD for the neutral complex $[(PhB(MesIm)_3)Fe^{IV}N]$ shown in Figure 1.8 **H**,[15,181] while a longer bond distance of 154(2) pm (EXAFS fit) was found for the cationic complex $[(P_3^B)Fe^{IV}N]^+$ (Figure 1.8 **I**).[37]

Interesting observations have been made for Fe^{IV}≡N/Fe^{V}≡N redox pairs $[(PhB(tBuIm)_3)Fe^{IV}N]^{0/+}$ on one hand,[175,176,181] and $[(TIMMN^{Mes})Fe^{IV}N]^{0/+}$ (Figure 1.8 **J**) on the other.[177] The oxidation should lead to shorter bond distances due to an increased Coulomb attraction between the formal Fe^{5+} and N^{3-} ions. However, in case of the former pair, the Fe−N bond distance decreases upon oxidation quite considerably from 153.2(5) pm to 150.6(2) pm, while this distance increases from about 151.3 pm (average, see Table 1.1) to 152.9(2) pm for the latter. This unexpected observation was attributed to the higher steric flexibility of the $TIMMN^{Mes}$ chelate ligand, allowing for a larger distortion of the d^3 metal orbitals. In addition, for both of the trigonal symmetric Fe^{V}≡N complexes the e^3 occupation lead to Jahn–Teller distortions which lift the degeneracy of the *e*-orbital set.

Lastly, the stretching frequency and bond distance of the diatomic FeN was determined to be 871 cm^{-1} and 158.0 pm, respectively, by Aiuchi and Shibuya[183] in 2000. Due to the many low-lying states its electronic ground state was very difficult to determine.[183–186] In the end, a doublet $^2\Delta$ ground state was obtained with a $(1\sigma^2)(2\sigma^2)(1\pi^2)(1\delta^3)(3\sigma^2)$ configuration,[187] which is consistent with the first prediction by Siegbahn and Blomberg[184] using CASSCF in 1984. The 3σ ($4s$) orbital is considered repulsive and this repulsion likely contributes to a low stretching frequency compared to other iron nitrido complexes bearing Fe≡N triple bonds.[184] In matrix-isolation studies, in which the reaction products of laser-ablated iron with dinitrogen were studied and isolated in solid argon, a stretching frequency of diatomic FeN was assigned to a band located at 938 cm^{-1}, significantly larger than the gas-phase value of 871 cm^{-1}.[185] This large frequency shift could be due to an ArFeN complex, but also a different electronic state of matrix-isolated FeN cannot be excluded.[183]

While this summary shows the enormous progress that has been made in recent years in the synthesis of molecular iron nitrido complexes, it also shows that with $[(Me_3cyclam\text{-}ac)Fe^{VI}N]^{2+}$ only one experimentally known hexavalent iron nitrido complex exist. Thus, no trigonal symmetric Fe(VI)-nitrido complex has so far been reported. It can be concluded that the influence of the stabilizing macrocyclic and chelating ligands on the electronic structure, the Fe−N bond length and the Fe−N stretching vibration frequency cannot be neglected. Thus, the available data only allow limited

conclusions about the electronic structure and the nature of the Fe−N bond in nitrido iron(VI) complexes which are not stabilized by bulky substituents.

Ruthenium Nitrido Complexes

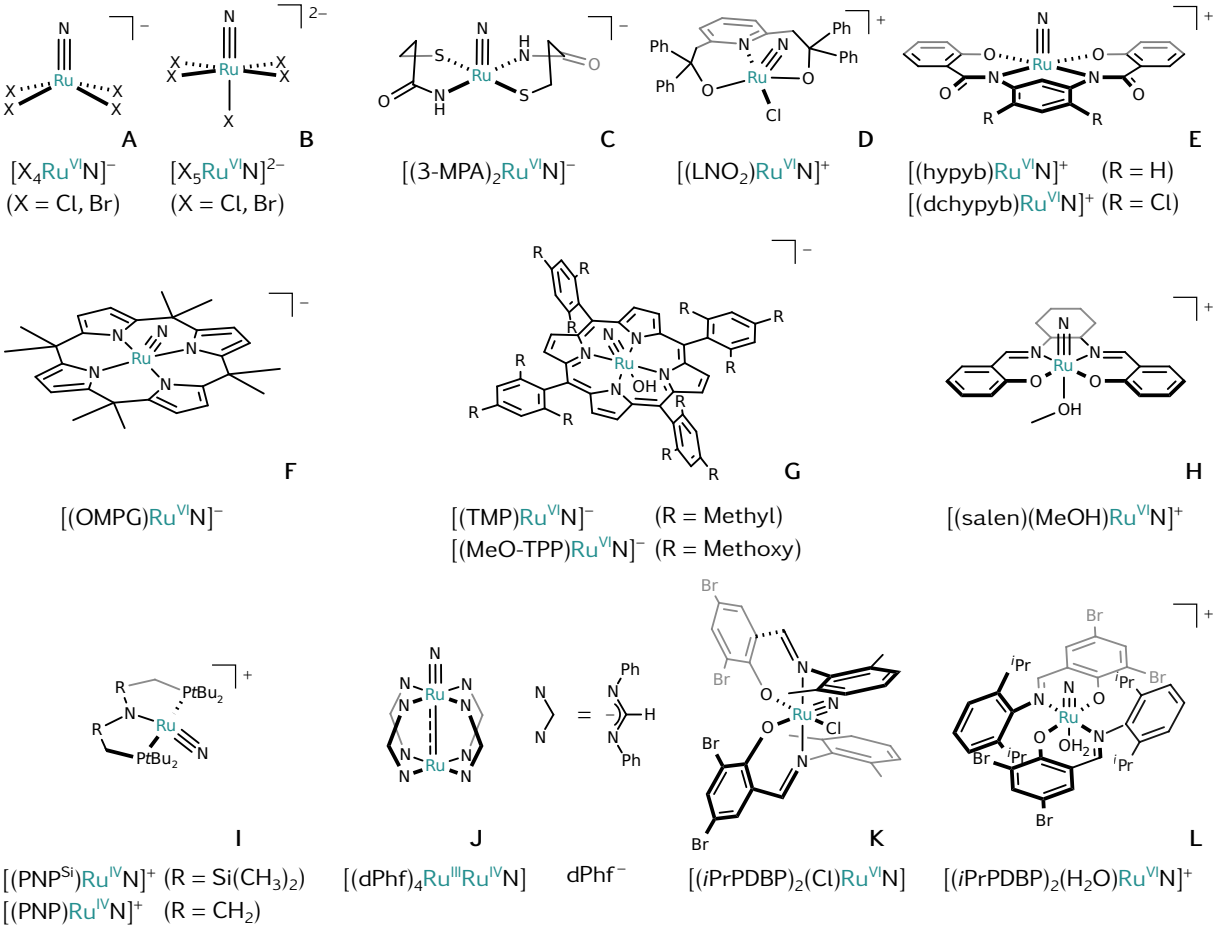

Figure 1.9. Selection of experimentally known terminal ruthenium nitrido complexes: **A**,[190] **B**,[190] **C**,[191] **D**,[191] **E**[191] **F**,[192] **G**,[193] **H**,[194] **I**,[17,195] **J**,[196] **K**,[197] and **L**.[197]

In 1973 the first terminal ruthenium nitrido complexes, $[(X_4)Ru^{VI}N]^-$ and $[(X_5)Ru^{VI}N]^-$ with X = Cl or Br (Figure 1.9 **A** and **B**, respectively), were published by Griffith and Pawson[190]. $[(Cl_4)Ru^{VI}N]^-$ turned out to be particularly useful, as numerous complexes have been derived from it (see below). It features a Ru−N bond distance of 157.0(7) pm[198] and a Ru−N stretching frequency of 1090 cm^{-1}, very close to the band at 1088 cm^{-1} obtained for the bromido congener. As evident from the lower stretching frequency of 1045 cm^{-1} obtained for $[(X_5)Ru^{VI}N]^-$ (X = Cl, Br) *trans* coordination weakens the Ru−N bond.

Bidentate ligands involving sulfide and amide donors were used by Schwab et al.[199] to obtain $[(3\text{-MPA})_2Ru^{VI}N]^-$ (Figure 1.9 **C**) from $[(Cl_4)Ru^{VI}N]^-$ in 1991. A Ru−N bond

Table 1.1: Selection of experimentally known terminal iron nitrido complexes. Reported Fe−N bond distances, d(Fe−N), in pm, and vibrational frequency, $\tilde{\nu}$, of the iron nitrido stretching mode [ν(Fe−N)] in cm^{-1} are included.

Complex	Syn [a]	Geom. [b]	d(Fe−N)	$\tilde{\nu}[\nu$(Fe−N)]	Year[REF]
$[(TPP)Fe^{V}N]$	P	SPY	—	876 [c]	1988[165]
$[(OEP)Fe^{V}N]$	P	SPY	—	876 [c]	1989[166]
$[(TMP)Fe^{V}N]$	P	SPY	—	873 [c]	1989[166]
$[(cyclam)(N_3)Fe^{V}N]^{+}$	P	PO	—	—	1999[168]
$[(cyclam\text{-}ac)Fe^{V}N]^{+}$	P	PO	161 [d]	855 [e]	2000[169]
$[(Me_3cyclam\text{-}ac)Fe^{VI}N]^{2+}$	P	PO	157(2) [f]	[1064]	2006[67]
$[(NN_4)Fe^{V}N]^{2+}$	P	PO	[160]	—	2008[170]
$[(MePy_2tacn)Fe^{V}N]^{2+}$	P	PO	164 [g]	855, 867 [h]	2017[171]
$[(Me_2Py_2tacn)Fe^{V}N]^{2+}$	P	PO	[158–160]	866	2018[172]
$[(TTPPP)Fe^{V}N]$	P	SPY	[159]	876 [c]	2021[167]
$[(PhB(CH_2PiPr_2)_3)Fe^{IV}N]$	L	PTD	153(2) [i]	1034 [j]	2004[173]
$[(TIMEN^{Mes})Fe^{IV}N]^{+}$	P	PTD	152.6(2) [k]	1008 [l]	2008[174]
$[(TIMEN^{Xyl})Fe^{IV}N]^{+}$	P	PTD	152.7(3) [k]	1008 [l]	2008[174]
$[(PhB(tBuIm)_3)Fe^{IV}N]$	P	PTD	153.2(5) [m]	1028 [c]	2008[175]
$[(PhB(MesIm)_3)Fe^{IV}N]$	P	PTD	150.9(2) [n]	—	2009[15]
$[(PhB(tBuIm)_3)Fe^{V}N]^{+}$	P	PTD	150.6(2) [o]	—	2011[176]
$[(P_3^B)Fe^{IV}N]^{+}$	P	PTD	154(2) [p]	—	2017[37]
$[(TIMMN^{Mes})Fe^{IV}N]^{+}$	P	PTD	150.0(3) [q]	—	2021[177]
$[(TIMMN^{Mes})Fe^{V}N]^{2+}$	P	PTD	152.9(2) [r]	—	2021[177]
[FeN]	E	LI	158.0 [s]	871 [t]	2000[183]

[a] Synthesis; P: Photolysis of corresponding azide; L: Using *N*-transfer reagent Li(dbabh) (dbadh = 2,3:5,6-dibenzo-7-aza bicyclo[2.2.1]hepta-2,5-diene) from chlorido precursor; E: From elements in gas-phase

[b] Coordination Geometry, see Figure 1.3; LI: Linear

[c] Resonance Raman

[d] EXAFS fit;[188] DFT: 161 pm[188]

[e] From IRPD spectroscopy;[172] NRVS: 864 cm^{-1}[178] DFT: 937 cm^{-1}[178,188]

[f] EXAFS fit; DFT: 153 pm

[g] EXAFS fit; DFT: 160 pm

[h] Coupling of the FeN stretching and ligand vibrational modes; From IRPD spectroscopy[172]

[i] EXAFS fit;[180] DFT: 149 pm,[173] 151 pm[189]

[j] Pentane solution

[k] From XRD

[l] KBr pellet

[m] From XRD;[181] Original publication solvated (MeCN): 151.1(2) pm[175,181]

[n] From XRD;[181] Original publication solvated (MeCN): 149.9(5) pm[15,181]

[o] From XRD at 35 K and 150.2(2) pm at 100 K

[p] EXAFS fit; DFT: 151 pm

[q] From XRD; Complex crystallizes in space group C2/*c* with two independent molecules per unit cell with Fe−N bond distances of 150.0(3) pm and 152.6(3) pm

[r] From XRD; DFT: 151 pm

[s] From laser-induced fluorescence (LIF) excitation spectroscopy

distance of 159.5(8) pm and a corresponding stretching frequency of 1094 cm^{-1} were reported.

In 1998 Ram et al.[200] studied diatomic, neutral RuN by using Fourier-transform infrared (FTIR) emission spectroscopy combined with multi-reference calculations. A doublet $^2\Sigma^+$ ground state with a stretching frequency of 1109 cm^{-1} and a configuration of $(1\sigma^2)(2\sigma^2)(1\pi^2)(1\delta^4)(3\sigma^1)$ was determined. The fully occupied non-bonding, degenerate 1δ orbital, and a single occupation of the slightly repulsive 3σ $[(n-1)d]$ orbital of RuN differs from the ground state configuration of FeN (see above). This study was followed by a second work of Ram and Bernath[201] in 2002 in which a refined equilibrium bond distance (r_e) of 157.1 pm was determined using Fourier-transform emission spectroscopy, which confirms the theoretical predictions of a strong triple bond from the earlier work and provides a basis for a comparison of terminal Ru−N bond distances.[200] On this basis the Ru−N bond length and stretching frequencies obtained for the anionic complexes $[(Cl_4)Ru^{VI}N]^-$ and $[(3\text{-MPA})_2Ru^{VI}N]^-$ are indicative for strong triple bonds and low-spin d^2 configurations without population of antibonding orbitals (cf. Figure 1.3). It is worth pointing out that the band at 982 cm^{-1}, assigned to RuN isolated in solid argon, also deviates significantly from the one obtained in the gas-phase (1109 cm^{-1}).[202]

Chan et al.[191] in 1998 presented a series of ruthenium(VI) nitrido complexes containing di-, tri- and tetra-anionic ligands, such as $[(LNO_2)Ru^{VI}N]^+$, $[(hypyb)Ru^{VI}N]^+$ and $[(dchypyb)Ru^{VI}N]^+$ (Figure 1.9, **D** and **E**). They were prepared by ligand substitution reactions from $[(Cl_4)Ru^{VI}N]^-$, and their Ru−N bond distances (XRD: 161.5(5) pm, 159.4(4) pm and 160.9(6) pm, respectively), and stretching frequencies (1026 cm^{-1}, 1073 cm^{-1} and 1010 cm^{-1}, respectively) were obtained. The electronic structure and bonding of the nitrido ligand was not discussed, but the Ru−N bond distances and vibrational frequencies indicate formal triple bonds, although the frequency of 1010 cm^{-1} assigned to $[(dchypyb)Ru^{VI}N]^+$ is considered to be on lower end of the spectrum for a Ru≡N triple bond.

A remarkably short Ru−N bond distance of 156.9(6) pm was determined for the anionic, hexavalent porphyrinogen complex $[(OMPG)Ru^{VI}N]^-$ (Figure 1.9 **F**) by Bonomo et al.[192] in 2001, however, no vibrational data were reported. This complex, that was obtained by reacting $[(OMPG)Ru^{II}]^{2-}$ with diphenyldiazomethane, shows an electrophilic nitrido nitrogen atom, and undergoes a reversible one-electron reduction to a dianionic ruthenium(v) nitrido complex, which is expected to show a longer bond distance due to the occupation of antibonding orbitals.[192]

The porphyrin based complexes $[(TMP)Ru^{VI}N]^-$ and $[(MeO\text{-}TPP)Ru^{VI}N]^-$ presented by Leung et al.[193] in 2003 and shown in Figure 1.9 **G** were prepared from the corresponding metal oxo complexes using $HN{=}CtBu_2$. The Ru−N stretching frequency

of the former was found at 1038 cm^{-1}, while the Ru−N bond distance for the structurally closely related latter complex amounts to 165.6(5) pm, both values indicate Ru≡N triple bonds.

Because of the highly electrophilic/oxidizing nature of the complex [(salen)(MeOH)$Ru^{VI}N]^+$ (Figure 1.9 **H**), bearing Schiff base salen ligand and published by Man et al.[194] in 2004, a number of reactivity studies have since been published. These include nitrogen atom transfer reactions to alkenes,[203] and the activation of C−H bonds.[204,205] It catalyzes the hydrosilylation of ketones and aldehydes,[206] the nitrogenation of alkynes,[207] as well as the oxidation of ascorbic acid, phenols, or hydroquinones.[208–210] This complex, obtained from $[(Cl_4)Ru^{VI}N]^-$, displays a characteristic Ru≡N triple bond distance of 159.2(4) pm and a stretching frequency of 1059 cm^{-1}.

The distorted square planar structure of the tetravalent pincer complexes $[(PNP^{Si})Ru^{IV}N]^+$[195] and $[(PNP)Ru^{IV}N]^+$[17] shown in Figure 1.9 **I** has been attributed to the preference of the d^4 configuration to adopt a pseudo tetrahedral geometry to optimize RuN multiple bonding. The Ru−N bond distances of these complexes amount to 162.7(2) pm and 165.8 pm, respectively. The reactivity and selectivity of the former complex against electrophilic attacks was studied.[211,212] The differences in the Ru−N bond distances is also reflected in their Ru−N stretching frequencies of 1030 cm^{-1} and 976 cm^{-1}, respectively. A considerable disorder regarding the nitrido ligand in the molecular structure derived by XRD of the latter complex was solved by applying a split model for the nitrido ligand with Ru−N bond lengths of 168.8(3) pm and 162.8(4) pm, accompanied by N−Ru−N angular distortions from a square planar structure of 147.3(2)° and 165.6(3)°, respectively. This observation was rationalized by the flat N−Ru−N bending potential attributed to competitive π bonding abilities of the nitrido and amido ligands.

The dinuclear complex $[(dPhf)_4Ru^{III}Ru^{IV}N]$ (Figure 1.9 **J**) reported by Pap et al.[196] demonstrates that a metal-metal multiply bonded complex is capable of binding a terminal ligand with multiple bonds. Despite the long Ru−N bond distance of 176 pm obtained by fitting EXAFS data and the low corresponding stretching frequency of 847 cm^{-1}, theoretical calculations confirm a formal Ru≡N triple bond which lies between the extremes of mononuclear ruthenium(VI) nitrido and a Ru-surface-bound nitrogen atom. This interaction is stabilized by electron delocalization over the second Ru atom leading to nonbonding MO combinations that can accommodate the electrons that would otherwise occupy antibonding orbitals in mononuclear species.[196]

Lastly, the ruthenium(VI) complex *cis*-$[(i\text{PrPDBP})_2(Cl)Ru^{VI}N]$ presented by Ng et al.[197] and shown in Figure 1.9 **K** features sterically bulky bidentate Schiff base ligands. The cationic complex *trans*-$[(i\text{PrPDBP})_2(H_2O)Ru^{VI}N]^+$ shown in Figure 1.9 **L** is obtained after chloride abstraction and undergoes a rearrangement where the ni-

trido ligand is positioned in a *trans* position to the aqua ligand. In contrast to [(salen)(MeOH)$Ru^{VI}N]^+$, this complex did not react with nucleophiles, demonstrating that electronic and steric factors of the co-ligands influence the stability and reactivity of ruthenium(VI) nitrido complexes.

So far and to the best of my knowledge, no tetrahedral ruthenium nitrido complexes are known. Further, ruthenium complexes with oxidation states beyond VI are rare. They include tetrapropylammonium perruthenate (TRAP), a mild oxidizing agent used in the Ley-Griffith-oxidation reaction to convert primary alcohols into aldehydes,[213] and was proposed as intermediate within the catalytic cycle of the oxidative cyclization of 5,6-dihydroxy alkenes.[214] However, no ruthenium(VII) nitrido species has been reported up to date.

Osmium Nitrido Complexes

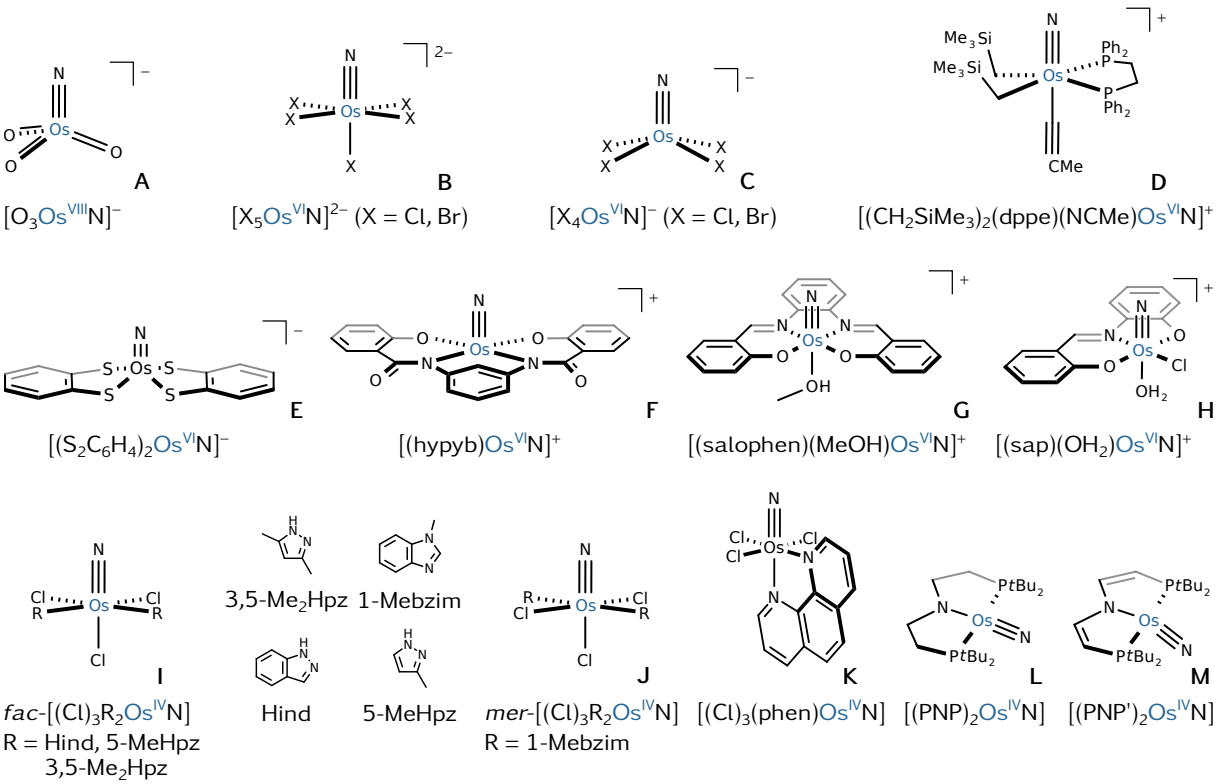

Figure 1.10. Selection of experimentally known terminal osmium nitrido complexes: **A**,[12] **B**,[215] **C**,[190] **D**,[216] **E**[217] **F**,[191] **G**,[218] **H**,[219] **I**,[28] **J**,[28] **K**,[220] **L**,[221] and **M**.[57]

The first osmium nitrido complex was produced almost 175 years ago when Fritzsche and Struve[12] treated osmium(VIII) tetroxide with ammonia in 1847. However, it took another 50 years until Werner and Dinklage[215] assigned the correct composition of the $[(O)_3Os^{VIII}N]^-$ complex (Figure 1.10 **A**) in 1901. Having a d^0 configuration it repre-

Table 1.2: Selection of experimentally known ruthenium nitrido complexes. Reported bond lengths, d(Ru−N), in pm and vibrational frequency, $\tilde{\nu}$, of the ruthenium nitrido stretching mode [ν(Ru−N)] in cm^{-1} are included. The Ru−N bond distances are obtained from XRD, unless noted otherwise.

Complex	**Syn.**[a]	**Geom.**[b]	d**(Ru−N)**	$\tilde{\nu}$**[**ν**(Ru−N)]**	**Year**[REF]
$[(Cl_4)Ru^{VI}N]^-$	Az [c]	SPY	157.0(7)[198]	1090 [d]	1973[190]
$[(Br_4)Ru^{VI}N]^-$	Az [c]	SPY	—	1088 [d]	1973[190]
$[(Cl_5)Ru^{VI}N]^{2-}$	Az [c]	PO	—	1045 [d]	1973[190]
$[(Br_5)Ru^{VI}N]^{2-}$	Az [c]	PO	—	1045 [d]	1973[190]
$[(3\text{-MPA})_2Ru^{VI}N]^-$	GP	SPY	159.5(8)	1094 [e]	1991[199]
$[(LNO_2)Ru^{VI}N]^+$	GP	SPY	161.5(4)	1025 [f]	1998[191]
$[(hypyb)Ru^{VI}N]^+$	GP	SPY	159.4(4)	1073 [f]	1998[191]
$[(dchypyb)Ru^{VI}N]^+$	GP	SPY	160.9(6)	1010 [f]	1998[191]
$[Ru^{III}N]$	EL	LI	157.1 [g]	1109 [g]	1998[200]
$[(OMPG)Ru^{VI}N]^-$	DA	SPY	156.9(6)	—	2001[192]
$[(TMP)Ru^{VI}N]^-$	OM	SPY	—	1038 [d]	2003[193]
$[(MeO\text{-}TPP)Ru^{VI}N]^-$	OM	SPY	165.6(5)	—	2003[193]
$[(salen)(MeOH)Ru^{VI}N]^+$	GP	PO	159.2(4)	1059 [d]	2004[194]
$[(PNP^{Si})Ru^{IV}N]^+$	Az	SPL[h]	162.7(2)	1030	2005[195]
$[(dPhf)_4Ru^{III}Ru^{IV}N]$	Az	PO	172 [i]	840 [j]	2008[196]
$[(PNP)Ru^{IV}N]^+$	Az	SPL[h]	165.8 [k]	976 [f]	2011[17]
$[(i\text{PrPDBP})_2(Cl)Ru^{VI}N]$	GP	PO	—	1025	2013[197]
$[(i\text{PrPDBP})_2(H_2O)Ru^{VI}N]^+$	GP	PO	165.1(6)	1029	2013[197]

[a] Synthesis; Az: From corresponding azide; GP: Starting from $[(Cl_4)Ru^{VI}N]^-$ (Griffith and Pawson[190]); EL: From elements in gas-phase; DA: By reaction with diphenyldiazomethane; OM: Reaction of oxo-metal complexes with an imine compound

[b] Coordination Geometry; See Figure 1.3; LI: Linear

[c] Reacting *trans*-$[RuO_2X_2]^{2-}$ with azide and CsX to get $[(X_4)Ru^{VI}N]^-$; Replacing CsX with $[Ph_4As]X$ or $[Bu_4N]X$ to get $[(X_5)Ru^{VI}N]^{2-}$ (X = Cl, Br)

[d] From solid

[e] From KBr pellet

[f] In Nujol

[g] From Fourier transform infrared emission spectroscopy; Bond distance from Ref[201]

[h] Distorted square planar

[i] From EXAFS fit

[j] From RR

[k] Average from 168.8(3) pm and 1.628(4) pm obtained by XRD and applying a split model for the nitride ligand because of considerable disorder regarding the nitrido ligand position.

sents the highest possible OS of osmium of VIII, with a OsN bond distance of 162 pm and a corresponding stretching frequency of 1023 cm^{-1}.[222–224] This complex reacts with hydrogen halides to $[(Cl)_5Os^{VI}N]^{2-}$ and $[(Br)_5Os^{VI}N]^{2-}$, depicted in Figure 1.10 **B**.[215,225] For the pentachloride complex, Os−N stretching frequencies of 1073 cm^{-1} to 1084 cm^{-1} (depending on the counter ion) and a bond distance of 161.4(13) pm have been recorded.[224,226] For the pentabromide complex an Os−N stretching frequency of 1073 cm^{-1} was reported for the potassium salt, which is 11 cm^{-1} lower than the one observed for $K_2[(Cl)_5Os^{VI}N]$.[190] The tetrahalides $[(Cl)_4Os^{VI}N]^-$ and $[(Br)_4Os^{VI}N]^-$ shown in Figure 1.10 **C** were published in 1973 by Griffith and Pawson[190]. For the nitrido bomide an Os−N stretching frequency of 1119 cm^{-1} was observed, while that of the chloride congener is slightly higher at 1123 cm^{-1}. For the latter a very short Os−N bond distance of 160.0(11) pm was determined.[227] To an even greater extent than for the ruthenium congener, the nitrido tetrachloride anion $[(Cl)_4Os^{VI}N]^-$ served as starting material for large number of complexes synthesized via ligand substitution reactions.[28,219,220,228–230] Among those, the phosphine osmium(VI) complex $[(dppe)(CH_2SiMe_3)_2(NCMe)Os^{VI}N]^+$ (Figure 1.10 **D**) that features an Os−N bond distance of 163.8(5) pm,[216] as well as the square planar thiolate osmium(VI) complex $[(S_2C_6H_4)_2Os^{VI}N]^-$ (Figure 1.10 **E**), for which an Os−N bond distance of 164(1) pm and an Os−N stretching frequency of 1063 cm^{-1} was obtained.[217]

The cationic complex $[(hypyb)Os^{VI}N]^+$ (Figure 1.10, **F**) allows comparison of M−N bond lengths and stretching frequencies with the complex of the lighter ruthenium congener $[(hypyb)Ru^{VI}N]^+$ published in the same work.[191] The Os−N bond distance is with 161.8(7) pm is about 1.4 pm longer, and the stretching frequency of 1108 cm^{-1} is 35 cm^{-1} higher than that of the lighter congener. These values are consistent with the ones obtained for $[(Cl)_4Os^{VI}N]^-$ and $[(Cl)_4Ru^{VI}N]^-$ which are 160.0(11) pm and 157.0(7) pm, as well as 1123 cm^{-1} and 1092 cm^{-1}, respectively.

A kinetic investigation of the reaction between the Schiff base complexes [(salophen)$(MeOH)Os^{VI}N]^+$ (Figure 1.10 **G**) and $[(salen)(MeOH)Os^{VI}N]^+$ with PPh_3 revealed that the electrophilic reactivity of the nitrido ligand increases with electron-withdrawing substituents at the salophen ligand.[218] A comparatively long Os−N bond distance of 165.1(7) pm has been determined by XRD of $[(salophen)(MeOH)Os^{VI}N]^+$. The OsN stretching frequencies of 1094 cm^{-1} for the salen substituted, and 1072 cm^{-1} for the salophen complex, are both well within the expected range for Os≡N triple bonds and somewhat larger than the frequency obtained for the ruthenium congener [(salen)$(MeOH)Ru^{VI}N]^+$ (1059 cm^{-1}, Table 1.2).

Owing to its labile aqua and chloro ligands in *trans* and *cis* position to the nitrido ligand, the $[(sap)(OH_2)(Cl)Os^{VI}N]^+$ complex (Figure 1.10 **H**), which makes use of the tridentate Schiff base ligand, displays prominent *in vitro* and *in vivo* anti-cancer pro-

perties.[219] While no structural data of this complex were reported, the Os−N stretching frequencies of 1092 cm^{-1} to 1098 cm^{-1} obtained for these derivates indicate strong Os≡N triple bonds. A family of eight $Os^{VI}N$ based complexes of the general formula $[(Cl)_3(Hazole)_2Os^{VI}N$ (Hazole = azole heterocycle) show antitumor activity as well.[28] Of these, the molecular structures of the complexes shown in Figure 1.10 **I** and **J** have been determined using XRD. The Os−N bond distances (and stretching frequencies) amount to 161.9(9) pm (1080 cm^{-1}), 161.5(5) pm (1060 cm^{-1}), 164.3(4) pm (1070 cm^{-1}) and 167.5(3) pm (1070 cm^{-1}) for the Hind, 5-MeHpz, 3,5-Me_2Hpz and 1-Mebzim substituted derivates, respectively. These complexes, however, do not display a meaningful relationship between their Os−N bond distances and stretching frequencies. The closely related nitrido trichloride complexes bearing bidentate ligands, such as bipy, phen, and derivatives, also show promising anti-cancer properties.[220,230] Especially $[(phen)(Cl)_3Os^{VI}N]$ (Figure 1.10 **K**) has shown promising results, and exhibits selective toxicity for breast cancer stem cell enriched cell populations.[230]

The low-valent, square planar $[(PNP)Os^{VI}N]$ (Figure 1.10 **L**) recently published by Schendzielorz et al.[221] is a rare example of an osmium(IV) nitrido complex produced by reductive deprotonation of an osmium(VI) hydride. It features a comparatively long Os−N bond distance of 168.32(18) pm and a stretching frequency of 999 cm^{-1}, which can be attributed to a *trans*-effect of the imide donor in *trans* position to the nitrido ligand. In this coordination geometry the d^4 configuration leads to a singlet configuration with populated non-bonding metal-centered $(d_{z^2})^2(d_{yz})^2$ orbitals. In reactivity investigations the nitrido ligand shows ambiphilic reactivity, and complete hydrogenolysis of the nitrido ligand to ammonia was observed in high yield.[221] The closely related complex $[(PNP')Os^{VI}N]$ depicted in Figure 1.10 **M** shows a weakened Os≡N bond because of the distorted structure with a bent N−Os≡N unit.[57] The Os≡N bond distance was determined to be 173.5(2) pm, which is exceptionally long for a formal Os≡N triple bond. Surprisingly, the associated stretching frequency of 1025 cm^{-1} is higher than the one observed for $[(PNP)Os^{VI}N]$.

The electronic structure of the group 8 diatomics (MN) was investigated extensively.[183,187,200,201,231] The gas-phase vibrational frequencies decrease from OsN to FeN, 1137 cm^{-1} (OsN), 1109 cm^{-1} (RuN), and 871 cm^{-1} (FeN), while the bond distances amount to 161.8 pm (OsN), 157.1 pm (RuN) and 158.0 pm (FeN). Interestingly, like FeN, but unlike RuN, OsN adopts a $^2\Delta$ electronic ground state. The stretching frequency obtained for diatomic OsN in solid argon is only shifted by −7 cm^{-1},[202] a considerable smaller gas-to-matrix shift than those observed for RuN (−140 cm^{-1}) and FeN (67 cm^{-1}). In the same matrix-isolation work it was discovered that laser ablated osmium atoms insert into the triple bond of dinitrogen to form bent $Os(N)_2$ under cryogenic conditions.[232] This follows from the observation of only two isotopologues,

$Os(^{15}N)_2$ and $Os(^{14}N)_2$ upon annealing.

It can be concluded that the osmium nitride chemistry is dominated by osmium(VI) in pseudo octahedral or square pyramidal coordination geometries. Rare exceptions to this include the high-valent pseudo tetrahedral $[(O)_3Os^{VIII}N]^-$ (Figure 1.10 **A**), and the low-valent distorted square planar [(PNP)Os^{IV}N] and [(PNP')Os^{IV}N] complexes (Figure 1.10 **L** and **M**, respectively).

Table 1.3: Selection of experimentally known osmium nitrido complexes. Reported bond distances, d(Os−N), in pm and vibrational frequencies, $\tilde{\nu}$, of the osmium nitrido stretching mode [ν(Os−N)] in cm^{-1} are included. The Os−N bond distances are obtained from XRD, unless noted otherwise.

Complex	**Syn.**[a]	**Geom.**[b]	d**(Os−N)**	$\tilde{\nu}$**[**ν**(Os−N)]**	**Year**[REF]
$[(O)_3Os^{VIII}N]^-$	Ox	PTD	162 [c]	1023 [d]	1847[12]
$[(Cl)_5Os^{VI}N]^{2-}$	HX	PO	161.4(13)	1073 [e]	1901[215]
$[(Br)_5Os^{VI}N]^{2-}$	HX	PO	—	1073 [f]	1906[225]
$[(Cl)_4Os^{VI}N]^-$	Az	SPY	160.0(11)	1123 [g]	1973[190]
$[(Br)_4Os^{VI}N]^-$	Az	SPY	—	1119 [g]	1973[190]
$[(dppe)(L^1)_2(L^2)Os^{VI}N]^+$ [h]	GP	PO	163.8(5)	—	1994[216]
$[(S_2C_6H_4)_2Os^{VI}N]^-$	GP	SPY	164(1) [i]	1063 [j]	1997[217]
$[(hypyb)Os^{VI}N]^+$	GP	SPY	161.8(7)	1108 [k]	1998[191]
$Os^{III}N$	EL	LI	161.8 [l]	1137 [m]	1999[231]
$Os(N)_2$	EL	BE	[168.3] [n]	901 [o]	1999[232]
$[(salen)(MeOH)Os^{VI}N]^+$	GP	TG	—	1094 [j]	1999[218]
$[(salophen)(L^3)Os^{VI}N]^+$ [h]	GP	TG	165.1(7)	1072 [j]	1999[218]
$[(sap)(OH_2)(Cl)Os^{VI}N]^+$	GP	TG	—	1098 [j]	2011[219]
$[(Hind)_2(Cl)_3Os^{VI}N]$	GP	TG	161.9(9)	1080 [j]	2012[28]
$[(5\text{-}MeHpz)_2(Cl)_3Os^{VI}N]$	GP	TG	161.5(5)	1060 [j]	2012[28]
$[(3,5\text{-}Me_2Hpz)_2(Cl)_3Os^{VI}N]$	GP	TG	164.3(4)	1070 [j]	2012[28]
$[(1\text{-}Mebzim)_2(Cl)_3Os^{VI}N]$	GP	TG	167.5(3)	1070 [j]	2012[28]
$[(phen)(Cl)_3Os^{VI}N]$	GP	TG	—	1080 [j]	2013[220]
$[(PNP)Os^{IV}N]$	Az	SQ	168.32(18)	999 [j]	2016[221]
$[(PNP')Os^{IV}N]$	Az	SQ	173.5(2)	1025 [k]	2017[57]

[a] Synthesis; Ox: From OsO_4 and NH_3; HX: From $(O)_3OsN$ and corresponding hydrogen halide; Az: From corresponding azide; GP: Starting from $[(Cl_4)Os^{VI}N]^-$ (Griffith and Pawson[190]); EL: From elements in gas-phase
[b] Geometry; See Figure 1.3, LI = Linear, BE = Bent, SQ: Distorted square planar
[c] XRD[222,223]
[d] Nujol[224]
[e] Potassium salt in nujol[224]
[f] From solid[190]
[g] From Raman spectroscopy
[h] L^1: CH_2SiMe_3; L^2: NCMe; L^3: MeOH
[i] Two independent molecules in the asymmetric unit with 164(1) pm and 166(1) pm, respectively
[j] KBr pellet
[k] In nujol
[l] r_e from Fourier transform emission spectroscopy
[m] Gas phase; In solid argon: 1130 cm^{-1}[232]
[n] From DFT calculation
[o] In solid argon

1.5.2. Group 9

The 9 valence electrons of the group 9 transition metals, in principle, facilitate OSs up to IX. However, the iridium tetroxide cation $[IrO_4]^+$ is the only compound with OS IX that has been reported to date.[63] In contrast to earlier transition metals, significantly fewer terminal group 9 nitrido and imido complexes exist.

Cobalt Imido and Nitrido Complexes

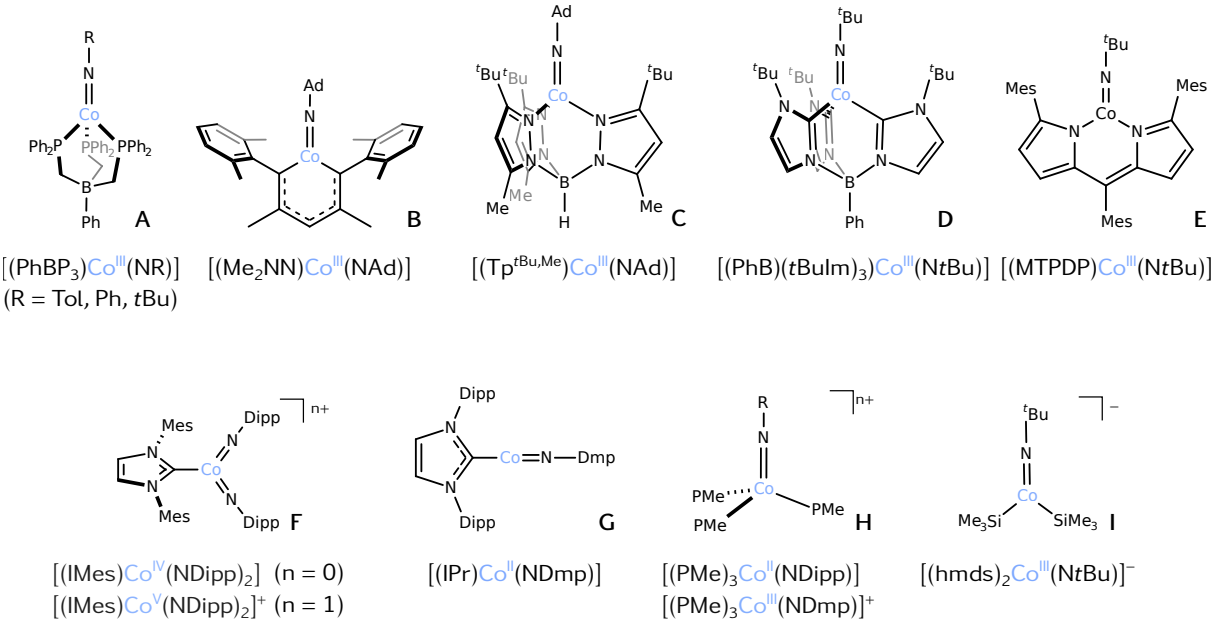

Figure 1.11. Selection of experimentally known terminal cobalt imido complexes: **A**,[233,234] **B**,[235] **C**,[236] **D**,[237] **E**[238] **F**,[239] **G**,[240] **H**,[241] and **I**.[242]

For a very long time cobalt with multiply bonded, strong π-donor ligands were unknown and to this day diatomic $Co^{III}N$ is the only known nitrido complex. It has been isolated in solid argon in 1998.[243] An experimental equilibrium bond length (r_e, estimated from B_{eff}) of 157.5 pm was reported in a theoretical study by Yamaki et al.[244] in 2003 from gas-phase LIF excitation spectra of CoN, carried out by Aiuchi and Shibuya (private communication).[244] Reminiscent of the iron congener (see Section 1.5.1), the determination of the electronic ground state of CoN has been subject to controversial discussions. Theoretical investigations[244,245] predict a $^1\Sigma^+$ electronic ground state based on rigorous multi-configurational studies by Gobbo and Borin[245] in 2006, while former DFT calculations carried out by Andrews et al.[243], and MRCI + Q calculations of Yamaki et al.[244] erroneously lead to $^5\Delta$ electronic ground state. The $X^1\Sigma^+$ state corresponds to a leading configuration of $7\sigma^2 8\sigma^2 9\sigma^2 3\pi^4 1\delta^4 4\pi^0$, where the 7σ, 9σ and 1δ orbitals correspond to the N centered 2s, Co centered 4s and $3d_{xy,\, x^2-y^2}$ orbitals, respectively. The bonding and antibonding orbitals are represented by 8σ,

3π and $4\pi^*$, respectively. Computed CoN bond distances of 156.1 pm (MRCI) and 157.3 pm (CASPT2) are in very good agreement with the experimental gas-phase value of 157.5 pm estimated from B_{eff}.[244] The computed vibrational frequencies of 914 cm^{-1} (MRCI) and 888 cm^{-1} (CASPT2) are, however, significantly higher than the experimental value of 827 cm^{-1} obtained in solid argon.[243]

The strong π-donating character of the N^{3-} ligand combined with the inability of cobalt to achieve higher OSs than V and the associated high *d*-electron counts make cobalt nitrido complexes appear unfavorable. In contrast, the imido ligand (RN^{2-}) is able to act as four or six electron donor[246] and a number of imido complexes have been synthesized since the first example, namely [($PhBP_3$)Co^{III}(Ntol)] (Figure 1.11 **A**), was published in 2002.[233] With only one exception, the complexes shown in Figure 1.11 were prepared by oxidative addition of organic nitrenes (NR), obtained by N_2 elimination from organic azides RN_3, while [(PhB(*t*BuIm)$_3$)Co^{II}(N*t*Bu)] (Figure 1.11 **D**) was prepared by deprotonation of [(PhB(*t*BuIm)$_3$)Co^{II}(NH*t*Bu)]. The OSs of cobalt in these imido complexes range from II[240,241] to V[239], with OS III being the most prominent (see Table 1.5).

Strikingly, there are no examples of cobalt imido complexes with tetragonal coordination geometry. This circumstance can easily be rationalized by the fact that *d*-electron counts lower than four have not yet been realized. A *d*-electron count d^n, with n > 2 in a tetragonal coordination (i.e., PO and SPY coordination geometries in Figure 1.3) would lead to a significant destabilization due to the occupation of antibonding orbitals (nitrido wall, see Section 1.1). A coordination geometry commonly found in cobalt nitrido complexes is pseudo tetrahedral with Co in the OSs of III. Co−N bond distances in these complexes range from 163.3(2) pm to 167.5(2) pm (Table 1.5 and Figure 1.11 **A**, **C**, **D**, and **H**). Low-spin configurations are dominant, and [($Tp^{tBu,Me}$)Co^{III}(NAd)] shown in Figure 1.11 **C** is the only example that shows a high-spin configuration in pseudo tetrahedral geometry.[241] In linear R−N−Co coordination the *d*-orbital splitting caused by the imido ligand is similar to that of the nitrido ligand N^{3-}, however, the antibonding d_{z^2} is surprisingly stable because of significant symmetry allowed cobalt $3d_z$ and $4p_z$ orbital mixing, which mitigates antibonding character of this orbital.[238,246] In this splitting scheme, the Co^{III} center adopts idealized $(d_{xy,\,x^2-y^2})^4(d_{z^2})^2(d_{xz,\,yz})^0$ low-spin[233,234,237,241,247] and $(d_{xy,\,x^2-y^2})^4(d_{z^2})^1(d_{xz,\,yz})^1$ high-spin[236] ground-state electron configurations. The only compound featuring a Co^{II} ion in this coordination geometry is [(PMe_3)Co^{II}(NDipp)] (Figure 1.11 **H**), which comprises a significantly elongated Co−N bond length of 170.89(15) pm compared to 165.40(17) pm of the analogous Co^{III} cation [(PMe_3)Co^{III}(NDmp)]$^+$. The elongated bond length of the Co^{II} complex is consistent with a low-spin ground state electron configuration of $(d_{xy,\,x^2-y^2})^4(d_{z^2})^2(d_{xz,\,yz})^1$ and a reduced formal BO of 1.5.[241]

Another reported coordination geometry of cobalt imido complexes is trigonal planar (TPL). Examples shown in Figure 1.11 include Co^{III} (**B**, **E** and **I**), as well as Co^{IV} and Co^{V} (**F**) centers with Co−N bond distances ranging from 162.1(3) pm to 170.67(12) pm (Table 1.5). For these three-coordinate species, the $d_{xz,\,yz}$ set is no longer degenerate, as d_{xy} bears antibonding character with respect to the ancillary ligands, whereas d_{yz} does not. The splitting and, consequently, the preferred spin-state depends on the nature of the imido substituent.[238] Low-spin configurations have been attributed to [$(Me_2NN)Co^{III}$(NAd)] (Figure 1.11 **B**) and [(giso)Co^{III}(NAd)] (Table 1.5), with similar valence configurations to those of the four-fold coordinated low-spin complexes described above.[235,248] Complexes bearing weak-field ancillary ligands have shown to stabilize high-spin complexes, such as [(MTPDP)Co^{III}(N*t*Bu)] and [$(hmds)_2Co^{III}$(N*t*Bu)]$^-$ (Figure 1.11 **E** and **I**, respectively).[238,242] The former undergoes a thermally induced spin crossover from a singlet ground state to the quintet state electron configuration $(d_{xy,\,x^2-y^2})^3(d_{z^2})^1(d_{yz})^1(d_{xz})^1$ according to DFT calculations and in accord with the observed elongation of all Co−N bonds.[238] The bis imido complexes shown in Figure 1.11 **F** possess a delocalized N−Co−N π electron system evident by the contraction of the N−Co−N bonds upon oxidation. According to a joint DFT and EPR study, the unpaired electron in the neutral Co^{IV} complex is removed upon oxidation to the Co^{V} complex from a singly occupied, delocalized π^* orbital.[239]

Furthermore, a *N*-heterocyclic carbene (NHC) stabilized high-spin cobalt(II) imido complex with linear coordination at the cobalt center has been reported (Figure 1.11 **G**) which accommodates two unpaired electrons in the π^* antibonding $d_{xz,\,yz}$ orbitals and one in a non-bonding $d_{x^2-y^2}$ MO, resulting in a quartet ground state.[240] The Co−N bond distance and the Co−N−C angle amount to 169.1(6) pm and 173.0(3)°, respectively.

Table 1.4: Vibrational frequencies (cm^{-1}) of $^{14/15}N$ isotopologues of cobalt nitrido and imido complexes. Only modes with significant nitrido or imido nitrogen contributions are listed.

Complex	^{14}**N**	^{15}**N**	**Year**[REF]
$Co^{III}N$	827	804	1998[243]
[$(PhBP_3)Co^{III}$(N*t*Bu)]	577, 1103, 1238	578, 1084, —[a]	2006[234]
[$(PhBP_3)Co^{III}$(NPh)]	956, 995, 1307, 1332	944, 992, 1295, 1313	2006[234]

[a] Band corresponding to 1238 cm^{-1} obscured in spectrum

Vibrational data for the complexes shown in Figure 1.11 and listed in Table 1.5 are scarce. With one exception,[234] $^{14/15}N$ isotopic substitution experiments are lacking, which makes it impossible to identify modes involving the imido group. Raman

experiments with ^{15}N and D substituted samples of [(PhBP$_3$)Co^{III}(N*t*Bu)] conducted by Mehn et al.[234] lead to an assignment of bands at 1103 cm^{-1} and 1238 cm^{-1} to primarily Co−N and N−C stretching modes, respectively. The first band shows a $^{14/15}N$ isotopic shifts of about −20 cm^{-1}, while the band associated to the ^{15}N isotopologue of the second band is obscured† in the spectrum. Isotopic ^{15}N subsitution of [(PhBP$_3$)Co^{III}(NPh)] revealed a high degree of coupling of the modes involving the imido group with the aryl ring vibrational modes. Vibrational data of these complexes are summarized in Table 1.4.

Lastly, it is worth pointing out that all known cobalt imido complexes adopt a linear (or nearly linear) Co−N−R geometry and the substituents are limited to organic, electron donating groups.

Table 1.5: Selection of published terminal cobalt nitrido and imido complexes. Including, where available, Co−N bond distances, *d*(Co−N) (pm) and (Co=N−R) bond angle (°). All structural data obtained from XRD, unless indicated otherwise. All imido complexes were obtained from the corresponding azides, unless indicated otherwise.

Complex	**Geom.**[a]	***d*(Co−N)**	**∠(Co=N−R)**	**Year**[REF]
Co^{III}N [b]	LI	157.5 [c]	—	1998[243]
[(PhBP$_3$)Co^{III}(Ntol)]	PTD	165.8(2)	169.51(2)	2002[233]
[(PhBP$_3$)Co^{III}(N*t*Bu)]	PTD	163.3(2)	176.9(1)	2006[234]
[(Me$_2$NN)Co^{III}(NAd)]	TPL	162.4(4)	161.5(3)	2004[235]
[(TIMEN^{Mes})Co^{III}(NMes)]	PTD	167.5(2)	168.6(2)	2004[247]
[(Tp^{tBu,Me})Co^{III}(NAd)]	PTD	165.5(2)	178.3(2)	2005[236]
[(PhB(*t*BuIm)$_3$)Co^{III}(N*t*Bu)] [d]	PTD	166.0(3)	179.7(3)	2007[237]
[(giso)Co^{III}(NAd)]	TPL	162.1(3)	172.1(3)	2009[248]
[(MTPDP)Co^{III}(N*t*Bu)]	TPL	160.9(3) [e]	177.5(3) [e]	2012[238]
[(IMes)Co^{IV}(NDipp)$_2$]	TPL	166.5(3)	173.0(3)	2014[239]
[(IMes)Co^{V}(NDipp)$_2$]$^+$	TPL	164.1(3) [f]	174.2(3) [f]	2014[239]
[(IPr)Co^{II}(NDmp)]	LI	169.1(6)	173.0(3)	2015[240]
[(PMe)$_3$Co^{II}(NDipp)]	PTD	170.89(15)	177.85(14)	2017[241]
[(PMe)$_3$Co^{III}(NDmp)]$^+$	PTD	165.40(17)	166.99(15)	2017[241]
[(hmds)$_2$Co^{III}(N*t*Bu)]$^-$	TPL	170.67(12)	160.78(12)	2020[242]

[a] Geometry; See Figure 1.3; LI: Linear
[b] By reacting laser-ablated cobalt atoms with N_2
[c] Equilibrium bond distance (r_e) evaluated from rotational constant B_{eff}[244]
[d] By deprotonation of [(PhB(*t*BuIm)$_3$)Co^{II}(NH*t*Bu)] obtained from reacting corresponding chloride with LiNH*t*Bu.
[e] At 150 K, at 300 K: 163.2(3) pm and 178.2(3)°
[f] Average; *d*(Co−N) = 164.0(3) pm and 164.2(3) pm; ∠(Co=N−R) = 173.7(3)° and 174.7(3)°

†The corresponding band of the iron congener shows an isotopic shift of −5 cm^{-1}.

Rhodium Imido and Nitrido Complexes

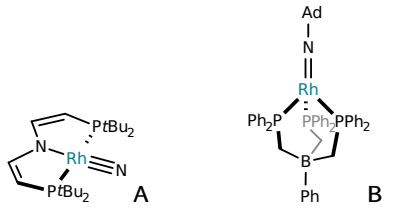

[(PNP')Rh^{IV}N] [(PhBP$_3$)Rh^{III}(NAd)]

Figure 1.12. Literature known non-binary terminal rhodium nitrido (**A**)[249] and rhodium-imido complexes (**B**).[250]

Despite the numerous cobalt imido complexes, the number of related rhodium complexes is remarkably low. The first rhodium-nitrogen multiple bond was realized in 1998 in the diatomic $Rh^{III}N$.[251] The electronic ground state was predicted to be $^1\Sigma^+$ using all-electron *ab initio* methods with a corresponding configuration of $10\sigma^2 11\sigma^2 12\sigma^2 5\pi^4 2\delta^4 4\pi^0$, which is isoelectronic to CoN.[252,253] Shortly after that it was first produced in the gas-phase,[251] and later isolated in solid argon.[254] In solid argon, a Rh−N stretching frequency of 895 cm^{-1} was obtained,[254] which is very close to gas-phase values of 897 cm^{-1} and 900 cm^{-1} found in LIF excitation, and dispersed fluorescence spectra, respectively.[255] The Rh−N equilibrium bond distance was estimated to 164.1 pm.[255] Additionally, in cryogenic matrices of the reaction products of laser-ablated rhodium and dinitrogen diluted in argon a band at 822.8 cm^{-1} has been assigned to bent $Rh(N)_2$, for which an electronic ground state of $^2B_1$ was claimed, however, no further investigation of the nature of the bonding was undertaken.[254]

Recently, the Rh^{IV} pincer complex shown in Figure 1.12 **A** was successfully isolated.[249] It was produced by irradiating the corresponding azide at 20 K and characterized by its EPR spectrum. IR spectra were taken from a KBr pellet containing the azide that was irradiated for a short time. The stretching frequency was observed at 874 cm^{-1}, which is close to the stretching frequency assigned to diatomic RhN. The EPR data are consistent with DFT calculations that predict a d^5 configuration with a singly occupied molecular orbital (SOMO) of π^* character and a Rh−N bond distance of 168 pm. Due to the high degree of covalency of the Rh≡N π system, the spin-density is delocalized over this unit, which results in a formal BO of 2.5.[249]

A significantly longer bond distance of 178.0(2) pm associated with a nearly linear Rh=N−C bond angle of 177.5(2)° was found in the thermally stable, pseudo-tetrahedral rhodium imido complex [(PhBP$_3$)Rh^{III}(NAd)], shown in Figure 1.12 **B**, using XRD.[250] Additionally, the related [(PhBP$_3$)Rh^{III}(NR)] (R = 2,6−*i*Pr$_2$C$_6$H$_6$ and C$_6$F$_5$) were successfully synthesized, but no crystals suitable for a crystal structure analysis could be obtained.[250] Theoretical calculation at DFT level revealed closed-

shell d^6 configurations for these complexes, consistent with Rh=N double bonds.

The experimentally isolated rhodium-imido and -nitrido complexes are summarized in Table 1.6.

Table 1.6: All published terminal rhodium-nitrido and rhodium-imido complexes. Including, where available, Rh−N bond lengths (d in pm) and Rh−N stretching frequencies ($\tilde{\nu}$ in cm^{-1}). All structural data obtained from XRD or DFT (square brackets).

Complex	Geometry [a]	d(Rh−N)	$\tilde{\nu}[\nu$(Rh−N)]	Year[REF]
$Rh^{III}N$	LI	164.1 [b]	895–900 [c]	1998[251]
$Rh(N)_2$	BE	[173]	823 [d]	1999[254]
$[(PNP')Rh^{IV}N]$	SPL	[168]	874 [e]	2013[249]
$[(PhBP_3)Rh^{III}(NAd)]$	PTD	178.0(2)	—	2014[250]

[a] See Figure 1.3; LI: Linear, BE: Bent
[b] Equilibrium bond distance (r_e) evaluated from rotational constant B_{eff}[255]
[c] Values from solid argon and gas-phase (see text)[254,255]
[d] Solid argon
[e] KBr pellet

Iridium Imido and Nitrido Complexes

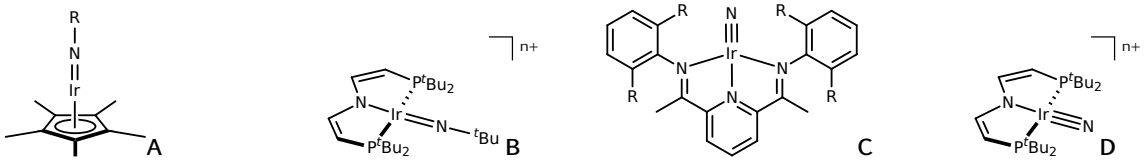

[(Cp*)Ir^{IV}(NR)]
R = *t*Bu, SiMe$_2$*t*Bu, Xyl, Dipp

[(PNP')Ir^{III}(N*t*Bu)] (n = 0)
[(PNP')Ir^{IV}(N*t*Bu)]$^+$ (n = 1)
[(PNP')Ir^{V}(N*t*Bu)]$^{2+}$ (n = 2)

[(*i*Pr$_4$PDI)Ir^{V}N] (R = *i*Pr)
[(Cl$_4$PDI)Ir^{V}N] (R = Cl)

[(PNP')Ir^{IV}N] (n = 0)
[(PNP')Ir^{V}N]$^+$ (n = 1)

Figure 1.13. Literature known non-binary terminal iridium imido (**A**[256,257] and **B**[258]) and iridium nitrido complexes (**C**[259,260] and **D**[261]).

As with rhodium, isolated iridium nitrido and imido complexes are scarce. Imido complexes were produced by treating the precursor complexes with lithium amides (LiNHR) in salt metathesis reactions, characterized as linear Cp* and square planar PNP' complexes.[256–258] The former, shown in Figure 1.13 **A**, comes with iridium in OS III and was crystallized, showing terminal imido ligands and with Ir−N bond distances ranging from 171.2(7) cm^{-1} to 175.0(7) cm^{-1}.[256,257] Due to the absence of ligands in the xy plane, the d-orbital splitting of these complexes feature two metal centered fully occupied non-bonding $(d_{xy})^2(d_{x^2-y^2})^2$ orbitals, along with $(d_{z^2})^2$ which only weakly interacts with the Cp* orbitals.[257] Very recently, the square planar PNP pincer com-

plexes shown in Figure 1.13 **B** with iridium OSs from III to V were investigated.[258] For the complexes with iridium in formal OSs III and IV crystal structures with very long Ir−N bond distances of 180.5(2) pm (Ir^{IV}) and 186.8(2) pm (Ir^{III}) were recorded. This is consistent with a d^5 triplet configurations of the Ir^{IV} complex, in which one electron is accomodated in the π^* LUMO (c.f. Figure 1.3, SPL), resulting in Ir−N bond elongation, reduced BO and an triplet electronic ground state. The Ir=N bond in $[(PNP')Ir^{IV}(N\textit{t}Bu)]^+$ was characterized by EPR spectroscopy. It is highly covalent and the imido ligand shows non-innocent character, evident by cylindrical spin density delocalization around the Ir=N bond attributed to orbital mixing of the near degenerate, perpendicular π^*-antibonding SOMO and LUMO.[258] Furthermore, the corresponding Fe^V dicationic complex was synthesized as well. As expected, its electronic ground state is a singlet state, however, no XRD analysis and no theoretical structural predictions were reported.

The equilibrium bond distance (r_e) of diatomic $Ir^{III}N$ was evaluated from the experimental rotational constant to 160.7 pm.[262] Like CoN and RhN (see above) the electronic ground state is a $^1\Sigma^+$ state.[262] A number of additional investigations of the ground- and excited states of IrN have been conducted experimentally and theoretically.[263–265] The first terminal iridium nitrido complex characterized by XRD, shown in Figure 1.13 **C** (R = *i*Pr), exhibits a Ir−N bond distance of 164.6(9) pm.[259] The authors refrain from assigning an OS, but suggest a d^6 electron configuration based on multi-reference calculations, while a formal OS of V with a d^4 electron configuration would be assigned in the ionic approximation, based on the neutral total charge of the complex and ligand charges of PDI^{2-} and N^{3-}. This corresponds to a singlet ground state with fully occupied set of non-bonding ($d_{xy,\, x^2-y^2}$) orbitals and empty anti-bonding σ^* and π^* MOs, resulting in an Ir≡N BO of three. It has been demonstrated that the nitrido ligand in this complex displays both electrophilic and nucleophilic properties, depending on the substrate employed.[266,267] Investigations focused on C−H activation reactivity and dimerization lead to the synthesis of the analog in which the *i*Pr-groups are substituted by chlorine (Figure 1.13 **C**) to hamper intramolecular C−H activation.[260,268] Both of these complexes show very similar Ir−N stretching frequencies of 958 cm^{-1} (R = *i*Pr, Raman shift) and 955 cm^{-1} (R = Cl).

The square planar closed and open-shell PNP pincer iridium nitrido complexes shown in Figure 1.13 **D** are closely related to the corresponding imido complexes presented above (Figure 1.10 **B**).[261] This becomes clear from the comparable covalent nature of the π-bonding and π^*-antibinding MOs. The formal OSs of IV and V are not consistent with the observed reactivity of the cationic complex, which exhibited electrophilic reactivity. This lead to a revised assignment of an effective OS of III for the cationic complex. The SOMO of the neutral complex is a π^*-antibonding

orbital and the covalent character of this orbital leads to a distribution of the spin-density over the Ir−N moiety and to a non-innocent character of the nitrido ligand. The Ir−N bond length of 167.8(4) pm (172 pm, DFT) and Ir−N stretching frequencies of 999 cm^{-1} (901 cm^{-1}) of the cationic (neutral) species are consistent with these findings. The nitrido ligands of these complexes can be oxidatively coupled to yield dinitrogen.[269]

It is worth point out that, so far, no matrix isolatation experiments of laser-ablated iridium and dinitrogen gas have been conducted. In addition to the potential formation of $Ir(N)_2$, this experiment may produce $Ir(N)_3$ with a formal iridium OS of IX. Furthermore, iridium complexes with terminal nitrido ligands and formal OSs beyond five were proposed very recently, but not yet characterized.[270]

Table 1.7: Known terminal iridium nitrido and iridium-imido complexes with reported Ir−N bond lengths (d in pm) and Ir−N stretching frequencies ($\tilde{\nu}$ in cm^{-1}). Structural data obtained from XRD or DFT calculations (in square brackets).

Complex	**Geometry** [a]	d**(Ir−N)**	$\tilde{\nu}[\nu$**(Ir−N)]**	**Year**[REF]
$[(Cp^*)Ir^{III}(N\mathit{t}Bu)]$	LI	171.2(7)	—	1989[256]
$[(Cp^*)Ir^{III}(NSiMe_2\mathit{t}Bu)]$	LI	175.0(7)	—	1991[257]
$[(Cp^*)Ir^{III}(NXyl)]$	LI	172.9(7)	—	1991[257]
$[(Cp^*)Ir^{III}(NDipp)]$	LI	174.9(7)	—	1991[257]
$Ir^{III}N$	LI	160.7 [b]	1114	1999[262]
$[(\mathit{i}Pr_4PDI)Ir^{V}N]$	SPL	164.6(9)	958 [c]	2009[259]
$[(Cl_4PDI)Ir^{V}N]$	SPL	[169]	955 [d]	2011[260]
$[(PNP')Ir^{V}N]^+$	SPL	167.8(4)	999 [e]	2012[261]
$[(PNP')Ir^{IV}N]$	SPL	[172]	901 [e]	2012[261]
$[(PNP')Ir^{III}(N\mathit{t}Bu)]$	SPL	186.8(2)	—	2018[258]
$[(PNP')Ir^{IV}(N\mathit{t}Bu)]^+$	SPL	180.5(2)	—	2018[258]

[a] See Figure 1.3; LI: Linear
[b] Equilibrium bond distance (r_e) evaluated from rotational constant
[c] Raman shift
[d] KBr pellet
[e] Nujol

1.5.3. Matrix-Isolation Works

Works in which group 8 and 9 metal nitrido complexes were studied using matrix-isolation spectroscopy are limited to reactions of laser-ablated metal atoms and dinitrogen (Table 1.8, M + N_2).[185,202,232,243,254] The exception is iridium, for which no nitrido complexes were investigated in matrix-isolation experiments to this date. In

these works, mononuclear nitrido (MN) and dinitrido complexes ($M(N)_2$) were observed, except for cobalt, where only CoN was detected. The reaction products of laser-ablated transition metal atoms and nitrogen trifluoride were investigated for group 4, 6, and 11 elements (Table 1.8, M + NF_3). These products consist of triplet nitrene trifluorides (group 4),[271] nitrido trifluorides (group 6),[272] as well as difluoroimino fluoride and fluoroimido difluoride complexes (group 11).[273] Metal fluorido complexes were investigated in matrix-isolation experiments of the group 8 and 9 elements iron,[78,274] ruthenium,[275,276], osmium,[277] cobalt,[278] rhodium,[275] and iridium.[277]

Table 1.8: Vibrational frequencies $\tilde{\nu}$ (cm^{-1}) obtained from matrix-isolation IR spectroscopic investigations of product molecules embedded in dinitrogen, argon or neon. These include nitrido complexes from reactions of laser-ablated group 8 and 9 metals and N_2, as well as laser-ablated group 4 and 6 metals and NF_3. Additionally included are fluoroimido and difluoroimino complexes from the reaction of laser-ablated group 11 metals and NF_3.

Complex	$\tilde{\nu}(N_2)$	$\tilde{\nu}$(Ar)	$\tilde{\nu}$(Ne)	[REF]
M + N_2				
FeN	934.8	938.0	—	[185]
$Fe(N)_2$	903.6[a]	903.4[a]	—	[185]
RuN	981.5	984.0	—	[202, 232]
$Ru(N)_2$	831.5[a]	831.9[a]	—	[202, 232]
OsN	1049.6	1130.3	—	[202, 232]
$Os(N)_2$	901.1[a]	900.4[a]	—	[202, 232]
CoN	—	826.5	—	[243]
RhN	—	894.9	—	[254]
$Rh(N)_2$	830.9[a]	822.8[a]	—	[254]
M + NF_3				
$NTiF_3$	—	596.7, 782.1, 705.1[b]	—	[271]
$NZrF_3$	—	553.1, 667.4, 658.2[b]	—	[271]
$NHfF_3$	—	548.1, 666.7, 643.9[b]	—	[271]
$NCrF_3$	—	1015, 792, 705[b]	1020, 798, 709[b]	[272]
$NMoF_3$	—	1075, 704, 682[b]	1080, 708, 688[b]	[272]
NWF_3	—	1091, 693, 699[b]	1096, 704, 699[b]	[272]
$FNCuF_2$	—	1139.6, 736.2[c]	—	[273]
F_2NCuF	—	1090.5, 985.0, 678.5, 597.5[d]	1094.3, 988.2, –, –[d]	[273]
F_2NAgF	—	1099.2, 1006.2, 529.6, –[d]	1102.4, 1010.8, –, –[d]	[273]
F_2NAuF	—	1089.7, 1006.3, –, –[d]	1095.3, –, –, –[d]	[273]

[a] Antisymmetric stretching mode
[b] a_1 [ν(MN)], e [ν(MF)], a_1 [ν(MF)] (notation based on C_{3v} point group symmetry)
[c] ν(NF), ν_{as}(FCuF)
[d] ν_s(FNF), ν_{as}(FNF), ν(MF), δ(FNF)

2. Objectives

The chemistry of high-valent late transition metal complexes is more intricate and convoluted than a simple MO picture based on the isoelectronegativity principle would suggest. In other words, the oxidation of a known nitrido metal complex in a low metal oxidation state, especially those of late transition metals, can often not simply be represented as removing of electrons from the metal center, as one might assume based on a simplified MO model. This widespread view completely neglects more recent developments in the chemistry of very high-valent metal complexes, such as the concept of *non-innocent oxo and nitrido ligands*,[75,76] the concept of an *inverted ligand field*,[279] as well as the enhanced *primogenic repulsion* in high-valent 1st row transition metal complexes,[96,97] and the near-degeneracy of excited electronic states in high-valent complexes. Also an appropriate quantum chemical description of such high-valent compounds is difficult and intricate.[62,125] Therefore, the spectroscopic characterization of reactive species bearing metals in their highest possible oxidation states and which currently cannot be synthesized using conventional methods is highly desired.

Although structural and vibrational data of a considerable number of terminal nitrido complexes of group 8 and 9 were already reported, only one nitrido compound of iron in the formal OS of VI has so far been described and for cobalt the diatomic CoN is, as far as I know, the only experimentally known example of a nitrido cobalt compound. As this work relies on a systematic experimental and computational study of high-valent late transition metal nitrido complexes it should be emphasized, that even in those cases where reliable XRD data are available, the electronic properties and the strength of the metal nitrido ligand multiple bond seems to be significantly influenced by the supporting complex ligands, especially in the presence of donor ligands or solvent molecules in a *trans*-position to the nitrido ligand. These data seems to be only of limited use for a systematic and rigorous computational investigation of high-valent late transition metal nitrido compounds. A much better experimental basis for such an investigation, on the other hand, is provided by vibrational data of closely related and more simple metal nitrido compounds using innocent auxiliary ligands that support and enable a rigorous computational investigation.

The aim of this work was therefore to use the matrix-isolation technique to prepare such high-valent late transition metal complexes with metal-nitrogen multiple bonds. These encompass metal-nitrido and metal-imido bonding with emphasis on high metal oxidation states as well as exploring the limits of attainable oxidation states in binary metal-nitrido complexes without supporting auxiliary ligands. In particular, this was achieved by reacting laser-ablated group 8 and 9 transition metal atoms with nitrido trifluoride, and laser-ablated iridium atoms with dinitrogen. For the former

reaction, products were expected to include NMF_3 and $FNMF_2$ compounds that either feature a metal-nitrido triple bond with high-valent metal centers, or the uncommon fluoro-substituated fluoroimido ligand, both stabilized by innocent fluorido (F^-) auxiliary ligands. The latter experiment with iridium atoms was aimed to explore the oxidation state limit that can be achieved in binary iridium nitrido complexes. Since iridium is able to reach formal oxidation states of up to IX, the goal was to generate and characterize molecular trinitrido iridium(IX), $Ir(N)_3$.

The results of this work are briefly outlined in the next section, followed by the corresponding articles in Section 4 and their Supporting Information in the Appendix.

3. Outline

The reaction of laser-ablated group 8 and 9 late transition metal atoms with nitrogen trifluoride diluted in inert gas provides access to products formed by metal insertion into one of the N−F bonds and subsequent rearrangement reactions shown in Reactions 1–3.

$$NF_3 + M \longrightarrow F_2N{-}MF \quad \{1\}$$

$$F_2N{-}MF \longrightarrow FN{=}MF_2 \quad \{2\}$$

$$FN{=}MF_2 \longrightarrow N{\equiv}MF_3 \quad \{3\}$$

Because the N−F bond can be expected to be much weaker than the corresponding M−F bonds and the barrier for an exothermic fluorine migration from nitrogen to the metal center is usually low, it should lead, in most cases, to the nitrido metal trifluorides with the metal in the OS of VI. Indeed, nitrido fluorides, $N{\equiv}MF_3$, were obtained for M = Fe, Ru, Os, Rh, Ir, while only for M = Co and Rh fluoroimido complexes, $FN{=}MF_2$, were observed. These products were deposited on a cryogenic matrix support trapped in solid inert gas.

The laser-ablation of iridium atoms in the presence of dinitrogen gas should not only lead to its dinitrogen complexes. Iridium atoms may also insert into the N≡N bond of N_2 to yield NIrN, but also N atoms will be generated by photo-decomposition of N_2, which is exposed to the broadband radiation emitted by the plasma plume. Reactions of nitrogen radicals with iridium atoms may lead to the formation of IrN, $Ir(N)_2$ and $Ir(N)_3$ product molecules with formal iridium OSs of up to IX. The product molecules are then rigorously investigated using IR spectroscopy in conjunction with quantum-chemical calculations. Of particular interest in these studies is the nature of the metal-nitrogen multiple bond to the group 8 and 9 metal centers in high OS facilitated by either innocent fluorido spectator ligands or additional nitrido ligands.

3.1. Group 8 Nitrido Fluoride Complexes

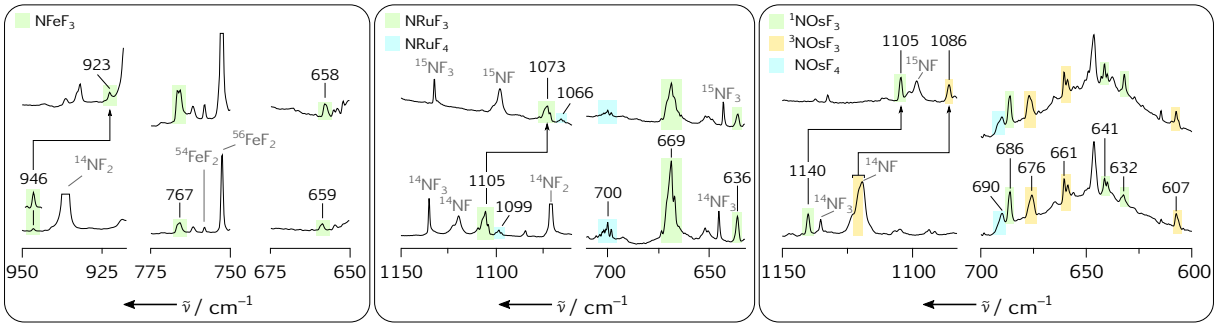

Figure 3.1. IR absorption spectra obtained from co-deposition of laser ablated group 8 metals iron (left), ruthenium (center) and osmium (right) with $^{15}NF_3$ (top) and $^{14}NF_3$ (bottom) in solid neon. For clarity, vibrational frequencies for just one isotopologue are given only when no $^{14/15}N$ isotopic shift was detected. For more details see Section 4.1.

The main reaction product of excited laser-ablated group 8 atoms with nitrogen trifluoride (NF_3) is nitrido metal(VI) trifluoride ($NM^{VI}F_3$, M = Fe, Ru, Os), with weaker signals of nitrido metal(VII) tetrafluorides ($NM^{VII}F_4$, M = Ru, Os). All NMF_3 and NMF_4 product formations are calculated to be considerably exothermic at the DFT level of theory. Excerpts from the IR spectra of the product molecules depicted in Figure 3.1 show all assigned product bands and their isotopic shifts caused by substituting the $^{14}NF_3$ reactant with $^{15}NF_3$. The assignment of the product molecules was facilitated by distinct $^{14/15}N$ isotopic shifts of vibrational frequencies of modes that involve nitrogen displacements and sophisticated quantum-chemical calculations. The latter allowed thorough investigations of the electronic and geometric structure of the main products. An overview of these results is presented in Figure 3.2.

As outlined in Section 1.5.1, the dicationic $[(Me_3cyclam\text{-}ac)Fe^{VI}N]^{2+}$ complex in pseudo octahedral (PO) coordination geometry is the only iron(VI) nitrido complex known to this date.[67] In accordance with the *d*-orbital splitting scheme (see Figure 1.3) for this coordination geometry, a singlet ground state was determined for this complex featuring a Fe≡N triple bond with a bond distance of 157(2) pm obtained by fitting EXAFS data.[67] Complexes in pseudo tetrahedral (PTD) geometries with Fe^{IV} and Fe^{V} centers have been successfully characterized as well, with Fe−N bond distances determined by XRD of 150.0(3) cm^{-1} to 153.2(5) cm^{-1},[15,174–177] and Fe−N vibrational frequencies of 1008 cm^{-1} to 1034 cm^{-1}.[173–175] The hexavalent, three-fold symmetric $NFe^{VI}F_3$ complex presented in this work features a d^2 high-spin ground state electronic configuration (Figure 3.2). The band position at 946 cm^{-1} assigned to the Fe−N stretching mode of the highly symmetric pseudo tetrahedral (PTD) complex with C_{3v} point group symmetry is consistent with a weakened Fe≡N triple bond

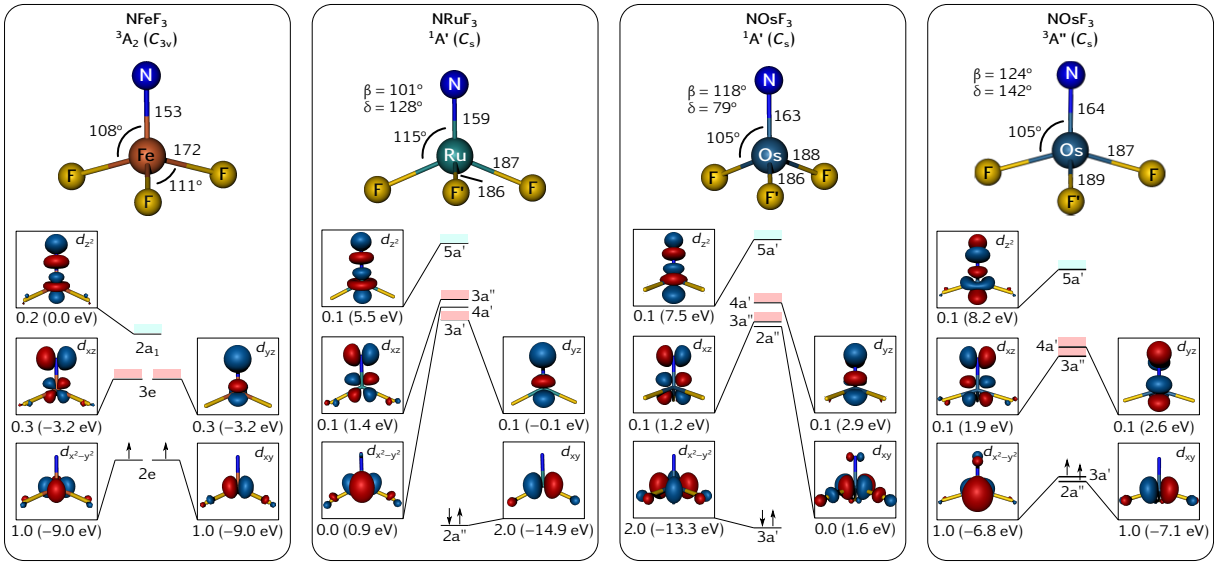

Figure 3.2. Calculated geometric structures and *d*-orbital splitting schemes, including occupation numbers and orbital energies, of the identified NMF_3 species. Antibonding σ^* and π^* MOs are highlighted in pink and light cyan, respectively. For more details see Section 4.1.

caused by configuration mixing evident by the increasing population of Fe−N antibonding 3e and $2a_1$ natural MOs shown in Figure 3.2. This results in an effective bond order (EBO) of 2.2 for the Fe≡N triple bond.

The bands assigned to the heavier ruthenium congener $NRu^{VI}F_3$ are consistent with a distorted PTD coordination geometry, the first terminal ruthenium nitrido complex in PTD coordination geometry. The band at 1105 cm^{-1} assigned to the Ru−N stretching vibration is indicative for a strong Ru≡N triple bond close to the frequency obtained for diatomic RuN at 1109 cm^{-1} (see Table 1.2). This observation is consistent with the computational results for $NRu^{VI}F_3$ which show a singlet electronic ground state. Analysis of the CASSCF wave function reveals low populations of the antibonding σ^*-type (5a′) and π^*-type (3a′, 3a″) natural MOs and an EBO of 2.7. Calculations at the CCSD(T)/CBS level of theory locate the C_{3v} symmetric $^3A_2$ triplet state only 5 $kJ\,mol^{-1}$ above the distorted singlet $^1A'$ electronic ground state. In the singlet configuration, the electrons are paired in one of the metal centered degenerate *e*-type MOs (c.f. 2e of $NFeF_3$), namely d_{xy}, which leads to the distorted ground state structure. In addition, bands at 1099 cm^{-1} and 700 cm^{-1} are assigned to $NRuF_4$ in C_{4v} point group symmetry. It adopts a $^2B_1$ doublet ground state and is the first heptavalent ruthenium nitrido complex (for details see Section 4.1).

The first osmium nitrido complex, $[(O)_3Os^{VIII}N]^-$, published in 1847 is not only the one with the highest OS, but also the only example in PTD coordination geometry (see Table 1.3).[12] The d^0 configuration of this complex, which was synthesized

from OsO_4 and NH_3, is consistent with its undistorted C_{3v} structure, an Os−N bond distance of 162 pm, and with a stretching frequency of 1023 cm^{-1}.[222–224] Quantum-chemical calculations at the CCSD(T)/CBS level for the pseudo-tetrahedral $NOsF_3$, on the other hand, predict quasi degenerate, distorted structures in singlet $^1A'$ and triplet $^3A''$ electronic states with an energy gap of −1.3 kJ mol^{-1} in favor of the triplet state. In fact, the spectra clearly show the formation of at least two different osmium nitrido species in good agreement with the predicted vibrational data (see Section 4.1). Consequently, the bands (Figure 3.1) were assigned to $NOsF_3$ molecules in two different electronic states, which are depicted in Figure 3.2. The Os−N stretching frequencies of 1140 cm^{-1} ($^1A'$) and 1086 cm^{-1} (Os−^{15}N, $^3A''$) and the calculated bond distances of 163 pm ($^1A'$) and 164 pm ($^3A''$) indicate strong Os≡N triple bonds. Furthermore, the band at 690 cm^{-1} provides evidence for the formation of $NOs^{VII}F_4$.

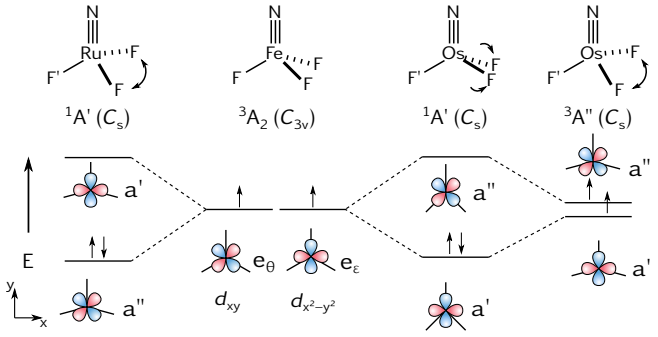

Figure 3.3. Hidden-pseudo-Jahn–Teller distortions and different d^2 electronic configurations of characterized group 8 nitrido metal fluorides NMF_3.

Interestingly, all four NMF_3 have different geometric and electronic structures. A high symmetry C_{3v} ground state was only verified for $NFeF_3$, albeit predicted by Hund's rule for two electrons in two-fold degenerate MOs. Figure 3.3 summarizes the metal centered *e* orbital occupations and correlates them to the distortions of the different d^2 NMF_3 species. Exhaustive potential energy surface (PES) scans of all electronic states arising from the e^2 configurations provides evidence that the origin of the ground state distortions are due to pseudo-Jahn–Teller effects "hidden" in the excited states.[280–282] For details see Section 4.1.

3.2. Group 9 Nitrido and Imido Complexes

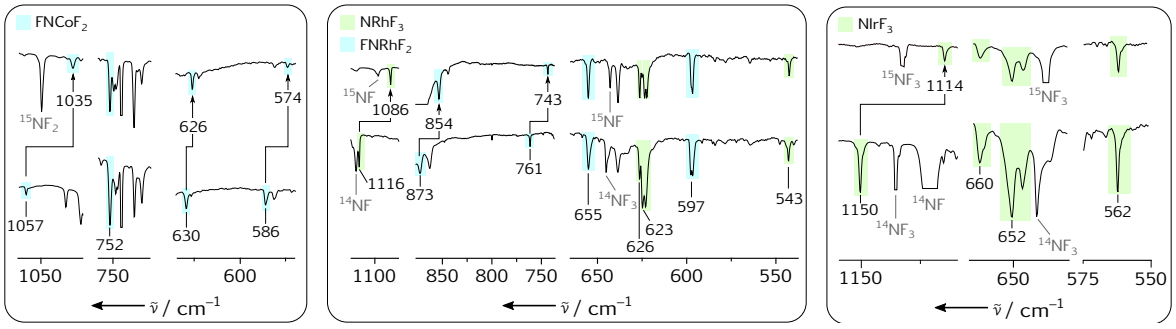

Figure 3.4. IR transmission spectra obtained from co-deposition of laser ablated group 9 metals cobalt (left), rhodium (center) and iridium (right) with $^{15}NF_3$ (top) and $^{14}NF_3$ (bottom) in solid neon. For clarity, vibrational frequencies for only one isotopologue are shown when no isotopic shift was detected. For more details see Section 4.2.

The most stable structural isomers obtained from NF_3 + M (M = Co, Rh, Ir) and predicted by DFT calculations are $FNCoF_2$, $NRhF_3$ and $NIrF_3$, which corroborates the assignments of the IR transmission spectra shown in Figure 3.4. Additional bands in the rhodium spectrum exhibit distinct $^{14/15}N$ isotopic shifts that lead to the assignment of $FNRhF_2$ which is only 12 kJ mol^{-1} higher in energy than the structural isomer $NRhF_3$. The metal-nitrogen bond found in the fluoroimido complexes of cobalt and rhodium is very different to the ones described in Section 1.5.2 for N−CR imido ligands. In the latter complexes bearing organic imido ligands the bonding is facilitated by π interactions of N($p_{x,y}$) and M($d_{xz,yz}$) orbitals and a linear or nearly linear coordination. The d-orbital interactions depicted in Figure 3.5 show that in $FNCoF_2$ and $FNRhF_2$ the metal-nitrogen bond is formed by a σ-type interaction of the M(d_{z^2}) and N(p_z) orbitals (Figure 3.5, 4a′ MO corresponds to the σ^* antibonding MO) that is perpendicular to the N−F bond, resulting in a strongly bent structure with a M−N−F bond angle of 113° for both $FNMF_2$ complexes. Additionally, a π-type bond is provided by the interaction of M(d_{xz}) and N(p_x) orbitals. The corresponding π^* antibonding orbital is labeled 3a″ in Figure 3.5. The highest occupied molecular orbital (HOMO) of the dianionic fluoroimido ligand NF^{2-} (HOMO not shown in Figure 3.5) has mainly π^* F−N antibonding character and is strongly polarized towards the N atom. Any electron density donated from this ligand orbitals into a metal-centered orbital results in a strengthening of the N−F bond. A low EBO of 1.1 for the N−Co bond follows from the high natural occupation numbers of the antibonding orbitals of $FNCoF_2$ (3a″ and 4a′ MOs in Figure 3.5), which results in a very long N−Co bond distance of 177 pm and a weak N−Co bond. This is in very good agreement with the band positions assigned to primarily N−Co and N−F stretching modes. The former is surprisingly low at 586 cm^{-1}, confirming

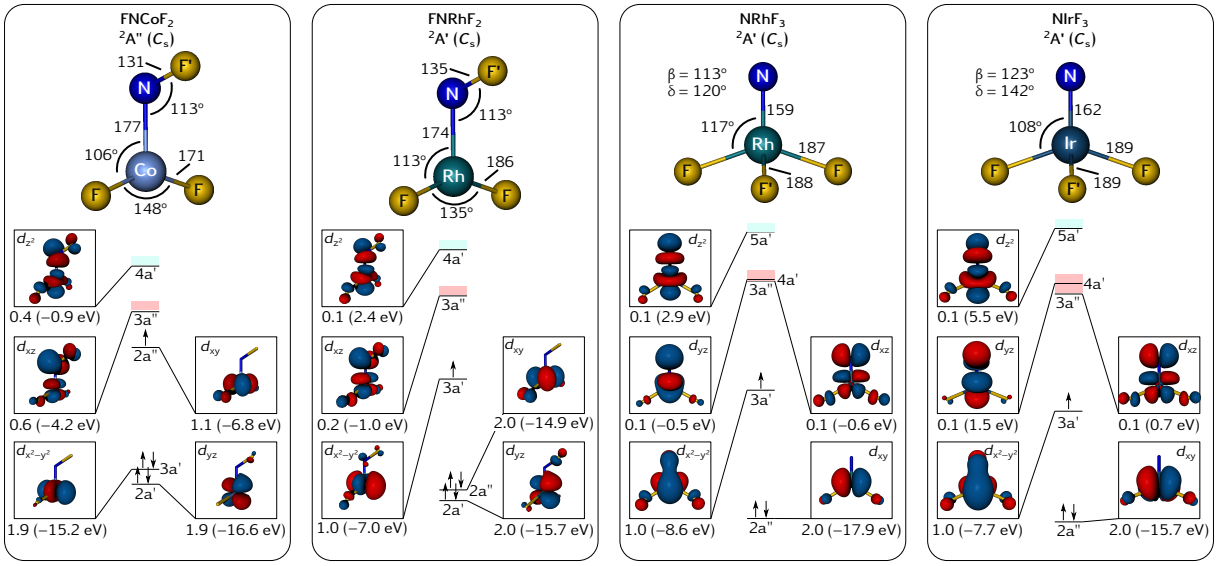

Figure 3.5. Calculated geometric structures and *d*-orbital splitting schemes, including occupation numbers and orbital energies, of the identified NMF_3 species. Antibonding σ^* and π^* MOs are highlighted in pink and light cyan, respectively. For more details see Section 4.2.

the weak Co−N bond strength. The latter is located at 1057 cm^{-1}, only red-shifted by 63 cm^{-1} from that of free, neutral NF in solid neon at 1119 cm^{-1}, which indicates a considerable oxidation of the formally dianionic FN^{2-} ligand. The non-innocent behavior of the NF^{2-} ligand in $FNCoF_2$ is further supported by the considerable spin populations of −0.46 and 1.46 at the nitrogen and cobalt atom, respectively, obtained by CASSCF calculations. In line with, according to natural population analysis (NPA) and QTAIM analyses, an almost uncharged NF ligand (instead of the formal dianionic FN^{2-}), the NF ligand features considerable imidyl/nitrene radical character. It is worth pointing out that this effect is even stronger pronounced in the FN stretching frequency of $FNCuF_2$ in solid argon.[273] It was assigned to a band at 1140 cm^{-1}, significantly higher than that of free NF in solid argon at 1115 cm^{-1}, hinting at a formal NF^{2-} ligand oxidation beyond neutral NF.[273] In contrast, the bands of $FNRhF_2$ assigned to these modes are located at 873 cm^{-1} and 761 cm^{-1}, indicating a stronger Rh−N, and a weaker N−F bond. This observation is in full agreement with the calculated stretching frequencies (872 cm^{-1} and 707 cm^{-1}), a higher Rh=N EBO of 1.7, and negative NPA and QTAIM total charge of the NF ligand (NPA: −0.13, QTAIM: −0.20). For details see Section 4.2.

The electronic and geometric structures of $NRhF_3$ and $NIrF_3$ are very similar. They both show Jahn–Teller distortions of the high-symmetry C_{3v} reference structure caused by an uneven occupation of the two-fold degenerate *e* orbital with three electrons. This leads to a widening of the F−M−F angle and a lifting of the degeneracy of the e^3 orbital

into $(2a'')^2(3a')^1$ (Figure 3.5). In fact, the geometric structures of these complexes are very similar to that of $NRuF_3$ whose $^1A'$ electronic ground state configuration corresponds to that determined for $NRhF_3$ and $NIrF_3$, with the outermost electron removed from the 3a′ orbital. The band positions of the symmetric and antisymmetric F−M−F stretching mode are red-shifted by about 45 cm^{-1} for M = Rh compared to that of M = Ru, which can be attributed to a weak F−M−F antibonding character of the 3a′ MO. At 1150.4 cm^{-1}, the Ir−N stretching frequency of $NIrF_3$ is the highest value determined so far for any metal-nitrogen bond. For details see Section 4.2.

While the diatomic IrN has been thoroughly investigated,[262–265,283] higher binary nitrido complexes have not been characterized so far. This is especially intriguing as it has been shown that molecular $M(N)_2$ species were formed by the reaction of nitrogen atoms with diatomic MN molecules isolated in noble gas matrices upon annealing.[185] Given the ability of iridium to achieve OSs of up to IX, this opens up the possibility to produce $Ir(N)_3$, a neutral complex with formal iridium OS of IX. The IR absorption of diatomic Ir≡N in solid neon was assigned to a band at 1111 cm^{-1}, in very good agreement with the gas-phase value of 1114 cm^{-1}.[262] The antisymmetric N−Ir−N stretching mode of $Ir(N_2)$ in solid neon was assigned to a band located at 853 cm^{-1}. The $^{14/15}N$ isotopic pattern for this mode showed no band corresponding to the $Ir(^{14}N)(^{15}N)$ isotopologue when the spectrum was recorded using a 1:1 mixture of $^{14}N_2$ and $^{15}N_2$ diluted in neon. However, when the spectrum is recorded in a pure 1:1 mixture of $^{14}N_2$ and $^{15}N_2$ an intensity pattern of approximately 1:2:1 is observed. This shows a formation of $Ir(N)_2$ in two different ways. Diluted in neon the reaction takes place by insertion of an iridium atom in the N≡N bond of dinitrogen, while in pure nitrogen it takes place by addition of a nitrogen atom to molecular IrN (Reaction 4 and 5, respectively).

$$Ir + N_2 \longrightarrow Ir(N)_2 \quad \{4\}$$

$$IrN + N \longrightarrow Ir(N)_2 \quad \{5\}$$

Although nitrogen atom mobility in cryogenic noble gas matrices was observed and the addition of a nitrogen atom to $Ir(N)_2$ is predicted to be considerably exothermic, no band could be assigned to $Ir(N)_3$. Since the formation of $Ir(N)_3$ through the insertion of IrN into the N≡N bond of N_2 has a high barrier and, on the other hand, its formation starting from $Ir(N)_2$ + N already requires a larger amount of $Ir(N)_2$, the yield of $Ir(N)_3$, if any, is expected to be very low. In addition, the calculated intensity of the IR active stretching band of $Ir(N)_3$ is much lower than that of $Ir(N)_2$, which renders the detection of this band in the IR spectrum very unlikely.

The SOMO of the $^2B_1$ doublet electronic ground state of $Ir(N)_2$ determined by quan-

tum-chemical calculations corresponds to a delocalized out of plane π^*-type MO. As a consequence, the spin density is well delocalized and the determination of an integer OS is not possible. The nitrido ligands in this case must be considered non-innocent and possess partial nitridyl ($N^{2-\bullet}$) character. The iridium OS in $Ir(N)_2$ is between V and VI. In the case of the C_{3v} point group symmetric $Ir(N)_3$, a $^1A_1'$ electronic ground state was calculated. The HOMO corresponds to a doubly occupied, non-bonding metal centered d_{z^2} orbital which indicates an iridium OS of VII associated with a partially oxidized nitrido ligands with an average OSs of −2.3, as well as an considerable nitridyl ($N^{2-\bullet}$) radical character. For details see Section 4.3.

4. Publications

4.1. High-Spin Iron(VI), Low-Spin Ruthenium(VI), and Magnetically Bistable of Osmium(VI): Molecular Group 8 Nitrido Trifluorides NMF_3

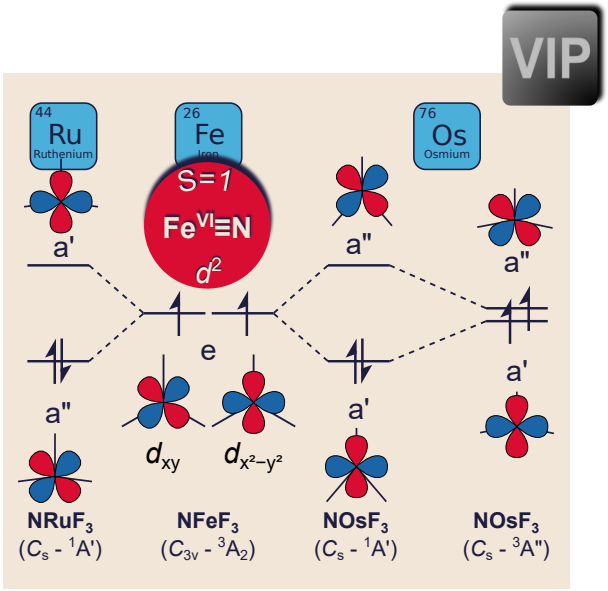

Tony Stüker, Xiya Xia, Helmut Beckers and Sebastian Riedel*
Chemistry — A European Journal, **2021**, Advance online publication.
DOI: 10.1002/chem.202101404
© *2021 The Authors. Published by Wiley-VCH GmbH*
For the Supporting Information see Appendix A.1.

Author Contribution

Tony Stüker did all calculations, wrote the manuscript and supervised the experiments. Tony Stüker and Xiya Xia carried out the experiments. Helmut Beckers and Sebastian Riedel managed the project and revised the manuscript.

Chemistry–A European Journal | Full Paper
doi.org/10.1002/chem.202101404
Chemistry Europe
European Chemical Societies Publishing

VIP High-Spin Iron(VI), Low-Spin Ruthenium(VI), and Magnetically Bistable Osmium(VI) in Molecular Group 8 Nitrido Trifluorides NMF_3

Tony Stüker,[a] Xiya Xia,[a] Helmut Beckers,[a] and Sebastian Riedel*[a]

Abstract: Pseudo-tetrahedral nitrido trifluorides $N{\equiv}MF_3$ (M = Fe, Ru, Os) and square pyramidal nitrido tetrafluorides $N{\equiv}MF_4$ (M = Ru, Os) were formed by free-metal-atom reactions with NF_3 and subsequently isolated in solid neon at 5 K. Their IR spectra were recorded and analyzed aided by quantum-chemical calculations. For a d^2 electron configuration of the $N{\equiv}MF_3$ compounds in C_{3v} symmetry, Hund's rule predict a high-spin $^3A_2$ ground state with two parallel spin electrons and two degenerate metal d(δ)-orbitals. The corresponding high-spin $^3A_2$ ground state was, however, only found for $N{\equiv}FeF_3$, the first experimentally verified neutral nitrido Fe^{VI} species. The valence-isoelectronic $N{\equiv}RuF_3$ and $N{\equiv}OsF_3$ adopt different angular distorted singlet structures. For $N{\equiv}RuF_3$, the triplet $^3A_2$ state is only 5 kJ mol^{-1} higher in energy than the singlet $^1A'$ ground state, and the magnetically bistable molecular $N{\equiv}OsF_3$ with two distorted near degenerate $^1A'$ and $^3A''$ electronic states were experimentally detected at 5 K in solid neon.

Introduction

The group 8 transition metals have eight electrons in their valence shell, but in addition to the well-known strong oxidizers RuO_4 and OsO_4, only Os has a variety of different complexes in oxidation state VIII.[1] While the oxidation state VI is abundant for ruthenium and osmium, the complex anion $[FeO_4]^{2-}$ was the only known Fe^{VI} compound for a long time.[2] In 2007 the neutral, dioxo Fe^{VI} peroxide $O_2Fe(\eta^2\text{-}O_2)$ was reported to be formed from molecular FeO_2 and O_2 under cryogenic conditions.[3] Tetrahedral $Fe^{VIII}O_4$ was shown to be metastable with respect to $O_2Fe^{VI}(\eta^2\text{-}O_2)$ in the gas phase,[4] and the oxidation state VII is so far the highest oxidation state of iron observed experimentally for the tetrahedral tetroxide anion FeO_4^-.[5] In addition to oxygen, nitrogen ligands are also able to stabilize high oxidation states of iron. Such terminal iron-nitrido complexes have already been the subject of several up-to-date reviews.[6] We restrict ourselves to some representative examples such as the square-pyramidal $[(TPP)Fe^{V}N]$ (TPP^{2-} = tetraphenylporphyrinate dianion), characterized by Raman spectroscopy,[7] the tetragonal nitrido Fe^{VI} dication $[(Me_3cyac)FeN]^{2+}$ ($[Me_3cyac]^-$ = *N,N,N*-tri-methyl-1,4,8,11-tetraazacyclotetra-decane-1-acetate), confirmed by Mössbauer and X-ray spectroscopy,[8] the pseudo-tetrahedral $[(PhB(PCH_2PiPr_2)_3)Fe^{IV}N]$ ($PhB(PCH_2PiPr_2)_3$ = tris(diisopropylphosphinophenyl)borane),[9] and, very recently, the crystal structure of a thermally stable four-coordinate Fe^{VI} bis(imido) cation, $[(H_2B(MesIm)_2)Fe(=NMes)_2]^+$ ($[H_2B[MesIm]_2]^-$ = dihydrobis-[1-(2,4,6-trimethylphenyl) imidazol-2-ylidene]borato).[10]

Nitrido iron complexes play an important role in a number of chemical and biological processes, for example in the catalytic cycle of cytochrome P450,[11] in the FeMo cofactor of the nitrogenase enzyme[6a] and in the Haber–Bosch process.[12] In analogy to the active iron surface nitride in the Haber–Bosch process, ammonia synthesis has also successfully achieved under mild conditions using the ruthenium pincer nitrido complex [(PNP)RuN] (PNP^- = $[N(CH_2CH_2P^tBu_2)_2)]^-$).[13] Quite recently osmium(VI) nitrides have emerged as a new class of potential anticancer and antitumor agents.[14] Examples include $[(bipy)Cl_3Os^{VI}N]$[15] (bipy = 2,2′-bipyridine)[16] and $[(sap)(py)ClOs^{VI}N]$ (sap = deprotonated *N*-salicylidene-2-aminophenol).[17] The wide field of possible applications of group 8 nitrido complexes underline the importance of a deeper understanding of the properties of this class of compounds. Especially the nitrido metal–ligand multiple bond and the valency of the metal are key factors for the reactivity and structure of these compounds.

In particular, there has been a tremendous progress in the synthesis and the chemistry of molecular Fe^{IV} and Fe^{V} nitrido compounds in the recent years that have been described in detail in several review articles.[6] They are supported by sterically encumbered macrocyclic or chelating ligands involving nitrogen or *N*-heterocyclic carbene donors based on, for example porphyrin or nitrogen- and boron-anchored tri- and tetrapodal chelates to protect the reactive Fe≡N moiety (see Scheme 1 for representative examples). The most common route to these nitrido compounds is the photolysis of an iron azido precursor and concomitant N_2 evolution, whereby the

[a] T. Stüker, X. Xia, Dr. H. Beckers, Prof. S. Riedel
Institut für Chemie und Biochemie, Anorganische Chemie
Freie Universität Berlin
Fabeckstr. 34/36, 14195 Berlin (Germany)
E-mail: s.riedel@fu-berlin.de

Supporting information for this article is available on the WWW under https://doi.org/10.1002/chem.202101404

© 2021 The Authors. Chemistry - A European Journal published by Wiley-VCH GmbH. This is an open access article under the terms of the Creative Commons Attribution License, which permits use, distribution and reproduction in any medium, provided the original work is properly cited.

Chemistry–A European Journal | Full Paper doi.org/10.1002/chem.202101404 | Chemistry Europe European Chemical Societies Publishing

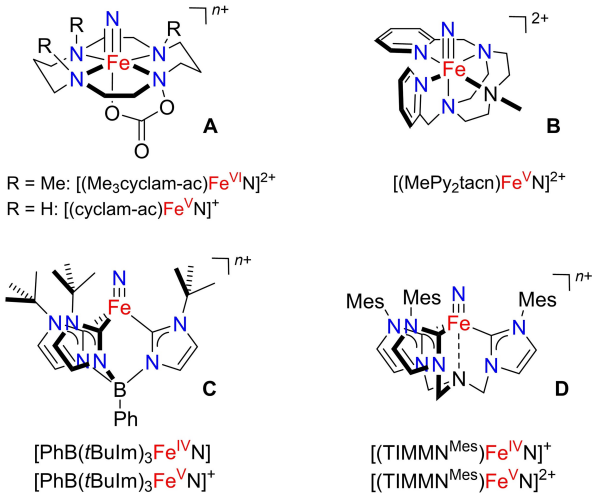

Scheme 1. Representative examples of ligand-supported tetragonal (**A**[8,22] and **B**[19d]) and trigonal (**C**[19a] and **D**[19b]) coordinated high-valent iron nitrido complexes.

one-electron oxidation of the Fe^{IV} nitrido complexes often represents an alternative route to Fe^{V} nitrido complexes.[6a,b]

The reactivity of these high-valent nitrido iron compounds in chemical transformations have been thoroughly explored,[6,18] their structures, and their electronic properties have been investigated in detail using a variety of experimental and quantum mechanical methods.[19] While these studies contributed greatly to the understanding of the iron nitride bonding motif, our knowledge about the behavior, the nature, and bond-strengths of the Fe≡N triple bond in high valent iron compounds upon iron oxidization is, however, still very limited and contradictory. Two questions arise here: *Is there a nitrido wall*[20] *from which the nitrido ligand gives up its innocent behavior,*[21] *and does the Fe≡N bond become stronger and stronger through oxidation of the iron center?*

It should be emphasized that the known iron nitrido species can be divided into trigonal (pseudo-tetrahedral) and tetragonal (pseudo-octahedral) complexes (Scheme 1), since these two groups show different ligand field splitting of the Fe(3d) orbitals.[9,23] In a trigonal C_{3v} ligand field there are two purely Fe≡N nonbonding *e*-type orbitals (d_{xy,x^2-y^2}), which allow the accommodation of up to four electrons energetically below the antibonding Fe≡N orbitals.[6a,c,9,23] This results in a relatively strong Fe≡N triple bonds, for example, low spin Fe^{IV} derivatives, for which very short experimental Fe–N distances (Table S1 in the Supporting Information) and Fe–N stretching vibrations at 1008–1034 cm^{-1} were found.[9,24]

Conversely, in the tetragonal C_{4v} ligand field there is only one purely nonbonding (d_{xy}) orbital with respect to the Fe≡N bond energetically below the π*-antibonding ($d_{xz,yz}$) MOs.[6a,c] A d-electron count larger than two results here in the occupation of π*(Fe≡N) orbitals, and, accordingly, Fe^{IV} (d^4) and Fe^{V} (d^3) nitrido complexes in tetragonal symmetry are generally thermally less stable and more reactive.[6b,18a,c] Note that the d^3 ground-state electron configuration of Fe^{V} nitrido complexes is subject to a Jahn–Teller distortion.[19b,c] To overcome the thermal instability and high reactivity of such tetragonal Fe^{V} nitride complexes their Fe≡N distances and stretching frequencies were obtained by a variety of spectroscopic methods either at cryogenic temperatures or at the gas phase (for representative examples, see Table S1). As expected, the experimental Fe–N distances for the two tetragonal complexes $[Fe^{V}(N)(MePy_2tacn)]^{2+}$ (Scheme 1, $3d^4$ configuration, Fe–N: 164(1) pm)[19d] and $[Fe^{V}(N)(cyclam\text{-}ac)]^{+}$ (Scheme 1, cyclam-ac = 1,4,8,11-tetraazacyclotetradecane-1-acetato, Fe–N: 161(1) pm),[22] estimated from extended X-ray absorption fine structure (EXAFS) analysis, were found to be longer than the Fe–N distance of the analogous Fe^{VI} dication $[Fe^{VI}(N)(Me_3cyclam\text{-}ac)]^{2+}$ (Scheme 1, 157(2) pm) with a singlet $3d^2$ configuration.[8]

In contrast, the formal Fe≡N bond order in trigonal Fe-nitrido complexes does not change by increasing the iron oxidation state from singlet Fe^{IV} to triplet Fe^{VI}, making predictions about the bond lengths less intuitive as other factors such as the geometry and the nature of the ligands come to the fore. X-ray structure analysis of the $Fe^{IV}N/Fe^{V}N$ derivatives of the two redox pairs $[PhB(tBuIm)_3FeN]^{0/+}$ (Scheme 1)[19a,24b] and $[(TIMMN^{MES})FeN]^{+/2+}$ (Scheme 1)[19b] show different trends. While the Fe–N length decreases slightly from 151.2(1) pm to 150.6(2) pm for the former, it increases from 151.3(3) pm to 152.9(1) pm for the latter. The different trend in these Fe≡N distances during oxidation of Fe^{IV} to Fe^{V} was attributed to a possibly stronger interaction between the ligand N anchor with the more electrophilic Fe^{V} center in $[Fe(N)(TIMMN^{MES})]^{2+}$ (Scheme 1).[19b] On the other hand, also coordinated solvent molecules can make it difficult to compare the Fe≡N distances of different complexes, since this leads to shortened experimental Fe≡N distances.[19e]

In this work, we describe the preparation of the molecular, neutral nitrido trifluorides $NM^{VI}F_3$ of the group 8 metals M = Fe, Ru, Os from IR laser ablated metal atoms and gaseous NF_3 and their IR-spectroscopic characterization under cryogenic conditions in a noble gas matrix. These trigonal nitrido trifluorides bear genuine M≡N triple bonds, unsupported by sterically encumbered electron donor substituents with the innocent fluoride ligand. The M≡N stretching vibration of theses derivatives is energetically sufficiently isolated from other fundamentals. Hence, it is considered to be a reliable experimental signature for M–N bond strength and M–N bond length in these nitrido complexes. This analysis overcomes the difficulties described above and also has the advantage that the experimental results can be supported and analyzed by reliable and accurate quantum mechanical calculations of these molecular, neutral compounds. Furthermore, this analysis enables a direct comparison of experimental M≡N stretching frequencies of $M = Fe^{VI}$ and its heavier group 8 congeners with those of the analogous nitrido trifluorides $N{\equiv}MF_3$ of group 6 (M = Cr, Mo, W)[25] and group 9 (Co, Rh, Ir)[26] transition metals which have been studied previously. To the best of our knowledge, $N{\equiv}Fe^{VI}F_3$ is the first experimentally verified neutral, nitrido iron(VI) complex. In addition, we have evidence for the formation of $NM^{VII}F_4$ (M = Ru, Os).

© 2021 The Authors. Chemistry - A European Journal published by Wiley-VCH GmbH

Chemistry–A European Journal | Full Paper doi.org/10.1002/chem.202101404 | Chemistry Europe European Chemical Societies Publishing

For an electronic metal d^2 configuration of these N≡MF_3 compounds in C_{3v} symmetry Hund's rule predict that two parallel spin electrons occupy the degenerate $M(d_{xy,x^2-y^2})$ orbitals of *e*-type symmetry resulting in a non-degenerate high-spin $^3A_2$ ground state. Although this $^3A_2$ state is not Jahn–Teller (JT) active, an electronic e^2 configuration can generally lead to a Jahn–Teller distorted ground state as a result of a strong pseudo-Jahn–Teller (PJT) mixing of two excited singlet electronic states.[27] This is because an electronic e^2 configuration in C_{3v} symmetry, in addition to the $^3A_2$ state, is generally associated with two electronic singlet states $^1A_1$ and ^1E. These electronic states are reminiscent of the well-known singlet excited states of molecular oxygen.[28]

It has been noted that the JT stabilization energy of the excited ^1E state is usually much weaker than the PJT stabilization resulting from mixing of the two excited $^1A_1$ and ^1E states. The stabilization energy of this PJT interaction can be so large that the lower of these excited states crosses the $^3A_2$ potential energy surfaces and become the distorted global minimum configuration.[27,31] We observed such a "hidden" PJT distortion for N≡RuF_3 and N≡OsF_3 but not for NFe≡F_3. Note that this distortion is also associated with a PJT-induced triplet-singlet spin crossover.[27a]

Results

Vibrational wavenumbers of group 8 nitrido trifluorides $NM^{VI}F_3$ and tetrafluorides $NM^{VII}F_4$

The IR spectra of the novel group 8 metal nitrido trifluorides, N≡MF_3 (M = Fe, Ru, Os) were recorded from the products obtained from laser-ablated free metal atoms with NF_3 seeded in a 1:1000 excess of neon after their deposition at 5 K on a gold-plated copper mirror (for experimental details see the Supporting Information). According to density functional theory calculations, the direct insertion of the metal atoms into an F–N bond of NF_3 to yield F_2N–MF, and the subsequent fluorine migration from nitrogen to the metal center to FN≡MF_2 is highly exothermic for all three metals (Figure 1, Table S2).

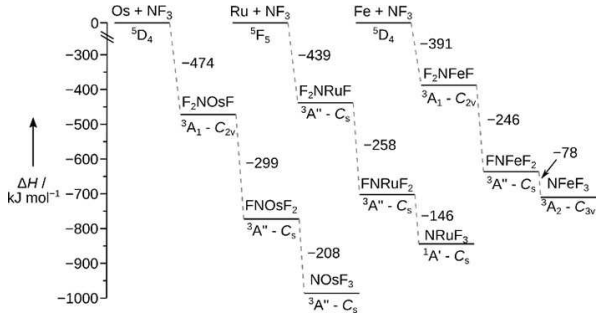

Figure 1. Stationary points on the reaction coordinate obtained at the BP86 level of theory for the formation of the nitrido metal complexes N≡MF_3 starting from the free metal atoms M and NF_3 (C_{3v} – $^1A_1$). See Table S2 for more details.

The rearrangement of the fluorimido complexes to the hexavalent nitrido trifluorides N≡MF_3 is found to be considerably exothermic for osmium (−208 kJ mol^{-1}), ruthenium (−146 kJ mol^{-1}), and iron (−78 kJ mol^{-1}) at the BP86/def2-QZVP[32] level of theory (details see the Supporting Information). Experimental IR spectra are shown from the deposits obtained in solid neon for the iron (Figures 2 and S1), ruthenium (Figures 3 and S2), and the osmium experiments (Figures 4 and S3), respectively. Experimental band positions are compared

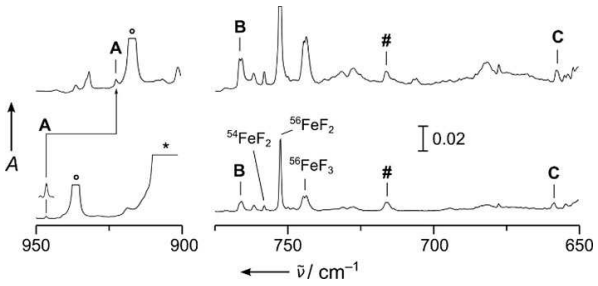

Figure 2. IR absorption spectra obtained from co-deposition of laser-ablated iron with 0.1 % $^{14}NF_3$ (bottom) and 0.1 % $^{15}NF_3$ (top) in solid Ne. Bands labeled with **A**, **B** and **C** are assigned to $NFeF_3$ (Table 1). Band **A** is enhanced by a factor of five. Known bands of binary iron fluorides[29] are labeled, and an unassigned band showing no $^{14/15}N$ isotopic shift is labeled with a hash mark. The bands associated with NF_2 and NF_3 are marked with circles and asterisks, respectively.[30] For more details, see Figure S1.

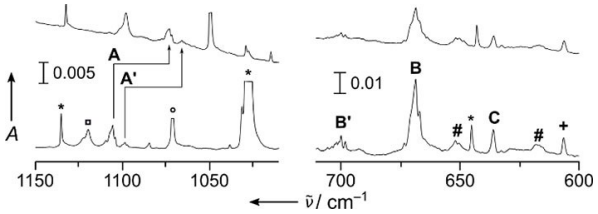

Figure 3. IR absorption spectra obtained from co-deposition of laser ablated ruthenium with 0.1 % $^{14}NF_3$ (bottom), and $^{15}NF_3$ (top) in solid Ne, respectively. Bands labeled **A**–**C** are attributed to $NRuF_3$ and **A'** and **B'** are due to $NRuF_4$. Unknown bands are labeled by a pound and a plus sign, respectively. The bands associated with ^{14}NF, $^{14}NF_2$ and $^{14}NF_3$ are marked with squares, circles, and asterisks, respectively.[30] For more details, see Figure S2.

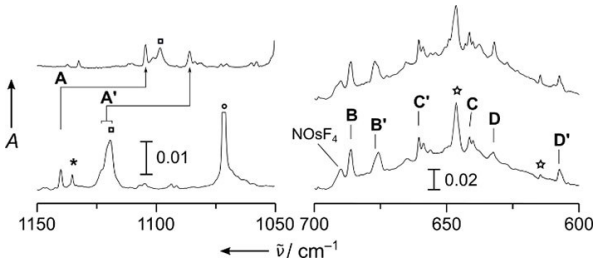

Figure 4. IR absorption spectra of laser ablated osmium co-deposited with 0.1 % $^{14}NF_3$ in solid Ne (bottom), with 0.1 % $^{15}NF_3$ in Ne (top). Bands labeled **A**–**D** are attributed to $NOsF_3$ ($^1A'$) and **A'**–**D'** to $NOsF_3$ ($^3A''$). The bands marked with a pentagram sign are binary osmium fluorides. The bands associated with NF, NF_2 and NF_3 are marked with squares, circles and asterisks, respectively.[30] For more details see Figure S3.

© 2021 The Authors. Chemistry - A European Journal published by Wiley-VCH GmbH

Chemistry–A European Journal | Full Paper doi.org/10.1002/chem.202101404 | Chemistry Europe European Chemical Societies Publishing

with predicted ones from quantum-chemical calculations in Tables 1 and S4 (for a detailed band assignment refer to the Supporting Information). The formation of molecular $NFeF_3$ (C_{3v}) is clearly proved by the assignment of all its stretching vibrations marked **A** (ν(NFe): 946.4 cm^{-1}), **B** ($\nu_{as}(FeF_3)$: 766.8 cm^{-1}), and **C** ($\nu_s(FeF_3)$: 658.8 cm^{-1}) in Figure 2 (Table 1). Bands at 743.6/744.7, 752.6 and 785.1 cm^{-1} were assigned to the known molecular binary iron fluorides $^{56}FeF_3$, $^{56}FeF_2$ and $^{54}FeF_2$, respectively.[29] Their high intensity and the high yield of these binary fluorides compared to the $NFeF_3$ product bands indicate the lower stability of $NFeF_3$ under the harsh conditions of the laser ablation process. The spectra recorded in the ruthenium experiment (Figure 3), clearly revealed the presence of two different nitrido ruthenium complexes, finally assigned to $NRuF_3$ (C_s) and $NRuF_4$ (C_{4v}). The characteristic Ru≡N stretching bands of $NRuF_3$ (C_s) and $NRuF_4$ (C_{4v}) are labeled **A** (1105.4 cm^{-1}, $NRuF_3$) and **A'** (1098.5 cm^{-1}, $NRuF_4$) in Figure 3. The RuF_3 stretching modes of C_s symmetric $NRuF_3$ split into three modes. The strong antisymmetric F–Ru–F appears at 668.5 cm^{-1} (labeled **B** in Figure 3) and likely overlaps with the nearby weaker F′–Ru band. The symmetric F–Ru–F mode is attributed to the band labeled **C** in Figure 3 at 635.8 cm^{-1} (Table 1).

Table 1. Calculated and experimental vibrational wavenumbers (ν(^{14}N) in cm^{-1}) and $^{14/15}$N isotopic shifts ($\Delta\nu$ in parentheses) for $NFeF_3$, $NRuF_3$, $NRuF_4$, $NOsF_3$ and $NOsF_4$.

Exp.[a]	CCSD (T)[b]	Assignment
$NFeF_3$ (C_{3v}, $^3A_2$)[c]		
946.4 (−23.7)[d]	1028 (−26)[e,f]	NFe str., a_1
766.8/766.7 (0)	737 (0)[f]	FeF_3 str., e
658.8 (−1.1)	689 (−2)[f]	FeF_3 str., a_1
$N^{102}RuF_3$ (C_s, $^1A'$)[g]		
1105.4 (−32.7)	1085 (−32)	NRu str., a′
_[h]	682 (0)	F′-Ru str., a′
668.5 (0)	678 (0)	antisym. F–Ru-F str., a″
635.8 (0)	649 (0)	sym. F–Ru-F str., a′
$N^{102}RuF_4$ (C_{4v}, $^2B_1$)[g]		
1098.5 (−32.5)	1080 (−32)	NRu str., a_1
700.1 (0)	711 (0)	RuF_4 stretch, e
_[h]	681 (0)	RuF_4 stretch, a_1
_[j]	598 (0)	RuF_4 stretch, b_2
$NOsF_3$ (C_s, $^1A'$)		
1140.1 (−35.5)	1152 (−36)	NOs str., a′
686.0/686.6 (0)	689 (0)	OsF_2 sym. str., a′
641.3/640.0 (0)	664 (0)	OsF′ sym. str., a′
632.3 (0)	652 (0)	OsF_2 antisym. str., a″
$NOsF_3$ (Cs, $^3A''$)		
1086.0 (—) [i]	1095 (−36) [i]	^{15}NOs str, a′
675.8/677.0	675 (0)	OsF_2 antisym. str., a″
660.5/658.9 (0)	668 (0)	OsF_2 sym. str., a′
607.4 (0.0)	614 (0)	OsF′ sym. str., a′
$NOsF_4$ (C_{4v}, $^2B_1$)		
_[k]	1145 (−36)	NOs str., a_1
_[k]	706 (0)	OsF_4 stretch, a_1
689.9 (0)	693 (0)	OsF_4 stretch, e
_[j]	635 (0)	OsF_4 stretch, b_2

[a] Neon matrix; matrix sites are separated by a slash. [b] Intensities from DFT calculations available in Table S4. [c] M06-L/def2-QZVP: 785 a_1 (−11) [12], 703 e (0) [200], 617 a_1 (−1) [40]. [d] $^{14/15}$N isotopic ratio: 1.0256. [e] $^{14/15}$N isotopic ratio: 1.0257. [f] NEVPT2/aug-cc-pwCVTZ-DK. [g] For the experimentally observed Ru isotope splitting see Tables S5–S7 and Figures S4 and S5). [h] Band is likely hidden by the stronger antisymmetric F–Ru-F stretching mode (a″). [i] ν(^{15}N–Os) in cm^{-1}, see text. [j] Not IR active. [k] Too weak or overlapped.

For $NRuF_4$ only the strongest RuF_4 stretching band, the degenerate *e*-type mode could safely be assigned to the band labeled **B'** in Figure 3 centered at 700.0 cm^{-1}.

In the spectra obtained from the reaction of osmium atoms with isotopic labeled $^{15}NF_3$ two Os≡N stretching bands appeared at 1104.6 and 1086 cm^{-1}, which are labeled **A** and **A'**, respectively, in Figure 4, and which are finally assigned to different "spin-isomers" of $NOsF_3$ in near-degenerate singlet $^1A'$ and triplet $^3A''$ electronic states (Table 1). In the $^{14}NF_3$ experiment **A** is observed at 1140 cm^{-1} (Figure 4), while **A'** is overlapped by a stronger band due to the ^{14}NF radical at 1120.8 cm^{-1}.[30b] All three Os–F stretching bands of singlet $NOsF_3$ ($^1A'$) are assigned (Table 1) and labeled **B** ($\nu_s(OsF_2)$: 686.0 cm^{-1}), **C** (ν(OsF′): 641.3 cm^{-1}), and **D** ($\nu_{as}(OsF_2)$: 632.3 cm^{-1}) in Figure 4, respectively. Bands labeled **B'**, **C'** and **D'** at 675.8 cm^{-1}, 660.5 cm^{-1} and 607.4 cm^{-1}, respectively, are assigned to the three Os–F stretching modes of triplet $NOsF_3$ ($^3A''$, Table 1). Finally, a band at 689.6 cm^{-1} in Figure 4 is tentatively assigned to the strongest vibrational mode of $NOsF_4$ (C_{4v}, Table 1). The tetrafluorides N≡MF_4 (M = Ru, Os) are likely formed by the exothermic addition of a fluorine atom to N≡MF_3 (Table S2).

Pseudo-Jahn–Teller distortion of molecular group 8 nitrido fluorides $NM^{VI}F_3$

The group 8 nitrido fluorides $NM^{VI}F_3$ adopt metal d^2 configurations, for which Hund's rule predicts a high-spin $^3A_2$ ground state in an undistorted C_{3v} symmetry and two parallel spin electrons in the twofold degenerate $e(d_{xy,x^2-y^2})$-orbital ($|e_\varepsilon\uparrow;e_0\uparrow\rangle$), labeled 9e for $NFeF_3$ in the Supporting Information Figure S6. Three e^2 terms (four states) can be formed, $^3A_2$ ($|e_\varepsilon\uparrow;e_0\uparrow\rangle$), $^1A_1$ ($\sqrt{1/2}$ [$|e_\varepsilon\uparrow;e_\varepsilon\downarrow\rangle + |e_0\uparrow;e_0\downarrow\rangle$]), $^1E_0$ ($\sqrt{1/2}$ [$|e_\varepsilon\uparrow;e_\varepsilon\downarrow\rangle - |e_0\uparrow;e_0\downarrow\rangle$]) and $^1E_\varepsilon$ ($\sqrt{1/2}$ [$|e_0\uparrow;e_\varepsilon\downarrow\rangle + |e_0\downarrow;e_\varepsilon\uparrow\rangle$]). Due to the nondegenerate nature and totally symmetric charge distribution of the $^3A_2$ state no Jahn–Teller distortion is expected.[31] Other distributions of the electrons, as outlined above, result in configurations with lower spin and the absence of low-lying triplet excited states rule out obvious ground state pseudo-Jahn–Teller distortions.

Nevertheless, as shown in Figure 5 and in agreement with experimental vibrational assignments, all four NMF_3 species possess surprisingly different structures and the C_{3v} symmetric ground state was only verified for $NFeF_3$. In case of $NRuF_3$, extensive CCSD(T)/CBS calculations (Table S10) find the high symmetric $^3A_2$ is just about 5 kJ mol^{-1} higher than the distorted $^1A'$ ground state. According to our experimental data, $NOsF_3$ features two quasi-degenerate, distorted structures in $^1A'$ and $^3A''$ electronic states, separated by only $\Delta E_{T-S} = -1.3$ kJ mol^{-1} (CCSD(T)/CBS, Table S11).

To elucidate these findings, adiabatic potential energy surface (APES) scans were carried out using state-averaged complete active space self-consistent field calculations by distributing eight electrons in the eight molecular orbits formed by the metal (n-1)*d* and N(2*p*) orbitals (SA-CASSCF(8,8)) with subsequent NEVPT2 treatment to recover dynamic correlation. Shown in Figure 6a–c are cross sections along a distortion coordinate (*D*) that connects the two stationary points of the

 © 2021 The Authors. Chemistry - A European Journal published by Wiley-VCH GmbH

Chemistry–A European Journal | Full Paper doi.org/10.1002/chem.202101404 | Chemistry Europe European Chemical Societies Publishing

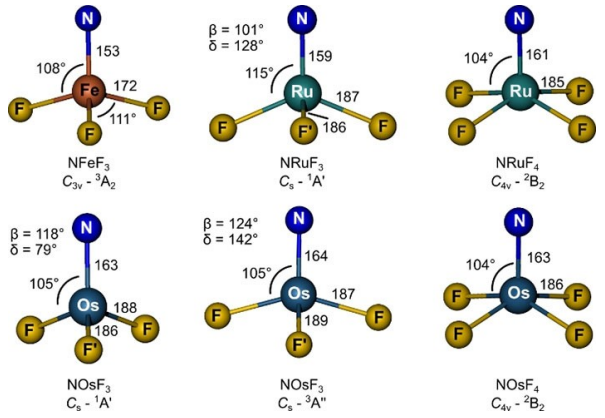

Figure 5. Ground-state structures of NMF_3 and NMF_4 calculated at the CCSD (T)/aVTZ (M = Ru, Os, M: aVTZ-PP) and the NEVPT2/aVTZ-DK ($NFeF_3$, Fe: awCVTZ-DK) levels of theory. Bond lengths are given in pm and angles in degrees. β denotes the N–M–F′ and δ the F–M–F angle for structures with C_s symmetry.

^{1}A′ surface, at $D=-1$ and 1, respectively, via the high-symmetry C_{3v} stationary point at $D=0$.

The distortions take place along one component of the lowest ($NFeF_3$, $NRuF_3$) or imaginary ($NOsF_3$) degenerate *e* normal mode in the high-symmetry C_{3v} configuration. Therefore, mainly bond angle distortions are involved, in particular the dihedral angle F′–M–N–F (α, Figure S9), and the valence angles N–M–F′ (β, Figure 5), and N–M–F (γ). The sign of the distortion *D* in Figure 6 indicates a widening (positive) or closing (negative) of α. Differences in these angles and in the three nonequivalent bond distances between two localized stationary points in C_S symmetry were divided into equal incremental steps and used as intermediate internal coordinates in the APES calculation for each step (Tables S14–S17). In the case of Figure 6d the distortion in the positive direction was carried out using the $NOsF_3$ ^{3}A″ minimum structure at $D=1$. The graphs shown in Figure 6a–d represent the energies of the terms arising from the electronic e^2 configuration, as outlined above. They demonstrate the propensity of trigonal group 8 nitrido complexes in the oxidation state VI to be subject to a PJT distortion. Other trigonal systems displaying a $(A+E)\otimes e$ Pseudo-Jahn–Teller effect (PJTE) that is "hidden" in excited states (h-PJTE) have already been described.[27a,31] The condition for a distorted ground state minimum structure caused by the h-PTJE is that the PJT stabilization energy of an excited state (E_{PJT}) is larger than the energy gap Δ_0 between the ground state in the high-symmetry configuration and the PJT active excited state ($E_{PJT} > \Delta_0$, see Figure 6, a–c).[27a] The global minimum of the APES of $NFeF_3$ shown in Figure 6a is located at the high-symmetry point. The stationary points on the ^{1}A′ (blue line) surface are a local minimum ($D=1$) and a first-order saddle point ($D=-1$) without surface crossings in between. Consistent with the experimental vibrational data the global minimum is the high symmetry configuration. The h-PJTE in the ^{1}E state is not strong enough to distort the high-

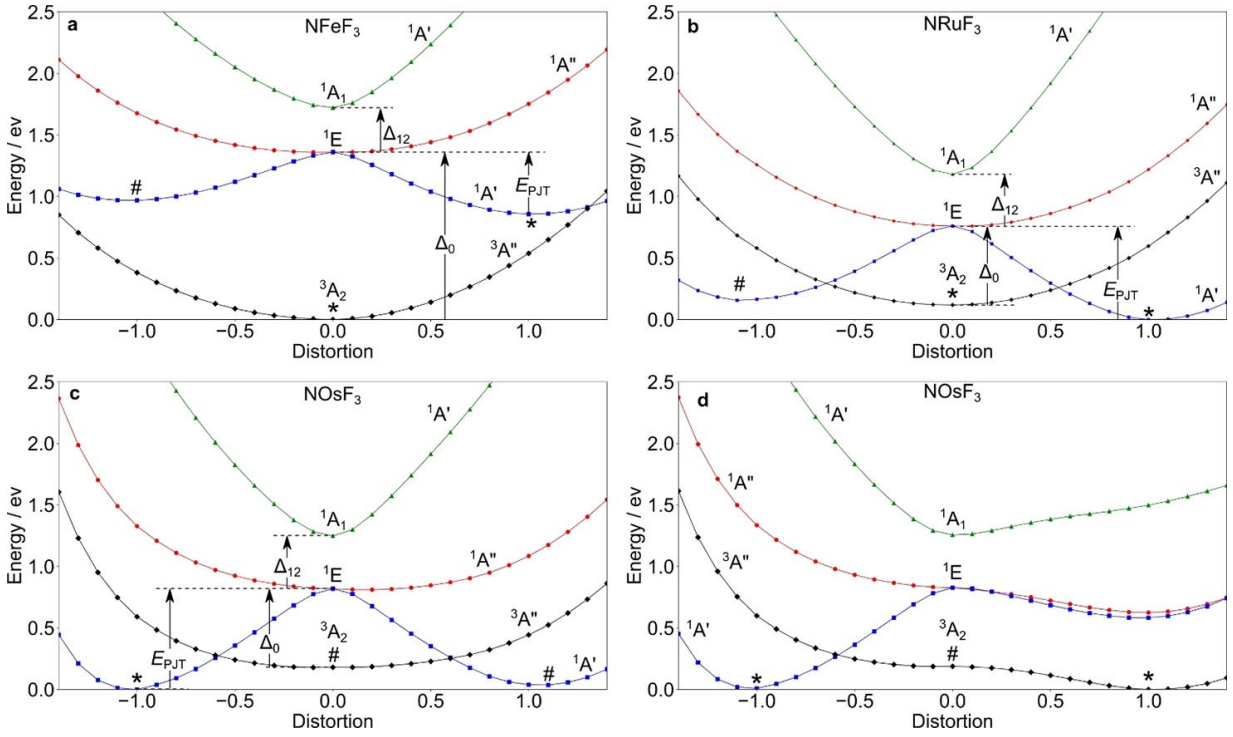

Figure 6. Cross section of the APES for the terms arising from the electronic e^2 configurations of a) $NFeF_3$, b) $NRuF_3$, c), d) $NOsF_3$ along the distortion coordinate (*D*) connecting stationary points located at $D=1$, 0 and −1, respectively, on the ^{1}A′ (blue line) and the $^3A_2$ (^{3}A″, black line) surfaces. Minimum points are marked with an asterisk, and first-order saddle points with a hash mark. The PJT stabilization energy (E_{PJT}) of the lowest excited state, its excitation energy at C_{3v} symmetry (Δ_0), and the ^{1}E–$^1A_1$ energy gap (Δ_{12}) are indicated in (a)–(c).

 © 2021 The Authors. Chemistry - A European Journal published by Wiley-VCH GmbH

Chemistry–A European Journal | Full Paper doi.org/10.1002/chem.202101404 | Chemistry Europe European Chemical Societies Publishing

symmetry configuration. The PJT stabilization energy, E_{PJT}, is about 0.39 eV and smaller than the ^1E-$^3A_2$ energy gap $\Delta_0 = 1.36$ eV. The $^1A'$ minima, which features a $(|e_\theta\uparrow;e_\theta\downarrow\rangle)$ electronic configuration, and the $^3A_2$ minima are separated by about 0.86 eV. The angular distortion from $D=-1$ to $D=1$ at the $^1A'$ surface extends from about 101 –132 (α), 100 –120 (β), and 112 –104 (γ).

The cross section of the APES of $NRuF_3$ along the distortion coordinate from $D=0$ to $D=1$ illustrated in Figure 6**b** shows that one of the components of the ^1E term is stabilized by the strong PJT coupling with the excited $^1A_1$ state. It crosses the $^3A_2$ ground state of the undistorted high-symmetry configuration to produce the global minimum with a distorted structure. The triplet-singlet spin crossover is associated with an orbital disproportionation,[27a] because in the distorted structure the electrons are paired in one e_θ orbital $(|e_\theta\uparrow;e_\theta\downarrow\rangle)$ instead of the symmetric distribution $(|e_\varepsilon\uparrow;e_\theta\uparrow\rangle)$ in the undistorted configuration. Accordingly, we find that $E_{PJT}=0.76$ eV is larger than $\Delta_0=0.64$ eV. The high-spin $^3A''$ state is higher in energy by only ~0.12 eV and it has an energy barrier of ~0.25 eV to the point of spin crossover with the low-spin $^1A'$ state.

Figures 6c and d exhibit four relevant low-lying stationary points on the $^1A'$ and $^3A''$ APES of $NOsF_3$. The h-PJTE in this case produces a minimum with a distorted $^1A'$ structure at $D=-1$ and accordingly, the orbital disproportionation and spin crossover leads to a $(|e_\varepsilon\uparrow;e_\varepsilon\downarrow\rangle)$ configuration with $E_{PJT}=0.82$ eV and $\Delta_0=0.60$ eV. Unlike the former two cases, the $^3A_2$ high-symmetry configuration of $NOsF_3$ does not represent a minimum point, but a first order saddle point. Following the ε component of the imaginary *e* mode in Figure 6d we find – in accordance with the CCSD(T)/CBS results – an energetically quasi-degenerate distorted $^3A''$ minimum that shows orbital disproportionation, but no spin crossover about 0.1 eV (or 0.7 kJ mol^{-1}) lower than the $^1A'$ state. The energy barrier of the spin crossover point is ~0.27 eV (CCSD(T)/VTZ-PP: 0.24 eV, Table S12), a significant barrier connecting both stationary points at the experimental cryogenic conditions. These findings support the observation of two different species in the experimental infrared spectra which correspond to species in different $^1A'$ and $^3A''$ electronic states. We did not analyze the source of the distortion of the high-spin minimum ($^3A''$). But, under the premise that PJTE is the only source for symmetry breaking of non-degenerate high-symmetry states,[27b,31] the source is most likely an interacting triplet ^3E excited state.

Discussion

All metal specific bands showing a $^{14/15}N$ isotopic shift were successfully assigned. Bands due to binary fluorides are always present in experiments using IR laser ablation of metals in the presence of molecular fluorides as precursors. They are likely formed by recombination of metal atoms and atomic fluorine radicals formed by thermal or photolytic decomposition of the fluoride precursor in the hot plasma plume region or by the decomposition of metal fluoride product molecules. However, the very strong NF_3 precursor bands and comparatively weak NF and NF_2 bands in all spectra suggest that the formation of the NMF_3 title product can be attributed to the reaction of M and NF_3. Lower nitrido fluorides NMF or NMF_2 could in principle also be formed through the cleavage of a metal-fluorine bond or by the reaction of metal atoms with NF or NF_2, but have so far not been identified.[25,26,30c,33] The addition of fluorine to NMF and NMF_2 to yield NMF_3 and also the formation of NMF_4 for M = Ru and Os are calculated to be exothermic (Table S2).

As shown here, all the trigonal NMF_3 species possess two equilibrium configurations with different spin multiplicities, while those of $NRuF_3$ and $NOsF_3$ are close in energy. Such a magnetic and structural PJT induced bistability may also be possible for ligand-stabilized trigonal nitrido d^2 metal complexes. Such compounds are of interest for molecular switching, especially when symmetry breaking is involved (as for $NFeF_3$ and $NRuF_3$).[34]

The different stationary structures that were obtained for the group 8 NMF_3 molecules shown in Figure 5 possess surprisingly different electronic configurations, as outlined above and summarized in Figure 7 (for molecular orbital plots, see Figures S6 and S8). The different $^1A'$ electronic ground states of $NRuF_3$ and $NOsF_3$ arise from the pairing of two unpaired electrons in different orbitals, which are associated with two different structural distortions. The HOMO of $NRuF_3$ ($^1A'$) is of a" symmetry, which is consistent with a widening of the F–M–F angle, whereas the HOMO of $NOsF_3$ ($^1A'$) is of a' symmetry, which shows a reduction in the F–M–F angle bisected by the σ plane in C_s symmetry (Figure 5). The d^1 metal configuration for the heptavalent tetrafluorides $NRu^{VII}F_4$ and $NOs^{VII}F_4$ (C_{4v}) give rise to a $^2B_2$ electronic ground state (see Figure S7 for the singly occupied MO).

The effective bond orders[35] (EBOs) for $NOsF_3$, $NRuF_3$ and $NFeF_3$ are 2.8, 2.7 and 2.2, respectively, which in fact corresponds to triple bonds for all these M–N bonds. The computed M–N bond lengths for the novel nitrido compounds (153 pm (FeN), 159 pm (RuN), 163–164 pm (OsN), Figure 7) are close to our published triple bond additive covalent radii: 156 pm (FeN), 157 pm (RuN) and 163 pm (OsN),[36] and also the experimental N–M stretching frequencies (Table 1) support the presence of strong M≡N triple bonds in the novel hexavalent nitrido complexes $NM^{VI}F_3$. We note that the experimental ν(Fe≡N) frequency of $NFe^{VI}F_3$ of 946 cm^{-1} (Table 1) is not well reproduced by calculations at DFT or CCSD(T) levels (Table S3) and is also

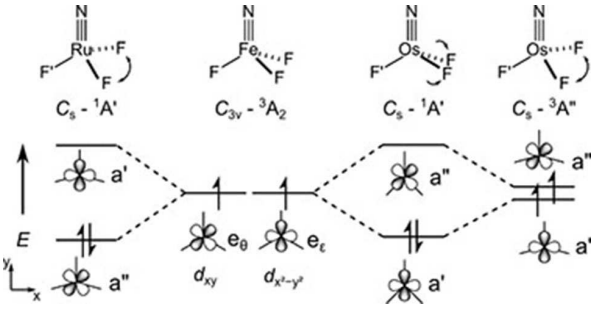

Figure 7. Comparison of the different d^2 electron configurations of the NMF_3 species (M = Fe, Ru, Os). The metal centered a' and a"-MOs are dominantly M($d_{x^2-y^2}$) and M(d_{xy}) atomic orbitals, respectively.

 © 2021 The Authors. Chemistry - A European Journal published by Wiley-VCH GmbH

Chemistry–A European Journal | Full Paper doi.org/10.1002/chem.202101404 | Chemistry Europe European Chemical Societies Publishing

overestimated by the more sophisticated NEVPT2 multi-reference approach (ν(Fe≡N) = 1027 cm^{-1}, Table S3). On the other hand, its comparison with experimental Fe≡N stretching frequencies for pseudo-tetrahedral $N^{IV}FeL_3$ complexes, previously reported at 1008 ([Fe^{IV}(N)(TIMEN^{Mes})]$^+$),[24c] 1028 ([Fe^{IV}(N)(PhB(^{t}Bulm)$_3$)],[24b] and 1034 cm^{-1} ([Fe^{IV}(N)-(PhB($CH_2P^iPr_2$)$_3$)];[9] Table S1) suggests that an increase in the iron oxidation state beyond V does not necessarily lead to a stronger Fe≡N bond.

Table 2 shows experimental M–N stretching frequencies of molecular NMF_3 species formed by the reaction of NF_3 with laser-ablated transition metals. For the d^0 configurations of all group 4 and group 6 nitrido trifluorides the ideal pseudo-tetrahedral C_{3v} symmetric arrangement was experimentally verified, since there are no electrons in the nonbonding $e(d_{xy,x^2-y^2})$ orbitals that could cause distortions.[25,33] The e^3 configuration of $NRhF_3$ and $NIrF_3$ leads to Jahn–Teller distorted spin doublet ground states in C_s symmetry.[26] So far, no experimental data are available for the group 10 derivatives, and for the group 11 analogues only the initial metal insertion products F_2N–$M^{II}F$ were detected after matrix deposition (irradiation of F_2NCuF led to rearrangement to metastable FN≡CuF_2).[30c]

The M–N stretching normal mode of the terminally bond nitrogen ligands of the nitrido trifluorides can regarded to be a good approximation as an almost pure and uncoupled metal-nitrogen stretching mode that can be used as a measure of the M–N bond strength. The $NM^{IV}F_3$ derivatives of the group 4 metals possess a singly bonded triplet nitrene ($^3N^-$) ligand, since the ligand cannot oxidize the d^0 metal center any further. The two unpaired electrons in the N(2p) orbitals are reported to be involved in weak degenerate π bonding interactions for M = Ti ≫ Zr, Hf.[33] In contrast, the group 6, 8 and 9 $NM^{VI}F_3$ molecules show a N≡M triple bond with one σ and two π bonds to the terminal nitrido (N^{3-}) ligand. The strength and overlap of these bonds increases going down the groups likely due to an improved M(πd)–N(πp) orbital overlap as a result of an increasing relativistic expansion[37] of the 4d and 5d orbitals and the absence of metal core/ligand repulsion proposed in first-row transition metal compounds.[38] The general trend of increasing N–M bond strength moving along the rows culminates in the highest observed M–N stretching frequency for $NIrF_3$. Unexpectedly, this trend does not apply to $NFeF_3$ which shows a lower M–N stretching frequency than the group 6 homologue (M = Cr). The lower stability of high-valent first row late transition metals is well known.[1a,39] In the series of 3d $NM^{VI}F_3$ compounds, for M = Fe it seems we have reached the limit of stability. $NCo^{VI}F_3$ is not a stable compound and only $FNCoF_2$ has been observed experimentally.[26] For the 4*d* element Rh it was found that the rearrangement of the fluoro nitrene complex $FNRhF_2$ into N≡$Rh^{VI}F_3$ is only slightly exothermic ($\Delta H^0 = -12$ kJ mol^{-1}, CCSD(T)), which enables the observation of both rearrangement products.[26]

Within the atoms in molecules (AIM) scheme[40] the partial negative charge at the nitrido ligand in $NM^{VI}F_3$ increases from M = Fe to Os (Tables S9 and S13), which indicates a decreasing electron withdrawing effect of the $M^{VI}F_3$ fragment within this group. For M = Fe and Ru the negative charge at the nitrogen atom also decreases from NMF_2 (M = Fe: −0.35, Ru: −0.40) to NMF_3 (M = Fe: −0.25, Ru: −0.35), while for M = Os it remains unchanged ($NOsF_2$: −0.50, $NOsF_3$: −0.49). As expected, fluorination of NMF_3 further decreases the atomic charge of the nitrido ligand in NMF_4 (M = Ru: −0.25, Os: −0.40, Table S9). The high oxidation potential of Fe^{VI} in $NFeF_3$ leads to relatively high σ* and π* occupation numbers (0.2 and 0.3 electrons, respectively; Figure S6). These indicates a weakened covalent N–Fe bond, for which the formal N^{3-} nitride notations seems to be a very poor approximation. The occupation of formally antibonding MOs also indicates an oxidation, and thus the onset of a redox non-innocent behavior of the nitrido ligand.

Conclusion

The nitrido complexes $NFeF_3$, $NRuF_3$, $NRuF_4$, $NOsF_3$ (^{1}A′), $NOsF_3$ (^{3}A″), and $NOsF_4$ were shown to be formed by the reaction of free group 8 metal atoms with NF_3 and established by their characteristic IR spectra recorded in solid neon matrices. Their assignment is supported by observed $^{14/15}$N isotope shifts and quantum-chemical predictions. All stretching fundamentals of the $NM^{VI}F_3$ complexes were confidently assigned. For the C_{4v} symmetric $NRuF_4$ two distinct bands were confidently assigned, whereas for $NOsF_4$ only the strongest band was tentatively assigned. Based on the joint experimental IR and quantum-chemical analysis the half-filled e^2 configuration of $NFeF_3$ can be assigned to an undistorted C_{3v} structure in a non-degenerate $^3A_2$ electronic ground state. $NFeF_3$ features an unprecedented low Fe≡N triple-bond frequency of 946.7 (^{14}N≡Fe) and 922.7 cm^{-1} (^{15}N≡Fe). The heavier group 8 NMF_3 homologues are subject to symmetry lowering and spin-crossover caused by a pseudo Jahn–Teller effect "hidden" in the excited states. While the electronic ground state of $NRuF_3$ is a structurally distorted singlet ^{1}A′ state (C_S symmetry), for molecular $NOsF_3$ two coexisting distorted C_S structures with high-spin and low-spin d^2 configurations (magnetic bistability) were detected at 5 K in solid neon. To the best of our knowledge, apart from $O_2Fe(\eta^2\text{-}O_2)$,[3–5] no other neutral Fe^{VI} complexes or molecular neutral complexes of Ru^{VII} have yet been reported, and after $OsOF_5$,[1f] $NOsF_4$ is the second known monomeric Os^{VII} compound.

Table 2. Experimental M–N stretching frequencies [cm^{-1}] of NMF_3 molecules formed by the reaction of NF_3 with transition metals of group 4, 6, 8, 9, and 11.

Row	Group 4[a]	Group 6[b]	Group 8[c]	Group 9[d]	Group 11[30c]
3*d*	596.7 (Ti, C_{3v}, $^3A_1$)	1015 (Cr, C_{3v}, $^1A_1$)	946.4 (Fe, C_{3v}, $^3A_2$)	FN≡CoF_2 only	F_2N-CuF, FN≡CuF_2
4*d*	553.1 (Zr, C_{3v}, $^3A_1$)	1075 (Mo, C_{3v}, $^1A_1$)	1098.5 (Ru, C_s, ^{1}A′)	1116.1 (Rh, C_s, ^{2}A′) [Ne] 1112.5 [Rh, Ar] [e]	F_2N–AgF only
5*d*	548.1 (Hf, C_{3v}, $^3A_1$)	1091 (W, C_{3v}, $^1A_1$)	1140.1 (Os, C_s, ^{1}A′) *1086.0 (Os, C_s, ^{3}A″)*	1150.4 (Ir, C_s, ^{2}A′) [Ne] 1144.6 [Ir, Ar]	F_2N–AuF only

[a] Ar matrix.[33] [b] Ar matrix.[25] [c] Ne matrix (this work). [d] Ne and Ar matrices.[26] [e] Formation of N≡RhF_3 along with FN≡RhF_2.

© 2021 The Authors. Chemistry - A European Journal published by Wiley-VCH GmbH

Chemistry–A European Journal | Full Paper doi.org/10.1002/chem.202101404 | Chemistry Europe European Chemical Societies Publishing

Acknowledgements

We gratefully acknowledge the Zentraleinrichtung für Datenverarbeitung (ZEDAT) of the Freie Universität Berlin for the allocation of computing resources.[41] We thank the ERC Project HighPotOx as well as the CRC 1349 (SFB 1349) Fluorine Specific Interactions – Project-ID 387284271 – for continuous support. Open access funding enabled and organized by Projekt DEAL.

Conflict of Interest

The authors declare no conflict of interest.

Keywords: ab initio calculations · high oxidation states · matrix isolation · N ligands · transition metals

[1] a) S. Riedel, M. Kaupp, *Coord. Chem. Rev.* **2009**, *253*, 606–624; b) O. Ruff, E. Vidic, *Z. Anorg. Allg. Chem.* **1924**, *136*, 49–61; c) W. J. Casteel Jr, D. A. Dixon, H. P. A. Mercier, G. J. Schrobilgen, *Inorg. Chem.* **1996**, *35*, 4310–4322; d) A. O. Chong, K. Oshima, K. B. Sharpless, *J. Am. Chem. Soc.* **1977**, *99*, 3420–3426; e) K. Muniz, *Chem. Soc. Rev.* **2004**, *33*, 166–174; f) H. Shorafa, K. Seppelt, *Inorg. Chem.* **2006**, *45*, 7929–7934.

[2] H. Schmidbaur, *Z. Anorg. Allg. Chem.* **2018**, *644*, 536–559.

[3] Y. Gong, M. Zhou, L. Andrews, *J. Phys. Chem. A* **2007**, *111*, 12001–12006.

[4] W. Huang, D.-H. Xing, J.-B. Lu, B. Long, Schwarz, W. H. Eugen, J. Li, *J. Chem. Theory Comput.* **2016**, *12*, 1525–1533.

[5] J.-B. Lu, J. Jian, W. Huang, H. Lin, J. Li, M. Zhou, *Phys. Chem. Chem. Phys.* **2016**, *18*, 31125–31131.

[6] a) J. Hohenberger, K. Ray, K. Meyer, *Nat. Commun.* **2012**, *3*, 720; b) J. M. Smith, D. Subedi, *Dalton Trans.* **2012**, *41*, 1423–1429; c) B. Mondal, L. Roy, F. Neese, S. Ye, *Isr. J. Chem.* **2016**, *56*, 763–772.

[7] W. D. Wagner, K. Nakamoto, *J. Am. Chem. Soc.* **1988**, *110*, 4044–4045.

[8] J. F. Berry, E. Bill, E. Bothe, S. D. George, B. Mienert, F. Neese, K. Wieghardt, *Science* **2006**, *312*, 1937–1941.

[9] T. A. Betley, J. C. Peters, *J. Am. Chem. Soc.* **2004**, *126*, 6252–6254.

[10] J. L. Martinez, S. A. Lutz, H. Yang, J. Xie, J. Telser, B. M. Hoffman, V. Carta, M. Pink, Y. Losovyj, J. M. Smith, *Science* **2020**, *370*, 356–359.

[11] E. W. Svastits, J. H. Dawson, R. Breslow, S. H. Gellman, *J. Am. Chem. Soc.* **1985**, *107*, 6427–6428.

[12] a) T. Kandemir, M. E. Schuster, A. Senyshyn, M. Behrens, R. Schlögl, *Angew. Chem. Int. Ed.* **2013**, *52*, 12723–12726; *Angew. Chem.* **2013**, *125*, 12955–12959; b) G. Ertl, *Chem. Rec.* **2001**, *1*, 33–45.

[13] a) B. Askevold, J. T. Nieto, S. Tussupbayev, M. Diefenbach, E. Herdtweck, M. C. Holthausen, S. Schneider, *Nat. Chem.* **2011**, *3*, 532–537; b) B. M. Lindley, Q. J. Bruch, P. S. White, F. Hasanayn, A. J. M Miller, *J. Am. Chem. Soc.* **2017**, *139*, 5305–5308.

[14] a) W.-X. Ni, W.-L. Man, M. T.-W. Cheung, R. W.-Y. Sun, Y.-L. Shu, Y.-W. Lam, C.-M. Che, T.-C. Lau, *Chem. Commun.* **2011**, *47*, 2140–2142; b) W.-X. Ni, W.-L. Man, S.-M. Yiu, M. Ho, M. T.-W. Cheung, C.-C. Ko, C.-M. Che, Y.-W. Lam, T.-C. Lau, *Chem. Sci.* **2012**, *3*, 1582.

[15] K. Suntharalingam, T. C. Johnstone, P. M. Bruno, W. Lin, M. T. Hemann, S. J. Lippard, *J. Am. Chem. Soc.* **2013**, *135*, 14060–14063.

[16] K. Suntharalingam, W. Lin, T. C. Johnstone, P. M. Bruno, Y.-R. Zheng, M. T. Hemann, S. J. Lippard, *J. Am. Chem. Soc.* **2014**, *136*, 14413–14416.

[17] W.-X. Ni, W.-L. Man, W.-Q. Huang, C.-X. Wang, T. Liu, Z.-X. Li, C. Pan, Y.-Z. Chen, X. Lian, *Dalton Trans.* **2020**, *49*, 17173–17182.

[18] a) H.-X. Wang, L. Wu, B. Zheng, L. Du, W.-P. To, C.-H. Ko, D. L. Phillips, C.-M. Che, *Angew. Chem. Int. Ed.* **2021**, *60*, 4796–4803; *Angew. Chem.* **2021**, *133*, 4846–4853; b) N. B. Thompson, M. T. Green, J. C. Peters, *J. Am. Chem. Soc.* **2017**, *139*, 15312–15315; c) P. Vöhringer, *Dalton Trans.* **2020**, *49*, 256–266.

[19] a) J. J. Scepaniak, C. S. Vogel, M. M. Khusniyarov, F. W. Heinemann, K. Meyer, J. M. Smith, *Science* **2011**, *331*, 1049–1052; b) M. Keilwerth, L. Grunwald, W. Mao, F. W. Heinemann, J. Sutter, E. Bill, K. Meyer, *J. Am. Chem. Soc.* **2021**, *143*, 1458–1465; c) G. E. Cutsail, B. W. Stein, D. Subedi, J. M. Smith, M. L. Kirk, B. M. Hoffman, *J. Am. Chem. Soc.* **2014**, *136*, 12323–12336; d) G. Sabenya, L. Lázaro, I. Gamba, V. Martin-Diaconescu, E. Andris, T. Weyhermüller, F. Neese, J. Roithova, E. Bill, J. Lloret-Fillol, M. Costas, *J. Am. Chem. Soc.* **2017**, *139*, 9168–9177; e) L. Bucinsky, M. Breza, W.-T. Lee, A. K. Hickey, D. A. Dickie, I. Nieto, J. A. DeGayner, T. D. Harris, K. Meyer, J. Krzystek, A. Ozarowski, J. Nehrkorn, A. Schnegg, K. Holldack, R. H. Herber, J. Telser, J. M. Smith, *Inorg. Chem.* **2017**, *56*, 4752–4769.

[20] The "oxo wall" concept for terminal tetragonal oxo complexes is associated with d-orbital occupations beyond 5 and the resulting population of all metal-oxo pi* antibonding orbitals. Here, we refer to the concept of non-innocent ligands, which is of general importance in transition-metal chemistry and is not restricted to tetragonal complexes or to the occupation of antibonding MOs, but to the more general concepts of covalency and ligand field inversion. See ref. [22] and: L. Li, H. Beckers, T. Stüker, T. Lindič, T. Schlöder, D. Andrae, S. Riedel, *Inorg. Chem. Front.* **2021**, *8*, 1215–1228.

[21] a) W. Kaim, *Eur. J. Inorg. Chem.* **2012**, *2012*, 343–348; b) R. Hoffmann, S. Alvarez, C. Mealli, A. Falceto, T. J. Cahill, T. Zeng, G. Manca, *Chem. Rev.* **2016**, *116*, 8173–8192.

[22] N. Aliaga-Alcalde, S. DeBeer George, B. Mienert, E. Bill, K. Wieghardt, F. Neese, *Angew. Chem. Int. Ed.* **2005**, *44*, 2908–2912; *Angew. Chem.* **2005**, *117*, 2968–2972.

[23] M. P. Hendrich, W. Gunderson, R. K. Behan, M. T. Green, M. P. Mehn, T. A. Betley, C. C. Lu, J. C. Peters, *Proc. Natl. Acad. Sci. USA* **2006**, *103*, 17107–17112.

[24] a) J.-U. Rohde, T. A. Betley, T. A. Jackson, C. T. Saouma, J. C. Peters, Q. Lawrence Jr, *Inorg. Chem.* **2007**, *46*, 5720–5726; b) J. J. Scepaniak, M. D. Fulton, R. P. Bontchev, E. N. Duesler, M. L. Kirk, J. M. Smith, *J. Am. Chem. Soc.* **2008**, *130*, 10515–10517; c) C. Vogel, F. W. Heinemann, J. Sutter, C. Anthon, K. Meyer, *Angew. Chem. Int. Ed.* **2008**, *47*, 2681–2684; *Angew. Chem.* **2008**, *120*, 2721–2724.

[25] X. Wang, L. Andrews, R. Lindh, V. Veryazov, B. O. Roos, *J. Phys. Chem. A* **2008**, *112*, 8030–8037.

[26] T. Stüker, T. Hohmann, H. Beckers, S. Riedel, *Angew. Chem. Int. Ed.* **2020**, *59*, 23174–23179; *Angew. Chem.* **2020**, *132*, 23374–23379.

[27] a) P. Garcia-Fernandez, I. B. Bersuker, J. E. Boggs, *J. Chem. Phys.* **2006**, *125*, 104102; b) I. B. Bersuker, *Chem. Rev.* **2021**, *121*, 1463–1512.

[28] M. Laing, *J. Chem. Educ.* **1989**, *66*, 453.

[29] T. Schlöder, T. Vent-Schmidt, S. Riedel, *Angew. Chem. Int. Ed.* **2012**, *51*, 12063–12067; *Angew. Chem.* **2012**, *124*, 12229–12233.

[30] a) M. E. Jacox, *J. Phys. Chem. Ref. Data* **1998**, *27*, 115–393; b) D. E. Milligan, M. E. Jacox, *J. Chem. Phys.* **1964**, *40*, 2461–2466; c) Y. Gong, L. Andrews, *Inorg. Chem.* **2012**, *51*, 667–673.

[31] I. B. Bersuker, *Chem. Rev.* **2013**, *113*, 1351–1390.

[32] a) A. D. Becke, *Phys. Rev. A* **1988**, *38*, 3098–3100; b) J. P. Perdew, *Phys. Rev. B* **1986**, *33*, 8822–8824; c) F. Weigend, F. Furche, R. Ahlrichs, *J. Chem. Phys.* **2003**, *119*, 12753–12762; d) F. Weigend, R. Ahlrichs, *Phys. Chem. Chem. Phys.* **2005**, *7*, 3297–3305; e) D. Andrae, U. Huermann, M. Dolg, H. Stoll, H. Preu, *Theor. Chim. Acta* **1990**, *77*, 123–141.

[33] X. Wang, J. T. Lyon, L. Andrews, *Inorg. Chem.* **2009**, *48*, 6297–6302.

[34] P. Garcia-Fernandez, I. B. Bersuker, *Phys. Rev. Lett.* **2011**, *106*, 246406.

[35] B. O. Roos, A. C. Borin, L. Gagliardi, *Angew. Chem. Int. Ed.* **2007**, *46*, 1469–1472; *Angew. Chem.* **2007**, *119*, 1491–1494.

[36] P. Pyykkö, S. Riedel, M. Patzschke, *Chem. Eur. J.* **2005**, *11*, 3511–3520.

[37] P. Pyykkö, *Chem. Rev.* **1988**, *88*, 563–594.

[38] M. Kaupp, *J. Comput. Chem.* **2007**, *28*, 320–325.

[39] S. X. Hu, W. L. Li, J. B. Lu, J. L. Bao, H. S. Yu, D. G. Truhlar, J. K. Gibson, J. Marçalo, M. Zhou, S. Riedel, Schwarz, W. H. Eugen, J. Li, *Angew. Chem. Int. Ed.* **2018**, *57*, 3242–3245; *Angew. Chem.* **2018**, *130*, 3297–3300.

[40] R. F. W. Bader, *Atoms in Molecules: A Quantum Theory*, Clarendon, Oxford, **1994**.

[41] L. Bennett, B. Melchers, B. Proppe, *Curta: A General-Purpose High-Performance Computer at ZEDAT, Freie Universität Berlin;* Freie Universität Berlin, **2020**.

Manuscript received: April 19, 2021
Accepted manuscript online: May 27, 2021
Version of record online: ■■, ■■■

 © 2021 The Authors. Chemistry - A European Journal published by Wiley-VCH GmbH

FULL PAPER

In different states: Molecular hexavalent group 8 nitrido fluorides feature different electronic ground-state d^2 configurations in solid Ne matrices. While $NFeF_3$ adopts a high symmetry structure, the heavier homologues are subject to symmetry lowering and spin-crossover caused by a pseudo Jahn–Teller effect "hidden" in the excited states. For $NOsF_3$ two coexisting high- and low-spin structures show triplet–singlet spin crossover and magnetic bistability. A weakened covalent N–Fe bond in $NFe^{VI}F_3$ indicates the non-innocent character of the nitrido ligand.

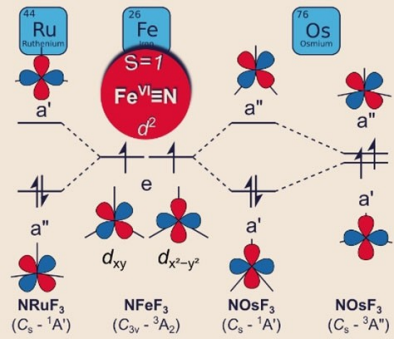

*T. Stüker, X. Xia, Dr. H. Beckers, Prof. S. Riedel**

1 – 9

High-Spin Iron(VI), Low-Spin Ruthenium(VI), and Magnetically Bistable Osmium(VI) in Molecular Group 8 Nitrido Trifluorides NMF_3

VIP

4.2. Fluoro Nitrenoid Complexes FN=MF_2 (M = Co, Rh, Ir): Electronic Structure Dichotomy and Formation of Nitrido Fluorides N≡MF_3

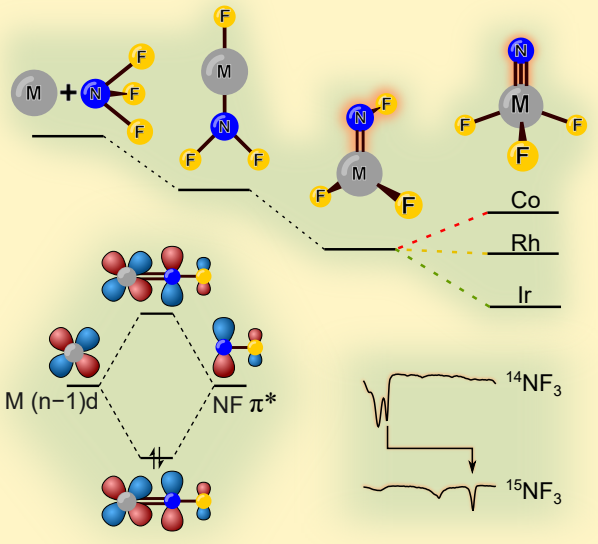

Tony Stüker, Thomas Hohmann, Helmut Beckers and Sebastian Riedel*
Angewandte Chemie International Edition **2020**, *59*, 23174–23179;
Angewandte Chemie **2020**, *132*, 23374–23379.
DOI: 10.1002/anie.202010950; 10.1002/ange.202010950
© *2020 The Authors. Published by Wiley-VCH GmbH*
For the Supporting Information see Appendix A.2.

Author Contribution

Tony Stüker did all calculations, wrote the manuscript and supervised the experiments and precursor synthesis. Tony Stüker and Thomas Hohmann carried out the experiments and the precursor synthesis. Helmut Beckers and Sebastian Riedel managed the project and revised the manuscript.

GDCh Research Articles Angewandte International Edition Chemie

Check for updates

How to cite: Angew. Chem. Int. Ed. 2020, 59, 23174–23179
International Edition: doi.org/10.1002/anie.202010950
German Edition: doi.org/10.1002/ange.202010950

Fluorine Chemistry

Fluoro Nitrenoid Complexes $FN{=}MF_2$ (M = Co, Rh, Ir): Electronic Structure Dichotomy and Formation of Nitrido Fluorides $N{\equiv}MF_3$

*Tony Stüker, Thomas Hohmann, Helmut Beckers, and Sebastian Riedel**

Abstract: *The fluoronitrenoid metal complexes $FNCoF_2$ and $FNRhF_2$ as well as the first ternary Rh^{VI} and Ir^{VI} complexes $NIrF_3$ and $NRhF_3$ are described. They were obtained by the reaction of excited Group-9 metal atoms with NF_3 and their IR spectra, isolated in solid rare gases (neon and argon), were recorded. Aided by the observed $^{14/15}N$ isotope shifts and quantum-chemical predictions, all four stretching fundamentals of the novel complexes were safely assigned. The F–N stretching frequencies of the fluoronitrenoid complexes $FNCoF_2$ (1056.8 cm^{-1}) and $FNRhF_2$ (872.6 cm^{-1}) are very different and their N–M bonds vary greatly. In $FNCoF_2$, the FN ligand is singly bonded to Co and bears considerable iminyl/nitrene radical character, while the N–Rh bond in $FNRhF_2$ is a strong double bond with comparatively strong σ- and π-bonds. The anticipated rearrangement of $FNCoF_2$ to the nitrido Co^{VI} complex is predicted to be endothermic and was not observed.*

Introduction

Fluoronitrenoid metal complexes are underexplored compounds as only two examples have been reported so far, $FNReF_5$ and $FNCuF_2$.[2] This is most likely due to the fact that they bear a reactive FN function and are not readily available. In general, late transition-metal-nitrogen multiple bonds have attracted particular interest after having been found to enable the conversion of ubiquitous C–H and C–C bonds into valuable C–N bonds as either catalysts or intermediates.[3,4–6] Detailed knowledge of the geometry and electronic structure of such compounds are vital to elucidate the nature and mechanism of these reactions.[4] While nitrido complexes usually feature a M≡N triple bond,[4,7] the imido ligand NR^{2-} exhibits a M=N double bond in complexes with a bent M=N–R linkage (Scheme 1).[4] However, it has been mentioned that the energy required to change the M=N–R angle from bent to linearity is often small, and indeed, transition metal imido complexes bearing sterically encumbered ligands to protect the reactive metal-nitrogen multiple bond often feature short M–N bond lengths and nearly linear angles about the M–N–R linkage (Scheme 1).[4,5]

In this bonding Scheme the anionic NR^{2-} imido ligand is expected to bear a nucleophilic character in its reactions. The polarities of both the σ and π bonds are important factors that govern the reactivity of imido complexes.[4,5] As one moves from early to late transition metals, the binding energy of the metal d-electrons increases, and an imido ligand becomes less nucleophilic. This applies in particular to late transition metals in higher oxidation states. In fact, the imido ligands in late 3d transition metal complexes are often so electrophilic that these complexes can be better described as metal-nitrene complexes (Scheme 1). Formally, an imido complex differs from a nitrene complex in the formal charge of the ligand and thus in the oxidation state of the metal (Scheme 1). An imido species suggests a dianionic imido ligand (NR^{2-}), whereas a neutral nitrene ligand is usually the result of a predominantly covalent nitrogen-metal bond. In the case of neutral, covalently bound ligands, no polarization of bonding electrons towards the ligand and no or only little charge transfer from the metal to the ligand is generally to be expected. Additionally, not long-ago a few examples were reported where an iminyl radical ($^2NR^{\bullet}$) is coordinated to a transition metal.[8] Metal-imido cores containing iminyl radical ligands are proposed as reactive intermediates in a number of metal

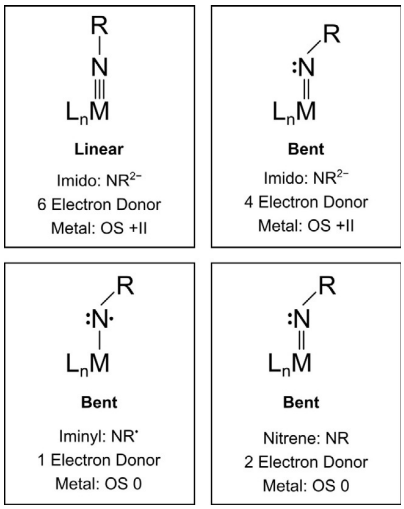

Scheme 1. Simplified scheme[1] for the interactions of a metal center and an anionic imido (formal NR^{2-}, top) and a neutral nitrene (bottom) ligand, respectively, in linear and bent nitrenoid complexes. The charge of the NR ligand in the ionic (NR^{2-}) and neutral (NR) approximation and the corresponding formal metal oxidation states are indicated below for uncharged donor ligands L.

[*] M. Sc. T. Stüker, M. Sc. T. Hohmann, Dr. H. Beckers, Prof. S. Riedel
Anorganische Chemie, Institut für Chemie und Biochemie, Freie Universität Berlin
14195 Berlin (Germany)
E-mail: s.riedel@fu-berlin.de
Supporting information and the ORCID identification number(s) for the author(s) of this article can be found under: https://doi.org/10.1002/anie.202010950.

© 2020 The Authors. Published by Wiley-VCH GmbH. This is an open access article under the terms of the Creative Commons Attribution License, which permits use, distribution and reproduction in any medium, provided the original work is properly cited.

catalyzed aziridination and amination reactions.[5] These and further possible interpretations of the electronic structures of terminal metal nitrenoid complexes (e.g., imido, $M(RN^{2-})$; iminyl, $M(^2RN^{\bullet})$; nitrene, M(RN); and triplet nitrene ($^3RN^{\bullet\bullet}$)[9] demonstrate the diversity of the metal-nitrogen bond in M–N–R complexes.

We became interested in fluoronitrenoid complexes of the group 9 metal difluorides, F–N=MF_2, M = Co, Rh, Ir. These simple nitrene complexes should allow a rigorous experimental and quantum-chemical comparison of the electronic properties of the Co^{IV} complex with those of its heavier congeners. Fluoronitrenoid-metal complexes show more complex nitrenoid-metal binding modes and new reactivities. The fluoronitrene ligand shares some similarities with the oxygen molecule, since the nitrogen 2p electrons involved in metal-nitrogen bonding are accommodated in a degenerate pair of π*(F–N) orbitals. Hence any metal-to-ligand charge transfer in a fluoronitrene complex will increase the occupancy of these π*(F–N) orbital, rendering the N–F stretching frequency a highly sensitive probe for the polarity and the strength of the N=M bond: a weak nitrogen-metal bond in a metal-nitrene complex result in a strong fluorine-nitrogen bond and vice versa. Utilizing the F–N functionality and relying upon a high metal-fluorine bond energy we have targeted the synthesis of high-valent nitridometal trifluorides N≡MF_3, starting from the fluoronitrene complexes by an oxidative F–N to M–F fluorine migration, by which the formal metal oxidation state will be increased by two units. As far as we know, molecular nitridometal trifluorides, NMF_3, are known only for the early transition metals of group IV (M = Ti, Zr, Hf[10]) and VI (Cr, Mo, W[11]). Notably, the formal metal oxidation state VI in N≡MF_3 (M = Co, Rh, Ir) is rare, with IrO_3, $Ir(\eta_2\text{-}O_2)O_2$, IrF_6, $Rh(\eta_2\text{-}O_2)O_2$ and RhF_6 as the only examples.[12] Terminal nitrido complexes of very high formal oxidation states have been predicted very recently,[13] however, such high-valent group 9 metals are still unknown. They would be of particular interest for cobalt, since the highest oxidation state reported for any molecular complex of cobalt is V, for example, the well-known $[Co(1\text{-norbornyl})_4]^+$ or in the tricoordinated cationic bis(nitrene) cobalt complex $[(IMes)Co(NDipp)_2]^+$.[6,14] The latter low-coordinated cationic complex is supported by the strongly electron-donating and sterically demanding *N*-heterocyclic carbene ligand IMes, and has been obtained by oxidation of the corresponding neutral bis(nitrene) Co^{IV} complex. Interestingly, theoretical calculations indicated that the frontier molecular orbitals of these bis(nitrene) complexes have near-equal contributions from both the cobalt center and the nitrene ligand orbitals, indicating that the spectroscopic oxidation states for these cobalt centers are likely to be lower than IV and V, respectively. Apart from these bis(nitrene) complexes, the majority of the known cobalt nitrenoid complexes have low spin Co^{III} centers which are supported, for example, by bulky ancillary tripodal or bidentate ligands to achieve kinetic stabilization.[15] To the contrary, terminal nitrido complexes of cobalt still remain elusive.[16]

Results and Discussion

To obtain the group 9 metal difluorides, F–N=MF_2 (M = Co, Rh, Ir), we have studied the gas-phase reaction of the laser-ablated free metal atoms with NF_3 seeded in a 1:1000 excess of neon or argon. The reaction products were deposited on a gold-plated copper mirror cooled to 5 and 12 K and IR-spectroscopically investigated (for experimental details see the Supporting Information). According to preliminary calculations at the DFT-B3LYP and BP86 levels of theory the direct insertion of the excited metal atoms into the F–N bond of NF_3 to F_2N–MF, and the subsequent fluorine migration from nitrogen to the metal center to yield the desired FN=MF_2 is highly exothermic for all three metals (Figure 1, Table S1). However, the expected rearrangement of the fluoronitrene to a high-valent nitrido trifluoride N≡MF_3 is found to be endothermic for the cobalt complex, rendering FN=CoF_2 the most stable CoF_3N isomer. To the contrary, this rearrangement is slightly exothermic for the rhodium nitrene complex ($\Delta H^0 = -12$ kJ mol^{-1}, CCSD(T)), and becomes strongly exothermic for the iridium congener ($\Delta H^0 = -98$ kJ mol^{-1}, CCSD(T), Table S1), which rendered the detection of the iridium nitrene complex difficult if not impossible.

These predictions were fully supported by the analysis of the experimental IR spectra of the deposits in solid neon shown for cobalt (Figure 2), rhodium (Figure 3) and iridium (Figure 4). Complementary argon spectra for the experiments using rhodium and iridium have also been recorded and shown in the supporting information, Figures S1–S3. These spectra are dominated by strong bands of the NF_3 precursor (Figure S4, Table S2 and Ref. [17]) and its plasma radiation induced decomposition products NF and NF_2.[18] However, the assignment of IR bands associated with the targeted nitrene and nitrido complexes is facilitated by a characteristic $^{14/15}N$ isotope shift exhibited by all modes in which the nitrogen atom is significantly involved. These isotope shifts are indicated in the experimental spectra shown in the Figures 2–4. They were obtained in experiments using $^{15}NF_3$, which was synthesized from $^{15}N_2$ and F_2 mixtures in an electric

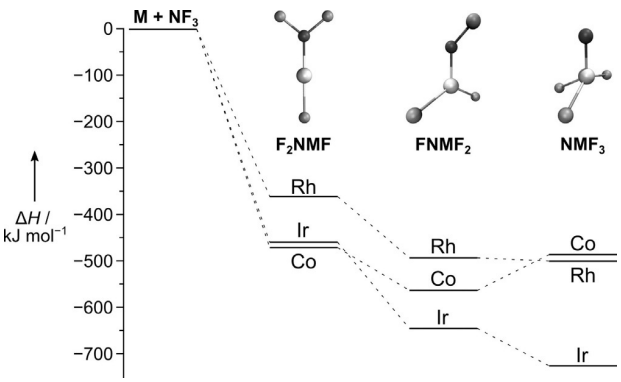

Figure 1. Stationary points on the reaction coordinate obtained at the B3LYP level of theory for the formation of the nitrido complexes N≡MF_3 (M = Co, Rh, and Ir) from the free metal atoms M and NF_3. See Table S1 for more details.

 © 2020 The Authors. Published by Wiley-VCH GmbH

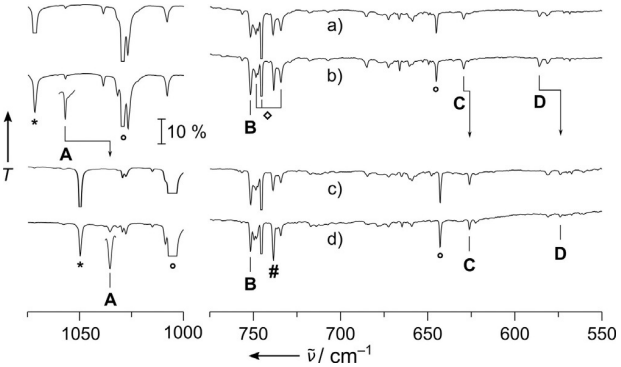

Figure 2. Infrared transmission spectra obtained after co-depositing laser-ablated cobalt atoms with 0.1 % $^{14}NF_3$ in neon (a), with $^{14}NF_3$ after annealing to 10 K (b) as well as with $^{15}NF_3$ (c), with subsequent annealing to 10 K (d). Bands attributed to $FNCoF_2$ are labeled **A**–**D**, and their $^{14/15}N$ isotope shift is indicated. The cutout band labeled **A** is enhanced by factor 5. Further assignments are NF_2 (asterisk), NF_3 (circle) and CoF_n (square). The pound sign marks an unassigned product band.

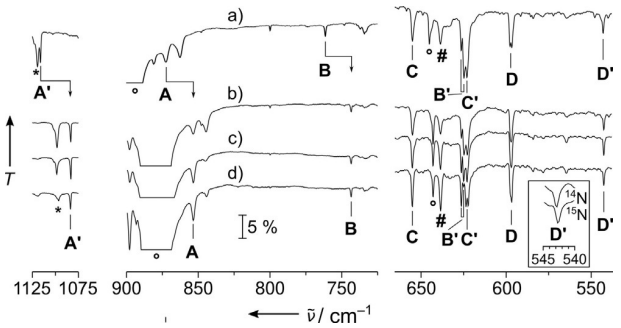

Figure 3. Infrared transmission spectra in the 1125–1075 cm^{-1} (left), 900–725 cm^{-1} (center) and 675–525 cm^{-1} (right) region from co-depositing laser-ablated rhodium atoms with 0.1 % $^{14}NF_3$ in neon (a), and co-depositing rhodium with $^{15}NF_3$ in neon (b) with subsequent full-arc photolysis (c) and annealing to 12 K (d). Bands attributed to $FNRhF_2$ are labeled **A**–**D** and those assigned to $NRhF_3$ are marked by **A′**–**D′**. Their $^{14/15}N$ isotope shift is indicated. The enhanced inset shows the small $^{14/15}N$ isotopic shift of **D′.** Further assignments are NF (asterisk) and NF_3 (circle). The pound sign marks an unassigned product band which is the only band that gains intensity upon annealing.

discharge.[19] While a detailed report about the spectral assignment is given in the Supporting Information, it should be mentioned here, that bands due to binary metal fluorides MF_n also appeared in these spectra, however these were safely assigned in nitrogen-free experiments, in which NF_3 was replaced by elemental fluorine. In these experiments none of the bands assigned to a nitrogen-containing species appeared. Furthermore, by comparing spectra of experiments using different group 9 metals, the desired metal dependent bands were identified. A list of all observed IR bands associated with the target compound is shown in Table 1 together with their approximate assignment and supporting predictions from quantum-chemical calculations.

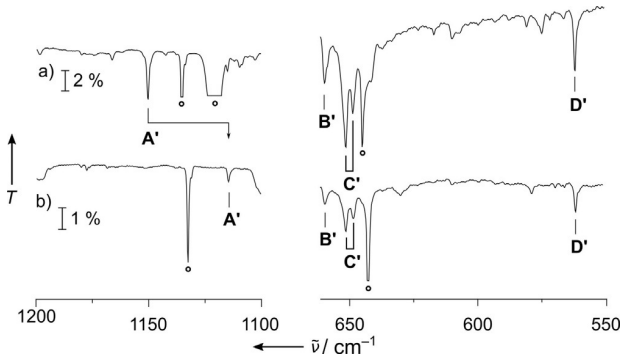

Figure 4. Infrared transmission spectra in the 1200–1100 cm^{-1} (left) and 630–550 cm^{-1} (right) region from co-deposition of laser-ablated iridium atoms with 0.1 % $^{14}NF_3$ (a) and 0.1 % $^{15}NF_3$ (b) in neon. Bands attributed to $NIrF_3$ are labeled **A′**–**D′**, and their $^{14/15}N$ isotope schift is indicated. Bands associated with NF_3 are marked by a circle.

In the experiment using laser-ablated Co atoms and NF_3 four IR bands were obtained that displayed a characteristic $^{14/15}N$ isotope shift (labeled **A**–**D** in Figure 2) and their assignment to the targeted fluoronitrene complex $FNCoF_2$ is well supported by prediction on the CASPT2/cc-pVTZ-DK level of theory (Table 1). The values obtained using single reference correlation methods did either not converge (CCSD(T)), or did not yield qualitatively consistent results (B3LYP and BP86). Bands associated to the desired nitrido complex $NCoF_3$ were not detected, which is consistent with the significant higher energy of this isomer. On the other side, in the spectra obtained from laser-ablated Ir atoms and NF_3 our search for bands due to $FNIrF_2$ was unsuccessful and only the nitrido complex $NIrF_3$ was formed. Again, this reflects the lower stability of the former species, which exothermically rearranged to the lowest energy isomer. Here, too, four bands were assigned to $NIrF_3$ (marked with **A′**–**D′** in Figure 4), of which only two revealed a $^{14/15}N$ isotope shift. Quantum-chemical calculations (Table 1) performed at the DFT (BP86, B3LYP) and CCSD(T) levels of theory fully support these assignments. The IrF_3 stretching modes are split into three components due to a first order Jahn–Teller distortion for the anticipated $5d^3$ configuration, which reduced the full C_{3v} point group symmetry to C_s symmetry (for structures see Figures 5, S5, and Table S3). All three Ir–F stretching modes were observed, but only the band associated with the Ir–F′ bond, which resides in the mirror plane together with the N–Ir bond, show a small $^{14/15}N$ isotope shift.

The assignment of the IR spectra obtained after co-depositing evaporated rhodium and diluted NF_3 (Figure 3) was more puzzling. In these experiments both the anticipated compounds are finally detected in the solid matrices and for each all four stretching bands were successfully assigned (Table 1). As described above for the corresponding Iridium compound also for $NRhF_3$ a $^{14/15}N$ isotope shift was observed for the N–Rh and the Rh–F′ stretching modes (Figure 3, **A′** and **D′**, respectively). Our CCSD(T) calculations for this species yield two imaginary frequencies which likely are caused by a close-lying excited electronic state which interferes with the calculation of displaced steps during the

 © 2020 The Authors. Published by Wiley-VCH GmbH

Table 1: Comparison of infrared band positions (cm^{-1}) and isotopic shifts (cm^{-1}, in parenthesis) observed in solid neon and argon with calculated values [intensities in km mol^{-1} in brackets] and their assignment in terms of an approximate description of the vibrational modes.[a]

Neon	Argon	BP86	B3LYP	CCSD(T)	Assignment
$FNCoF_2$					
1056.8 (−21.4)	–[b]	870 (−19) [220]	1080 (−20) [293]	1152 (−22) [–] [c]	F–N str. [a′]
751.7 (−0.1)	–[b]	732 (0) [123]	764 (0) [171]	859 (−0.3)[–][c]	antisym. F–Co–F str. [a″]
629.6 (−3.5)	–[b]	627 (−1) [63]	611 (0) [60]	651 (−1) [–][c]	sym. F–Co–F str. [a′]
586.1 (−12.1)	–[b]	765 (−17) [37]	442 (−13) [12]	609 (−16) [–] [c]	N–Co str. [a′]
$NRhF_3$					
1116.1 (−33.0)	1112.56 (−33)	1087 (−32) [48]	1113 (−33) [55]	–	N–Rh str. [a′]
626.2/ 624.8 (0)[d]	612.0	603 (0) [96]	625 (0) [118]	–	antisym. F–Rh–F str. [a″]
622.2/ 622.8 (0)[d]	610.5	601 (0) [48]	618 (0) [63]	–	sym. F–Rh–F str. [a′]
542.5 (−0.4)	539.9 (−0.5)	562 (0) [45]	581 (0) [52]	–	Rh–F′ str. [a′]
$FNRhF_2$[e]					
872.6 (−18.9)	–[b]	850 (−24) [103]	935 (−24) [168]	872 (−16) [–]	F–N str. [a′]
761.4 (−18.0)	760.1 (−19.6)	721 (−12) [181]	786 (−16) [117]	707 (−19) [–]	N–Rh str. [a′]
655.1 (0)	638.9 (0)	625 (0) [132]	641 (0) [150]	652 (0) [–]	antisym. F–Rh–F str. [a″]
596.7 (0)	585.9 (−0.5)	572 (−0.3) [101]	594 (−0.3) [75]	580 (−2) [–]	sym. F–Rh–F str. [a′]
$NIrF_3$					
1150.4 (−36.0)	1144.6 (−35.8) [f]	1121 (−35) [22]	1158 (−36) [23]	1126 (−36) [–]	N–Ir str. [a′]
659.8 (0)	–[g]	618 (0) [34]	635 (0) [43]	653 (0) [–]	sym. F–Ir–F str. [a′]
651.6/648.9 (0)[c]	–[g]	618 (0) [132]	634 (0) [147]	650 (0) [–]	antisym. F–Ir–F str. [a″]
562.1 (−0.2)	560.1 (−0.5)[f]	562 (0) [36]	581 (0) [40]	607 (0) [–]	Ir–F′ str. [a′]

[a] Only normal modes predicted in the experimentally observable range ($\tilde{\nu}$ >400 cm^{-1}) are listed. A full list of computed frequencies is presented in the Supporting Information. For CASPT2 and CCSD(T) no intensities are available; [b] Bands not observed, or too weak. [c] Wavenumbers (isotopic shifts) obtained at the CASPT2/cc-pVTZ-DK level; [d] Two matrix sites; [e] Wavenumbers (isotopic shifts, in cm^{-1}) obtained using CASPT2/cc-pVTZ-DK: 981 (−19.5), 756 (−20.4), 672 (0), 623 (−0.5); [f] Weak bands tentatively assigned. [g] Too weak or overlapped by broad and strong NF_3 bands in this area.

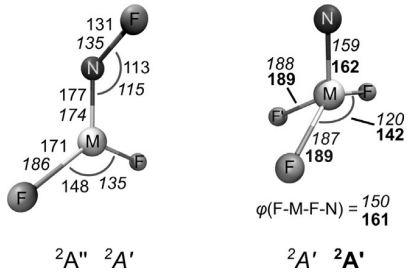

Figure 5. Electronic ground state structures of $FNMF_2$ for M = Co (^{2}A″, regular) and Rh (^{2}A′, italic) calculated at the CASPT2/cc-pVTZ-DK level and of NMF_3 for M = Rh (^{2}A′, italic) and Ir (^{2}A′, bold) obtained at the CCSD(T)/aug-cc-pVTZ(-PP) level of theory. Bond lengths are given in pm and angles in degree (φ denotes the dihedral angle of F-M-F-N).

numerical hessian calculation where the symmetry is lowered to C_1. However, the structure obtained at the B3LYP level of theory is close to the one obtained at the CCSD(T) level (Figures 5 and S5) and the good agreement of the B3LYP results for $NIrF_3$ with the experimental frequencies suggest a good performance also for the $NRhF_3$ species. The $^{14/15}$N isotope shift observed for the nitrene complex $FNRhF_2$ is well distributed between the F–N and the N–Rh stretching bands (Figure 3, bands **A** and **B**, respectively) indicating a strong vibrational coupling between these two modes. Analyzing the N–M and F–N stretching frequencies of $FNCoF_2$ and $FNRhF_2$ we found surprisingly large differences in the bonding of the fluoronitrene ligand. In general, the two singly occupied anti bonding π*(F–N)-orbitals of the FN ligand form a σ and a π bond to these metal centers, as depicted in the qualitative molecular orbital (MO) interaction diagram shown in Figure 6. The F–N mode of $FNCoF_2$ (1056.8 cm^{-1}) appeared red-shifted by 62.6 cm^{-1} from the absorption of free, neutral FN (1119.4 cm^{-1}),[11] indicating the presence of an almost neutral nitrene ligand, while the corresponding mode of $FNRhF_2$ (872.6 cm^{-1}) is much stronger red-shifted by 246.8 cm^{-1}.

On the other side, the low N–Co stretching frequency of $FNCoF_2$ (586.1 cm^{-1}) is most likely associated with a N–Co single bond, while the N–Rh frequency of $FNRhF_2$

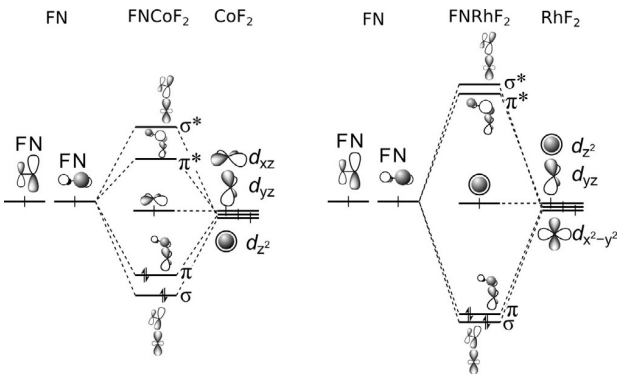

Figure 6. Simplified MO diagrams for the leading electronic configurations of the 4-electron-3-center F-N-M bond of $FNCoF_2$ (left) and $FNRhF_2$ (right). The low-energy F–N bonding orbitals are not shown.

 © 2020 The Authors. Published by Wiley-VCH GmbH

(761.4 cm^{-1}) can be attributed to a N=Rh double bond. These experimental observations are consistent with calculated atomic charges for the FN fragment in $FNCoF_2$ (NPA: 0.02, AIM: −0.02) and $FNRhF_2$ (NPA: −0.25, AIM: −0.20), as well as Mayer and Wiberg bond orders for the N−M bonds listed in Table 2, and the calculated N−M bond lengths (M = Co: 177 pm, Rh: 174 pm, Figure 5). To shed light on these striking bonding differences non-dynamical electron-correlation effects were taken into account. The results of CASSCF calculations revealed that the leading configuration ($\sigma^2\pi^2\delta^1\pi^{*0}\sigma^{*0}$) associated with the qualitative MO Scheme shown in Figure 6 contributes only 48% to the $^2A''$ ground state of $FNCoF_2$, followed by states with significant weights which contain single and double $\pi\rightarrow\pi^*$ excitations (Table S4). For $FNRhF_2$ a much smaller extend of non-dynamic correlation was determined, since the most dominant configuration as depicted in Figure 6 contributes to 84% to its $^2A'$ electronic ground state. As a consequence of these correlation effects significant higher σ* and π* populations (0.37 and 0.61, Figure S6) were found for $FNCoF_2$ compared to $FNRhF_2$ (σ*: 0.11, π*: 0.18). The effective bond orders (EBO)[20] derived from the natural orbitals obtained at the CASSCF level are 1.1 for the Co−N and 1.7 for the Rh=N bond. We also note a considerable amount of minority spin population at the N atom (−0.46) in $FNCoF_2$ (Table 2 and Figure S7) antiferromagnetically coupled to the majority spin at the Co center (1.46). The latter spin density can mainly be attributed to the singly occupied nonbonding δ-MO of a″ symmetry (Figures 6 and S6). Taking these effects into account, the FN unit in $FNCoF_2$ has at least a considerable fraction of iminyl/nitrene radical character, which explains the shortened single bond. The disparities in the metal-nitrogen bonds of these nitrene complexes can likely be attributed to the peculiarity of bonding of the strongly correlated first-row transition metal-ligand bonds. Especially the close internuclear distance required for an optimum orbital overlap for π bonding is likely hindered due to Pauli repulsion of the Co 3s,3p core–shell and the nitrogen ligand orbitals.[21]

Table 2: NPA and AIM charges, spin populations, as well as Mayer and Wiberg bond orders obtained from electronic ground state wavefunctions calculated at the CASSCF(9,7)/cc-pVTZ-DK levels of theory. All units in atomic units.

Property		F′NCoF$_2$ ($^2A''$, C_s)	F′NRhF$_2$ ($^2A'$, C_s)
NPA	F′	−0.2342	−0.2508
Charge	N	0.2552	0.1196
	M	1.6134	1.6264
	F	−0.8172	−0.7476
AIM	F′	−0.3780	−0.3932
Charge	N	0.3576	0.1916
	M	1.6158	1.6929
	F	−0.7977	−0.7457
Spin	F′	−0.0239	−0.0006
Population	N	−0.4639	−0.1149
	M	1.4593	1.0627
	F	0.0143	0.0264
Mayer Bond Order	F′-N	0.976	0.909
	N-M	0.561	1.395
	M-F	0.647	0.647
Wiberg Bond Order	F′-N	1.429	1.337
	N-M	1.246	2.156
	M-F	1.180	1.167

For the nitrido complexes $NRhF_3$ and $NIrF_3$ the computed bond length (162 pm (IrN), 159 (RhN); for comparison: triple-bond additive covalent radii: 160 pm (IrN) and 160 pm (RhN),[22] Figure 5) and the experimental stretching frequencies (Table 1) indicate strong N≡M triple bonds. An analysis of the CASSCF(9,8) natural molecular orbitals (Figure S8) reveals EBOs of 2.7 and 2.8 for N≡Rh and N≡Ir, respectively. Consistent with the assignment of oxidation state +VI for both metal centers, a d^3 configuration and a Jahn–Teller distorted $^2A'$ electronic ground state was determined for both species. The N−Ir stretching frequency in neon of 1150.4 cm^{-1} is moderately higher than that observed for diatomic IrN embedded in solid neon (1111.1 cm^{-1}).[23] However, in case of rhodium a significant blue-shift of the N−Rh stretching mode (1112.6 cm^{-1}) of 221.2 cm^{-1} occurred compared to diatomic RhN embedded in argon (891.4 cm^{-1}).[24] The increased force constant of 920 $N\,m^{-1}$ in $NRhF_3$ from 580 $N\,m^{-1}$ in RhN indicates a significant strengthening of the nitrogen-metal bond induced by the fluorine ligands. This fluorine effect is less pronounced for the already strong triple bond in IrN, where force constants increase from 950 to 1020 $N\,m^{-1}$ for IrN and $NIrF_3$, respectively.

Conclusion

In summary, we described the exothermic formation of the fluoronitrenoid complexes $FNCoF_2$ and $FNRhF_2$ and of the nitrido complexes $NRhF_3$ and $NIrF_3$ by the reaction of the free group 9 metal atoms with NF_3. The IR spectra of these compounds isolated in solid rare gases (neon and argon) were recorded and, aided by the observed $^{14/15}N$ isotope shifts and quantum-chemical predictions, all four stretching fundamentals of these complexes were safely assigned. Neither nitrido nor other ternary complexes of Rh^{VI} and Ir^{VI} have yet been reported. The anticipated rearrangement of $FNCoF_2$ to the nitrido Co^{VI} complex was not observed, because this reaction is endotherm. The covalently bound FN ligand in these high-valent metal complexes is almost neutrally charged, and the formal picture of an FN^{2-} ligand bound to a MF_2 fragment is a rather coarse approximation for these fluoronitrenoid complexes. However, the bonding of the FN ligand in $FNCoF_2$ and $FNRhF_2$ was found to be strikingly different. In $FNCoF_2$ the FN ligand is singly bonded to Co and bears considerable iminyl/nitrene radical character, while the N=Rh double bond in $FNRhF_2$ shows comparatively strong σ- and π-bonds. The stretched N-Co bond and the poor overlap especially between the ligand π- and the metal 3d-orbitals can likely be attributed to a repulsion between the ligand orbitals and the outermost core 3s,3p shell of cobalt.

 © 2020 The Authors. Published by Wiley-VCH GmbH

Acknowledgements

We gratefully acknowledge the Zentraleinrichtung für Datenverarbeitung (ZEDAT) of the Freie Universität Berlin for the allocation of computing resources. We thank the ERC Project HighPotOx as well as the CRC 1349 (SFB 1349) Fluorine Specific Interactions—Project-ID 387284271—for continuous support. We also thank Prof. Ralf Haiges for fruitful discussions. Open access funding enabled and organized by Projekt DEAL.

Conflict of interest

The authors declare no conflict of interest.

Keywords: ab-initio calculations · high oxidation states · matrix isolation · N ligands · transition metals

[1] Note that the dash (–) between two bonded atoms will depict a two-electron "iono-covalent" bond. It will generally not distinguish between an ionic bond to an Imido ligand or a covalent bond to a neutral NR ligand (see P. Karen, P. McArdle, J. Takats, *Pure Appl. Chem.* **2014**, *86*, 1017).
[2] a) J. Fawcett, R. D. Peacock, D. R. Russell, *Dalton Trans.* **1987**, 567; b) K. Dehnicke, J. Straehle, *Chem. Rev.* **1993**, *93*, 981; c) Y. Gong, L. Andrews, *Inorg. Chem.* **2012**, *51*, 667.
[3] a) A. I. Olivos Suarez, V. Lyaskovskyy, J. N. H. Reek, J. I. van der Vlugt, B. de Bruin, *Angew. Chem.* **2013**, *125*, 12740; b) Y. Park, Y. Kim, S. Chang, *Chem. Rev.* **2017**, *117*, 9247; c) M. Kinauer, M. Diefenbach, H. Bamberger, S. Demeshko, E. J. Reijerse, C. Volkmann, C. Würtele, J. van Slageren, B. de Bruin, M. C. Holthausen et al., *Chem. Sci.* **2018**, *9*, 4325; d) H. M. L. Davies, J. R. Manning, *Nature* **2008**, *451*, 417; e) Y. Liu, J. Du, L. Deng, *Inorg. Chem.* **2017**, *56*, 8278; f) T. A. Ramirez, B. Zhao, Y. Shi, *Chem. Soc. Rev.* **2012**, *41*, 931; g) A. Reckziegel, C. Pietzonka, F. Kraus, C. G. Werncke, *Angew. Chem. Int. Ed.* **2020**, *59*, 8527; *Angew. Chem.* **2020**, *132*, 8605; h) J. L. Roizen, M. E. Harvey, J. Du Bois, *Acc. Chem. Res.* **2012**, *45*, 911; i) J. Schöffel, A. Y. Rogachev, S. DeBeer George, P. Burger, *Angew. Chem. Int. Ed.* **2009**, *48*, 4734; *Angew. Chem.* **2009**, *121*, 4828; j) J. Schöffel, N. Šušnjar, S. Nückel, D. Sieh, P. Burger, *Eur. J. Inorg. Chem.* **2010**, 4911; k) T. Xiong, Q. Zhang, *Chem. Soc. Rev.* **2016**, *45*, 3069; l) A. I. Olivos Suarez, V. Lyaskovskyy, J. N. H. Reek, J. I. van der Vlugt, B. de Bruin, *Angew. Chem. Int. Ed.* **2013**, *52*, 12510; *Angew. Chem.* **2013**, *125*, 12740; m) F. Collet, R. H. Dodd, P. Dauban, *Chem. Commun.* **2009**, 5061; n) P. F. Kuijpers, J. I. van der Vlugt, S. Schneider, B. de Bruin, *Chem. Eur. J.* **2017**, *23*, 13819.
[4] J. F. Berry, *Comments Inorg. Chem.* **2009**, *30*, 28.
[5] K. Ray, F. Heims, F. F. Pfaff, *Eur. J. Inorg. Chem.* **2013**, 3784.
[6] L. Zhang, Y. Liu, L. Deng, *J. Am. Chem. Soc.* **2014**, *136*, 15525.
[7] J. M. Smith in *Progress in Inorganic Chemistry* (Ed.: K. D. Karlin), Wiley, Hoboken, **2014**, pp. 417–470.
[8] a) C. C. Lu, S. DeBeer George, T. Weyhermüller, E. Bill, E. Bothe, K. Wieghardt, *Angew. Chem. Int. Ed.* **2008**, *47*, 6384; *Angew. Chem.* **2008**, *120*, 6484; b) A. N. Walstrom, B. C. Fullmer, H. Fan, M. Pink, D. T. Buschhorn, K. G. Caulton, *Inorg. Chem.* **2008**, *47*, 9002; c) A. Takaoka, L. C. H. Gerber, J. C. Peters, *Angew. Chem. Int. Ed.* **2010**, *49*, 4088; *Angew. Chem.* **2010**, *122*, 4182; d) A. C. Bowman, C. Milsmann, E. Bill, Z. R. Turner, E. Lobkovsky, S. DeBeer, K. Wieghardt, P. J. Chirik, *J. Am. Chem. Soc.* **2011**, *133*, 17353; e) S. P. Heins, W. D. Morris, P. T. Wolczanski, E. B. Lobkovsky, T. R. Cundari, *Angew. Chem. Int. Ed.* **2015**, *54*, 14407; *Angew. Chem.* **2015**, *127*, 14615; f) E. Kogut, H. L. Wiencko, L. Zhang, D. E. Cordeau, T. H. Warren, *J. Am. Chem. Soc.* **2005**, *127*, 11248; g) Y. Dong, J. T. Lukens, R. M. Clarke, S.-L. Zheng, K. M. Lancaster, T. A. Betley, *Chem. Sci.* **2020**, *11*, 1260; h) M. J. T. Wilding, D. A. Iovan, A. T. Wrobel, J. T. Lukens, S. N. MacMillan, K. M. Lancaster, T. A. Betley, *J. Am. Chem. Soc.* **2017**, *139*, 14757.
[9] K. M. Carsch, I. M. DiMucci, D. A. Iovan, A. Li, S.-L. Zheng, C. J. Titus, S. J. Lee, K. D. Irwin, D. Nordlund, K. M. Lancaster et al., *Science* **2019**, *365*, 1138.
[10] X. Wang, J. T. Lyon, L. Andrews, *Inorg. Chem.* **2009**, *48*, 6297.
[11] X. Wang, L. Andrews, R. Lindh, V. Veryazov, B. O. Roos, *J. Phys. Chem. A* **2008**, *112*, 8030.
[12] a) H. C. Mattraw, N. J. Hawkins, D. R. Carpenter, W. W. Sabol, *J. Chem. Phys.* **1955**, *23*, 985; b) A. Citra, L. Andrews, *J. Phys. Chem. A* **1999**, *103*, 4182; c) Y. Gong, M. Zhou, M. Kaupp, S. Riedel, *Angew. Chem. Int. Ed.* **2009**, *48*, 7879; *Angew. Chem.* **2009**, *121*, 8019; d) A. Citra, L. Andrews, *J. Phys. Chem. A* **1999**, *103*, 4845; e) C. L. Chernick, H. H. Claassen, B. Weinstock, *J. Am. Chem. Soc.* **1961**, *83*, 3165.
[13] a) M. Domański, Ł. Wolański, P. Szarek, W. Grochala, *J. Mol. Model.* **2020**, *26*, 1; b) Ł. Wolański, M. Domański, W. Grochala, P. Szarek, *Chem. Eur. J.* **2019**, *25*, 10290.
[14] E. K. Byrne, K. H. Theopold, *J. Am. Chem. Soc.* **1989**, *111*, 3887.
[15] a) C. Jones, C. Schulten, R. P. Rose, A. Stasch, S. Aldridge, W. D. Woodul, K. S. Murray, B. Moubaraki, M. Brynda, G. La Macchia et al., *Angew. Chem. Int. Ed.* **2009**, *48*, 7406; *Angew. Chem.* **2009**, *121*, 7542; b) M. P. Mehn, S. D. Brown, D. M. Jenkins, J. C. Peters, L. Que, *Inorg. Chem.* **2006**, *45*, 7417; c) T. A. Betley, J. C. Peters, *J. Am. Chem. Soc.* **2003**, *125*, 10782; d) X. Dai, P. Kapoor, T. H. Warren, *J. Am. Chem. Soc.* **2004**, *126*, 4798; e) X. Hu, K. Meyer, *J. Am. Chem. Soc.* **2004**, *126*, 16322; f) R. E. Cowley, R. P. Bontchev, J. Sorrell, O. Sarracino, Y. Feng, H. Wang, J. M. Smith, *J. Am. Chem. Soc.* **2007**, *129*, 2424.
[16] a) D. Sengupta, C. Sandoval-Pauker, E. Schueller, A. M. Encerrado-Manriquez, A. Metta-Magaña, W.-Y. Lee, R. Seshadri, B. Pinter, S. Fortier, *J. Am. Chem. Soc.* **2020**, *142*, 8233; b) E. M. Zolnhofer, M. Käß, M. M. Khusniyarov, F. W. Heinemann, L. Maron, M. van Gastel, E. Bill, K. Meyer, *J. Am. Chem. Soc.* **2014**, *136*, 15072; c) C. C. Hojilla Atienza, A. C. Bowman, E. Lobkovsky, P. J. Chirik, *J. Am. Chem. Soc.* **2010**, *132*, 16343.
[17] M. K. Wilson, S. R. Polo, *J. Chem. Phys.* **1952**, *20*, 1716.
[18] M. E. Jacox, *J. Phys. Chem. Ref. Data* **1998**, *27*, 115.
[19] W. Maya, *Inorg. Chem.* **1964**, *3*, 1063.
[20] B. O. Roos, A. C. Borin, L. Gagliardi, *Angew. Chem. Int. Ed.* **2007**, *46*, 1469; *Angew. Chem.* **2007**, *119*, 1491.
[21] M. Kaupp, *J. Comput. Chem.* **2007**, *28*, 320.
[22] P. Pyykkö, S. Riedel, M. Patzschke, *Chem. Eur. J.* **2005**, *11*, 3511.
[23] T. Stüker, H. Beckers, S. Riedel, *Chem. Eur. J.* **2020**, *26*, 7384.
[24] A. Citra, L. Andrews, *J. Phys. Chem. A* **1999**, *103*, 3410.

Manuscript received: August 12, 2020
Revised manuscript received: August 30, 2020
Accepted manuscript online: September 4, 2020
Version of record online: October 15, 2020

 © 2020 The Authors. Published by Wiley-VCH GmbH

4.3. A Cornucopia of Iridium Nitrogen Compounds Produced from Laser-Ablated Iridium Atoms and Dinitrogen

Tony Stüker, Helmut Beckers and Sebastian Riedel*
Chemistry — A European Journal **2020**, *26*, 7384–7394.
DOI: 10.1002/chem.201905514
© *2020 The Authors. Published by Wiley-VCH GmbH*
For the Supporting Information see Appendix A.3.

Author Contribution

Tony Stüker did all calculations, carried out all experiments and wrote the manuscript. Sebastian Riedel and Helmut Beckers managed the project and revised the manuscript.

Chemistry–A European Journal | Full Paper
doi.org/10.1002/chem.201905514

Check for updates
Chemistry Europe
European Chemical Societies Publishing

Iridium Compounds | *Hot Paper*

A Cornucopia of Iridium Nitrogen Compounds Produced from Laser-Ablated Iridium Atoms and Dinitrogen

Tony Stüker, Helmut Beckers, and Sebastian Riedel*[a]

Abstract: The reaction of laser-ablated iridium atoms with dinitrogen molecules and nitrogen atoms yield several neutral and ionic iridium dinitrogen complexes such as $Ir(N_2)$, $Ir(N_2)^+$, $Ir(N_2)_2$, $Ir(N_2)_2^-$, IrNNIr, as well as the nitrido complexes IrN, $Ir(N)_2$ and IrIrN. These reaction products were deposited in solid neon, argon and nitrogen matrices and characterized by their infrared spectra. Assignments of vibrational bands are supported by ab initio and first principle calculations as well as $^{14/15}N$ isotope substitution experiments. The structural and electronic properties of the new dinitrogen and nitrido iridium complexes are discussed. While the formation of the elusive dinitrido complex $Ir(N)_2$ was observed in a subsequent reaction of IrN with N atoms within the cryogenic solid matrices, the threefold coordinated iridium trinitride $Ir(N)_3$ could not be observed so far.

Introduction

Molecular complexes combining nitrogen and platinum group metals (PGM), such as dinitrogen complexes $L_mM(N_2)_n$ and polynitrido metal complexes $L_mM(N)_n$ have recently attracted much attention.[1] Molecular dinitrogen complexes are of vivid interest in nitrogen fixation and reduction since 1966, when the first iridium dinitrogen complex was published, shortly after the first transition metal dinitrogen complexes $[Ru(NH_3)_5N_2]X_2$ with X = Br^-, I^- and BF_4^- were reported in 1965.[2] The activation and weakening of the strong triple bond in the N_2 molecule is facilitated by π-back-bonding from orthogonal d_{xz} and d_{yz} or even p orbitals into the antibonding π*-orbitals of the N_2 ligand.[1a,2c,3] This effect is readily observable spectroscopically by a red-shift of the N–N stretching mode compared to free dinitrogen in the IR spectra. All binary PGM dinitrogen complexes, except those of iridium, were investigated experimentally using matrix isolation techniques, where metal atoms are generated by thermal evaporation or laser ablation for Ru,[4] Rh,[5] Pd,[6] Re,[7] Os,[4] and Pt.[6b,8] By these methods homoleptic dinitrogen complexes $M(N_2)_n$ can be prepared, which allow the investigation of metal–nitrogen bonding interactions independent of the influence of other ligands and thus give important insight into the bonding properties and mechanisms of dinitrogen activation.

Polynitrido metal complexes have recently attracted attention as the nitrido ligand facilitates high oxidation states. Examples are the group 6 complexes $NM^{+VI}F_3$ (with M = Cr, Mo and W)[9] and the more recently predicted but so far unknown $NIr^{+IX}O_3$.[1b] The concept of "formal oxidation states" is a popular and important method of counting and assigning electrons to chemical elements in molecular and solid-state structures.[10] In recent years the range of compounds in high and unusual formal oxidation states has been expanded experimentally as well as theoretically. The so far highest experimentally attained formal oxidation state across all chemical elements is +IX of iridium in the $[IrO_4]^+$ cation.[11] It was generated in the gas phase and detected using infrared photodissociation spectroscopy after it was predicted theoretically.[12] But also compounds with iridium in the oxidation states of +VI and +VIII are scarce: $Ir^{+VI}F_6$, IrO_3, $Ir^{+VI}(\eta^2\text{-}O_2)(O)_2$ and $Ir^{+VIII}(O)_4$ are the only experimentally known examples.[13] Nitrogen is the third most electronegative element and with a formal oxidation number of −3 it can increase the formal oxidation state of the metal center by three units, while occupying only a single coordination site. The problem associated with the N^{3-} ligand is that, compared to F^- and O^{2-}, it is more easily oxidized by strong oxidizing metal centers, especially in complexes bearing metals in high oxidation states. Several binary transition metal nitrides were previously prepared by the reaction of laser-ablated metal atoms with pure dinitrogen or dinitrogen diluted in rare gases, and subsequent deposition on a cold matrix support. Although this method mainly yields metal dinitrogen complexes, also molecular mono- and dinitrides of the platinum group metals, such as RuN and $Ru(N)_2$,[4] RhN and $Rh(N)_2$,[5b] OsN and $Os(N)_2$,[4] and PtN[8c] were formed as well. So far, the only known binary molecular iridium nitrogen compound is the IrN molecule, first produced by laser ablation of

[a] *T. Stüker, Dr. H. Beckers, Prof. S. Riedel*
Institut für Chemie und Biochemie, Anorganische Chemie
Freie Universität Berlin, Fabeckstr. 34/36, 14195 Berlin (Germany)
E-mail: s.riedel@fu-berlin.de

Supporting information and the ORCID identification number(s) for the author(s) of this article can be found under: https://doi.org/10.1002/chem.201905514.

© 2020 The Authors. Published by Wiley-VCH Verlag GmbH & Co. KGaA. This is an open access article under the terms of the Creative Commons Attribution License, which permits use, distribution and reproduction in any medium, provided the original work is properly cited.

Chemistry–A European Journal | Full Paper doi.org/10.1002/chem.201905514 | Chemistry Europe European Chemical Societies Publishing

iridium atoms in the presence of NH_3 and characterized by optical/Stark spectroscopy.[14] Subsequently, its spectral and bonding properties were studied further experimentally and theoretically.[15] Furthermore, high-pressure materials of the composition Ir_2N, $Ir(N)_2$ and $Ir(N)_3$, respectively, are potentially (super) hard materials and their structural, electronic and mechanical properties were previously investigated theoretically[16] and experimentally.[17] These materials however contain quasi-molecular N_2^{2-} or N_2^{4-} units rather than N^{3-}.[18]

We have carried out reactions of laser-ablated iridium atoms with dinitrogen molecules and studied the reaction products by matrix-isolation IR spectroscopy. The photodecomposition of N_2 molecules and the formation of N atoms induced by plasma radiation in the laser-ablation process should also facilitate the formation of molecular binary iridium nitrides up to $Ir^{+IX}(N)_3$. These molecular binary iridium nitrides will allow to gauge the ability of the N atom to oxidize the iridium metal center and to investigate the nature of the chemical bonding independent of the influence of other ligands.

Experimental and Computational Methods

Matrix-isolation experiments

$^{14}N_2$ (99.999%, Linde) and $^{15}N_2$ (98+ atom %, Campro) were premixed with neon or argon (both 99.999%, Linde) in a stainless-steel cylinder. The mixing vessel was connected to a stainless-steel vacuum line connected to a self-made matrix chamber by a stainless-steel capillary. The gas mixture was then co-deposited with laser-ablated iridium atoms onto a CsI window (argon and dinitrogen matrices) or onto a gold plated copper mirror (neon matrices) and cooled to 4 K by using a closed-cycle helium cryostat (Sumitomo Heavy Industries, RDK-205D) inside the vacuum chamber. For the laser-ablation, the 1064 nm fundamental of a Nd:YAG laser (Continuum, Minilite II, 10 Hz repetition rate, 35–50 mJ pulse^{-1}) was focused onto a rotating iridium metal target through a hole in the cold window. Infrared spectra were recorded on a Bruker Vertex 70 spectrometer purged with dry air (argon and dinitrogen matrices) or a Bruker Vertex 80v with evacuated optical path (neon matrices) at 0.5 cm^{-1} resolution in the region 4000–430 cm^{-1} by using a liquid-nitrogen-cooled mercury cadmium telluride (MCT) detector. Far-IR (FIR) spectra were recorded at a resolution of 0.5 cm^{-1} at the Bruker Vertex 80v equipped with a FIR multilayer mylar beam-splitter (680–30 cm^{-1}), a CsI window (>180 cm^{-1}), and a liquid helium cooled bolometer. The matrix samples were irradiated by a mercury arc streetlamp (Osram HQL 250) with the outer globe removed. Wavelength selective irradiations in the visible spectrum were realized with OSRAM LEDs with typical powers between 5 and 10 watts.

Electronic-structure calculations

Density functional theory (DFT) calculations were performed using the TURBOMOLE 7.0.1 program package[19] employing the GGA exchange-correlation density functional BP86[20] with the polarized quadruple-ξ basis set def2-QZVP[21] which applies the Stuttgart-Dresden effective core potential for iridium.[22] All Coupled Cluster Single Double and perturbative Triple excitations (CCSD(T)) combined with Dunning's augmented correlation consistent polarized triple-ξ basis sets aug-cc-pVTZ for nitrogen,[23] and aug-cc-pVTZ-PP combined with the ECP60MDF effective core potential for iridium[24] were performed using the CFOUR 2.00beta software.[25] State-averaged complete active space self-consistent field (SA-CASSCF) calculations combined with Dunning's correlation consistent polarized valence triple-ξ basis sets cc-pVTZ[26] and cc-pVTZ-PP[24] for nitrogen and iridium and the effective core potential (ECP60MDF) for iridium were carried out for iridium dinitride using the Molpro 2019 software.[27] The active space was chosen to consist of the molecular orbitals formed by the 2p(N), 5d(Ir) and 6s(Ir) atomic orbitals, yielding 15 electrons in 12 molecular orbitals. One calculation for each spin multiplicity, doublet, quartet and sextet was carried out employing the state-averaging formalism in C_{2v} point group symmetry, including two states of each state symmetry (A_1, B_1, B_2 and A_2), resulting in eight states with equal weights of 0.125. Harmonic vibrational frequency calculations were carried out for all optimized structures analytically (BP86) or numerically (CCSD(T)). The decomposition pathways of $Ir(N)_2$ and $Ir(N)_3$ were analyzed by optimizing the geometries of the nitrides, the complexes formed by the rearrangement, and the transition states connecting both minima using the BP86 exchange-correlation density functional with the application of the zeroth-order regular relativistic approximation (ZORA)[28] combined with the adapted version of the def2 basis set ZORA-def2-TZVPP for nitrogen and the segmented all-electron relativistic contracted SARC-ZORA-TZVPP for iridium[29] as implemented in ORCA 4.1.2.[30] Additionally, the *meta*-GGA M06-L exchange correlation density functional[31] was used for calculating the energy barriers associated with the decompositions of $Ir(N)_2$ and $Ir(N)_3$. The NBO and AIM analyses were carried out using wavefunctions obtained at the BP86/def2-QZVP level of theory using NBO 7.0[31] and Multiwfn 3.5,[33] respectively. Because of the multitudes of combinations and the rapidly increasing computational challenges, compounds of the formula Ir_xN_y, with y and x greater than two are not explicitly considered.

Results and Discussion

Laser-ablated iridium atoms were reacted with diluted dinitrogen in a vacuum chamber and the reaction products were subsequently deposited on a matrix support under cryogenic conditions and studied using IR spectroscopy. The experimental details are presented in the experimental section. The obtained products can be separated in two different sets: dinitrogen and nitrido complexes. The N–N stretching vibrations of the dinitrogen complexes occur in the region from 2350–1850 cm^{-1}, and the Ir–N stretching vibrations of dinitrogen and nitrido complexes in the region below 1150 cm^{-1} (Table 1). The main absorptions that appeared in the N–N stretching region of the IR spectra are located at 2270.3, 2241.6, 2154.0, 2097.4, 1956.4 cm^{-1}. They are assigned and labeled in Figures 1 and 2 to the dinitrogen complexes $[Ir(N_2)]^+$, $NIr(N_2)$, $Ir(N_2)_2$, $Ir(N_2)$ and $[Ir(N_2)_2]^-$, respectively. In the Ir–N stretching region of these spectra absorptions of IrN, IrIrN, $Ir(N)_2$ and IrNNIr were detected. These are indicated in Figures 3, 4 and 5 to bands at 1111.1, 1004.4, 853.5 and 786.5 cm^{-1}, respectively. Additional bands were observed when the reaction products are deposited in neat nitrogen matrices (Table 2 and Figure 2, trace d). In the $^{14}N_2$ matrices a band appeared at 2221.7 cm^{-1}, accompanied by a matrix site at 2214.3 cm^{-1} (Figure 2), which is probably associated with clusters of $Ir_x(N_2)_y$.

Complementary spectra were also recorded in solid argon (Figures S1 and S2), and in the FIR region using neon as matrix

 © 2020 The Authors. Published by Wiley-VCH Verlag GmbH & Co. KGaA, Weinheim

Chemistry–A European Journal | Full Paper doi.org/10.1002/chem.201905514 | Chemistry Europe European Chemical Societies Publishing

Table 1. Infrared absorptions (cm^{-1}) and $^{14}N_2/^{15}N_2$ isotopic ratios obtained from the reaction of laser-ablated iridium atoms co-deposited with dinitrogen diluted in neon at 4–5 K.

$^{14}N_2$	$^{15}N_2$	$^{14}N_2$ and $^{15}N_2$	$^{14}N_2/^{15}N_2$ ratio	Assignment
2327.6	2250.1	2327.6, 2250.1	1.0344	N_2 (perturbed)
2270.3	2194.8	2270.7, 2194.8	1.0344	$Ir(N_2)^+$
2241.6	2167.0	2241.6, 2167.0	1.0344	$Ir_x(N_2)_y$
2237.4	2163.1	[a]	1.0343	N_4^+
2158.0	2086.1	[a], 2158.0 [a], 2086.1	1.0345	$Ir(N_2)_2$ (site)
2154.0	2082.4	2194.6, 2154.0 2100.3, 2082.4	1.0344	$Ir(N_2)_2$
2099.8	2030.0	2099.9, 2030.0	1.0344	$Ir(N_2)$
2097.4	2027.9	[a]	1.0343	$Ir(N_2)$ (site)
1956.4	1890.3	1988.1, 1956.4 1912.9, 1891.5	1.0350	$Ir(N_2)_2^-$
1111.1	1076.4	1111.1, 1076.4	1.0322	IrN
1004.4	972.8	1004.4, 972.8	1.0322	IrIrN
931.5	931.5	931.5		OIrO
921.6	921.6	921.6		OIrO (site)
853.5	827.7	853.3, 827.7	1.0312	$Ir(N)_2$
786.5	761.6	786.5, 774.1, 761.6	1.0327	IrNNIr
		402.8, 397.4 393.1	1.0247	$Ir(N_2)_2$

[a] Not observed.

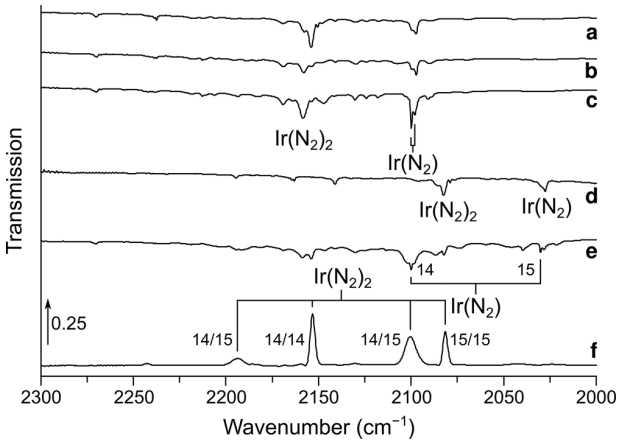

Figure 1. Infrared spectra in the 2000–2350 cm^{-1} region of the reaction products of laser-ablated iridium atoms with 0.5% $^{14}N_2$ in neon after deposition (a), 10 min broadband irradiation (b), annealing to $T=10$ K (c), with 0.5% $^{15}N_2$ in neon after deposition (d), with 0.5% of a 1:1 mixture of $^{14}N_2$ and $^{15}N_2$ in neon after 10 min of broadband irradiation and subsequent annealing of $T=10$ K (e) and with 10% of a 1:1 mixture of $^{14}N_2$ and $^{15}N_2$ in neon after 10 min of irradiation with LED light $\lambda=455$ nm (f). Bands due to iridium nitrogen compounds and some selected $^{14/15}N$ isotope patterns are indicated.

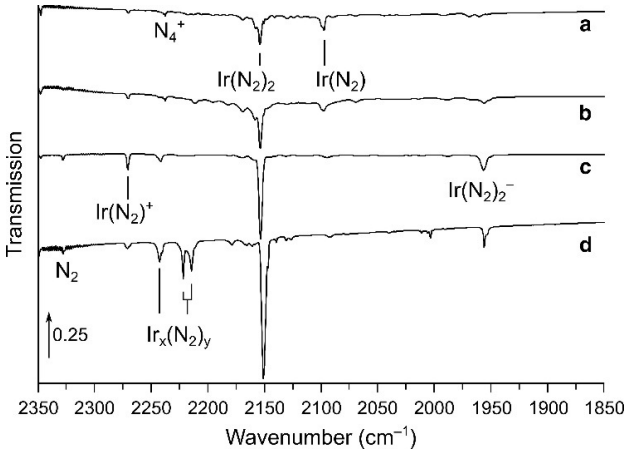

Figure 2. Infrared spectra in the 1850–2350 cm^{-1} region of the reaction products of laser-ablated iridium atoms with 0.5% (a), 3% (b), 10% (c) $^{14}N_2$ in neon, and neat $^{14}N_2$ (d). Bands due to iridium nitrogen compounds are indicated.

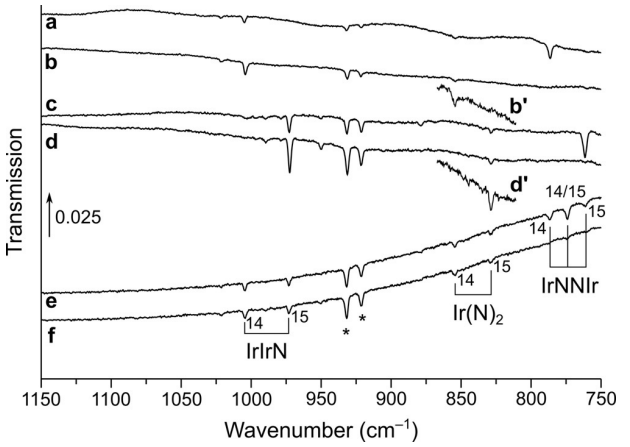

Figure 3. Infrared spectra in the 1150–750 cm^{-1} region of the reaction products of laser-ablated iridium atoms in neon doped with 10% $^{14}N_2$ after deposition (a), after 10 min of 455 nm irradiation (b), with 10% $^{15}N_2$ in neon after deposition (c) after irradiation with 455 nm (d), as well as with 10% of a 1:1 mixture of $^{14}N_2$ and $^{15}N_2$ in neon after deposition (e), and 10 min of irradiation with 455 nm (f). Bands due to iridium nitrogen compounds and some selected $^{14/15}N$ isotope patterns are indicated. The sections showing the $Ir(N)_2$ absorption in the spectra b and d are enhanced by a factor of 5 and tagged with b′ and d′.

host (Figure S3). A full list of absorptions found in argon matrices are given in Table 3. The bands centered at 2144.7, 2110.6, 2087.6, 1004.1, 848.2 cm^{-1} were assigned and marked in the Figures S1 and S2 to $Ir(N_2)_2$, $Ir_x(N_2)$, $Ir(N_2)$, IrIrN and $Ir(N)_2$, respectively. Bands obtained in the FIR region are shown in Figure S3. They are due to the three $^{14/15}N$ isotopologues of $Ir(N_2)_2$ embedded in solid neon and located at 402.8, 397.4 and 393.1 cm^{-1}, respectively. Optimized structures of the above-mentioned dinitrogen and nitrido complexes of iridium were obtained at the DFT and CCSD(T) levels of theory and depicted in Figure 6. Computed harmonic frequencies of the reaction products are summarized in Table S1, and computed reaction enthalpies related to the formation of the observed reaction products are listed in Table 4. In the following the infrared spectra and the annealing and photolysis behavior of the reaction products, as well as our computational results are discussed, starting with the dinitrogen iridium complexes.

 © 2020 The Authors. Published by Wiley-VCH Verlag GmbH & Co. KGaA, Weinheim

Chemistry–A European Journal | Full Paper doi.org/10.1002/chem.201905514 | Chemistry Europe European Chemical Societies Publishing

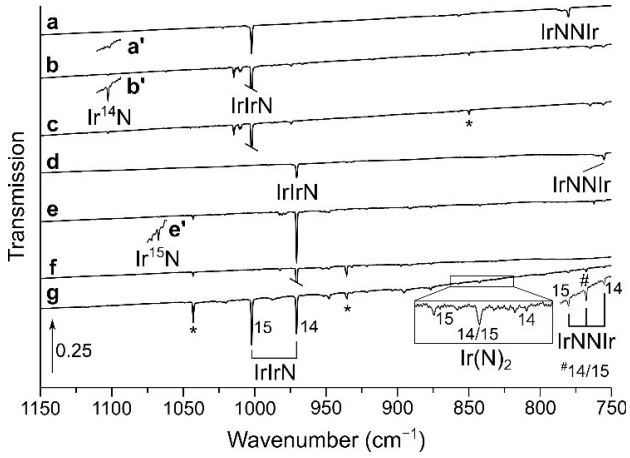

Figure 4. Infrared spectra in the 1150–750 cm^{-1} region of the reaction products of laser-ablated iridium atoms with $^{14}N_2$ after deposition (a), annealing to 35 K (b) and broadband irradiation (c), as well as with $^{15}N_2$ after deposition (d), annealing to 35 K (e), broadband irradiation (f) and finally after deposition with a 1:1 mixture of $^{14}N_2$ and $^{15}N_2$ (g). Bands due to iridium nitrogen compounds and some selected $^{14/15}N$ isotope patterns are indicated. Bands marked by an asterisk exhibit no isotopic shift and remained unassigned. The transmission of the bands shown in the sections a′, b′ and e′ are enhanced by a factor of 10, 10, and 15, respectively.

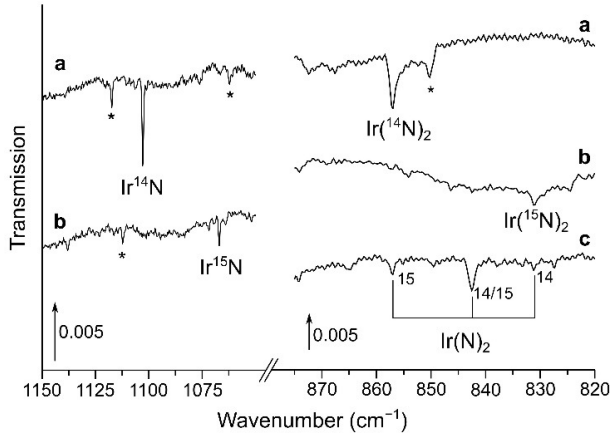

Figure 5. Infrared spectra in the 1150–1050 cm^{-1} and 875–820 cm^{-1} regions of the reaction products of laser-ablated iridium atoms with $^{14}N_2$ (a), $^{15}N_2$ (b) as well as a 1:1 mixture of $^{14}N_2$ and $^{15}N_2$ (c). Bands due to iridium nitrogen compounds and some selected $^{14/15}N$ isotope patterns are indicated. Bands marked with an asterisk exhibit no isotopic shift and remained unassigned.

Table 2. Infrared absorptions (cm^{-1}) and $^{14}N_2/^{15}N_2$ isotopic ratios obtained from the reaction of laser-ablated iridium atoms co-deposited with pure dinitrogen at 4–5 K.

$^{14}N_2$	$^{15}N_2$	$^{14}N_2$ and $^{15}N_2$	$^{14}N_2/^{15}N_2$ ratio	Assignment
2327.9	2249.9	2327.9, 2249.9	1.0347	N_2 (perturbed)
2271.3	2195.2	[a]	1.0347	$Ir(N_2)^+$
2242.8	2168.2	[b]	1.0344	$Ir_x(N_2)_y$
2221.7	2147.6	[b]	1.0345	$Ir_x(N_2)_y$
2217.5	2143.5	[b]	1.0345	$Ir_x(N_2)_y$
2214.3	2140.5	[b]	1.0345	$Ir_x(N_2)_y$
2151.1	2079.5	2196.4, 2189.6 2151.1, 2101.8 2094.8, 2079.5	1.0344	$Ir(NN)_2$
2150.0	2078.3	[a]	1.0345	$Ir(NN)_2$ (site)
2003.2	1937.6	2003.3, 1992.8 1948.7, 1937.5	1.0339	N_3^-
1955.8	1890.7	1955.8, 1912.4 1890.7	1.0344	$Ir(N_2)_2^-$
1657.5	1603.3	1657.6, 1649.2 1612.9, 1603.3	1.0338	N_3
1652.4	1597.6	[a]	1.0343	N_3 (site)
1102.8	1066.9	[a]	1.0336	IrN
1002.2	970.7	1002.2, 970.7	1.0325	IrIrN
857.1	831.2	857.1, 842.6 831.2	1.0312	$Ir(N)_2$
780.2	755.2	780.2, 767.7 755.2	1.0331	IrNNIr

[a] Too weak. [b] Fall into congested area of the spectrum.

Table 3. Infrared absorptions (cm^{-1}) and $^{14}N_2/^{15}N_2$ isotopic ratios obtained from the reaction of laser-ablated iridium atoms co-deposited with dinitrogen diluted in argon at 4–5 K.

$^{14}N_2$	$^{15}N_2$	$^{14}N_2$ and $^{15}N_2$	$^{14}N_2/^{15}N_2$ ratio	Assignment
2327.1	2249.2		1.0346	N_2 (perturbed)
2144.7	2073.7	2187.5, 2144.7 2092.6, 2073.7	1.0342	$Ir(N_2)_2$
2138.5	2138.5			CO
2110.6	2040.1	2110.6, 2040.1	1.0346	$Ir_x(N_2)$
2087.6	2018.2	2018.2	1.0344	$Ir(N_2)$
1004.1	972.7	1004.1, 972.7	1.0323	IrIrN
848.2				$Ir(N)_2$

$Ir(N_2)$

The band observed at 2097.4 cm^{-1} in neon doped with 0.5% $^{14}N_2$ with a weaker matrix site at 2099.8 cm^{-1} is assigned to the $Ir(N_2)$ complex (Figure 1). This band is unaffected by broadband irradiation and grows upon annealing, while the sharp matrix site at 2099.8 cm^{-1} overtakes the initially stronger band at 2097.4 cm^{-1}. The ^{15}N counterpart exhibits the same behavior upon irradiation and is located at 2027.6 and 2030.0 cm^{-1}, giving an isotopic frequency ratio of 1.0344 typical for N–N stretching modes. In the mixed $^{14}N_2$ and $^{15}N_2$ isotopic experiment the band at 2097.4 cm^{-1} is interfered by a stronger band associated with $Ir(^{14}N_2)(^{15}N_2)$. However, due to the sharp, distinctive band shape of the matrix site at 2099.8 cm^{-1} after annealing, the weaker $Ir(N_2)$ band clearly stands out (Figure 1 e). The spectrum does not show any band related to a scrambled $^{14}N/^{15}N$ species in the mixed $^{14}N_2+^{15}N_2$ experiment, thus, the characteristic doublet isotope pattern indicates a carrier bearing a single N_2 unit. The corresponding absorption in the argon matrix is red-shifted by 9.8 cm^{-1} relative to neon and the same isotopic ratio is found (Figure S1). Due to the formation of the higher coordinated species $Ir(N_2)_2$, the intensity of the $Ir(N_2)$ absorption band decreases with increasing amount of N_2 and is absent in the neat dinitrogen spectrum. The assignments are supported by harmonic frequency calculations at the DFT and CCSD(T) level of theory. In analogy with RhNN, DFT and CCSD(T) calculations on $Ir(N_2)$ result in a linear $C_{\infty v}$ point group symmetry (Figure 6) for the $^2\Delta$ electronic ground

 © 2020 The Authors. Published by Wiley-VCH Verlag GmbH & Co. KGaA, Weinheim

Chemistry–A European Journal | Full Paper doi.org/10.1002/chem.201905514 | Chemistry Europe European Chemical Societies Publishing

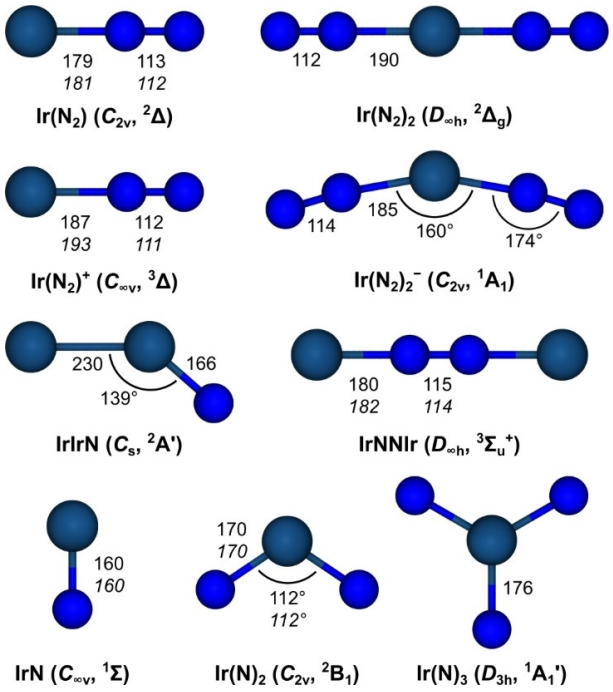

Figure 6. Structures, point group symmetries and electronic ground states calculated and optimized at the BP86/def2-QZVP (regular font) and CCSD(T)/aVTZ(-PP) (italic font) levels of theory.

Table 4. Selected reaction enthalpies for the formation of iridium nitrogen compounds calculated at the DFT BP86/def2-QZVP level of theory.

Reaction		ΔH [kJ mol^{-1}]
Ir + N_2	→Ir(N_2)	−168
Ir(N_2) + N_2	→Ir(N_2)$_2$	−174
Ir(N_2)$_2$ + N_2	→Ir(N_2)$_3$	−32
Ir(N_2)$_3$ + N_2	→Ir(N_2)$_4$	−15
2 IrN	→IrNNIr	−96
Ir(N_2) + Ir	→IrNNIr	−169
Ir + N	→IrN	−612
IrN + N	→Ir(N_2)	−350
Ir(N_2) + N	→Ir(N_3)	−243
Ir(N_2)	→Ir + N_2	−20
Ir(N_3)	→IrN + N_2	−388
2 Ir	→IrIr	−422
IrIr + N	→IrIrN	−508
Ir(N_3)	→Ir(N_3) TS	44[a]/41[b]
Ir(N_3) TS	→Ir(N)(N_2)	−460[a]
Ir(N_2)	→Ir(N_2) TS	244[a]/247[b]
Ir(N_2) TS	→Ir(N_2)	−375[a]

[a] BP86/ZORA-def2-TZVPP(N)/SARC-ZORA-TZVPP(Ir). [b] M06-L/ZORA-def2-TZVPP(N)/SARC-ZORA-TZVPP(Ir).

state bearing an unpaired electron in an iridium centered degenerate δ molecular orbital, originating from $d_{x^2-y^2}$ and d_{xy} iridium atomic orbitals. The lowest quartet state (^{4}A′) is 104 kJ mol^{-1} higher in energy (Table S1). The deviations between the experimental N_2 band position of Ir(N_2) embedded in Ne and the computed values are 22 and 43 cm^{-1} for DFT and CCSD(T), respectively. The larger deviation of the superior CCSD(T) method is due to the fact that no harmonic contributions are considered, while the apparently better DFT value benefits from fortunate error cancelation. The NN stretching isotopic ratios $\tilde{\nu}(^{14}N^{14}N)/\tilde{\nu}(^{15}N^{15}N)$ obtained by both, the DFT and CCSD(T) levels of theory are 1.0350, which is in good agreement with the experimental value of 1.0343.

Ir(N_2)$^+$

The N–N stretching band of the cationic species Ir(N_2)$^+$ appeared red-shifted by 172 at 2270.3 cm^{-1} and is observed in all experiments using N_2/Ne mixtures as well as in neat N_2, in which the band is blue-shifted by 1.0 cm^{-1} (Figure 1). Selective irradiations using LED light sources of $\lambda = 656$, 455, 405 and 365 nm did not affect the absorption intensity. However, full arc irradiation depleted, and annealing of the dinitrogen matrix to 30 K, destroyed the band entirely. The N–N stretch of the Ir($^{15}N_2$)$^+$ isotopologue is located at 2194.8 cm^{-1}, resulting in an isotopic ratio of 1.0344, typical for modes involving two nitrogen atoms. As for the neutral species, no additional bands could be assigned to this species in the 1:1 $^{14}N_2/^{15}N_2$ mixed isotope experiment, implying the presence of a single dinitrogen unit. Computational results at the DFT and CCSD(T) levels of theory support the assignment further. The calculated harmonic frequencies are at 2212 and 2286 cm^{-1}, respectively. For [Ir(N_2)]$^+$ a $^3\Delta$ electronic ground state was found with one electron removed from a non-bonding σ type molecular orbital. Compared to the neutral species the electronic ground state of the cation was computed to be 848 kJ mol^{-1} higher in energy.

Ir(N_2)$_2$

The band centered at 2154.0 cm^{-1} with a matrix site at 2158.0 cm^{-1} obtained in solid neon doped with 0.5% $^{14}N_2$ and shown in Figure 2 remained unaffected by annealing but decreased dramatically upon irradiation with LED light of $\lambda =$ 455 nm. Annealing after photolysis increased the intensity of the initially weaker matrix site at 2158.0 cm^{-1}. The ^{15}N counterparts at 2082.4 and 2086.1 cm^{-1} result in an isotopic ratio of 1.0344. Increasing the amount of N_2 in the solid Ne matrices strongly increases the intensity of the band and it is red-shifted by 4.0 cm^{-1} in neat N_2 (Figure 2). The mixed $^{14}N_2$ and $^{15}N_2$ spectrum displays a characteristic pattern for linear Ir(N_2)$_2$ consisting of the three antisymmetric N–N stretching modes of ($^{14}N_2$)Ir($^{14}N_2$), ($^{14}N_2$)Ir($^{15}N_2$) and ($^{15}N_2$)Ir($^{15}N_2$) at 2154.0, 2100.3 and 2082.4 cm^{-1}, respectively. Additionally, the symmetric N–N stretching mode of the ($^{14}N_2$)Ir($^{15}N_2$) species becomes IR active due to lower point group symmetry $C_{\infty v}$ and is found at 2194.6 cm^{-1}. Figure 1 f shows the ^{14}N/^{15}N isotope pattern of Ir(N_2)$_2$ arising from a 1:1 mixture of $^{14}N_2$ and $^{14}N_2$ (10% in Ne), shown in a difference spectrum obtained by subtracting the spectra after and prior to selective photolysis with LED light of $\lambda = 455$ nm. In the FIR spectrum shown in Figure S3 a 1:2:1 triplet $^{14/15}N_2$ isotope pattern of Ir(N_2)$_2$ was also observed at 402.8, 397.4 and 393.1 cm^{-1} originating from a 1:1 mixture of $^{14}N_2$ and $^{14}N_2$ in solid neon which results in an isotopic ratio

 © 2020 The Authors. Published by Wiley-VCH Verlag GmbH & Co. KGaA, Weinheim

Chemistry–A European Journal | Full Paper doi.org/10.1002/chem.201905514 | Chemistry Europe European Chemical Societies Publishing

of 1.0247. Comparing our assignments to the frequencies calculated at the DFT level of theory there is a very good agreement for the antisymmetric N–N stretching mode at 2149 cm^{-1} and an isotopic ratio of 1.0349. The symmetric N–N stretching mode in $Ir(^{14}N_2)(^{15}N_2)$ is calculated to be centered at 2182 cm^{-1} and the position of the antisymmetric Ir–N stretching mode at 439 cm^{-1}, leading to an isotopic ratio of 1.0267. In analogy to the $Ir(N_2)$ complex, DFT and CCSD(T) calculations on $Ir(N_2)_2$ find a $^2\Delta_g$ ground state ($D_{\infty h}$ point group symmetry) having an unpaired electron located in a degenerate δ_g molecular orbital. The HOMO→LUMO ($1\delta_g \rightarrow 2\pi_u$) excitation gives rise to the lowest quartet state $^4\Pi_u$, which is 246 kJ mol^{-1} higher in energy than the electronic ground state.

$Ir(N_2)_2^-$

A strong band observed at 1955.8 cm^{-1} in neat $^{14}N_2$ shown in Figures 2 and S7 decreases completely on annealing and is unaffected by broadband irradiation. The corresponding absorption in solid neon doped with 10% $^{14}N_2$ at 1956.4 cm^{-1} lead to a related ^{15}N isotopologue absorption at 1890.3 cm^{-1} (Figure S7). Together with a stronger band at 1912.9 and a weak band at 1988.1 cm^{-1} which appeared in the 1:1 $^{14}N_2/^{15}N_2$ spectrum a $^{14/15}N$ isotope pattern similar to that of $Ir(N_2)_2$ is observed. Therefore, the band is assigned to the anionic complex $Ir(N_2)_2^-$. The assignment is supported by DFT calculations, which predict a $^1A_1$ singlet ground state of C_{2v} point group symmetry and infrared absorptions at 1988, 1940 and 1921 cm^{-1} for the antisymmetric N–N stretching modes of $Ir(^{14}N_2)(^{14}N_2)^-$, $Ir(^{14}N_2)(^{15}N_2)^-$ and $Ir(^{15}N_2)(^{15}N_2)^-$. The experimental and calculated isotopic ratios are 1.0344 (in neat N_2), 1.0350 (in solid Ne) and 1.0349 (DFT calc.) and are in very good agreement for the less interacting neon matrix. For a bent structure of $Ir(NN)_2^-$ and unlike the case of a linear $Ir(N_2)_2$, the symmetric N–N stretching mode is IR active. However, this band is not observed in the experiment, probably because of its low intensity, which is calculated to be 50 times lower than that of the antisymmetric mode. In the $Ir(^{14}N_2)(^{15}N_2)^-$ isotopologue the intensity ratio of the symmetric and antisymmetric modes change to 1:4, and hence, the symmetric N–N stretching combination can be observed at 2031 cm^{-1} in the neat 1:1 $^{14}N_2/^{15}N_2$ spectrum. Compared to the neutral complex the anion $Ir(NN)_2^-$ is 224 kJ mol^{-1} lower in energy at the DFT level of theory, which corresponds to the adiabatic electron affinity of $Ir(N_2)_2$.

IrNNIr

Laser-ablated iridium atoms co-deposited with 10% $^{14}N_2$ in neon give raise to a band at 786.5 cm^{-1} which is unaffected by annealing to 12 K and vanishes after 10 min of irradiation with $\lambda = 455$ nm (Figure 4). The same response was observed for a band at 761.6 cm^{-1} under the same conditions using $^{15}N_2$. The isotopic triplet observed at 786.5, 774.1 and 761.6 cm^{-1} in a 1:1 mixture of $^{14}N_2$ and $^{15}N_2$ indicates an Ir–N stretching mode involving two equivalent nitrogen atoms. The intensity pattern of 1:2:1 suggests the presence of the isotopologue containing both isotopes, ^{14}N and ^{15}N Based on the very good agreement of the band positions, isotopic pattern and isotopic ratio of the antisymmetric Ir–N stretching mode obtained by our quantum-chemical calculations, the band was assigned to IrNNIr. This dimer could probably be formed by an oxidative coupling of two IrN molecules (Equation 1):

$$2\ IrN \rightarrow IrNNIr \qquad \Delta H = -96\ kJ\ mol^{-1} \qquad (1)$$

The observed isotopic ratios in solid neon and solid dinitrogen are 1.0327 and 1.0331, which are in very good agreement with the calculated DFT value of 1.0324. The calculated absorptions are 782, 769 and 757 cm^{-1} for the $Ir^{14}N^{14}NIr$, $Ir^{14}N^{15}NIr$ and $Ir^{15}N^{15}NIr$ isotopologues, respectively. The electronic ground state is found to be a triplet $^3\Sigma_u^+$, with the two unpaired electrons located at each of the metal centers in degenerated molecular orbitals of $d_{x^2-y^2}$- and d_{xy}-character, reminiscent of the $Ir(N_2)$ complex. The N–N stretching mode is IR inactive and calculated to be centered at 2081 cm^{-1} at the DFT level of theory.

IrN

A very weak band at 1102.8 cm^{-1} which was not observed in the initially formed solid $^{14}N_2$ deposit but grew in upon annealing to 35 K and was destroyed by broadband irradiation, returned on subsequent annealing to 35 K (Figure 4). The corresponding absorption in $^{14}N_2$ doped neon is blue-shifted to 1111.1 cm^{-1} and the ^{15}N counterparts were found at 1076.4 and 1066.9 cm^{-1} in neon and $^{15}N_2$, respectively, while no band due to a mixed $^{14/15}N$ isotopologue occurred in experiments using a 1:1 mixture of $^{14}N_2$ and $^{15}N_2$ (Figure 5). The assignment of this band to IrN is supported by a previous Fourier transform emission spectroscopic study of Ram and Bernath,[15a] in which a ground-state fundamental Ir-N stretching frequency of 1113.6 cm^{-1} for $^{193}Ir^{14}N$ was reported, revealing reasonable matrix shifts of −2.5 and −10.8 cm^{-1} for neon and solid dinitrogen. For the sake of completeness, DFT and CCSD(T) calculations were carried out and the results are listed in Table S1. The annealing behavior of IrN suggests a temperature induced mobility of N radicals reacting with iridium atoms to IrN ($\Delta H = -612$ kJ mol^{-1}).

IrIrN

An intense band at 1002.2 cm^{-1} in solid $^{14}N_2$ matrices and their ^{15}N counterparts at 970.7 cm^{-1} grow in upon annealing to 35 K and remains unaffected by broadband irradiation (Figure 4). The much weaker bands located at 1004.4 and 972.8 cm^{-1} in solid neon doped with 10% N_2 depicted in Figure 3 show the same behavior and in experiments using a $^{14}N_2/^{15}N_2$ mixture no additional band due to a mixed $^{14/15}N$ isotopologue occurred, suggesting an Ir–N stretching mode with a single nitrogen atom involved. With IrN already assigned to a band centered about 100 cm^{-1} blue-shifted, the carrier of this unknown band could be $Ir(N)(N_2)$, a dinitrogen complex of IrN, or IrIrN. Calculations at the DFT level of theory predict a fairly strong N≡N stretching mode for $Ir(N)(N_2)$ at 2110 cm^{-1}, much higher than

 © 2020 The Authors. Published by Wiley-VCH Verlag GmbH & Co. KGaA, Weinheim

Chemistry–A European Journal | Full Paper doi.org/10.1002/chem.201905514 | Chemistry Europe European Chemical Societies Publishing

the Ir≡N stretching mode at 1085 cm^{-1}, however, no such N≡N band could be identified in the spectrum and hence, ruled out an assignment to Ir(N)(N_2). On the other side, infrared absorptions computed at the DFT level of theory support the assignment of the band at 1004.4 in solid neon to IrIrN, with calculated harmonic frequencies of 1054 and 1021 cm^{-1} for Ir^{14}N and Ir^{15}N, respectively, accounting for an isotopic ratio of 1.0323, which is very close to the experimental ones of 1.0325 in solid dinitrogen and neon. In analogy to IrN, the observed behavior upon annealing suggests a formation by mobilizing nitrogen radicals which react with Ir_2 units present in the matrix. This is further supported by a computed reaction enthalpy for the formation of IrIrN from N atoms and the iridium dimer obtained at the DFT level of theory of $\Delta H = -508\ kJ\,mol^{-1}$ (Table 4). The electronic ground state of the bent IrIrN structure in the C_s point group symmetry is a doublet $^2A'$ state.

Ir(N)$_2$

A very weak band, located at 853.5 cm^{-1} in solid neon doped with 0.5% $^{14}N_2$ and unaffected by broadband irradiations, presents a doublet pattern in neon doped with 0.5% of a 1:1 mixture of $^{14}N_2$ and $^{15}N_2$ at 853.5 and 827.7 cm^{-1} (Figure 3). The picture changes when pure dinitrogen is used as matrix host: besides a slight blue-shift of these bands to 857.1 and 831.2 cm^{-1}, an intermediate band at 842.6 cm^{-1} appears, yielding a triplet pattern with an intensity ratio of about 1:2:1 (Figure 5). The observed triplet pattern is consistent with the involvement of two equivalent nitrogen atoms in an antisymmetric Ir–N stretching mode, such as in iridium dinitride, Ir(N)$_2$. This assignment is supported by the fact that the intermediate band belonging to the ^{14}NIr^{15}N isotopologue is red-shifted 1.6 cm^{-1} from the center, indicating a coupling between the symmetric and the anti-symmetric Ir–N stretching modes, which in the lower point group symmetry C_s have the same a′ symmetry. The different patterns observed in solid neon and pure dinitrogen matrices can be explained by different reaction mechanisms leading to Ir(N)$_2$: While a direct insertion of iridium atoms into a dinitrogen bond is proposed in nitrogen doped neon mixtures (Equation 2a), the reaction of IrN with N atoms preferentially occurred in solid dinitrogen matrices (Equation 2b).

$$Ir + N_2 \rightarrow Ir(N)_2 \qquad \Delta H = +20\ kJ\,mol^{-1} \qquad (2a)$$

$$IrN + N \rightarrow Ir(N)_2 \qquad \Delta H = -612\ kJ\,mol^{-1} \qquad (2b)$$

While the reaction enthalpy of the direct insertion is slightly positive on the DFT level of theory, the high temperature of laser ablated iridium atoms can overcome this barrier and cryogenic conditions prevent the spontaneous elimination of a N_2 unit. In contrast to osmium, spontaneous insertion into the NN triple bond at cryogenic conditions is not observed.[4] Harmonic frequencies obtained by calculations on the DFT level of theory are in very good agreement, resulting in antisymmetric b_2 stretching frequencies of 869, 853 and 842 cm^{-1} for Ir(^{14}N)$_2$, Ir(^{14}N)(^{15}N) and Ir(^{15}N)$_2$. The symmetric a_1 Ir–^{14}N stretching mode was not observed and calculated to be located at 1027 cm^{-1} having an intensity less than 4% of the antisymmetric one. From the band positions of the antisymmetric stretching modes in the isotope substitution experiment an estimate of the upper limit of the N-Ir-N bond angle can be estimated to 130°,[34] which is in agreement with the calculated angle of 112° for the C_{2v} ($^2B_1$) electronic ground state geometry.

Ir(N)$_3$

No band could be assigned to iridium trinitride, although we observed nitrogen atom mobility in the formation of Ir(N)$_2$, and the third addition of a nitrogen atom was calculated to be exothermic ($\Delta H = -243\ kJ\,mol^{-1}$, Table 4). However, Table S1 shows that the integrated intensity of the IR active Ir–N stretching absorption in the observable region, the degenerate e′ mode, is calculated to be 1.4 $km\,mol^{-1}$, which is about 3% of the calculated integrated intensity of the corresponding very weak band assigned to Ir(N)$_2$. The amount of iridium trinitride formed according to that mechanism would certainly be very low.

Bonding considerations

Dinitrogen complexes of iridium

The nature of the metal nitrogen bond in selected product molecules and in Ir(N)$_3$ will be discussed in terms of the relevant vibrational stretching modes as well as by analysis of the wavefunctions obtained at the BP86/def2-QZVP level of theory. The coordination chemistry of the dinitrogen molecule is limited because it is a comparatively poor σ-donor, weak π-acceptor and its lack of dipole moment.[35] The π-donation of the iridium center into the π* molecular orbitals of the dinitrogen unit results in a weakening, or activation of the dinitrogen triple bond. The weakening of the N–N bond in dinitrogen complexes can be quantified experimentally by the red-shift of the N–N stretching mode in the IR spectrum, comparing the N–N bond distances and, theoretically, by extracting information from the wavefunction. Several neutral PGM dinitrogen complexes have previously been studied by matrix isolation spectroscopy.[4–8] Their experimental N–N stretching frequencies embedded in argon are given in Table S2 and provide a solid basis for discussing the nature of bonding in such homoleptic dinitrogen complexes. The red-shift of the N–N stretching mode of Ir(N$_2$) relative to that in free dinitrogen (2327.1 cm^{-1}, Table 3) is 240.3 cm^{-1}, which is less than the one for the group 8 metal dinitride Os(N$_2$) and greater than that for the group 10 analogue Pt(N$_2$). This trend is consistent with a decreasing ability of late transition metals to donate electron density into the π* orbitals of the coordinated N_2 moiety due to less MO overlap caused by larger bond distances and decreasing d-orbital energies. The same trend is observed with the corresponding first row transition metals.[1a]

The electron density at the bond critical point (ρ_b) in a molecule can be taken as measure of the character of a bond and its bond order.[36] The data presented in Table S3 shows a sig-

 © 2020 The Authors. Published by Wiley-VCH Verlag GmbH & Co. KGaA, Weinheim

Chemistry–A European Journal | Full Paper doi.org/10.1002/chem.201905514 | Chemistry Europe European Chemical Societies Publishing

nificant decrease of ρ_b(NN) going from Ir(N_2) (0.622) over Ir(N_2)$_2$ (0.592) down to IrNNIr (0.579), indicating a weakening of the corresponding N–N bond of the dinitrogen ligand within this series. This is also evident in the minimum structures shown in Figure 6, where the longest N–N bond lengths within this series of 115 pm is exhibited in the binuclear complex IrNNIr. In contrast to the electron density at the bond critical point (ρ_b), which seems to be mainly affected by σ donation from the N_2 ligand to the iridium center, the slightly longer N–N bond length in Ir(N_2) (113 pm) compared to Ir(N_2)$_2$ (112 pm), is consistent with an increasing experimental N–N stretching frequency from Ir(N_2) (2087.6 cm^{-1}) to Ir(N_2)$_2$ (2144.7 cm^{-1}), and can most likely be rationalized by a stronger π backdonation from the iridium center to the N_2 ligand bonding in the Ir(N_2) complex. Weakly activated N–N bond lengths are typically less than 112 pm,[35] placing Ir(N_2) and Ir(N_2)$_2$ at the upper end of the scale for what is considered weakly activated. The slightly stronger N_2 activation in Ir(N_2) compared to Ir(N_2)$_2$ is also supported by an NBO analysis, which results in NPA bond orders for the N–N bonds in Ir(N_2), Ir(N_2)$_2$, and IrNNIr of 2.56, 2.64 and 2.51, respectively, as well as by the shorter calculated Ir–N bond distance in Ir(N_2) of 179 pm compared to 190 pm in Ir(N_2)$_2$ (Table S3).

Comparing the N–N stretching modes of the ions [Ir(N_2)]$^+$ and [Ir(N_2)$_2$]$^-$ with those of their neutral counterparts, a blue-shift for the cation and a red-shift for the anion is observed, which is consistent with the calculated changes in the corresponding N–N bond lengths (Table S3, Figure 6) and with the notion that oxidation of the metal center leads to a lower ability of π-back-donation, while reduction leads to an increase.[2c] In both cases, the addition or subtraction of an electron does not change the occupation number of the π-system, but leads to an oxidation or reduction of the iridium center. Compared to a shift for the C–O stretching frequency in Ir(CO)$^+$ and Ir(CO)$_2^-$ with respect to neutral Ir(CO) of +132 and −29 cm^{-1}, respectively,[37] the frequency shift for the isoelectronic dinitrogen complexes is with +170 and −198 cm^{-1} significantly larger. The higher sensitivity of the N–N stretching frequency upon oxidation or reduction of the metal center compared to the C–O frequency is another indication for the importance of π-back-bonding as the most significant contribution to the Ir–N bond strength.[2c] On the other side, the red-shift of the N–N and C–O stretching frequencies in the neutral Ir(N_2) and Ir(CO) complexes with respect to the free ligands is with 170 cm^{-1} (9.8%) higher in Ir(N_2) compared to 132 cm^{-1} (5.4%) in Ir(CO). As pointed out by Pelikán and Boča,[2c] the larger red-shift for the N–N stretch does not indicate a stronger π-back-donation in the Ir(N_2) complex, since both interactions, σ-donation and π-acceptance lead to a weakening of the N–N bond, while in the Ir(CO) complex σ-donation leads to an increase and π back-donation to a decrease in the C–O bond strength. Taking the better σ-donor ability of CO compared to NN into account,[38] CO must be considered a stronger π-acceptor than the N_2 ligand.

In Figure 7 the frontier molecular orbitals of the π-system are shown for the neutral, linear dinitrogen complexes Ir(N_2), Ir(N_2)$_2$, and IrNNIr. Each of them is comprised of the degenerate

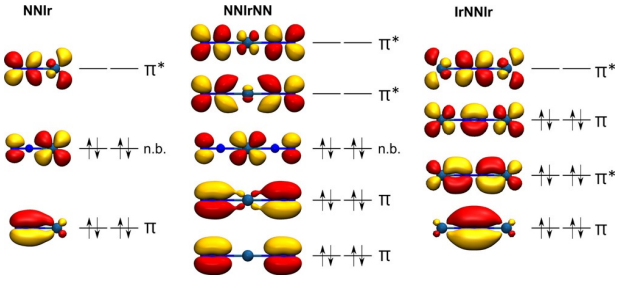

Figure 7. Ir(N_2), IrNNIr and Ir(N_2)$_2$ Kohn–Sham molecular orbitals of their π-system with an iso surface value of 0.04 $Å^{-1}$ obtained at the BP86/def2-QZVP level of theory.

2p_y and 2p_z atomic orbitals of the nitrogen atoms and the 3d_{xy} and 3d_{xz} atomic orbitals of the iridium atoms involved. For IrNNIr with 12 π-electrons the first three of four pairs of the molecular π-orbitals are fully occupied (Figure 7, right). The first pair essentially forms the π-bonds of the NN unit, the second pair contains the corresponding N–N anti-bonding molecular orbitals of the first set, and the third pair of the π-bonding orbitals are Ir–N anti-bonding and N–N bonding. The electronic ground state of $^3\Sigma_u^+$ arises from two unpaired electrons residing in non-bonding molecular orbitals, essentially formed by the non-bonding iridium 3d_{yz} atomic orbitals (not shown in Figure 7). From isotopic triplet observed in a 1:1 mixture of $^{14}N_2$ and $^{15}N_2$ for the Ir–N stretching vibration in the IR spectrum it has been concluded that IrNNIr is likely formed during matrix deposition by the coupling of two IrN units. A very similar behavior was reported for the [N_2{Ir(PNP)}$_2$] (PNP = N(CHCHP*t*Bu$_2$)$_2$) pincer complex, holding the same 12 electron IrNNIr π-system, which was observed to be formed in solution at room temperature by coupling of two terminal [IrN(PNP)] nitrido complexes.[1c] This coupling reaction can be viewed as the reverse of splitting a bridging dinitrogen ligand into separate nitrido complexes, which recently was investigated for [NIr(PNP)]$_2^{n+}$ (n = 0, 1, 2).[39] For these complexes reaction enthalpies of the coupling reaction of 2[NIr(PNP)]$^{n+}$, with $2n$ = 0, 1, and 2, are exotherm and calculated to ΔH = −510, −425 and −382 kJ mol^{-1} (D3BJ-PBE0(Cosmo (THF))/def2-TZVP//D3BJ-PBE0/def2-SVP) respectively.[39] In contrast to these results coupling of two IrN complexes, bare of any additional ligands and under solvent-free conditions in an argon matrix, is significantly less exothermic with ΔH = −96 kJ mol^{-1}. The lower reaction enthalpy for the latter coupling reaction can be explained by the formation of two strong triple bonds in the Ir≡N units.

Nitrido complexes of iridium

The diatomic iridium nitride, IrN, was investigated extensively using emission[14,15a,b] and optical Zeeman[15e] spectroscopy as well as high level ab initio methods.[15b] It has a closed shell $^1\Sigma^+$ ground state comprising an Ir≡N triple bond. Our AIM analysis assign charges of 0.278 to iridium and −0.278 to nitrogen (Table S3), while NBO analysis shows NPA charges of −0.032 and 0.032 for iridium and nitrogen, respectively, and

 © 2020 The Authors. Published by Wiley-VCH Verlag GmbH & Co. KGaA, Weinheim

Chemistry–A European Journal | Full Paper doi.org/10.1002/chem.201905514 | Chemistry Europe European Chemical Societies Publishing

an NPA bond order of 2.82. The NPA charge close to zero and the low AIM charges imply that the bond nature is mostly covalent.

The calculated Ir–N bond lengths of iridium dinitride, $Ir(N)_2$, in its $^2B_1$ electronic ground state of 170 pm is considerably larger than the expected ones for a triple bond judged on the calculated bond lengths in iridium mononitride of 160 pm, which also corresponds well to the sum of the triple-bond covalent radii of iridium and nitrogen of 160 pm.[40] From the sum of reported double-[41] and triple-bond covalent radii of iridium and nitrogen of 160 and 175 pm, respectively, the bond order in $Ir(N)_2$ can be estimated to be between a triple and a double bond, while the computed NPA bond order is 2.06. The NPA (AIM) charges are significantly higher compared to diatomic Ir≡N, amounting to 0.588 (0.896) and −0.294 (−0.448) for iridium and nitrogen, respectively. The higher charges and lower covalent bond order of the dinitride compared to the mononitride suggest an Ir=N double bond in the former one, which is shortened due to a higher ionic character. The valence molecular orbitals and occupation numbers obtained from SA-CASSCF(15,12)/cc-pVTZ(-PP) calculations (for details see Computational Details) for the $^2B_1$ electronic ground state are depicted in Figure S4. These calculations reveal a lone pair ($5a_1$) at the iridium center, two σ-bonding orbitals ($6a_1$ and $4b_2$), two π-bonding orbitals ($2b_1$ and $1a_2$), and their anti-bonding σ* ($8a_1$ and $6b_2$) and π* counterparts ($3b_1$ and $2a_2$). We note that one unpaired electron resides in the $3b_1$ π* orbital. Additionally, two essentially doubly occupied non-bonding orbitals ($7a_1$ and $5b_2$) remain at the nitrogen ligands, and finally, there is a high-lying, low-occupied non-bonding orbital ($9a_1$) with contributions from the Ir(6s), Ir($5d_{x^2-y^2}$), Ir($6p_z$) and N($2p_z$) atomic orbitals (Figure S4). An effective bond order (EBO) of 1.56 can be estimated for the Ir–N bond by counting the occupation numbers of the bonding- and anti-bonding molecular orbitals, neglecting the slightly bonding characters of the nonbonding orbitals $7a_1$ and $5b_2$. For the $^2B_1$ electronic ground state the presence of nitrogen-centered unpaired electrons can be ruled out, however, an estimation of low-lying electronic states using SA-CASSCF(15,12)/cc-pVTZ(-PP) calculations show that the lowest lying quartet state is 84 kJ mol^{-1} and the lowest lying sextet state 252 kJ mol^{-1} higher in energy than the electronic ground state (Figure S5 and Table S4). The most dominant configuration of the electronic ground state is $a_1^6\ b_1^3\ b_2^4\ a_2^2$ with a weight of 0.86 (74%). Other contributions are small and distributed over the whole expansion space. This electron configuration can be described by the resonance Lewis structure shown in Scheme 1, in which an integral formal oxidation state cannot be assigned to the iridium center a priori.

If we resort to MO theory and wavefunction analysis, spin populations can give insight into which extend the unpaired electron is localized either on iridium, or at the nitrido ligands. Mulliken and Loewdin population analysis yield spin populations of 0.40 and 0.47 at the iridium center, which means the ligands do not allow the definition of a clear-cut integral oxidation state. The formal oxidation state lies between +V and +VI, with slightly more weight on the side of +V. The nitrido ligands must be considered as non-innocent.[42]

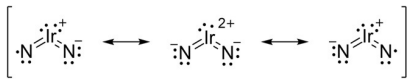

Scheme 1. Lewis structure for the homoleptic diinitrido iridium.

Iridium trinitride is an intriguing compound since iridium would formally be considered in the oxidation state +IX, which so far was experimentally realized only for the cation $[IrO_4]^+$, and more recently claimed for the experimentally unknown nitrido compound $NIrO_3$. Another candidate for the oxidation state +IX could be $Ir(N)_3$, provided that all 5d electrons from the valence shell of iridium can be formally assigned to the nitrogen ligands and no lone pair remains on the iridium atom. We have investigated $Ir(N)_3$ at the BP86/def2-QZVP level of theory and found a regular D_{3h} structure with an Ir–N bond length of 176 pm in the $^1A_1'$ ground electronic state (Figure 6). We have further analyzed the occupied molecular orbitals at the R-BP86/ZORA-def2-TZVPP(N)/SARC-ZORA-TZVPP(Ir) level of theory and depicted the valence molecular orbitals in Figure S6. These calculation reveals a degenerate pair of σ-bonding orbitals (4e′) as well as a degenerate pair of π-bonding orbitals (1e″). In addition, seven ligand-centered lone pairs ($4a_1'$, $2a_2''$, 2×5e′, MO's arising from the N(2s) orbitals are not shown in Figure S6) can be assigned and a metal centered d-orbital is attributed to the highest occupied MO (HOMO, $5a_1'$). We note that the lowest unoccupied MO (LUMO, $1a_2'$) is a nonbonding ligand-centered MO. Thus, our analysis shows that the nitrido ligands in $Ir(N)_3$ behave as non-innocent ligands as well,[42] meaning that an essentially non-bonding iridium (d_{z^2}) orbital ($5a_1'$) is filled by two electrons at the expense of a ligand delocalized nonbonding LUMO ($1a_2'$). This bonding situation, which is consistent with a formal oxidation state of +VII rather than +IX for the iridium atom in $Ir(N)_3$, can be approximately described by the resonance Lewis structures shown in Scheme 2.

This electronic description is supported by the calculated AIM and NPA charges shown in Table S3. While the nitrogen atoms in $Ir(N)_3$ adopt a charge, which is very close to the one found in $Ir(N)_2$, the charge at the iridium center raised to about 3/2 of those in $Ir(N)_2$.

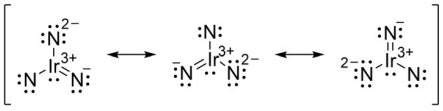

Scheme 2. Lewis resonance structure for the homoleptic trinitrido iridium(VII) complex $Ir(N)_3$.

The most favored decomposition pathway for doublet $Ir(N)_2$ and singlet $Ir(N)_3$ is found to be the elimination of dinitrogen, which is exothermic by $\Delta H = -20$ and -388 kJ mol^{-1} for $Ir(N)_2$ and $Ir(N)_3$, respectively. According to our all-electron R-BP86/ZORA-def2-TZVPP(N)/SARC-ZORA-TZVPP(Ir) calculation the lowest energy pathway for dinitrogen elimination proceed by cleavage of an Ir–N bond and formation a dinitrogen complex (Figure 8). The nitrido complexes are separated from their dini-

 © 2020 The Authors. Published by Wiley-VCH Verlag GmbH & Co. KGaA, Weinheim

Chemistry–A European Journal | Full Paper doi.org/10.1002/chem.201905514 | Chemistry Europe European Chemical Societies Publishing

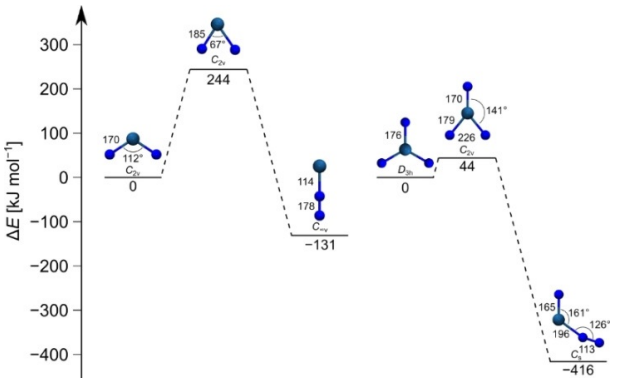

Figure 8. Stationary points on the doublet (singlet) potential energy surface of the decomposition pathways of $Ir(N)_2$ ($Ir(N)_3$) leading to elimination and complexation of N_2 calculated at the BP86/ZORA-def2-TZVPP(N)/SARC-ZORA-TZVPP(Ir) level of theory.

trogen coordinated isomers by a barrier of 244 and 44 kJ mol^{-1} for $Ir(N)_2$ and $Ir(N)_3$, respectively. The corresponding transition states on the quartet and triplet surfaces of $Ir(N)_2$ and $Ir(N)_3$, respectively, have also been investigated, and found to be higher in energy with 257 and 114 kJ mol^{-1} above the respective minimum structures. According to these results the kinetic stability with respect to dinitrogen elimination of $Ir(N)_3$ is rather low, while $Ir(N)_2$ is kinetically stable and the isomeric dinitrogen complex $Ir(N_2)$ has indeed been detected in the present study.

Conclusions

Laser-ablated iridium atoms were allowed to react with dinitrogen and nitrogen atoms formed from N_2 molecules by plasma radiation and the products were isolated in solid neon, argon and nitrogen matrices and identified by their infrared spectra. The assignments are supported by ab initio and first principle calculations as well as $^{14/15}N$ isotope substitution experiments. The neutral and ionic iridium dinitrogen complexes $Ir(N_2)$, $Ir(N_2)^+$, $Ir(N_2)_2$, $Ir(N_2)_2^-$, IrNNIr were formed and assigned by their characteristic *N*-N stretching frequencies at 2097.4, 2270.3, 2154.0, 1956.4 and 786.5 cm^{-1}, respectively. In addition, the nitrido complexes IrN, $Ir(N)_2$ and IrIrN were observed and assigned to Ir–N stretching bands centered at 1111.1, 853.5 and 1004.4 cm^{-1}, respectively. While $Ir(N)_2$ can be formed by a photo-rearrangement of the corresponding dinitrogen complex $Ir(N_2)$ or from N atoms and IrN, the latter process was deduced from $^{14/15}N$ isotopic experiments. The threefold coordinated iridium trinitride complex $Ir(N)_3$ was not be observed. The structural and electronic properties of the dinitrogen ligand in the N_2 complexes are discussed with respect to dinitrogen activation upon complexation. The largest dinitrogen activation was observed in the neutral, linear binuclear IrNNIr complex and in the anionic $Ir(N_2)_2^-$. Also, the electronic structures of the nitrido complexes $Ir(N)_2$ and $Ir(N)_3$ were investigated by DFT and ab initio calculations. The dinitride $Ir(N)_2$ adopts a bent structure in a $^2B_1$ electronic ground state with one unpaired electron in a delocalized π^* molecular orbital ($3b_1$) and an additional lone pair on the iridium center. $Ir(N)_3$ has a D_{3h} structure in the lowest energy electronic state in which a lone pair can be attributed to a nonbonding iridium centered $5d_z2$ orbital ($5a_1'$) and a formal oxidation state for iridium of +VII rather than +IX can be deduced. The lowest energy decomposition pathway of these nitrido complexes has been found computationally to proceed via a rearrangement to the isomeric dinitrogen complexes.

Acknowledgements

Computing resources and support were granted by the Zentraleinrichtung für Datenverarbeitung (ZEDAT) of the Freie Universität Berlin. Furthermore, we thank the DFG (HA 5639/10) for financial support.

Conflict of interest

The authors declare no conflict of interest.

Keywords: density functional calculations · high oxidation states · matrix isolation · nitrogen fixation · transition metals

[1] a) H.-J. Himmel, M. Reiher, *Angew. Chem. Int. Ed.* **2006**, *45*, 6264–6288; *Angew. Chem.* **2006**, *118*, 6412–6437; b) Ł. Wolański, M. Domański, W. Grochala, P. Szarek, *Chem. Eur. J.* **2019**, *25*, 10290–10293; c) M. G. Scheibel, B. Askevold, F. W. Heinemann, E. J. Reijerse, B. de Bruin, S. Schneider, *Nat. Chem.* **2012**, *4*, 552–558.
[2] a) A. D. Allen, C. V. Senoff, *Chem. Commun. (London)* **1965**, 621; b) J. P. Collman, M. Kubota, F. D. Vastine, J. Y. Sun, J. W. Kang, *J. Am. Chem. Soc.* **1968**, *90*, 5430–5437; c) P. Pelikán, R. Boča, *Coord. Chem. Rev.* **1984**, *55*, 55–112.
[3] M.-A. Légaré, G. Bélanger-Chabot, R. D. Dewhurst, E. Welz, I. Krummenacher, B. Engels, H. Braunschweig, *Science* **2018**, *359*, 896–900.
[4] a) A. Citra, L. Andrews, *J. Am. Chem. Soc.* **1999**, *121*, 11567–11568; b) A. Citra, L. Andrews, *J. Phys. Chem. A* **2000**, *104*, 1152–1161.
[5] a) G. A. Ozin, A. V. Voet, *Can. J. Chem.* **1973**, *51*, 3332–3343; b) A. Citra, L. Andrews, *J. Phys. Chem. A* **1999**, *103*, 3410–3417; c) X. Wang, L. Andrews, *J. Phys. Chem. A* **2002**, *106*, 2457–2464.
[6] a) H. Huber, E. P. Kuendig, M. Moskovits, G. A. Ozin, *J. Am. Chem. Soc.* **1973**, *95*, 332–344; b) W. Klotzbuecher, G. A. Ozin, *J. Am. Chem. Soc.* **1975**, *97*, 2672–2675; c) W. Schrittenlacher, W. Schroeder, H. H. Rotermund, H. Wiggenhauser, R. Grinter, D. M. Kolb, *J. Chem. Phys.* **1986**, *85*, 1348–1354; d) G. A. Ozin, J. G. Prieto, *J. Phys. Chem.* **1988**, *92*, 325–337.
[7] M. Zhou, L. Andrews, *J. Phys. Chem. A* **1998**, *102*, 9061–9071.
[8] a) D. W. Green, J. Thomas, D. M. Gruen, *J. Chem. Phys.* **1973**, *58*, 5453–5463; b) E. P. Kündig, M. Moskovits, G. A. Ozin, *Can. J. Chem.* **1973**, *51*, 2710–2721; c) A. Citra, X. Wang, W. D. Bare, L. Andrews, *J. Phys. Chem. A* **2001**, *105*, 7799–7811.
[9] X. Wang, L. Andrews, R. Lindh, V. Veryazov, B. O. Roos, *J. Phys. Chem. A* **2008**, *112*, 8030–8037.
[10] a) C. K. Jørgensen, *Oxidation Numbers and Oxidation States*, Springer, New York, **1969**; b) S. Riedel, M. Kaupp, *Coord. Chem. Rev.* **2009**, *253*, 606–624; c) S. X. Hu, W. L. Li, J. B. Lu, J. L. Bao, H. S. Yu, D. G. Truhlar, J. K. Gibson, J. Marçalo, M. Zhou, S. Riedel, W. H. E. Schwarz, J. Li, *Angew. Chem. Int. Ed.* **2018**, *57*, 3242–3245; *Angew. Chem.* **2018**, *130*, 3297–3300.
[11] G. Wang, M. Zhou, J. T. Goettel, G. J. Schrobilgen, J. Su, J. Li, T. Schlöder, S. Riedel, *Nature* **2014**, *514*, 475–477.
[12] D. Himmel, C. Knapp, M. Patzschke, S. Riedel, *ChemPhysChem* **2010**, *11*, 865–869.
[13] a) H. C. Mattraw, N. J. Hawkins, D. R. Carpenter, W. W. Sabol, *J. Chem. Phys.* **1955**, *23*, 985–986; b) A. Citra, L. Andrews, *J. Phys. Chem. A* **1999**,

 © 2020 The Authors. Published by Wiley-VCH Verlag GmbH & Co. KGaA, Weinheim

Chemistry–A European Journal | Full Paper doi.org/10.1002/chem.201905514 | Chemistry Europe European Chemical Societies Publishing

103, 4182 – 4190; c) Y. Gong, M. Zhou, M. Kaupp, S. Riedel, *Angew. Chem. Int. Ed.* **2009**, *48*, 7879 – 7883; *Angew. Chem.* **2009**, *121*, 8019 – 8023.
[14] A. J. Marr, M. E. Flores, T. C. Steimle, *J. Chem. Phys.* **1996**, *104*, 8183 – 8196.
[15] a) R. S. Ram, P. F. Bernath, *J. Mol. Spectrosc.* **1999**, *193*, 363 – 375; b) R. S. Ram, J. Liévin, P. F. Bernath, *J. Mol. Spectrosc.* **1999**, *197*, 133 – 146; c) B. Hong, L. Cheng, M. Y. Wang, Z. J. Wu, *Mol. Phys.* **2010**, *108*, 25 – 33; d) H. F. Pang, A. S. C. Cheung, *Chin. J. Chem. Phys.* **2009**, *22*, 157 – 161; e) T. C. Steimle, A. J. Marr, S. A. Beaton, J. M. Brown, *J. Chem. Phys.* **1997**, *106*, 2073 – 2077.
[16] a) R. Yu, Q. Zhan, L. C. de Jonghe, *Angew. Chem. Int. Ed.* **2007**, *46*, 1136 – 1140; *Angew. Chem.* **2007**, *119*, 1154 – 1158; b) R. Yu, X. F. Zhang, *Phys. Rev. B* **2005**, *72*, 054103; c) Z.-j. Wu, E.-j. Zhao, H.-p. Xiang, X.-f. Hao, X.-j. Liu, J. Meng, *Phys. Rev. B* **2007**, *76*, 054115.
[17] a) J. C. Crowhurst, A. F. Goncharov, B. Sadigh, C. L. Evans, P. G. Morrall, J. L. Ferreira, A. J. Nelson, *Science* **2006**, *311*, 1275 – 1278; b) A. F. Young, C. Sanloup, E. Gregoryanz, S. Scandolo, R. J. Hemley, H.-k. Mao, *Phys. Rev. Lett.* **2006**, *96*, 155501.
[18] M. Wessel, R. Dronskowski, *J. Am. Chem. Soc.* **2010**, *132*, 2421 – 2429.
[19] TURBOMOLE GmbH, *TURBOMOLE V7.0.1*, **2015**.
[20] a) A. D. Becke, *Phys. Rev. A* **1988**, *38*, 3098 – 3100; b) J. P. Perdew, *Phys. Rev. B* **1986**, *33*, 8822 – 8824.
[21] a) F. Weigend, F. Furche, R. Ahlrichs, *J. Chem. Phys.* **2003**, *119*, 12753 – 12762; b) F. Weigend, R. Ahlrichs, *Phys. Chem. Chem. Phys.* **2005**, *7*, 3297 – 3305.
[22] D. Andrae, U. Huermann, M. Dolg, H. Stoll, H. Preu, *Theor. Chim. Acta* **1990**, *77*, 123 – 141.
[23] R. A. Kendall, T. H. Dunning, R. J. Harrison, *J. Chem. Phys.* **1992**, *96*, 6796 – 6806.
[24] D. Figgen, K. A. Peterson, M. Dolg, H. Stoll, *J. Chem. Phys.* **2009**, *130*, 164108.
[25] J. F. Stanton, J. Gauss, L. Cheng, M. E. Harding, D. A. Matthews, P. G. Szalay, CFOUR, Coupled-Cluster techniques for Computational Chemistry, a quantum-chemical program package.
[26] T. H. Dunning, *J. Chem. Phys.* **1989**, *90*, 1007 – 1023.
[27] H.-J. Werner, P. J. Knowles, G. Knizia, F. R. Manby, M. Schütz, P. Celani, W. Györffy, D. Kats, T. Korona, R. Lindh, A. Mitrushenkov, G. Rauhut, K. R. Shamasundar, T. B. Adler, R. D. Amos, S. J. Bennie, A. Bernhardsson, A. Berning, D. L. Cooper, M. J. O. Deegan, A. J. Dobbyn, F. Eckert, E. Goll, C. Hampel, A. Hesselmann, G. Hetzer, T. Hrenar, G. Jansen, C. Köppl, S. J. R. Lee, Y. Liu, A. W. Lloyd, Q. Ma, R. A. Mata, A. J. May, S. J. McNicholas, W. Meyer, T. F. Miller III, M. E. Mura, A. Nicklass, D. P. O'Neill, P. Palmieri, D. Peng, K. Pflüger, R. Pitzer, M. Reiher, T. Shiozaki, H. Stoll, A. J. Stone, R. Tarroni, T. Thorsteinsson, M. Wang, M. Welborn, MOLPRO, version 2019.1, a package of ab initio programs.
[28] a) E. van Lenthe, E. J. Baerends, J. G. Snijders, *J. Chem. Phys.* **1993**, *99*, 4597 – 4610; b) C. van Wüllen, *J. Chem. Phys.* **1998**, *109*, 392 – 399.
[29] D. A. Pantazis, X.-Y. Chen, C. R. Landis, F. Neese, *J. Chem. Theory Comput.* **2008**, *4*, 908 – 919.
[30] a) F. Neese, *WIREs Comput. Mol. Sci.* **2012**, *2*, 73 – 78; b) F. Neese, *WIREs Comput. Mol. Sci.* **2018**, *8*, e1327.
[31] Y. Zhao, D. G. Truhlar, *J. Chem. Phys.* **2006**, *125*, 194101.
[32] E. D. Glendening, J. K. Badenhoop, A. E. Reed, J. E. Carpenter, J. A. Bohmann, C. M. Morales, P. Karafiloglou, C. R. Landis, F. Weinhold, *NBO 7.0*; Theoretical Chemistry Institute, University of Wisconsin, Madison, WI, **2018**.
[33] T. Lu, F. Chen, *J. Comput. Chem.* **2012**, *33*, 580 – 592.
[34] M. Allavena, R. Rysnik, D. White, V. Calder, D. E. Mann, *J. Chem. Phys.* **1969**, *50*, 3399 – 3410.
[35] M. D. Fryzuk, S. A. Johnson, *Coord. Chem. Rev.* **2000**, *200 – 202*, 379 – 409.
[36] a) P. Popelier, *Atoms in Molecules: An introduction*, Prentice Hall, Harlow, **2000**; b) *The Chemical Bond* (Eds.: G. Frenking, S. Shaik), Wiley-VCH, Weinheim, **2014**.
[37] M. Zhou, L. Andrews, *J. Phys. Chem. A* **1999**, *103*, 7773 – 7784.
[38] H. H. Jaffé, M. Orchin, *Tetrahedron* **1960**, *10*, 212 – 214.
[39] J. Abbenseth, M. Finger, C. Würtele, M. Kasanmascheff, S. Schneider, *Inorg. Chem. Front.* **2016**, *3*, 469 – 477.
[40] P. Pyykkö, S. Riedel, M. Patzschke, *Chem. Eur. J.* **2005**, *11*, 3511 – 3520.
[41] P. Pyykkö, M. Atsumi, *Chem. Eur. J.* **2009**, *15*, 12770 – 12779.
[42] C. K. Jørgensen, *Coord. Chem. Rev.* **1966**, *1*, 164 – 178.

Manuscript received: December 6, 2019
Accepted manuscript online: January 17, 2020
Version of record online: April 30, 2020

 © 2020 The Authors. Published by Wiley-VCH Verlag GmbH & Co. KGaA, Weinheim

5. Conclusion and Outlook

5.1. Conclusion

The reaction products of laser-ablated late transition metals of groups 8 and 9 with NF_3 comprise the fluoroimido difluorides $FNMF_2$, M = Co, and Rh, the nitrido trifluorides NMF_3, M = Fe, Ru, Rh, Os, Ir, and the nitrido tetrafluorides NMF_4, M = Ru and Os. By reacting laser-ablated iridium atoms with N_2 the binary iridium nitrido complexes IrN and $Ir(N)_2$ along with the dinuclear IrIrN and dinitrogen complexes of iridium were obtained, while $Ir(N)_3$ was not observed. The product molecules embedded in solid inert gas matrices were characterized by IR spectroscopy, accompanied by thorough quantum-chemical calculations.

The unusual σ and π metal-nitrogen bonds in $FNMF_2$ (M = Co, Rh) are formed by the interaction of M($d_{z^2,xz}$)-orbitals with the N($p_{z,x}$)-orbitals leading to strongly bent F−N−M units. Compared to $FNRhF_2$, the metal-nitrogen bond in $FNCoF_2$ is significantly weakened and bears imidyl/nitrene character, evident by the considerable nitrogen centered spin density.

Formal metal oxidation state of VI and M≡N bond orders of 3 were determined for all NMF_3 compounds. With the exception of $NFeF_3$ and the magnetically bistable $NOsF_3$, all characterized NMF_3 species possess low-spin configurations. Except for the iron congener, all NMF_3 complexes exhibit a (pseudo) Jahn–Teller distorted structure with d^2 (group 8 metals) and d^3 (group 9 metals) configurations. Compared to the group 6 nitrido trifluorides, the stretching frequencies of the metal-nitrogen triple bond are slightly increased in the group 8 and 9 NMF_3 compounds, with $NFeF_3$ again being an exception, due to the partial oxidation of its nitrido ligand.

IR spectroscopic evidence for the formation of the C_{4v} symmetric spin doublet $NM^{VII}F_4$ (M = Ru, Os) species is presented. The electron configuration of these complexes corresponds to those of the known $NRuCl_4^-$ and $NOsCl_4^-$ anions with one electron removed from the doubly occupied metal centered $d_{x^2-y^2}$ orbital.

The novel rhodium(VI) and iridium(VI) nitrido trifluorides represent rare examples of terminal group 9 nitrido complexes in the unprecedented formal oxidation state VI. Moreover, it has been shown that the metal-nitrogen multiple bonds in $NFeF_3$, $FNCoF_2$ and $Ir(N_2)$ cannot be well described by an oxidation state formalism in which the more electronegative nitrogen atom adopts an OS of –III. The calculated spin densities of $FNCoF_2$ and $Ir(N_2)$ clearly show significant ligand radical character by means of spin polarization and spin delocalization, respectively. Molecular $Ir(N)_3$ was found not to contain Ir(IX), but rather Ir(VII) with a metal localized $(d_{z^2})^2$ configuration.

5.2. Outlook

While the reaction of laser-ablated cobalt atoms and NF_3 did not lead to the $NCoF_3$ species, lower nitrido fluorides might be stable. The reaction of cobalt with NF could lead to NCoF, an elusive terminal cobalt-nitrido species.

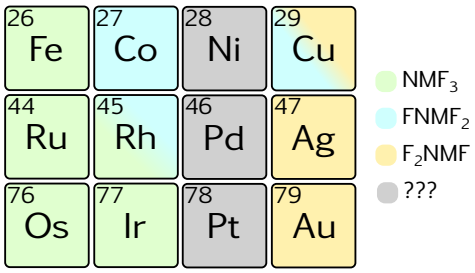

Figure 5.1. Reaction products obtained from NF_3 and laser-ablated group 8 (this work), group 9 (this work) as well as group 11 atoms.[272]

Figure 5.1 clearly shows that the obvious missing link in the series of known molecular compounds with F_3MN stoichiometry are the group 10 metals. Imido and nitrido group 10 complexes are very rare. From Figure 5.1 it can be speculated that the F_3MN molecules of group 10 could include all possible products of the reaction cascade shown in Reaction 6.

$$M + NF_3 \longrightarrow F_2NMF \longrightarrow FNMF_2 \longrightarrow NMF_3 \qquad \{6\}$$

6. References

[1] W. A. Nugent, J. M. Mayer, *Metal-Ligand Multiple Bonds: The Chemistry of Transition Metal Complexes Containing Oxo, Nitrido, Imido, Alkylidene, or Alkylidyne Ligands*, Wiley, New York, **1988**.

[2] R. R. Schrock, D. N. Clark, J. Sancho, J. H. Wengrovius, S. M. Rocklage, S. F. Pedersen, *Organometallics* **1982**, *1*, 1645–1651, DOI 10.1021/om00072a018.

[3] S. T. Nguyen, L. K. Johnson, R. H. Grubbs, J. W. Ziller, *J. Am. Chem. Soc.* **1992**, *114*, 3974–3975, DOI 10.1021/ja00036a053.

[4] P. Schwab, M. B. France, J. W. Ziller, R. H. Grubbs, *Angew. Chem. Int. Ed.* **1995**, *34*, 2039–2041, DOI 10.1002/anie.199520391; *Angew. Chem.* **1995**, *107*, 2179–2181, DOI 10.1002/ange.19951071818.

[5] P. Schwab, R. H. Grubbs, J. W. Ziller, *J. Am. Chem. Soc.* **1996**, *118*, 100–110, DOI 10.1021/ja952676d.

[6] M. Scholl, S. Ding, C. W. Lee, R. H. Grubbs, *Org. Lett.* **1999**, *1*, 953–956, DOI 10.1021/ol990909q.

[7] B. Meunier, *Metal-Oxo and Metal-Peroxo Species in Catalytic Oxidations*, *Vol. 97*, Springer, **2003**.

[8] J. Raymond, R. E. Blankenship, *Coord. Chem. Rev.* **2008**, *252*, 377–383, DOI 10.1016/j.ccr.2007.08.026.

[9] R. B. King, *Encyclopedia of Inorganic Chemistry*, *Vol. 4*, John Wiley & Sons, Inc., **1994**.

[10] P. J. Blower, J. R. Dilworth, J. P. Hutchinson, T. Nicholson, J. Zubieta, *J. Chem. Soc. Dalton Trans.* **1986**, 1339, DOI 10.1039/dt9860001339.

[11] R. J. Angelici, *Acc. Chem. Res.* **1988**, *21*, 387–394, DOI 10.1021/ar00155a001.

[12] J. Fritzsche, H. Struve, *J. prakt. Chem.* **1847**, *41*, 97–113, DOI 10.1002/prac.18470410113.

[13] D. V. Yandulov, R. R. Schrock, *Science* **2003**, *301*, 76–78, DOI 10.1126/science.1085326.

[14] R. R. Schrock, *Acc. Chem. Res.* **2005**, *38*, 955–962, DOI 10.1021/ar0501121.

[15] J. J. Scepaniak, J. A. Young, R. P. Bontchev, J. M. Smith, *Angew. Chem. Int. Ed.* **2009**, *48*, 3158–3160, DOI 10.1002/anie.200900381; *Angew. Chem.* **2009**, *121*, 3204–3206, DOI 10.1002/ange.200900381.

[16] K. Arashiba, Y. Miyake, Y. Nishibayashi, *Nat. Chem.* **2011**, *3*, 120–125, DOI 10.1038/nchem.906.

[17] B. Askevold, J. T. Nieto, S. Tussupbayev, M. Diefenbach, E. Herdtweck, M. C. Holthausen, S. Schneider, *Nat. Chem.* **2011**, *3*, 532–537, DOI 10.1038/nchem.1051.

[18] B. M. Lindley, Q. J. Bruch, P. S. White, F. Hasanayn, A. J. M. Miller, *J. Am. Chem. Soc.* **2017**, *139*, 5305–5308, DOI 10.1021/jacs.7b01323.

[19] Y. Nishibayashi, *Nat. Chem.* **2011**, *3*, 502–504, DOI 10.1038/nchem.1077.

[20] K. Nakajima, H. Toda, K. Sakata, Y. Nishibayashi, *Nat. Chem.* **2019**, *11*, 702–709, DOI 10.1038/s41557-019-0293-y.

[21] J. Fajardo, J. C. Peters, *J. Am. Chem. Soc.* **2017**, *139*, 16105–16108, DOI 10.1021/jacs.7b10204.

[22] S. J. K. Forrest, B. Schluschaß, E. Y. Yuzik-Klimova, S. Schneider, *Chem. Rev.* **2021**, DOI 10.1021/acs.chemrev.0c00958.

[23] J. J. Curley, E. L. Sceats, C. C. Cummins, *J. Am. Chem. Soc.* **2006**, *128*, 14036–14037, DOI 10.1021/ja066090a.

[24] M. J. Bezdek, P. J. Chirik, *Angew. Chem. Int. Ed.* **2016**, *55*, 7892–7896, DOI 10.1002/anie.201603142; *Angew. Chem.* **2016**, *128*, 8022–8026, DOI 10.1002/ange.201603142.

[25] I. Klopsch, M. Kinauer, M. Finger, C. Würtele, S. Schneider, *Angew. Chem. Int. Ed.* **2016**, *55*, 4786–4789, DOI 10.1002/anie.201600790; *Angew. Chem.* **2016**, *128*, 4864–4867, DOI 10.1002/ange.201600790.

[26] Z.-J. Lv, J. Wei, W.-X. Zhang, P. Chen, D. Deng, Z.-J. Shi, Z. Xi, *Natl. Sci. Rev.* **2020**, *7*, 1564–1583, DOI 10.1093/nsr/nwaa142.

[27] M. Ting-WaiáCheung, R. Wai-YináSun, et al., *Chem. Commun.* **2011**, *47*, 2140–2142.

[28] W.-X. Ni, W.-L. Man, S.-M. Yiu, M. Ho, M. T.-W. Cheung, C.-C. Ko, C.-M. Che, Y.-W. Lam, T.-C. Lau, *Chem. Sci.* **2012**, *3*, 1582–1588, DOI 10.1039/C2SC01031C.

[29] W.-Q. Huang, C.-X. Wang, T. Liu, Z.-X. Li, C. Pan, Y.-Z. Chen, X. Lian, W.-L. Man, W.-X. Ni, *Dalton Trans.* **2020**, *49*, 17173–17182, DOI 10.1039/D0DT02715D.

[30] M. Hanif, M. V. Babak, C. G. Hartinger, *Drug Discov. Today* **2014**, *19*, 1640–1648, DOI 10.1016/j.drudis.2014.06.016.

[31] R. L. Gdula, M. J. A. Johnson, *J. Am. Chem. Soc.* **2006**, *128*, 9614–9615, DOI 10.1021/ja058036k.

[32] E. S. Wiedner, K. J. Gallagher, M. J. A. Johnson, J. W. Kampf, *Inorg. Chem.* **2011**, *50*, 5936–5945, DOI 10.1021/ic1024247.

[33] M. H. Chisholm, E. E. Delbridge, A. R. Kidwell, K. B. Quinlan, *Chem. Commun.* **2003**, *0*, 126–127, DOI 10.1039/B210286B.

[34] G. Ertl, *Chem. Rec.* **2001**, *1*, 33–45, DOI 10.1002/1528-0691(2001)1:1<33::AID-TCR6>3.0.CO;2-V.

[35] T. Kandemir, M. E. Schuster, A. Senyshyn, M. Behrens, R. Schlögl, *Angew. Chem. Int. Ed.* **2013**, *52*, 12723–12726, DOI 10.1002/anie.201305812; *Angew. Chem.* **2013**, *125*, 12955–12959, DOI 10.1002/ange.201305812.

[36] M. Georgiadis, H. Komiya, P. Chakrabarti, D. Woo, J. Kornuc, D. Rees, *Science* **1992**, *257*, 1653–1659, DOI 10.1126/science.1529353.

[37] N. B. Thompson, M. T. Green, J. C. Peters, *J. Am. Chem. Soc.* **2017**, *139*, 15312–15315, DOI 10.1021/jacs.7b09364.

[38] D. N. Zarubin, N. A. Ustynyuk, *Russ. Chem. Rev.* **2006**, *75*, 671, DOI 10.1070/RC2006v075n08ABEH003595.

[39] E. R. King, E. T. Hennessy, T. A. Betley, *J. Am. Chem. Soc.* **2011**, *133*, 4917–4923, DOI 10.1021/ja110066j.

[40] T. A. Ramirez, B. Zhao, Y. Shi, *Chem. Soc. Rev.* **2012**, *41*, 931–942, DOI 10.1039/C1CS15104E.

[41] D. A. Iovan, T. A. Betley, *J. Am. Chem. Soc.* **2016**, *138*, 1983–1993, DOI 10.1021/jacs.5b12582.

[42] Y. Baek, T. A. Betley, *J. Am. Chem. Soc.* **2019**, *141*, 7797–7806, DOI 10.1021/jacs.9b01262.

[43] Y. Baek, A. Das, S.-L. Zheng, J. H. Reibenspies, D. C. Powers, T. A. Betley, *J. Am. Chem. Soc.* **2020**, *142*, 11232–11243, DOI 10.1021/jacs.0c04252.

[44] G. Coin, R. Patra, S. Rana, J. P. Biswas, P. Dubourdeaux, M. Clémancey, S. P. de Visser, D. Maiti, P. Maldivi, J.-M. Latour, *ACS Catal.* **2020**, *10*, 10010–10020, DOI 10.1021/acscatal.0c01427.

[45] P. J. Walsh, A. M. Baranger, R. G. Bergman, *J. Am. Chem. Soc.* **1992**, *114*, 1708–1719, DOI 10.1021/ja00031a026.

[46] P. L. McGrane, M. Jensen, T. Livinghouse, *J. Am. Chem. Soc.* **1992**, *114*, 5459–5460, DOI 10.1021/ja00039a087.

[47] M. Nobis, B. Drießen-Hölscher, *Angew. Chem. Int. Ed.* **2001**, *40*, 3983–3985, DOI 10.1002/1521-3773(20011105)40:21<3983::AID-ANIE3983>3.0.CO;2-8; M. Nobis, B. Drießen-Hölscher, *Angew. Chem.* **2001**, *113*, 4105–4108, DOI 10.1002/1521-3757(20011105)113:21<4105::AID-ANGE4105>3.0.CO;2-0.

[48] T.-G. Ong, G. P. A. Yap, D. S. Richeson, *J. Am. Chem. Soc.* **2003**, *125*, 8100–8101, DOI 10.1021/ja035716j.

[49] L. L. Anderson, J. Arnold, R. G. Bergman, *Org. Lett.* **2004**, *6*, 2519–2522, DOI 10.1021/ol0492851.

[50] C. Lorber, R. Choukroun, L. Vendier, *Organometallics* **2004**, *23*, 1845–1850, DOI 10.1021/om0342762.

[51] Y. Li, Y. Shi, A. L. Odom, *J. Am. Chem. Soc.* **2004**, *126*, 1794–1803, DOI 10.1021/ja038320g.

[52] R. Severin, S. Doye, *Chem. Soc. Rev.* **2007**, *36*, 1407–1420, DOI 10.1039/B600981F.

[53] L. Xu, W.-X. Zhang, Z. Xi, *Organometallics* **2015**, *34*, 1787–1801, DOI 10.1021/acs.organomet.5b00251.

[54] R. R. Schrock, A. H. Hoveyda, *Angew. Chem. Int. Ed.* **2003**, *42*, 4592–4633, DOI 10.1002/anie.200300576; *Angew. Chem.* **2003**, *115*, 4740–4782, DOI 10.1002/ange.200300576.

[55] R. R. Schrock, *J. Mol. Catal. Chem.*, The 15th. International Symposium on Olefin Metathesis and Related Chemistry **2004**, *213*, 21–30, DOI 10.1016/j.molcata.2003.10.060.

[56] J. R. Winkler, H. B. Gray in *Molecular Electronic Structures of Transition Metal Complexes I*, Springer Berlin Heidelberg, **2011**, pp. 17–28, DOI 10.1007/430_2011_55.

[57] J. Abbenseth, S. C. Bete, M. Finger, C. Volkmann, C. Würtele, S. Schneider, *Organometallics* **2017**, *37*, 802–811, DOI 10.1021/acs.organomet.7b00707.

[58] H. B. Gray, J. R. Winkler, *Acc. Chem. Res.* **2018**, *51*, 1850–1857, DOI 10.1021/acs.accounts.8b00245.

[59] M. Miao, Y. Sun, E. Zurek, H. Lin, *Nat. Rev. Chem.* **2020**, *4*, 508–527, DOI 10.1038/s41570-020-0213-0.

[60] G. Monsch, P. Klüfers, *Angew. Chem. Int. Ed.* **2019**, *58*, 8566–8571, DOI 10.1002/anie.201902374; *Angew. Chem.* **2019**, *131*, 8654–8659, DOI 10.1002/ange.201902374.

[61] C. K. Jørgensen in Structure And Bonding, Springer, Berlin, Heidelberg, **1966**, pp. 234–248, DOI 10.1007/BFb0119554.

[62] S. Riedel, M. Kaupp, *Coord. Chem. Rev.* **2009**, *253*, 606–624, DOI 10.1016/j.ccr.2008.07.014.

[63] G. Wang, M. Zhou, J. T. Goettel, G. J. Schrobilgen, J. Su, J. Li, T. Schlöder, S. Riedel, *Nature* **2014**, *514*, 475–477, DOI 10.1038/nature13795.

[64] S. P. Cramer, K. O. Hodgson in *Prog. Inorg. Chem.* John Wiley & Sons, Inc., **1979**, pp. 1–39, DOI 10.1002/9780470166260.ch1.

[65] E. I. Solomon, B. Hedman, K. O. Hodgson, A. Dey, R. K. Szilagyi, *Coord. Chem. Rev.* **2005**, *249*, 97–129, DOI 10.1016/j.ccr.2004.03.020.

[66] S. Sproules, K. Wieghardt, *Coord. Chem. Rev.* **2011**, *255*, 837–860, DOI 10.1016/j.ccr.2010.12.006.

[67] J. F. Berry, E. Bill, E. Bothe, S. D. George, B. Mienert, F. Neese, K. Wieghardt, *Science* **2006**, *312*, 1937–1941, DOI 10.1126/science.1128506.

[68] S.-X. Hu, W.-L. Li, J.-B. Lu, J. L. Bao, H. S. Yu, D. G. Truhlar, J. K. Gibson, J. Marçalo, M. Zhou, S. Riedel, W. H. E. Schwarz, J. Li, *Angew. Chem. Int. Ed.* **2018**, *57*, 3242–3245, DOI 10.1002/anie.201711450; *Angew. Chem.* **2018**, *130*, 3297–3300, DOI 10.1002/ange.201711450.

[69] S. Ganguly, A. Ghosh, *Acc. Chem. Res.* **2019**, *52*, 2003–2014, DOI 10.1021/acs.accounts.9b00115.

[70] W. P. Griffith, J. Lewis, G. Wilkinson, *J. Chem. Soc.* **1958**, 3993–3998, DOI 10.1039/JR9580003993.

[71] A. Wanat, T. Schneppensieper, G. Stochel, R. van Eldik, E. Bill, K. Wieghardt, *Inorg. Chem.* **2002**, *41*, 4–10, DOI 10.1021/ic010628q.

[72] H.-Y. Cheng, S. Chang, P.-Y. Tsai, *J. Phys. Chem. A* **2004**, *108*, 358–361, DOI 10.1021/jp031136x.

[73] V. Lyaskovskyy, B. de Bruin, *ACS Catal.* **2012**, *2*, 270–279, DOI 10.1021/cs200660v.

[74] P. J. Chirik, *Inorg. Chem.* **2011**, *50*, 9737–9740, DOI 10.1021/ic201881k.

[75] W. Kaim, *Eur. J. Inorg. Chem.* **2012**, *2012*, 343–348, DOI 10.1002/ejic.201101359.

[76] A. I. Olivos Suarez, V. Lyaskovskyy, J. N. H. Reek, J. I. van der Vlugt, B. de Bruin, *Angew. Chem. Int. Ed.* **2013**, *52*, 12510–12529, DOI 10.1002/anie.201301487; *Angew. Chem.* **2013**, *125*, 12740–12760, DOI 10.1002/ange.201301487.

[77] E. Whittle, D. A. Dows, G. C. Pimentel, *J. Chem. Phys.* **1954**, *22*, 1943–1943, DOI 10.1063/1.1739957.

[78] T. Schlöder, T. Vent-Schmidt, S. Riedel, *Angew. Chem. Int. Ed.* **2012**, *51*, 12063–12067, DOI 10.1002/anie.201206464; *Angew. Chem.* **2012**, *124*, 12229–12233, DOI 10.1002/ange.201206464.

[79] F. Brosi, T. Vent-Schmidt, S. Kieninger, T. Schlöder, H. Beckers, S. Riedel, *Chem. - Eur. J.* **2015**, *21*, 16455–16462, DOI 10.1002/chem.201502849.

[80] L. Fredin, B. Nelander, G. Ribbegård, *J. Mol. Spectrosc.* **1974**, *53*, 410–416, DOI 10.1016/0022-2852(74)90077-0.

[81] O. M. Wilkin, N. Harris, J. F. Rooms, E. L. Dixon, A. J. Bridgeman, N. A. Young, *J. Phys. Chem. A* **2018**, *122*, 1994–2029, DOI 10.1021/acs.jpca.7b09734.

[82] M. J. Linevsky, A Method for the Observation of the Infrared Spectrum of High Temperature Vapors by Matrix Isolation. I. The Infrared Spectrum of Lithium Fluoride, General Electric Co. Missile and Space Vehicle Dept., Philadelphia, **1960**.

[83] C. A. Wight, B. S. Ault, L. Andrews, *J. Chem. Phys.* **1976**, *65*, 1244–1249, DOI 10.1063/1.433233.

[84] P. L. Timms, *J. Chem. Soc. D* **1969**, 1033a–1033a, DOI 10.1039/C2969001033A.

[85] T. R. Burkholder, L. Andrews, *J. Chem. Phys.* **1991**, *95*, 8697–8709, DOI 10.1063/1.461814.

[86] L. Shao, L. Zhang, M. Chen, H. Lu, M. Zhou, *Chem. Phys. Lett.* **2001**, *343*, 178–184, DOI 10.1016/S0009-2614(01)00675-3.

[87] F. A. Redeker, Dissertation, Freie Universität Berlin, **2020**, DOI 10.17169/REFUBIUM-26725.

[88] M. Reiher, A. Wolf, *Relativistic Quantum Chemistry*, John Wiley & Sons, Inc., **2009**.

[89] K. Pierloot, *Int. J. Quantum Chem.* **2011**, *111*, 3291–3301, DOI 10.1002/qua.23029.

[90] G. Frenking, S. Shaik, *The Chemical Bond: Chemical Bonding Across the Periodic Table*, *Vol. 2*, John Wiley & Sons, **2014**.

[91] A. Szabo, N. S. Ostlund, *Modern Quantum Chemistry: Introduction to Advanced Electronic Structure Theory*, Dover, **1996**.

[92] M. Karplus, *J. Phys. Chem.* **1990**, *94*, 5435–5436, DOI 10.1021/j100377a002.

[93] W. Jiang, N. J. DeYonker, A. K. Wilson, *J. Chem. Theory Comput.* **2012**, *8*, 460–468, DOI 10.1021/ct2006852.

[94] J. Wang, S. Manivasagam, A. K. Wilson, *J. Chem. Theory Comput.* **2015**, *11*, 5865–5872, DOI 10.1021/acs.jctc.5b00861.

[95] B. O. Roos in *Advances in Chemical Physics*, (Ed.: K. P. Lawley), John Wiley & Sons, Inc., Hoboken, NJ, USA, **2007**, pp. 399–445, DOI 10.1002/9780470142943.ch7.

[96] M. Kaupp, *J. Comput. Chem.* **2006**, *28*, 320–325, DOI 10.1002/jcc.20522.

[97] P. Pyykkö, *Phys. Scr.* **1979**, *20*, 647–651, DOI 10.1088/0031-8949/20/5-6/016.

[98] H.-J. Werner, P. J. Knowles, *J. Chem. Phys.* **1988**, *89*, 5803–5814, DOI 10.1063/1.455556.

[99] P. J. Knowles, H.-J. Werner, *Chem. Phys. Lett.* **1988**, *145*, 514–522, DOI 10.1016/0009-2614(88)87412-8.

[100] P. Celani, H.-J. Werner, *J. Chem. Phys.* **2000**, *112*, 5546–5557, DOI 10.1063/1.481132.

[101] K. Andersson, P.-Å. Malmqvist, B. O. Roos, *J. Chem. Phys.* **1992**, *96*, 1218–1226, DOI 10.1063/1.462209.

[102] C. Angeli, R. Cimiraglia, S. Evangelisti, T. Leininger, J.-P. Malrieu, *J. Chem. Phys.* **2001**, *114*, 10252–10264, DOI 10.1063/1.1361246.

[103] G. Knizia, T. B. Adler, H.-J. Werner, *J. Chem. Phys.* **2009**, *130*, 054104, DOI 10.1063/1.3054300.

[104] T. Shiozaki, H.-J. Werner, *Mol. Phys.* **2013**, *111*, 607–630, DOI 10.1080/00268976.2013.779393.

[105] C. Riplinger, P. Pinski, U. Becker, E. F. Valeev, F. Neese, *J. Chem. Phys.* **2016**, *144*, 024109, DOI 10.1063/1.4939030.

[106] P. Hohenberg, W. Kohn, *Phys. Rev.* **1964**, *136*, B864–B871, DOI 10.1103/PhysRev.136.B864.

[107] W. Kohn, L. J. Sham, *Phys. Rev.* **1965**, *140*, A1133–A1138, DOI 10.1103/PhysRev.140.A1133.

[108] J. P. Perdew, K. Schmidt, *AIP Conf. Proc.* **2001**, *577*, 1–20, DOI 10.1063/1.1390175.

[109] J. P. Perdew, *MRS Bull.* **2013**, *38*, 743–750, DOI 10.1557/mrs.2013.178.

[110] A. D. Becke, *Phys. Rev. A* **1988**, *38*, 3098–3100, DOI 10.1103/PhysRevA.38.3098.

[111] J. P. Perdew, *Phys. Rev. B* **1986**, *33*, 8822–8824, DOI 10.1103/PhysRevB.33.8822.

[112] A. D. Becke, *J. Chem. Phys.* **1993**, *98*, 5648–5652, DOI 10.1063/1.464913.

[113] C. Lee, W. Yang, R. G. Parr, *Phys. Rev. B* **1988**, *37*, 785–789, DOI 10.1103/PhysRevB.37.785.

[114] P. J. Stephens, F. J. Devlin, C. F. Chabalowski, M. J. Frisch, *J. Phys. Chem.* **1994**, *98*, 11623–11627, DOI 10.1021/j100096a001.

[115] S. H. Vosko, L. Wilk, M. Nusair, *Can. J. Phys.* **1980**, DOI 10.1139/p80-159.

[116] P. Verma, D. G. Truhlar, *Trends Chem.* **2020**, *2*, 302–318, DOI 10.1016/j.trechm.2020.02.005.

[117] J.-D. Chai, M. Head-Gordon, *J. Chem. Phys.* **2008**, *128*, 084106, DOI 10.1063/1.2834918.

[118] J.-D. Chai, M. Head-Gordon, *Phys. Chem. Chem. Phys.* **2008**, *10*, 6615–6620, DOI 10.1039/B810189B.

[119] J.-D. Chai, M. Head-Gordon, *J. Chem. Phys.* **2009**, *131*, 174105, DOI 10.1063/1.3244209.

[120] Y. Zhao, D. G. Truhlar, *J. Phys. Chem. A* **2006**, *110*, 13126–13130, DOI 10.1021/jp066479k.

[121] Y. Zhao, D. G. Truhlar, *J. Chem. Phys.* **2006**, *125*, 194101, DOI 10.1063/1.2370993.

[122] Y. Wang, X. Jin, H. S. Yu, D. G. Truhlar, X. He, *Proc. Natl. Acad. Sci.* **2017**, *114*, 8487–8492, DOI 10.1073/pnas.1705670114.

[123] Y. Zhao, D. G. Truhlar, *Theor. Chem. Acc.* **2007**, *120*, 215–241, DOI 10.1007/s00214-007-0310-x.

[124] F. Jensen, *Introduction to Computational Chemistry*, 2nd ed., John Wiley & Sons, Inc., **2007**.

[125] M. Reiher, *Chimia* **2009**, *63*, 140–145, DOI 10.2533/chimia.2009.140.

[126] M. Dolg in *Theoretical and Computational Chemistry*, Elsevier, **2002**, pp. 793–862, DOI 10.1016/s1380-7323(02)80040-1.

[127] M. Douglas, N. M. Kroll, *Ann. Phys.* **1974**, *82*, 89–155, DOI 10.1016/0003-4916(74)90333-9.

[128] B. A. Hess, *Phys. Rev. A* **1986**, *33*, 3742–3748, DOI 10.1103/PhysRevA.33.3742.

[129] E. van Lenthe, E. J. Baerends, J. G. Snijders, *J. Chem. Phys.* **1993**, *99*, 4597–4610, DOI 10.1063/1.466059.

[130] E. van Lenthe, E. J. Baerends, J. G. Snijders, *J. Chem. Phys.* **1994**, *101*, 9783–9792, DOI 10.1063/1.467943.

[131] X. Cao, M. Dolg, *J. Chem. Phys.* **2001**, *115*, 7348–7355, DOI 10.1063/1.1406535.

[132] R. Gulde, P. Pollak, F. Weigend, *J. Chem. Theory Comput.* **2012**, *8*, 4062–4068, DOI 10.1021/ct300302u.

[133] K. A. Peterson, D. Figgen, E. Goll, H. Stoll, M. Dolg, *J. Chem. Phys.* **2003**, *119*, 11113–11123, DOI 10.1063/1.1622924.

[134] F. Weigend, R. Ahlrichs, *Phys. Chem. Chem. Phys.* **2005**, *7*, 3297–3305, DOI 10.1039/B508541A.

[135] D. Andrae, U. Häußermann, M. Dolg, H. Stoll, H. Preuß, *Theoret. Chim. Acta* **1990**, *77*, 123–141, DOI 10.1007/BF01114537.

[136] M. Kaupp, P. v. R. Schleyer, H. Stoll, H. Preuss, *J. Chem. Phys.* **1991**, *94*, 1360–1366, DOI 10.1063/1.459993.

[137] T. Leininger, A. Nicklass, W. Küchle, H. Stoll, M. Dolg, A. Bergner, *Chem. Phys. Lett.* **1996**, *255*, 274–280, DOI 10.1016/0009-2614(96)00382-X.

[138] B. Metz, H. Stoll, M. Dolg, *J. Chem. Phys.* **2000**, *113*, 2563–2569, DOI 10.1063/1.1305880.

[139] N. B. Balabanov, K. A. Peterson, *J. Chem. Phys.* **2005**, *123*, 064107, DOI 10.1063/1.1998907.

[140] N. B. Balabanov, K. A. Peterson, *J. Chem. Phys.* **2006**, *125*, 074110, DOI 10.1063/1.2335444.

[141] T. H. Dunning, *J. Chem. Phys.* **1989**, *90*, 1007–1023, DOI 10.1063/1.456153.

[142] J. Koput, K. A. Peterson, *J. Phys. Chem. A* **2002**, *106*, 9595–9599, DOI 10.1021/jp026283u.

[143] B. P. Prascher, D. E. Woon, K. A. Peterson, T. H. Dunning, A. K. Wilson, *Theor. Chem. Acc.* **2011**, *128*, 69–82, DOI 10.1007/s00214-010-0764-0.

[144] A. K. Wilson, D. E. Woon, K. A. Peterson, T. H. Dunning, *J. Chem. Phys.* **1999**, *110*, 7667–7676, DOI 10.1063/1.478678.

[145] D. E. Woon, T. H. Dunning, *J. Chem. Phys.* **1993**, *98*, 1358–1371, DOI 10.1063/1.464303.

[146] D. E. Woon, T. H. Dunning, *J. Chem. Phys.* **1994**, *100*, 2975–2988, DOI 10.1063/1.466439.

[147] D. Figgen, G. Rauhut, M. Dolg, H. Stoll, *Chem. Phys.*, Relativistic Effects in Heavy-Element Chemistry and Physics. In Memoriam Bernd A. Hess (1954–2004) **2005**, *311*, 227–244, DOI 10.1016/j.chemphys.2004.10.005.

[148] D. Figgen, K. A. Peterson, M. Dolg, H. Stoll, *J. Chem. Phys.* **2009**, *130*, 164108, DOI 10.1063/1.3119665.

[149] B. Metz, M. Schweizer, H. Stoll, M. Dolg, W. Liu, *Theor. Chem. Acc.* **2000**, *104*, 22–28, DOI 10.1007/s002149900101.

[150] K. A. Peterson, *J. Chem. Phys.* **2003**, *119*, 11099–11112, DOI 10.1063/1.1622923.

[151] K. A. Peterson, C. Puzzarini, *Theor. Chem. Acc.* **2005**, *114*, 283–296, DOI 10.1007/s00214-005-0681-9.

[152] K. A. Peterson, B. C. Shepler, D. Figgen, H. Stoll, *J. Phys. Chem. A* **2006**, *110*, 13877–13883, DOI 10.1021/jp0658871.

[153] K. A. Peterson, D. Figgen, M. Dolg, H. Stoll, *J. Chem. Phys.* **2007**, *126*, 124101, DOI 10.1063/1.2647019.

[154] W. A. de Jong, R. J. Harrison, D. A. Dixon, *J. Chem. Phys.* **2001**, *114*, 48, DOI 10.1063/1.1329891.

[155] K. A. Peterson, T. H. Dunning, *J. Chem. Phys.* **2002**, *117*, 10548–10560, DOI 10.1063/1.1520138.

[156] K. A. Peterson, K. E. Yousaf, *J. Chem. Phys.* **2010**, *133*, 174116, DOI 10.1063/1.3503659.

[157] D. Feller, K. A. Peterson, J. Grant Hill, *J. Chem. Phys.* **2011**, *135*, 044102, DOI 10.1063/1.3613639.

[158] R. S. Mulliken, *J. Chem. Phys.* **1962**, *36*, 3428–3439, DOI 10.1063/1.1732476.

[159] P.-O. Löwdin in *Advances in Quantum Chemistry, Vol. 5*, (Ed.: P.-O. Löwdin), Academic Press, **1970**, pp. 185–199, DOI 10.1016/S0065-3276(08)60339-1.

[160] F. Weinhold, C. R. Landis, *Discovering Chemistry with Natural Bond Orbitals*, 1. ed, Wiley, Hoboken, NJ, **2012**.

[161] R. F. W. Bader, *Chem. Rev.* **1991**, *91*, 893–928, DOI 10.1021/cr00005a013.

[162] R. F. W. Bader, *Atoms in Molecules: A Quantum Theory*, Oxford University Press, Oxford, New York, **1994**.

[163] P. Popelier, *Atoms In Molecules: An Introduction*, Prentice Hall, Harlow, **2000**.

[164] B. O. Roos, A. C. Borin, L. Gagliardi, *Angew. Chem. Int. Ed.* **2007**, *46*, 1469–1472, DOI 10.1002/anie.200603600; *Angew. Chem.* **2007**, *119*, 1491–1494, DOI 10.1002/ange.200603600.

[165] W. D. Wagner, K. Nakamoto, *J. Am. Chem. Soc.* **1988**, *110*, 4044–4045, DOI 10.1021/ja00220a057.

[166] W. D. Wagner, K. Nakamoto, *J. Am. Chem. Soc.* **1989**, *111*, 1590–1598, DOI 10.1021/ja00187a010.

[167] H.-X. Wang, L. Wu, B. Zheng, L. Du, W.-P. To, C.-H. Ko, D. L. Phillips, C.-M. Che, *Angew. Chem. Int. Ed.* **2021**, *60*, 4796–4803, DOI 10.1002/anie.202014191; *Angew. Chem.* **2021**, *133*, 4846–4853, DOI 10.1002/ange.202014191.

[168] K. Meyer, E. Bill, B. Mienert, T. Weyhermüller, K. Wieghardt, *J. Am. Chem. Soc.* **1999**, *121*, 4859–4876, DOI 10.1021/ja983454t.

[169] C. A. Grapperhaus, B. Mienert, E. Bill, T. Weyhermüller, K. Wieghardt, *Inorg. Chem.* **2000**, *39*, 5306–5317, DOI 10.1021/ic0005238.

[170] M. Schlangen, J. Neugebauer, M. Reiher, D. Schröder, J. P. López, M. Haryono, F. W. Heinemann, A. Grohmann, H. Schwarz, *J. Am. Chem. Soc.* **2008**, *130*, 4285–4294, DOI 10.1021/ja075617w.

[171] G. Sabenya, L. Lázaro, I. Gamba, V. Martin-Diaconescu, E. Andris, T. Weyhermüller, F. Neese, J. Roithova, E. Bill, J. Lloret-Fillol, M. Costas, *J. Am. Chem. Soc.* **2017**, *139*, 9168–9177, DOI 10.1021/jacs.7b00429.

[172] E. Andris, R. Navrátil, J. Jašík, G. Sabenya, M. Costas, M. Srnec, J. Roithová, *Chem. – Eur. J.* **2018**, *24*, 5078–5081, DOI 10.1002/chem.201705307.

[173] T. A. Betley, J. C. Peters, *J. Am. Chem. Soc.* **2004**, *126*, 6252–6254, DOI 10.1021/ja048713v.

[174] C. Vogel, F. W. Heinemann, J. Sutter, C. Anthon, K. Meyer, *Angew. Chem. Int. Ed.* **2008**, *47*, 2681–2684, DOI 10.1002/anie.200800600; *Angew. Chem.* **2008**, *120*, 2721–2724, DOI 10.1002/ange.200800600.

[175] J. J. Scepaniak, M. D. Fulton, R. P. Bontchev, E. N. Duesler, M. L. Kirk, J. M. Smith, *J. Am. Chem. Soc.* **2008**, *130*, 10515–10517, DOI 10.1021/ja8027372.

[176] J. J. Scepaniak, C. S. Vogel, M. M. Khusniyarov, F. W. Heinemann, K. Meyer, J. M. Smith, *Science* **2011**, *331*, 1049–1052, DOI 10.1126/science.1198315.

[177] M. Keilwerth, L. Grunwald, W. Mao, F. W. Heinemann, J. Sutter, E. Bill, K. Meyer, *J. Am. Chem. Soc.* **2021**, *143*, 1458–1465, DOI 10.1021/jacs.0c11141.

[178] T. Petrenko, S. DeBeer George, N. Aliaga-Alcalde, E. Bill, B. Mienert, Y. Xiao, Y. Guo, W. Sturhahn, S. P. Cramer, K. Wieghardt, F. Neese, *J. Am. Chem. Soc.* **2007**, *129*, 11053–11060, DOI 10.1021/ja070792y.

[179] H.-C. Chang, Y.-H. Lin, C. Werlé, F. Neese, W.-Z. Lee, E. Bill, S. Ye, *Angew. Chem. Int. Ed.* **2019**, *58*, 17589–17593, DOI 10.1002/anie.201908689; *Angew. Chem.* **2019**, *131*, 17753–17757, DOI 10.1002/ange.201908689.

[180] J.-U. Rohde, T. A. Betley, T. A. Jackson, C. T. Saouma, J. C. Peters, L. Que, *Inorg. Chem.* **2007**, *46*, 5720–5726, DOI 10.1021/ic700818q.

[181] L. Bucinsky, M. Breza, W.-T. Lee, A. K. Hickey, D. A. Dickie, I. Nieto, J. A. DeGayner, T. D. Harris, K. Meyer, J. Krzystek, A. Ozarowski, J. Nehrkorn, A. Schnegg, K. Holldack, R. H. Herber, J. Telser, J. M. Smith, *Inorg. Chem.* **2017**, *56*, 4751–4768, DOI 10.1021/acs.inorgchem.7b00512.

[182] J. J. Scepaniak, R. P. Bontchev, D. L. Johnson, J. M. Smith, *Angew. Chem. Int. Ed.* **2011**, *50*, 6630–6633, DOI 10.1002/anie.201102028; *Angew. Chem.* **2011**, *123*, 6760–6763, DOI 10.1002/ange.201102028.

[183] K. Aiuchi, K. Shibuya, *J. Mol. Spectrosc.* **2000**, *204*, 235–261, DOI 10.1006/jmsp.2000.8226.

[184] P. E. M. Siegbahn, M. R. A. Blomberg, *Chem. Phys.* **1984**, *87*, 189–201, DOI 10.1016/0301-0104(84)85045-4.

[185] G. V. Chertihin, L. Andrews, M. Neurock, *J. Phys. Chem.* **1996**, *100*, 14609–14617, DOI 10.1021/jp961423j.

[186] A. Fiedler, S. Iwata, *Chem. Phys. Lett.* **1997**, *271*, 143–151, DOI 10.1016/S0009-2614(97)00444-2.

[187] P. M. Sheridan, L. M. Ziurys, T. Hirano, *Astrophys. J.* **2003**, *593*, L141–L144, DOI 10.1086/378177.

[188] N. Aliaga-Alcalde, S. D. George, B. Mienert, E. Bill, K. Wieghardt, F. Neese, *Angew. Chem. Int. Ed.* **2005**, *44*, 2908–2912, DOI 10.1002/anie.200462368; N. Aliaga-Alcalde, S. D. George, B. Mienert, E. Bill, K. Wieghardt, F. Neese, *Angew. Chem.* **2005**, *117*, 2968–2972, DOI 10.1002/ange.200462368.

[189] M. P. Hendrich, W. Gunderson, R. K. Behan, M. T. Green, M. P. Mehn, T. A. Betley, C. C. Lu, J. C. Peters, *Proc. Natl. Acad. Sci.* **2006**, *103*, 17107–17112, DOI 10.1073/pnas.0604402103.

[190] W. P. Griffith, D. Pawson, *J. Chem. Soc. Dalton Trans.* **1973**, 1315–1320, DOI 10.1039/DT9730001315.

[191] P.-M. Chan, W.-Y. Yu, C.-M. Che, K.-K. Cheung, *J. Chem. Soc. Dalton Trans.* **1998**, *0*, 3183–3190, DOI 10.1039/A804204G.

[192] L. Bonomo, E. Solari, R. Scopelliti, C. Floriani, *Angew. Chem. Int. Ed.* **2001**, *40*, 2529–2531, DOI 10.1002/1521-3773(20010702)40:13<2529::AID-ANIE2529>3.0.CO;2-B; *Angew. Chem.* **2001**, *113*, 2597–2599, DOI 10.1002/1521-3757(20010702)113:13<2597::AID-ANGE2597>3.0.CO;2-H.

[193] S. K.-Y. Leung, J.-S. Huang, J.-L. Liang, C.-M. Che, Z.-Y. Zhou, *Angew. Chem. Int. Ed.* **2003**, *42*, 340–343, DOI 10.1002/anie.200390111; *Angew. Chem.* **2003**, *115*, 354–357, DOI 10.1002/ange.200390079.

[194] W.-L. Man, T.-M. Tang, T.-W. Wong, T.-C. Lau, S.-M. Peng, W.-T. Wong, *J. Am. Chem. Soc.* **2004**, *126*, 478–479, DOI 10.1021/ja037899f.

[195] A. Walstrom, M. Pink, X. Yang, J. Tomaszewski, M.-H. Baik, K. G. Caulton, *J. Am. Chem. Soc.* **2005**, *127*, 5330–5331, DOI 10.1021/ja050361k.

[196] J. S. Pap, S. DeBeer George, J. F. Berry, *Angew. Chem. Int. Ed.* **2008**, *47*, 10102–10105, DOI 10.1002/anie.200804397; *Angew. Chem.* **2008**, *120*, 10256–10259, DOI 10.1002/ange.200804397.

[197] H.-Y. Ng, N.-M. Lam, M. Yang, X.-Y. Yi, I. D. Williams, W.-H. Leung, *Inorganica Chim. Acta* **2013**, *394*, 171–175, DOI 10.1016/j.ica.2012.07.025.

[198] F. L. Phillips, A. C. Skapski, *Acta Crystallogr. B* **1975**, *31*, 2667–2670, DOI 10.1107/S0567740875008424.

[199] J. J. Schwab, E. C. Wilkinson, S. R. Wilson, P. A. Shapley, *J. Am. Chem. Soc.* **1991**, *113*, 6124–6129, DOI 10.1021/ja00016a031.

[200] R. S. Ram, J. Liévin, P. F. Bernath, *J. Chem. Phys.* **1998**, *109*, 6329–6337, DOI 10.1063/1.477275.

[201] R. S. Ram, P. F. Bernath, *J. Mol. Spectrosc.* **2002**, *213*, 170–178, DOI 10.1006/jmsp.2002.8565.

[202] A. Citra, L. Andrews, *J. Phys. Chem. A* **2000**, *104*, 1152–1161, DOI 10.1021/jp993338s.

[203] W.-L. Man, W. W. Y. Lam, S.-M. Yiu, T.-C. Lau, S.-M. Peng, *J. Am. Chem. Soc.* **2004**, *126*, 15336–15337, DOI 10.1021/ja045845f.

[204] W.-L. Man, W. W. Y. Lam, H.-K. Kwong, S.-M. Peng, W.-T. Wong, T.-C. Lau, *Inorg. Chem.* **2010**, *49*, 73–81, DOI 10.1021/ic901374f.

[205] W.-L. Man, W. W. Y. Lam, H.-K. Kwong, S.-M. Yiu, T.-C. Lau, *Angew. Chem. Int. Ed.* **2012**, *51*, 9101–9104, DOI 10.1002/anie.201204136; *Angew. Chem.* **2012**, *124*, 9235–9238, DOI 10.1002/ange.201204136.

[206] T. V. Truong, E. A. Kastl, G. Du, *Tetrahedron Lett.* **2011**, *52*, 1670–1672, DOI 10.1016/j.tetlet.2011.01.139.

[207] W.-L. Man, J. Xie, P.-K. Lo, W. W. Y. Lam, S.-M. Yiu, K.-C. Lau, T.-C. Lau, *Angew. Chem. Int. Ed.* **2014**, *53*, 8463–8466, DOI 10.1002/anie.201404421; *Angew. Chem.* **2014**, *126*, 8603–8606, DOI 10.1002/ange.201404421.

[208] Q. Wang, W.-L. Man, W. W. Y. Lam, T.-C. Lau, *Chem. Commun.* **2014**, *50*, 15799–15802, DOI 10.1039/C4CC07568D.

[209] J. Xie, W.-L. Man, C.-Y. Wong, X. Chang, C.-M. Che, T.-C. Lau, *J. Am. Chem. Soc.* **2016**, *138*, 5817–5820, DOI 10.1021/jacs.6b02923.

[210] J. Xie, P.-K. Lo, W. W. Y. Lam, W.-L. Man, L. Ma, S.-M. Yiu, K.-C. Lau, T.-C. Lau, *Chem. Commun.* **2016**, *52*, 11430–11433, DOI 10.1039/C6CC06231H.

[211] A. Walstrom, M. Pink, H. Fan, J. Tomaszewski, K. G. Caulton, *Inorg. Chem.* **2007**, *46*, 7704–7706, DOI 10.1021/ic700789y.

[212] A. Walstrom, H. Fan, M. Pink, K. G. Caulton, *Inorganica Chim. Acta*, Protagonist in Chemistry: Paul S. Pregosin **2010**, *363*, 633–636, DOI 10.1016/j.ica.2008.11.010.

[213] S. V. Ley, J. Norman, W. P. Griffith, S. P. Marsden, *Synthesis* **1994**, *1994*, 639–666, DOI 10.1055/s-1994-25538.

[214] H. Cheng, C. B. W. Stark, *Angew. Chem. Int. Ed.* **2010**, *49*, 1587–1590, DOI 10.1002/anie.200903090; *Angew. Chem.* **2010**, *122*, 1632–1635, DOI 10.1002/ange.200903090.

[215] A. Werner, K. Dinklage, *Berichte Dtsch. Chem. Ges.* **1901**, *34*, 2698–2703, DOI 10.1002/cber.190103402220.

[216] P. A. Shapley, R. M. Marshman, J. M. Shusta, Z. Gebeyehu, S. R. Wilson, *Inorg. Chem.* **1994**, *33*, 498–502, DOI 10.1021/ic00081a017.

[217] D. Sellmann, M. W. Wemple, W. Donaubauer, F. W. Heinemann, *Inorg. Chem.* **1997**, *36*, 1397–1402, DOI 10.1021/ic961240b.

[218] T.-W. Wong, T.-C. Lau, W.-T. Wong, *Inorg. Chem.* **1999**, *38*, 6181–6186, DOI 10.1021/ic9814571.

[219] W.-X. Ni, W.-L. Man, M. T.-W. Cheung, R. W.-Y. Sun, Y.-L. Shu, Y.-W. Lam, C.-M. Che, T.-C. Lau, *Chem. Commun.* **2011**, *47*, 2140–2142, DOI 10.1039/C0CC04515B.

[220] K. Suntharalingam, T. C. Johnstone, P. M. Bruno, W. Lin, M. T. Hemann, S. J. Lippard, *J. Am. Chem. Soc.* **2013**, *135*, 14060–14063, DOI 10.1021/ja4075375.

[221] F. S. Schendzielorz, M. Finger, C. Volkmann, C. Würtele, S. Schneider, *Angew. Chem. Int. Ed.* **2016**, *55*, 11417–11420, DOI 10.1002/anie.201604917; *Angew. Chem.* **2016**, *128*, 11589–11592, DOI 10.1002/ange.201604917.

[222] F. M. Jaeger, J. E. Zanstra, *Proc. R. Neth. Acad. Arts Sci.* **1932**, *35*, 610–624.

[223] F. M. Jaeger, J. E. Zanstra, *Recl. Trav. Chim. Pays-Bas* **1932**, *51*, 1013–1053, DOI 10.1002/recl.19320511106.

[224] J. Lewis, G. Wilkinson, *J. Inorg. Nucl. Chem.* **1958**, *6*, 12–13, DOI 10.1016/0022-1902(58)80094-9.

[225] A. Werner, K. Dinklage, *Berichte Dtsch. Chem. Ges.* **1906**, *39*, 499–503, DOI 10.1002/cber.19060390181.

[226] D. Bright, J. A. Ibers, *Inorg. Chem.* **1969**, *8*, 709–716, DOI 10.1021/ic50074a002.

[227] S. R. Fletcher, W. P. Griffith, D. Pawson, F. L. Phillips, A. C. Skapski, *Inorg. Nucl. Chem. Lett.* **1973**, *9*, 1117–1120, DOI 10.1016/0020-1650(73)80016-9.

[228] D. W. Pipes, M. Bakir, S. E. Vitols, D. J. Hodgson, T. J. Meyer, *J. Am. Chem. Soc.* **1990**, *112*, 5507–5514, DOI 10.1021/ja00170a014.

[229] R. Eikey, *Coord. Chem. Rev.* **2003**, *243*, 83–124, DOI 10.1016/S0010-8545(03)00048-1.

[230] K. Suntharalingam, W. Lin, T. C. Johnstone, P. M. Bruno, Y.-R. Zheng, M. T. Hemann, S. J. Lippard, *J. Am. Chem. Soc.* **2014**, *136*, 14413–14416, DOI 10.1021/ja508808v.

[231] R. S. Ram, J. Liévin, P. F. Bernath, *J. Chem. Phys.* **1999**, *111*, 3449–3456, DOI 10.1063/1.479630.

[232] A. Citra, L. Andrews, *J. Am. Chem. Soc.* **1999**, *121*, 11567–11568, DOI 10.1021/ja993211g.

[233] D. M. Jenkins, T. A. Betley, J. C. Peters, *J. Am. Chem. Soc.* **2002**, *124*, 11238–11239, DOI 10.1021/ja026852b.

[234] M. P. Mehn, S. D. Brown, D. M. Jenkins, J. C. Peters, L. Que, *Inorg. Chem.* **2006**, *45*, 7417–7427, DOI 10.1021/ic060670r.

[235] X. Dai, P. Kapoor, T. H. Warren, *J. Am. Chem. Soc.* **2004**, *126*, 4798–4799, DOI 10.1021/ja036308i.

[236] D. T. Shay, G. P. A. Yap, L. N. Zakharov, A. L. Rheingold, K. H. Theopold, *Angew. Chem. Int. Ed.* **2005**, *44*, 1508–1510, DOI 10.1002/anie.200462529; *Angew. Chem.* **2005**, *117*, 1532–1534, DOI 10.1002/ange.200462529.

[237] R. E. Cowley, R. P. Bontchev, J. Sorrell, O. Sarracino, Y. Feng, H. Wang, J. M. Smith, *J. Am. Chem. Soc.* **2007**, *129*, 2424–2425, DOI 10.1021/ja066899n.

[238] E. R. King, G. T. Sazama, T. A. Betley, *J. Am. Chem. Soc.* **2012**, *134*, 17858–17861, DOI 10.1021/ja307699u.

[239] L. Zhang, Y. Liu, L. Deng, *J. Am. Chem. Soc.* **2014**, *136*, 15525–15528, DOI 10.1021/ja509731z.

[240] J. Du, L. Wang, M. Xie, L. Deng, *Angew. Chem. Int. Ed.* **2015**, *54*, 12640–12644, DOI 10.1002/anie.201505937; *Angew. Chem.* **2015**, *127*, 12831–12835, DOI 10.1002/ange.201505937.

[241] Y. Liu, J. Du, L. Deng, *Inorg. Chem.* **2017**, *56*, 8278–8286, DOI 10.1021/acs.inorgchem.7b00941.

[242] A. Reckziegel, C. Pietzonka, F. Kraus, C. G. Werncke, *Angew. Chem. Int. Ed.* **2020**, *59*, 8527–8531, DOI 10.1002/anie.201914718; *Angew. Chem.* **2020**, *132*, 8605–8609, DOI 10.1002/ange.201914718.

[243] L. Andrews, A. Citra, G. V. Chertihin, W. D. Bare, M. Neurock, *J. Phys. Chem. A* **1998**, *102*, 2561–2571, DOI 10.1021/jp9802836.

[244] T. Yamaki, M. Sekiya, K. Tanaka, *Chem. Phys. Lett.* **2003**, *376*, 487–492, DOI 10.1016/S0009-2614(03)01035-2.

[245] J. P. Gobbo, A. C. Borin, *J. Phys. Chem. A* **2006**, *110*, 13966–13973, DOI 10.1021/jp065005i.

[246] J. F. Berry, *Comments Inorg. Chem.* **2009**, *30*, 28–66, DOI 10.1080/02603590902768875.

[247] X. Hu, K. Meyer, *J. Am. Chem. Soc.* **2004**, *126*, 16322–16323, DOI 10.1021/ja044271b.

[248] C. Jones, C. Schulten, R. P. Rose, A. Stasch, S. Aldridge, W. D. Woodul, K. S. Murray, B. Moubaraki, M. Brynda, G. La Macchia, L. Gagliardi, *Angew. Chem. Int. Ed.* **2009**, *48*, 7406–7410, DOI 10.1002/anie.200900780; *Angew. Chem.* **2009**, *121*, 7542–7546, DOI 10.1002/ange.200900780.

[249] M. G. Scheibel, Y. Wu, A. C. Stückl, L. Krause, E. Carl, D. Stalke, B. de Bruin, S. Schneider, *J. Am. Chem. Soc.* **2013**, *135*, 17719–17722, DOI 10.1021/ja409764j.

[250] A. M. Geer, C. Tejel, J. A. López, M. A. Ciriano, *Angew. Chem. Int. Ed.* **2014**, *53*, 5614–5618, DOI 10.1002/anie.201400023; *Angew. Chem.* **2014**, *126*, 5720–5724, DOI 10.1002/ange.201400023.

[251] X. Li, L.-S. Wang, *J. Chem. Phys.* **1998**, *109*, 5264–5268, DOI 10.1063/1.477143.

[252] I. Shim, K. Mandix, K. A. Gingerich, *J. Mol. Struct. THEOCHEM* **1997**, *393*, 127–139, DOI 10.1016/S0166-1280(96)04802-6.

[253] R. Du, B. Suo, H. Han, Y. Lei, G. Zhai, *Int. J. Quantum Chem.* **2013**, *113*, 2464–2470, DOI 10.1002/qua.24484.

[254] A. Citra, L. Andrews, *J. Phys. Chem. A* **1999**, *103*, 3410–3417, DOI 10.1021/jp9846274.

[255] S. G. Fougère, W. J. Balfour, J. Cao, C. X. W. Qian, *J. Mol. Spectrosc.* **2000**, *199*, 18–25, DOI 10.1006/jmsp.1999.7972.

[256] D. S. Glueck, F. J. Hollander, R. G. Bergman, *J. Am. Chem. Soc.* **1989**, *111*, 2719–2721, DOI 10.1021/ja00189a059.

[257] D. S. Glueck, J. Wu, F. J. Hollander, R. G. Bergman, *J. Am. Chem. Soc.* **1991**, *113*, 2041–2054, DOI 10.1021/ja00006a026.

[258] M. Kinauer, M. Diefenbach, H. Bamberger, S. Demeshko, E. J. Reijerse, C. Volkmann, C. Würtele, J. van Slageren, B. de Bruin, M. C. Holthausen, S. Schneider, *Chem. Sci.* **2018**, *9*, 4325–4332, DOI 10.1039/C8SC01113C.

[259] J. Schöffel, A. Y. Rogachev, S. DeBeer George, P. Burger, *Angew. Chem. Int. Ed.* **2009**, *48*, 4734–4738, DOI 10.1002/anie.200901494; *Angew. Chem.* **2009**, *121*, 4828–4832, DOI 10.1002/ange.200901494.

[260] D. Sieh, J. Schöffel, P. Burger, *Dalton Trans.* **2011**, *40*, 9512–9524, DOI 10.1039/C1DT10886G.

[261] M. G. Scheibel, B. Askevold, F. W. Heinemann, E. J. Reijerse, B. de Bruin, S. Schneider, *Nat. Chem.* **2012**, *4*, 552–558, DOI 10.1038/nchem.1368.

[262] R. S. Ram, P. F. Bernath, *J. Mol. Spectrosc.* **1999**, *193*, 363–375, DOI 10.1006/jmsp.1998.7753.

[263] R. S. Ram, J. Liévin, P. F. Bernath, *J. Mol. Spectrosc.* **1999**, *197*, 133–146, DOI 10.1006/jmsp.1999.7911.

[264] H. F. Pang, A. S. C. Cheung, *Chin. J. Chem. Phys.* **2009**, *22*, 157–161, DOI 10.1088/1674-0068/22/02/157-161.

[265] Q.-C. Fan, W.-G. Sun, H.-D. Li, H. Feng, *Chinese Phys. B* **2012**, *21*, 023301, DOI 10.1088/1674-1056/21/2/023301.

[266] D. Sieh, P. Burger, *J. Am. Chem. Soc.* **2013**, *135*, 3971–3982, DOI 10.1021/ja311905h.

[267] D. Sieh, P. Burger, *Z. Anorg. Allg. Chem.* **2015**, *641*, 52–55, DOI 10.1002/zaac.201400235.

[268] J. Schöffel, N. Šušnjar, S. Nückel, D. Sieh, P. Burger, *Eur. J. Inorg. Chem.* **2010**, *2010*, 4911–4915, DOI 10.1002/ejic.201000899.

[269] J. Abbenseth, M. Finger, C. Würtele, M. Kasanmascheff, S. Schneider, *Inorg. Chem. Front.* **2016**, *3*, 469–477, DOI 10.1039/C5QI00267B.

[270] Ł. Wolański, M. Domański, W. Grochala, P. Szarek, *Chem. – Eur. J.* **2019**, *25*, 10290–10293, DOI 10.1002/chem.201902142.

[271] X. Wang, J. T. Lyon, L. Andrews, *Inorg. Chem.* **2009**, *48*, 6297–6302, DOI 10.1021/ic900633k.

[272] X. Wang, L. Andrews, R. Lindh, V. Veryazov, B. O. Roos, *J. Phys. Chem. A* **2008**, *112*, 8030–8037, DOI 10.1021/jp804469a.

[273] Y. Gong, L. Andrews, *Inorg. Chem.* **2012**, *51*, 667–673, DOI 10.1021/ic2021758.

[274] S. B. Osin, D. I. Davliasthin, J. S. Ogden, *J. Fluor. Chem.* **1996**, *76*, 187–192, DOI 10.1016/0022-1139(95)03371-8.

[275] A. K. Brisdon, P. J. Jones, W. Levason, J. S. Ogden, J. H. Holloway, E. G. Hope, G. Stanger, *J. Chem. Soc. Dalton Trans.* **1990**, 715–718, DOI 10.1039/DT9900000715.

[276] S. B. Osin, D. I. Davlyatshin, D. S. Ogden, *Russ. J. Phys. Chem. A* **2001**, *75*, 1312–1318.

[277] J. H. Holloway, G. Stanger, E. G. Hope, W. Levason, J. Steven Ogden, *J. Chem. Soc. Dalton Trans.* **1988**, *0*, 1341–1345, DOI 10.1039/DT9880001341.

[278] J. V. Rau, S. Nunziante Cesaro, N. S. Chilingarov, G. Balducci, *Inorg. Chem.* **1999**, *38*, 5695–5697, DOI 10.1021/ic990294t.

[279] R. Hoffmann, S. Alvarez, C. Mealli, A. Falceto, T. J. Cahill, T. Zeng, G. Manca, *Chem. Rev.* **2016**, *116*, 8173–8192, DOI 10.1021/acs.chemrev.6b00251.

[280] I. B. Bersuker, *Chem. Rev.* **2013**, *113*, 1351–1390, DOI 10.1021/cr300279n.

[281] P. Garcia-Fernandez, I. B. Bersuker, *Phys. Rev. Lett.* **2011**, *106*, 246406, DOI 10.1103/PhysRevLett.106.246406.

[282] P. Garcia-Fernandez, I. B. Bersuker, J. E. Boggs, *J. Chem. Phys.* **2006**, *125*, 104102, DOI 10.1063/1.2346682.

[283] V. Kalamse, S. Gaikwad, A. Chaudhari, *Bull. Mater. Sci.* **2010**, *33*, 233–238, DOI 10.1007/s12034-010-0036-6.

7. List of Publications

Articles

[1] **Tony Stüker**, Xiya Xia, Helmut Beckers, and Sebastian Riedel, "High-Spin Iron(VI), Low-Spin Ruthenium(VI), and Magnetically Bistable Osmium(VI) in Molecular Group 8 Nitrido Trifluorides NMF_3", *Chem. Eur. J.*, **2021**, Advance online publication
https://doi.org/10.1002/chem.202101404

[2] Lin Li, Helmut Beckers, **Tony Stüker**, Tilen Lindič, Tobias Schlöder, Dirk Andrae, and Sebastian Riedel, "Molecular Oxofluorides OMF_n of Nickel, Palladium and Platinum: Oxyl Radicals with Moderate Ligand Field Inversion", *Inorg. Chem. Front.*, **2021**, *8*, 1215–1228
https://doi.org/10.1039/D0QI01151G

[3] **Tony Stüker**, Thomas Hohmann, Helmut Beckers, and Sebastian Riedel, "Fluoro Nitrenoid Complexes $FN{=}MF_2$ (M = Co, Rh, Ir): Electronic Structure Dichotomy and Formation of Nitrido Fluorides $N{\equiv}MF_3$", *Angew. Chem. Int. Ed.*, **2020**, *59*, 23174–23179; *Angew. Chem.*, **2020**, *132*, 23374–23379
https://doi.org/10.1002/anie.202010950
https://doi.org/10.1002/ange.202010950

[4] **Tony Stüker**, Helmut Beckers, and Sebastian Riedel, "A Cornucopia of Iridium Nitrogen Compounds Produced from Laser-Ablated Iridium Atoms and Dinitrogen", *Chem. Eur. J.*, **2020**, *26*, 7384–7394
https://doi.org/10.1002/chem.201905514

[5] Hongmin Li, Helmut Beckers, Lin Li, Günther Thiele, **Tony Stüker** and Sebastian Riedel, "Reactions of Titanium, Zirconium and Hafnium Atoms with Hydrogen Selenide: A Matrix-Isolation Study", *Chem. Phys. Let.*, **2020**, *740*, 137063
https://doi.org/10.1016/j.cplett.2019.137063

[6] Jan H. Nissen, Lucas Wickemeyer, **Tony Stüker**, Simon Steinhauer, Helmut Beckers, and Sebastian Riedel, "From Hypochlorites to Perfluorinated Dialkyl Peroxides", *J. Fluor. Chem.*, **2020**, *230*, 109416
https://doi.org/10.1016/j.jfluchem.2019.109416

[7] Lin Li,[+] **Tony Stüker**,[+] Lester Andrews, Helmut Beckers, and Sebastian Riedel, "Infrared Spectra of the HAnX and H_2AnX_2 Molecules (An=Th and U, X=Cl and Br) in Argon Matrices Supported by Electronic Structure Calculations", *Chem. Eur. J.*, **2019**, *25*, 1795–1805
https://doi.org/10.1002/chem.201805372
[+] Lin Li and Tony Stüker contributed equally to this work.

[8] Jan H. Nissen, **Tony Stüker**, Thomas Drews, Simon Steinhauer, Helmut Beckers, and Sebastian Riedel, "No Fear of Perfluorinated Peroxides: Syntheses and Solid-State Structures of Surprisingly Inert Perfluoroalkyl Peroxides", *Angew. Chem. Int. Ed.*, **2019**, *58*, 3584–3588; *Angew. Chem.*, **2019**, *131*, 3622–3626
https://doi.org/10.1002/anie.201814417
https://doi.org/10.1002/ange.201814417

[9] Lin Li, **Tony Stüker**, Stefanie Kieninger, Dirk Andrae, Tobias Schlöder, Yu Gong, Lester Andrews, Helmut Beckers, and Sebastian Riedel, "Oxygen radical character in group 11 oxygen fluorides", *Nat. Commun.*, **2018**, *9*, 1267
https://doi.org/10.1038/s41467-018-03630-0

[10] Klaus Banert, Madhu Chityala, Manfred Hagedorn, Helmut Beckers, **Tony Stüker**, Sebastian Riedel, Tobias Rüffer, and Heinrich Lang, "Tricyanomethane and Its Ketenimine Tautomer: Generation from Different Precursors and Analysis in Solution, Argon Matrix, and as a Single Crystal", *Angew. Chem. Int. Ed.*, **2017**, *56*, 9582–9586; *Angew. Chem.*, **2017**, *129*, 9710–9714
https://doi.org/10.1002/anie.201704561
https://doi.org/10.1002/ange.201704561

Conference Contributions — Poster Presentations

[1] **Tony Stüker**, Helmut Beckers, Sebastian Riedel, "Reaction of Laser-Ablated Iridium with Dinitrogen: Infrared Spectra of Matrix Isolated Iridium Nitrides, Dinitrogen-Complexes, and Anions", *Chemistry and Physics at Low Temperatures*, **2016**, Biarritz, France

[2] **Tony Stüker**, Helmut Beckers, Sebastian Riedel, "Reaction of Laser-Ablated Iridium with Dinitrogen: Infrared Spectra of Matrix Isolated Iridium Nitrides, Dinitrogen-Complexes, and Anions", *GDCh Wissenschaftsforum Chemie*, **2017**, Berlin, Germany

Appendix A Supporting Information of Publications

A.1 High-Spin Iron(VI), Low-Spin Ruthenium(VI), and Magnetically Bistable of Osmium(VI): Molecular Group 8 Nitrido Trifluorides NMF_3

Table of Contents

Experimental and Computational Details 2

Experimental Details 2

Computational Details 2

Detailed Assignments 4

$NFeF_3$ 5

$NRuF_3$ and $NRuF_4$ 6

$NOsF_3$ and $NOsF_4$ 7

Supplemental Computational Results 8

$NFeF_3$ 8

Supporting Figures 10

Supplementary Tables 19

Calculated molecular structures and vibrational data 35

Supporting Information References 84

Experimental and Computational Details

Experimental Details

$^{14}NF_3$ and $^{15}NF_3$ (synthesis described elsewhere[1]) were premixed 1:1000 with neon (99.999 %, Linde) in a stainless-steel cylinder. The mixing vessel was connected to a stainless-steel vacuum line connected to a self-made matrix chamber by a stainless-steel capillary. The gas mixture was then co-deposited for 100 min with laser-ablated iron, ruthenium or osmium atoms onto a gold plated copper mirror and cooled to 5 K by using a closed-cycle helium cryostat (Sumitomo Heavy Industries, RDK–205D) inside the vacuum chamber. For the laser-ablation, the 1064 nm fundamental of a Nd:YAG laser (Continuum, Minilite II, 10 Hz repetition rate, 35–50 mJ $pulse^{-1}$) was focused onto a rotating metal target. Infrared spectra were recorded on a Bruker Vertex 80v with evacuated optical path at 0.1 or 0.5 cm^{-1} resolution in the region 4000–430 cm^{-1} by using a liquid-nitrogen-cooled mercury cadmium telluride (MCT) detector.

Computational Details

Density functional theory (DFT) calculations are performed using the TURBOMOLE 7.0.1 program package[2] employing the GGA, meta-GGA or hybrid exchange-correlation density functionals BP86,[3] M06-L[4] and B3LYP,[5] respectively, with the polarized quadruple-ξ basis set def2-QZVP[6] which applies the Stuttgart-Dresden effective core potential for ruthenium and osmium.[7] The Coupled Cluster Single Double and perturbative Triple excitations (CCSD(T)) calculations are carried out in the spin unrestricted ROHF-UCCSD(T) open-shell coupled cluster formalism[8] using default frozen core settings as implemented in the Molpro 2019 software package.[9] The same software was used for all complete active space self-consistent field (CASSCF)[10] and n-electron valence state perturbation theory (NEVPT2)[11]

calculations. Unless stated otherwise, all CCSD(T) calculations were combined with the augmented triple-ξ basis sets aug-cc-pVTZ (for short: aVTZ) for nitrogen, fluorine, iron[12] and aug-cc-pVTZ-PP (for short: aVTZ-PP) for ruthenium and osmium.[13] Only the valence electrons [N,F: 2p 2s, M: (*n*-1)d *n*s] are correlated in the CCSD(T) and NEVPT2 dynamic correlation procedure when the (aug)-cc-pV*N*Z(-PP/-DK)[12a,12c,13] [for short: (a)VNZ(-PP/-DK)] basis sets are used. Whereas the metal based (*n*-1)s (*n*-1)p orbitals were included when the aug-cc-pwCV*N*Z(-PP/-DK)[12a,12c,13] [for short: awCV*N*Z(-PP/-DK), *N* = cardinal number D, T, Q or 5] basis sets are used. The active space for the state-specific complete active-space (SS-CASSCF) reference wavefunctions is chosen to consist of 8 electrons in 8 orbitals covering the Fe≡N three bonding, three antibonding and the two metal centered molecular orbitals. Larger active spaces including the Fe(4s) or Fe–F bonding molecular orbitals of (8,9) (14,11) and (14,12) were also applied. However, the larger active space did either not improve the wavefunction [(8,9)], or the optimization process led to wavefunctions which did not contain the desired molecular orbitals in the active space [(14,11), (14,12)]. NEVPT2 calculations for $NFeF_3$ were carried out with relativistic corrections using the second order Douglas-Kroll-Hess Hamiltonian.[14] Three diagnostic criteria, T_1, D_1 and the $\%TAE_e$[(T)] from CCSD(T) calculations were examined for all NMF_3 compounds under consideration. Except $NFeF_3$, all values shown in Table S7 are well within the limits of $T_1 \leq 0.05$, $D_1 \leq 0.15$ and %TAE ≤ 10 for 3d transition metal (TM) containing species[15] and $T_1 < 0.045$, $D_1 < 0.120$ and %TAE < 10 for 4d TM containing species.[16] The $NOsF_3$ ^{1}A'/ ^{3}A" minimum energy crossing point (MECP) was calculated at the UB3LYP/def2-TZVP[6b] and UHF-UCCSD(T)/cc-pVTZ(Os: cc-pVTZ-PP) level of theory using SurfCrossOpt as implemented in ORCA 4.2.0.[17] Harmonic vibrational frequency calculations were carried out for optimized structures analytically (BP86,

B3LYP, M06-L) or numerically (CCSD(T) and NEVPT2, step size of numerical differentiation: 0.01 a.u.) The $NFeF_3$, $NRuF_3$ and $NOsF_3$ APES scans were carried out with the same active space as described above in C_s point group symmetry. For $NFeF_3$ 9 electronic states ($3 \times {}^1A'$, $2 \times {}^1A''$, $2 \times {}^3A'$ and $2 \times {}^3A''$), for $NRuF_3$ and $NOsF_3$ 8 electronic states ($2 \times {}^1A'$, $1 \times {}^2A''$, $2 \times {}^3A'$ and $3 \times {}^3A''$) were averaged with equal weights with subsequent NEVPT2 treatment of all states individually. The Atoms in Molecules (AIM) charges[18] (Tables S8 and S12) were calculated using Multiwfn 3.6.[19] The NLMO/NPA Bond Orders,[20] Natural Charges (NPA)[20] and Wiberg Bond Indices[21] (Tables S8 and S12) were calculated using the NBO 7.0 software.[22] All rendered figures showing molecular structures and orbitals were obtained using the vmd 1.9.2 program.[23]

Detailed Assignments

By comparing spectra of the reaction products of different metal targets, metal dependent bands were identified. Further simplification was achieved by taking into account band positions of molecular binary fluorides MF_n, which were obtained by recording complementary spectra of the reaction products of metal atoms with elementary fluorine under the same conditions described above for the reaction with NF_3. For each experiment those bands were selected which are absent in the spectra obtained with other metal targets and which could not be assigned to the binary metal fluorides NF_n. Only this set of selected bands can be considered for the assignment of any novel species formed in this particular experiment. Their further assignment is based on the observed $^{14/15}N$ isotope shift and on their similar behavior in different experiments, such as e.g. in annealing or photolysis experiments. Only a few bands

from this selected set of bands could not be assigned to a NMF_n (n = 3, 4) species. They remained unassigned and were labelled e.g. with a diamond in each spectrum.

Photolysis experiments were conducted using LED light of λ = 730, 656, 617, 590, 528, 470, 455 and 273 nm and subsequently ArF excimer laser light of λ = 193 nm.

$NFeF_3$

The formation of molecular $NFeF_3$ (C_{3v}) is proved by the assignment of all stretching vibrations marked **A**, **B** and **C** at 946.4, 766.8 and 658.8 cm^{-1} in the IR spectrum obtained after co-depositing laser-ablated iron and NF_3 in excess neon shown in Figure S1 (see also Table S3). The FeF_3 stretching modes split into a degenerate e and an a_1 component at 766.8 and 658.8 cm^{-1}, respectively. The latter shows a small $^{14/15}N$ isotopic shift of −1.1 cm^{-1}. The corresponding bands for the group 6 $NCrF_3$ congener of C_{3v} point group symmetry (798 cm^{-1} (e), 709 cm^{-1} (a_1))[24] are located about 30 cm^{-1} and 50 cm^{-1}, respectively, higher than those assigned to $NFeF_3$. This redshift is the result of a weakening of the M-F bonds due to the partial e^2 occupation of the Fe centered orbitals that are slightly antibonding with respect to these bonds. This is further supported by the computed, slightly elongated Fe-F bond distances (Cr–F: 170 pm, Fe–F: 172 pm). The vibrational *e*-type mode of $NFeF_3$ exhibits a small splitting in two components (766.8 cm^{-1} and 766.7 cm^{-1}) with different intensities, which indicates that the degeneracy is moderately lifted, most likely due to different orientations of the $NFeF_3$ molecule within the matrix cavity. The Fe–N stretch at 946.4 cm^{-1}, marked **A** in Figure S1, shows a $^{14/15}N$ isotopic shift of −23.7 cm^{-1} (isotopic ratio of 1.0257). The band position of the previously reported cationic complex $[(TIMEN^R)Fe^{IV}(N)]BPh_4$ (R = xylyl, mesityl)[25] is with 1008 cm^{-1} higher, but (within given precision) exhibits the same isotopic ratio. Quantum-chemical calculations at the NEVPT2 level overestimate the N-Fe band position, but the predicted isotopic ratio of

1.0256 is very close to the experimentally observed value of 1.0257. Known bands at 744.7/744.7, 752.6 and 785.1 cm^{-1} were assigned to the molecular binary iron fluorides $^{56}FeF_3$, $^{56}FeF_2$ and $^{54}FeF_2$, respectively.[26]

$NRuF_3$ and $NRuF_4$

The spectra recorded after co-depositing laser-ablated ruthenium and NF_3 in excess of neon (Figure S2), clearly revealed the presence of two different nitrido ruthenium complexes, finally assigned to $NRuF_3$ (C_s) and $NRuF_4$ (C_{4v}). Their characteristic Ru≡N stretching bands are labeled **A** (1105.4 cm^{-1}, $NRuF_3$) and **A'** (1098.5 cm^{-1}, $NRuF_4$) in Figure S2. These bands show the same $^{14/15}N$ isotopic ratio of 1.0305 (Table S3). Their isotopic pattern due to seven naturally occurring, stable ruthenium isotopes obtained from spectra recorded at 0.1 cm^{-1} are listed in Table S4 and compared in Figure S4 with the predicted pattern. For the **A'** band the $^{96/104}Ru$ isotopic ratio were not experimentally determined, because of a low natural abundance (5.52 %) of the $N^{96}RuF_4$ isotopologue. $NRuF_4$ is likely formed by the exothermic addition of a fluorine atom to $NRuF_3$ (see Table S1).

The RuF_3 stretching modes of C_s symmetric $NRuF_3$ split into three modes. The strong antisymmetric F–Ru–F appears at 668.5 cm^{-1} (labeled **B** in Figure S2) and likely overlaps with the nearby weaker F'–Ru band. A control experiment in which laser-ablated Ru was deposited with F_2 instead of NF_3 revealed that also a band associated with a ruthenium fluoride might contribute to the strong **B** absorption. The symmetric F–Ru–F mode is attributed to the band labelled **C** at 635.8 cm^{-1}. From the RuF_4 stretching modes of $NRuF_4$ only the strongest band, the degenerate e-type mode could safely be assigned to the band labeled **B'** in Figure S2 centered at 700.0 cm^{-1}. The much weaker predicted RuF_4 a_1 band was not detected, probably because it is either too weak or overlapped by another band. The high-resolution spectrum shown

in Figure S5 reveals a distinct ruthenium isotopic pattern for all these three assigned Ru–F stretching modes (Tables S5 and S6). The band positions and isotopic pattern observed for $NRuF_4$ can be compared well with those reported for $ORuF_4$ isolated in solid nitrogen.[27] The reported $^{102}Ru{\equiv}O$ stretching mode (1059.5 cm^{-1}) is red-shifted by about 39 cm^{-1} with respect to $\nu(^{102}Ru{\equiv}N)$ (1098.5 cm^{-1}, Table S3), while the RuF_4 e-type mode is blue-shifted by about 10 cm^{-1}. Considering the greater mass of oxygen and the more interacting nitrogen matrix, the small red-shift suggests very similar bonding in both species. In fact, the bond order of $Ru{\equiv}O$ in $ORuF_4$ is predicted to be three as well.[28]

A few Ru–F stretching bands remained unassigned. The $^{96/104}Ru$ isotopic ratio of the band labeled by a plus sign at 651.9 cm^{-1} in Figure S2 exhibits a characteristic ruthenium isotopic pattern expected for a mononuclear Ru complex, and the two bands labeled with a pound sign at 606.5 and 616.5 cm^{-1} show a different isotopic pattern, probably caused by a Ru dimer complex.

$NOsF_3$ and $NOsF_4$

The metal-nitrogen stretching region of the spectra obtained by co-depositing of laser-ablated osmium and $^{14}NF_3$ contains one band labeled **A** in Figure S3 at 1140.1 cm^{-1}, while the spectra obtained using isotopic label $^{15}NF_3$ contains two N–Os stretching bands. The first band at 1104.6 cm^{-1} is caused by the ^{15}N isotopologue of **A** and shows a $^{14/15}N$ isotopic shift of −35.5 cm^{-1} and a $^{14/15}N$ isotopic ratio of 1.03214. By applying the isotopic ratio obtained for **A** to the second band at 1086.0 cm^{-1}, we obtain 1120.9 cm^{-1} as an estimated value for the ^{14}N isotopologue of the second band labeled **A'** in Figure S3. This band is overlapped by the stronger band associated with the ^{14}NF radical. Both bands are assigned to $NOsF_3$ in two electronic states. Band **A**

is assigned to the Os≡N stretching mode of $NOsF_3$ in the $^1A'$ ground state, and band **A'** to $NOsF_3$ in a near-by excited $^3A''$ electronic state. The Os–F stretching bands assigned to $NOsF_3$ ($^1A'$) are labeled **B**, **C** and **D** in Figure S3 and are at 686.0, with a matrix site at 686.6 cm^{-1}, at 641.3 with a weaker matrix site at 640.1 cm^{-1} and at 632.3 cm^{-1}, respectively. Bands **B** and **D** are assigned to the symmetric and antisymmetric F–Os–F stretching mode, respectively, and **C** to the F'–Os stretching mode. Bands labeled **B'**, **C'** and **D'** at 675.8 cm^{-1} (with a matrix site at 677.0 cm^{-1}), 660.5 cm^{-1} (matrix site at 658.9 cm^{-1}), and 607.4 cm^{-1}, respectively, are assigned to $NOsF_3$ ($^3A''$). Finally, the band labeled **A''** at 689.6 cm^{-1} is tentatively assigned to the OsF_4 e-type mode of $NOsF_4$ in C_{4v} symmetry. The N–Os stretching band and the remaining Os–F stretching bands of $NOsF_4$ are predicted with significantly lower intensity and were not detected. The intensity of the bands assigned to $NOsF_3$ and $NOsF_4$ did not change in annealing and photolysis experiments. All assignments and isotopic shifts are in excellent agreement with values obtained at the CCSD(T) level of theory summarized in Table S3.

Supplemental Computational Results

$NFeF_3$

The B3LYP hybrid functional was found to perform worst when comparing the Fe–N bond length and stretching frequency with results from other single-reference methods (DFT and CCSD(T)) or multi-reference NEVPT2 calculations (Table S2). To obtain reliable structural and vibrational data for $NFeF_3$ by taking dynamical, non-dynamical and core-valence correlation effects, as well as scalar relativistic effects into account the NEVPT2/CASSCF(8,8)/aVTZ-DK(Fe: awCVTZ-DK) method was employed. The

rearrangement of the iron fluoroimino intermediate, $FN=FeF_2$, to the high-valent iron nitrido trifluoride $N\equiv FeF_3$ is predicted to be exothermic by only −7 kJ mol^{-1} at the B3LYP level (Table S1), while the GGA and meta-GGA functionals BP86 and M06-L predict more exothermic reaction enthalpies of −78 and −74 kJ mol^{-1}, respectively. The latter predictions agree better with the NEVPT2 results (Table S2). CASSCF(8,8) calculations reveal that the leading configuration of $NFeF_3$ is $\sigma^2\pi^2\pi^2\delta^1\delta^1\pi^{*0}\pi^{*0}\sigma^{*0}$, which contributes only 60 % to the $^3A_2$ ground state. The small ligand field splitting, i. e. the low energy gap between the non-bonding 3d(Fe,δ)-MOs and the antibonding MOs indicates a poor overlap between the 3d(Fe) orbitals with the N^{3-} ligand orbitals,[29] and leads to a significant population of Fe≡N antibonding π^* and σ^* orbitals (Figure S6). The effective bond order[30] (EBO) of the individual bonds is 0.8 (σ) and 0.7 (π), a total of 2.2, or an integer BO of 3. The NLMO bond order of 2.30 and the Wiberg bond index of 2.52 obtained from analyzing the DFT wavefunction (Table S8) further support the assignment of a Fe≡N triple bond. The short calculated Fe≡N bond length of 153 pm is within the range of reported crystallographic data for iron complexes with triply bonded nitride ligands of 153 pm ([(TIMEN^R)Fe^{IV}(N)]BPh$_4$, R = xylyl, mesityl),[25] 151 pm ([PhB(^{t}BuIm)$_3$Fe^{IV}(N)])[31] and 150–151 pm ([PhB(^{t}BuIm)$_3$Fe^{V}(N)]BarF$_{24}$)[31], or 157 pm ([(Me$_3$cyac)Fe^{VI}(N)](PF$_6$)$_2$, derived from EXAFS data)[32].

Supporting Figures

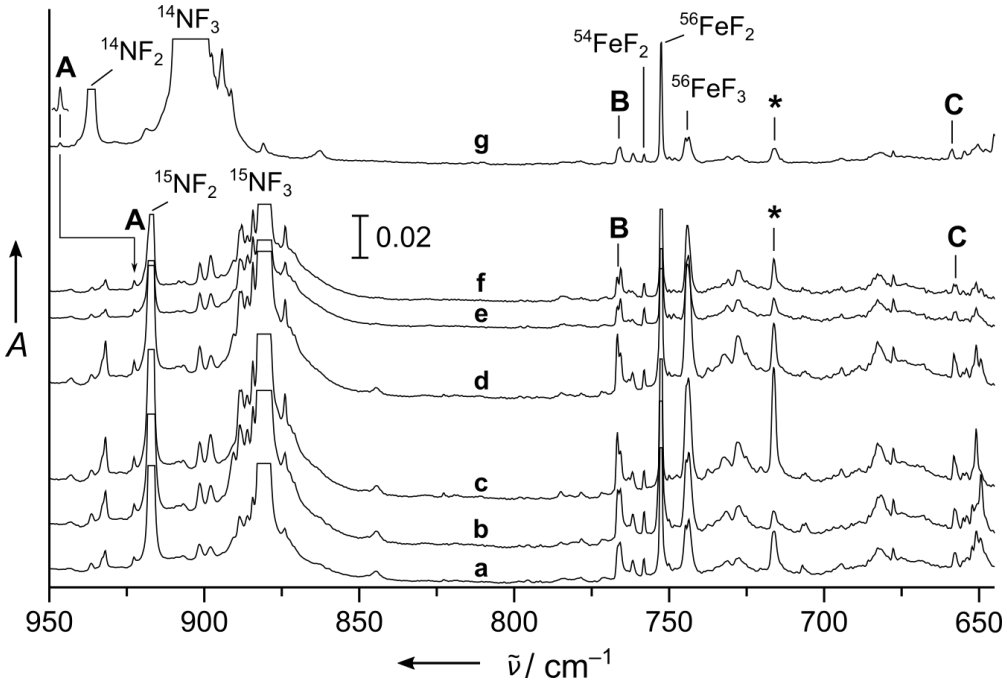

Figure S1. IR spectra of laser ablated iron co-deposited with 0.1 % $^{15}NF_3$ in Ne (**a**), after 10 min irradiation using LED light of λ = 656±10 nm (**b**), 470±10 nm (**c**), 273±10 nm (**d**), as well as a 193 nm excimer laser radiation (**e**), and successive annealing to *T* = 10 K (**f**). Experiment using 0.1 % $^{14}NF_3$ in Ne (g). Bands labeled **A**, **B** and **C** are assigned to $NFeF_3$ (see Table S3). Band **A** is by a factor of five in spectrum **g**. Known bands of binary iron fluorides[26] are indicated, and an unassigned band showing no$^{14/15}$N isotopic shift is marked with an asterisk. Note that $NFeF_3$ is unaffected by annealing to 10 K or the selective LED radiations, but this band slightly gains intensity upon irradiation with LED light with λ = 656 nm and lose intensity when irradiated with laser light of λ = 193 nm.

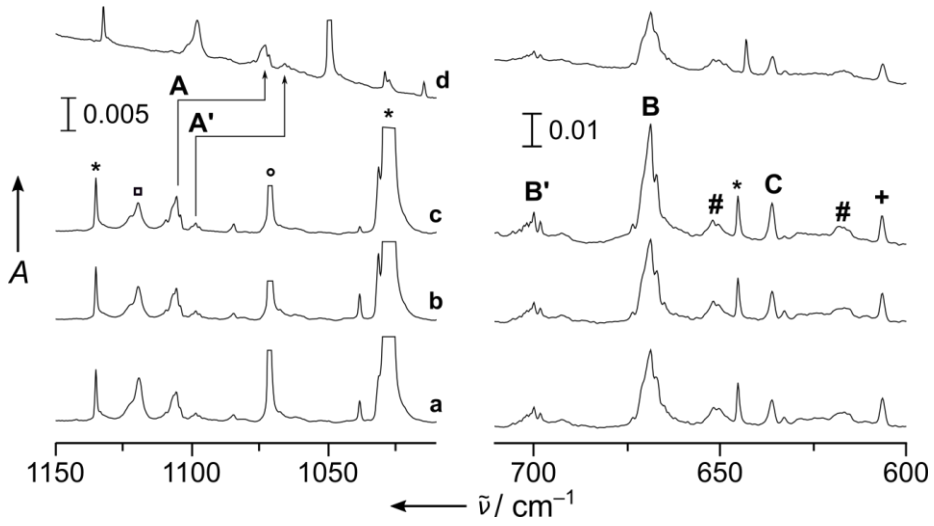

Figure S2. IR spectra of laser ablated ruthenium co-deposited with 0.1 % $^{14}NF_3$ in Ne (**a**), after annealing to 10 K (**b**), and broadband photolysis (**c**). Co-deposition of Ru with 0.1 % $^{15}NF_3$ in Ne (**d**). Bands labeled **A** – **C** are attributed to $NRuF_3$ and **A'** and **B'** are due to $NRuF_4$. Unknown product bands are labeled by a pound and plus sign, respectively. The bands associated with ^{14}NF, $^{14}NF_2$ and $^{14}NF_3$ are marked with squares, circles and asterisks, respectively.[33]

Note that the $^{96/104}$Ru isotopic ratio of the band labeled by a plus sign at 651.9 cm^{-1} exhibits a characteristic ruthenium isotopic pattern expected for a mononuclear Ru complex, while the two bands labeled with a pound sign at 606.5 and 616.5 cm^{-1} show a different isotopic pattern, probably caused by a Ru dimer complex.

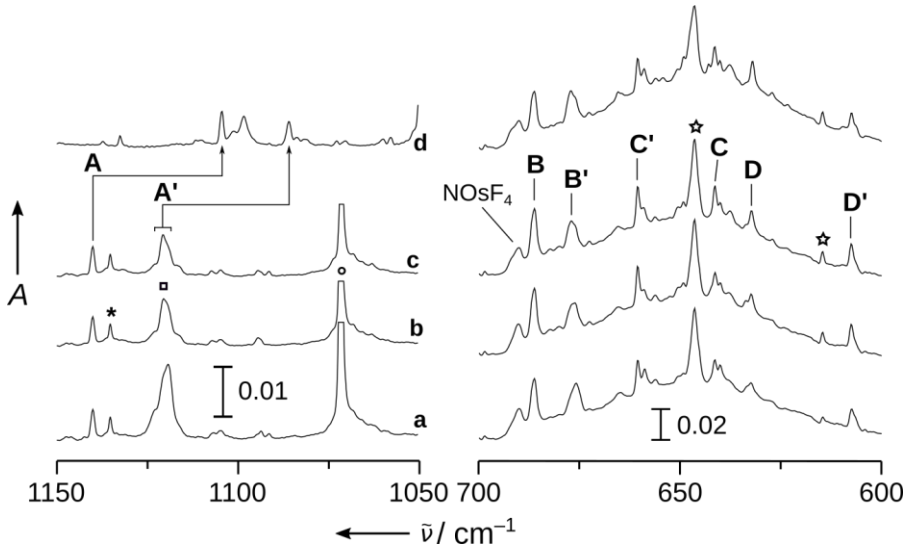

Figure S3. IR spectra of laser ablated osmium co-deposited with 0.1 % $^{14}NF_3$ in Ne (**a**), after annealing to 10 K (**b**), and broadband photolysis (**c**). Co-deposition of Os with 0.1 % $^{15}NF_3$ in Ne (**d**). Bands labeled **A**–**D** are attributed to $NOsF_3$ and **A'**–**D'** to $NOsF_3$ ($^3A''$). Bands of binary osmium fluorides are marked with star symbols. The bands associated with ^{14}NF, $^{14}NF_2$ and $^{14}NF_3$ are marked with squares, circles and asterisks, respectively.[33]

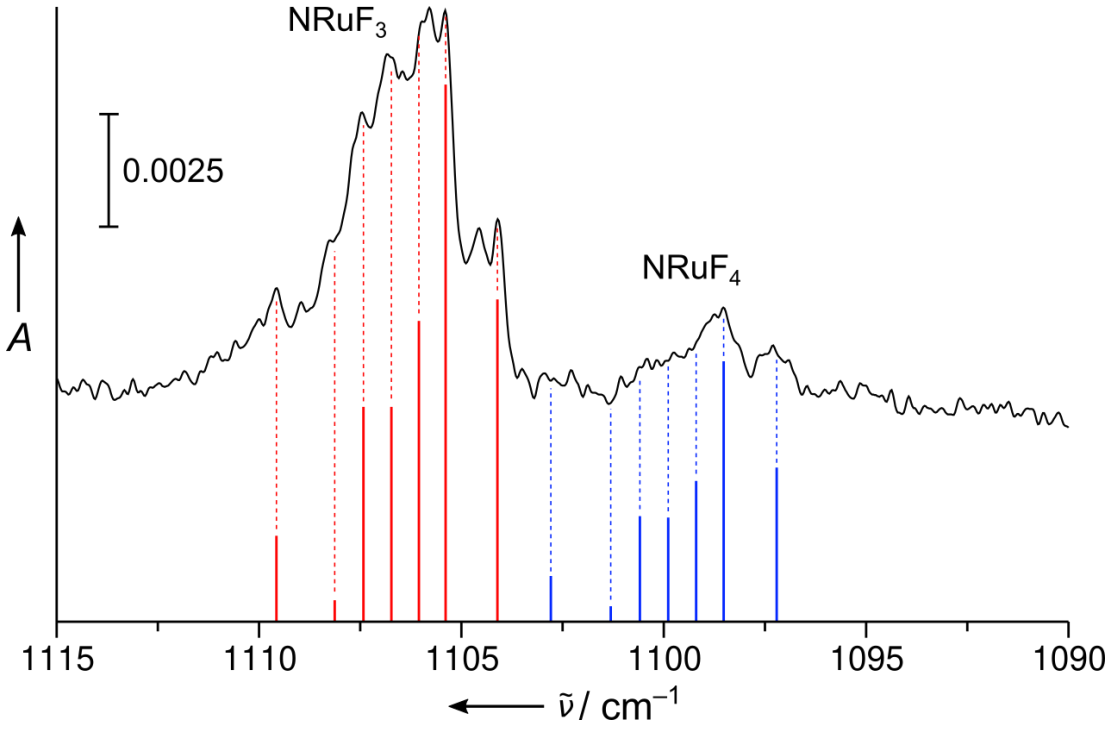

Figure S4. Infrared absorption spectrum of laser ablated ruthenium with 0.1 % NF_3 displaying the N-Ru stretching bands of $NRuF_3$ and $NRuF_4$ in a spectral resolution of 0.1 cm^{-1}. The pattern is caused by the seven naturally occurring, stable ruthenium isotopes (see Table S4).

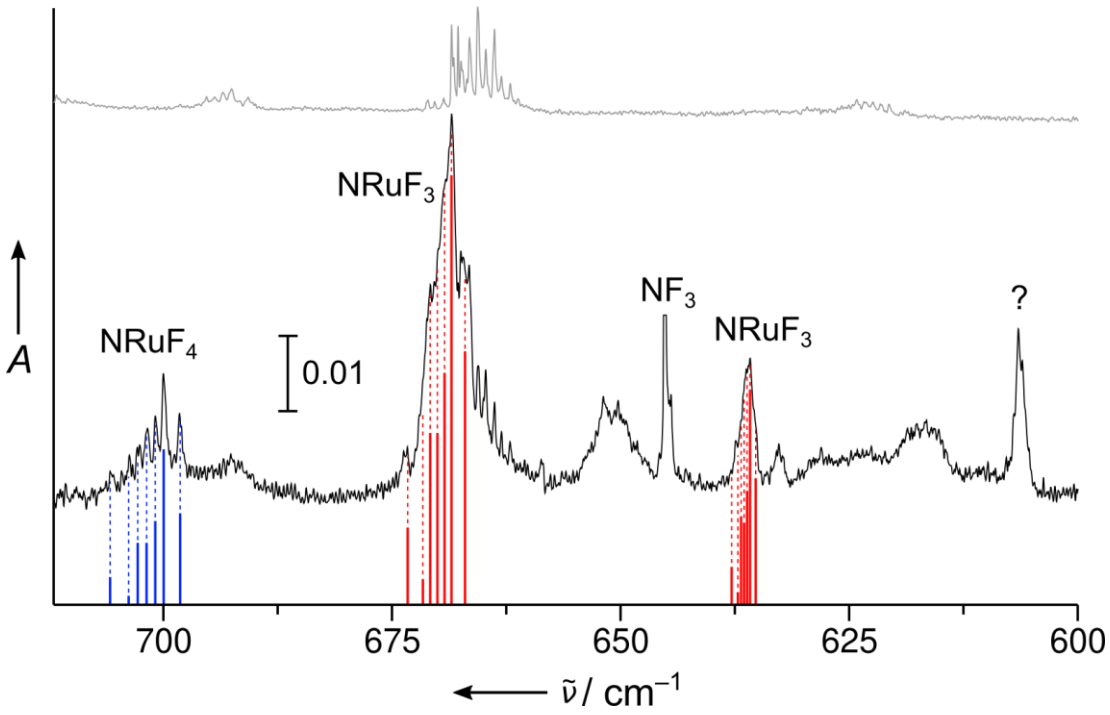

Figure S5. Infrared absorption spectrum of laser ablated ruthenium with 0.1 % NF_3 displaying the RuF stretching bands of $NRuF_3$ and $NRuF_4$ in a spectral resolution of 0.1 cm^{-1}. The pattern is caused by the seven naturally occurring, stable ruthenium isotopes (see Tables S5 and S6).

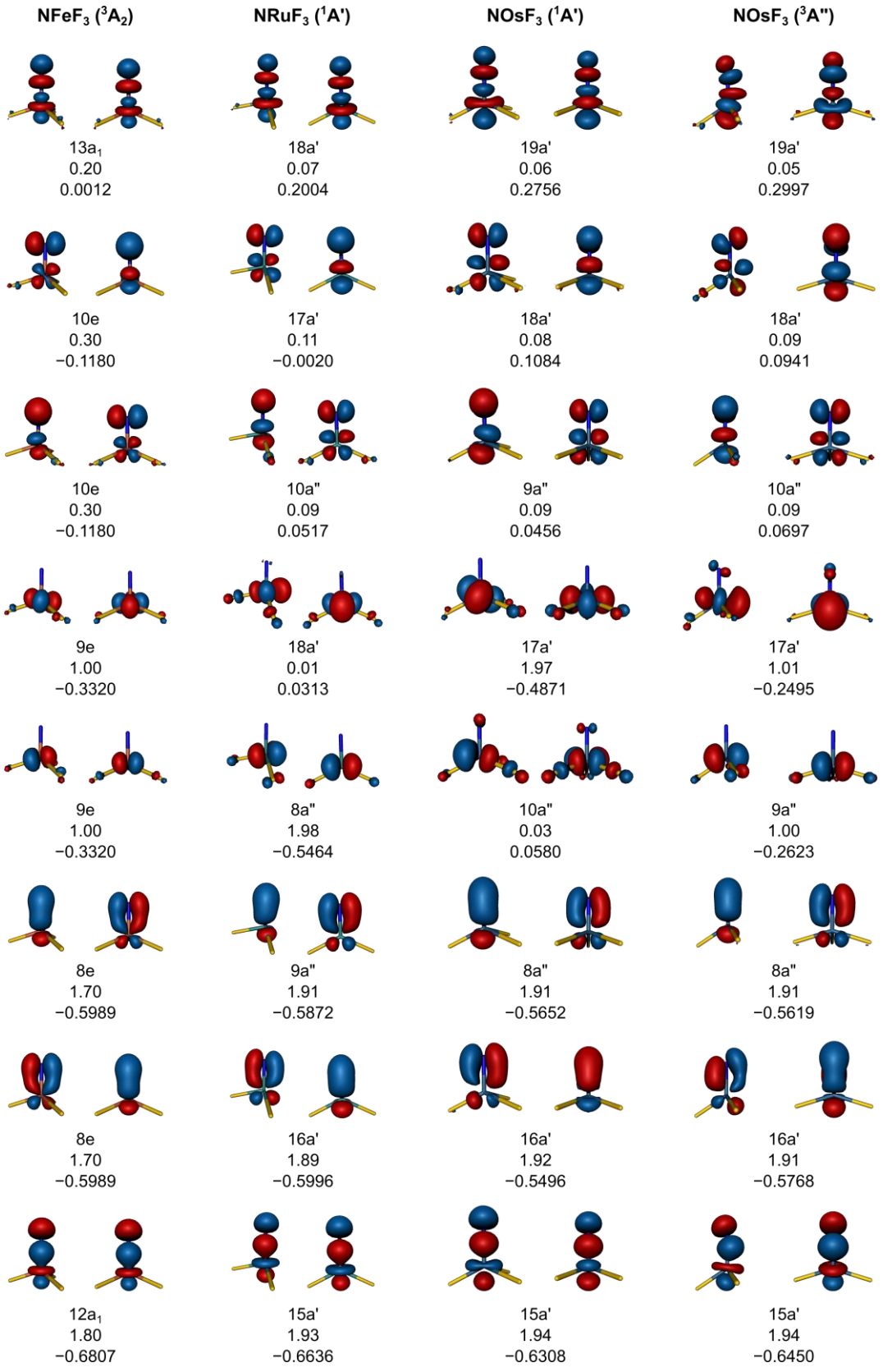

Figure S6. Active space natural molecular orbital plot at σ = 0.1 e Bohr^{-3}, irreproducible representations, occupation numbers and orbital energies (hartree) of $NFeF_3$ ($^3A_2$), $NRuF_3$ ($^1A'$), $NOsF_3$ ($^1A'$) and $NOsF_3$ ($^3A''$) calculated at the CASSCF(8,8)/aug-cc-pVTZ(-PP) level of theory at the

CCSD(T)/aug-cc-pVTZ-(-PP) (M = Ru, Os) or NEVPT2/aug-cc-pwCVTZ-DK (M = Fe) optimized ground state structures. For the singlet states of $NRhF_3$ and $NOsF_3$ a state-averaging procedure (Molpro: “states,2;weight,0.9,0.1”) was applied to include the desired orbitals into the active space. Two columns are shown for each species: In the right column the molecules are shown in the xz plane, whereas they are shown in the yz plane in the left column. The molecular orbitals for each species are ordered according to those of $NFeF_3$ as reference.

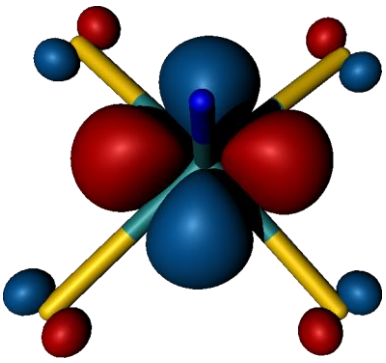

Figure S7. Singly occupied molecular orbital (SOMO) plot of $NRuF_4$ at σ = 0.1 e $Bohr^{-3}$ obtained at the ROHF/aug-cc-pVTZ(Ru: aug-cc-pVTZ-PP) level of theory.

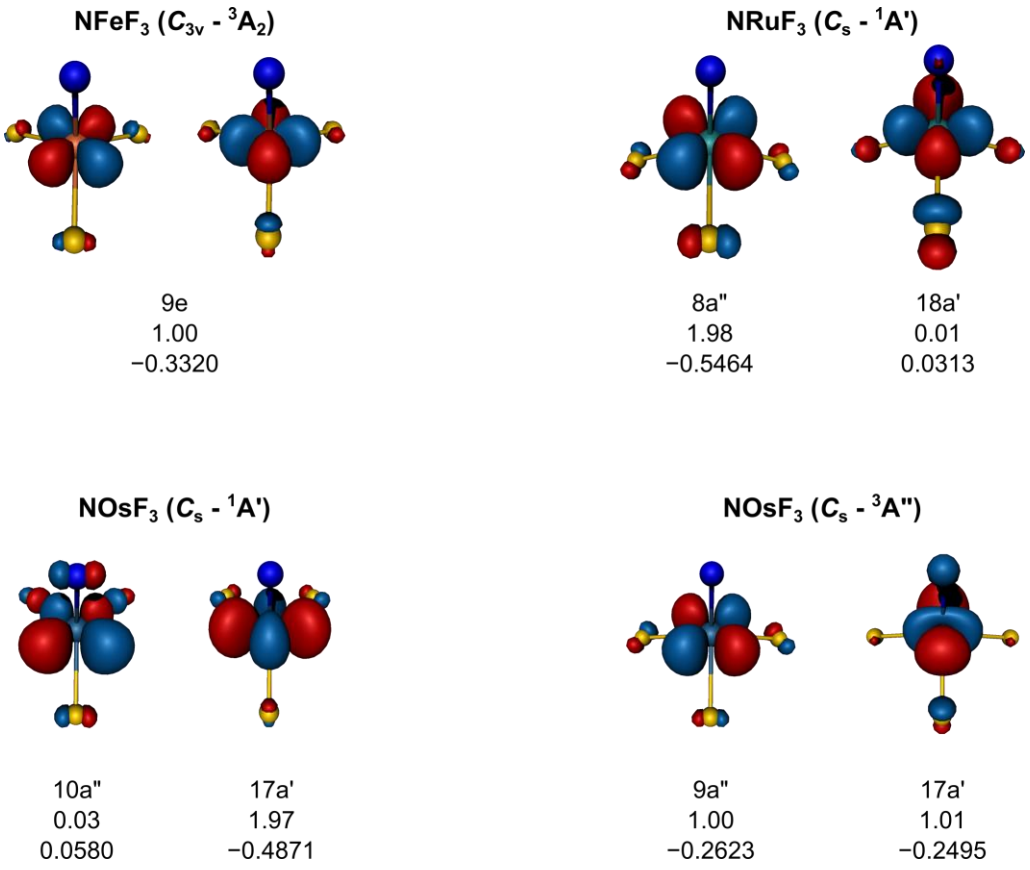

Figure S8. Plot of the metal centered e-type natural molecular orbitals of NMF_3 at σ = 0.1 e Bohr^{-3}, irreproducible representations, occupation numbers and orbital energies (hartree) of $NFeF_3$ ($^3A_2$), $NRuF_3$ ($^1A'$), $NOsF_3$ ($^1A'$) and $NOsF_3$ ($^3A''$) calculated at the CASSCF(8,8)/aug-cc-pVTZ(-PP) level of theory at the CCSD(T)/aug-cc-pVTZ-(-PP) (M = Ru, Os) or NEVPT2/aug-cc-pwCVTZ-DK (M = Fe) optimized ground state structures. For the singlet states of $NRhF_3$ and $NOsF_3$ a state-averaging procedure (Molpro: "states,2;weight,0.9,0.1") was applied to include the desired orbitals into the active space.

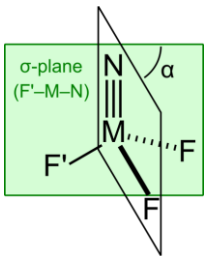

Figure S9. Dihedral angle α between the F'–M–N σ-plane and a F–M–N plane.

Supplementary Tables

Table S1. Experimental Fe−N distances (Å) and stretching fundamentals (cm^{-1}) of representative high-valent iron nitride complexes.

Complex	Fe−N distances (Å)	Fe−^{14}N stretch (cm^{-1})
$[Fe^{V}N(OEP)]$ [a]		876 (RR)
$[Fe^{V}N(TPP)]$ [a]		876 (RR)
$[Fe^{V}N(TTPPP)]$ [b]		876 (RR)
$[Fe^{V}(N)(Me_2Py_2TACN)]^{2+}$ [c]		866 (IRPD)
$[Fe^{V}(N)(MePy_2TACN)](PF_6)_2$ [34]	1.64(1) (EXAFS)	855 (IRPD)
$[Fe^{V}(N)(cyclam\text{-}ac)]^{+}$ [d]	1.61(1) (EXAFS)	864 (NRVS)
$[Fe^{VI}(N)(Me_3cyclam\text{-}ac)]^{2+}$ [32]	1.57(2) (EXAFS)	
$[Fe^{IV}(N)(PhB(CH_2P^{i}Pr_2)_3]$ [35]	1.51–1.55 (EXAFS)	1034
$[Fe^{IV}(N)(P_3{}^{B})]^{+}$ [e]	1.54(2) (EXAFS)	
$[Fe^{IV}(N)(PhB(^{t}BuIm)_3)]$ [36] [f]	1.532(5) (X-Ray)	
$[Fe^{IV}(N)(PhB(^{t}BuIm)_3)]$ [37]	1.512(1) (X-Ray)	1028 (RR)
$[Fe^{V}(N)(PhB(^{t}BuIm)_3)]^{+}$ [31]	1.506(2)/1.502(2) (X-Ray)	
$[Fe^{IV}(N)(TIMEN^{Mes})]^{+}$ [g] [25]	1.526(2) (X-Ray)	1008
$[Fe^{IV}(N)(TIMMN^{Mes})]^{+}$ [38]	1.513(3) (X-Ray)	
$Fe^{V}(N)(TIMMN^{Mes})]^{2+}$ [38]	1.529(1) (X-Ray)	

[a]: RR: Resonance Raman (OEP^{2-}: octaethylporphinato dianion, TPP^{2-}: tetraphenylporphinato dianion).[39] ν(M=N) of stable nitridomanganese(V) porphyrins and nitridochromium(V) porphyrins were observed at 1049–1052 cm^{-1} for the former[40] and at 1017 cm^{-1} for the latter.[41]

[b]: RR: Resonance Raman ($TTPPP^{2-}$ = tetrakis-(2,4,6-triphenylphenyl)porphyrinato dianion).[42]

[c]: (Me_2Py_2tacn): 1-(di(pyridin-2-yl) methyl)-4,7-dimethyl-1,4,7-triazacyclononane, IRPD: infrared photodissociation;[34b]

[d]: NRVS: nuclear resonant vibrational spectroscopy.[43]

[e]: $P_3{}^{B}$:= tris(o-diisopropylphosphinophenyl)borane.[44]

[f]: $PhB(^{t}BuIm)_3)^{-}$ = phenyltris(3-tert-butylimidazol-2-ylidene.

[g]: $TIMEN^{Mes}$ = tris[2-(3-mesityl-imidazol-2-ylidene)ethyl]-amine.

[h]: $TIMMN^{Mes}$ = tris-[2-(3-mesityl-imidazol-2-ylidene)methyl]-amine.

Table S2. Selected reaction enthalpies at T = 0 for MNF_n compounds (n = 1–3 for M = Fe and n = 1–4 for M = Ru, Os) obtained at the B3LYP, BP86 and M06-L (Fe only) levels of theory.[a]

Reaction		ΔH^0 [kJ mol^{-1}]		
		B3LYP	**BP86**	**M06-L**
Fe + NF_3	→ F_2NFeF ($^3A'$)	−331	−391	−351
F_2NFeF ($^3A'$)	→ $FNFeF_2$ ($^3A''$)	−239	−246	−267
$FNFeF_2$ ($^2A''$)	→ $NFeF_3$ (C_{3v}, $^3A_2$) [a]	−4	−78	−74
$NFeF_3$ ($^3A_2$ – C_{3v})	→ $NFeF_2$ ($^2A_2$) + F	277	327	324
$NFeF_3$ ($^3A_2$ – C_{3v})	→ $NFeF_2$ ($^2A_2$) + ½ F_2	204	224	250
$NFeF_3$ ($^3A_2$ – C_{3v})	→ NFeF ($^1A'$) + F_2	597	592	604
$NFeF_3$ ($^3A_2$ – C_{3v}) + F	→ $NFeF_2$ ($^2A_2$) + F_2	131	121	177
Ru + NF_3	→ F_2NRuF ($^3A''$)	−386	−439	-
F_2NRuF ($^3A''$)	→ $FNRuF_2$ ($^3A''$)	−238	−258	-
$FNRuF_2$ ($^3A''$)	→ $NRuF_3$ (C_{3v}, $^3A_2$)	−153	−162	-
$FNRuF_2$ ($^3A''$)	→ $NRuF_3$ ($^1A'$)	−143	−146	-
$NRuF_3$ ($^1A'$) + F	→ $NRuF_4$ (C_{4v}, $^2B_2$)	−305	−371	-
$NRuF_3$ ($^3A''$)	→ $NRuF_2$ (C_{2v}, $^2A_2$) + F	286	332	-
$NRuF_3$ ($^3A''$)	→ $NRuF_2$ (C_{2v}, $^2A_2$) + ½ F	213	232	-
$NRuF_3$ ($^3A''$)	→ NRuF ($^1A'$) + F_2	535	577	-
$NRuF_3$ ($^3A''$) + F	→ $NRuF_2$ (C_{2v}, $^2A_2$) + F_2	140	129	-
Os + NF_3	→ F_2NOsF (C_{2v}, $^3A_1$)	−413	−474	-
F_2NOsF ($^3A_1$ - C_{2v})	→ $FNOsF_2$ ($^3A''$)	−295	−299	-
$FNOsF_2$ ($^3A''$)	→ $NOsF_3$ ($^1A'$)	−196	−193	-
$FNOsF_2$ ($^3A''$)	→ $NOsF_3$ ($^3A''$)	−206	−208	-
$NOsF_3$ ($^3A''$)	→ $NOsF_2$ ($^3A''$) + F	288	330	-
$NOsF_3$ ($^3A''$)	→ $NOsF_2$ ($^3A''$) + ½ F	215	227	-
$NOsF_3$ ($^3A''$)	→ NOsF ($^1A'$) + F_2	674	686	-
$NOsF_3$ ($^3A''$) + F	→ $NOsF_2$ (C_{2v}, $^2A_1$) + F_2	142	124	-

[a] Unless stated otherwise, complexes were optimized in *C*s point group symmetry.
[b] ROB3LYP/def2-QZVP: −31 kJ mol^{-1}, CCSD(T)/aug-cc-pVTZ-DK: −66 kJ mol

Table S3. Comparison of the computed N–Fe stretching frequency (ν(Fe–N) in cm^{-1}) and bond length (r(Fe–N) in pm) in $NFeF_3$ obtained at spin unrestricted and restricted open-shell DFT, CCSD(T) and NEVPT2 levels of theory.

Method	**ν(Fe–N)**	**r(N–Fe)**	**SC / T_1 / C_0^2 [a]**
UB3LYP	421	163.8	1.343
UM06-L	785	154.5	0.556
UBP86	1096	151.1	0.070
ROB3LYP [b]	1192	148.0	-
CCSD(T)	757	161.2	0.101
NEVPT2	1028	153.3	0.599

[a] Diagnostics of multi-reference character: SC (spin contamination) for unrestricted DFT methods UB3LYP, UM06-L and UBP86, T_1 diagnostic for CCSD(T) and the weight of the leading configuration C_0^2 of the CASSCF wave function. [b] Calculated using Molpro 2019.

Table S4. Calculated and experimental vibrational wavenumbers ($\nu(^{14}N)$ in cm^{-1}) and $^{14/15}N$ isotopic shifts ($\Delta\nu$ in parentheses) for $NFeF_3$, $NRuF_3$, $NRuF_4$, $NOsF_3$ and $NOsF_4$.

Exp. [a]	BP86 [b]	B3LYP [b]	CCSD(T) [b]	Assignment
		$NFeF_3$ (C_{3v}, $^3A_2$) [c]		
946.4 (−23.7)	1096 (−28) [34]	421 (−12) [21]	1028 (−26) [-] [d]	NFe str., a_1
766.8 (0) / 766.7 (0)	691 (0) [2 × 100]	701 [2 × 146]	737(0) [-] [d]	FeF_3 str., e
658.8 (−1.1)	650 (−1) [40]	683 (1) [33]	689 (−2) [-] [d]	FeF_3 str., a_1
		$N^{102}RuF_3$ (C_s, $^1A'$)		
1105.4 (−32.7)	1150 (−34) [40]	1202 (−35) [43]	1085 (−32) [-]	NRu str., a’
[e]	651 (0) [46]	669 (0) [54]	682 (0) [-]	F’-Ru str., a’
668.5 (0)	641 (0) [150]	661 (0) [171]	678 (0) [-]	antisym. F-Ru-F str., a”
635.8 (0)	618 (0) [48]	634 (0) [58]	649 (0) [-]	sym. F-Ru-F str., a’
		$N^{102}RuF_4$ (C_{4v}, $^2B_1$)		
1098.5 (−32.5)	1060 (−31) [16]	1175 (−35) [15]	1080 (−32) [-]	NRu str., a_1
700.1 (0)	675 (0) [2 × 162]	694 (0) [2 × 196]	711 (0) [-]	RuF_4 stretch, e
- [e]	645 (0) [22]	670 (0) [27]	681 (0) [-]	RuF_4 stretch, a_1
- [f]	576 (0) [0]	588 (0) [0]	598 (0) [-]	RuF_4 stretch, b_2
		$NOsF_3$ (C_s, $^1A'$)		
1140.1 (−35.5)	1148 (−36) [23]	1196 (−38) [28]	1152 (−36) [-]	NOs str., a’
686.0 / 686.6 (0)	657 (0) [98]	671 (0) [94]	689 (0) [-]	OsF_2 sym. str., a’
641.3 / 640.0 (0)	637 (0) [45]	647 (0) [75]	664 (0) [-]	OsF’ sym. str., a’
632.3 (0)	609 (0) [51]	629 (0) [59]	652 (0) [-]	OsF_2 antisym. str., a”
		$NOsF_3$ (C_s, $^3A''$)		

1086.0 (-) [f]	1089 (-35) [27]	1130 (-37) [31]	1095 (-36) [-]	^{15}NOs str, a’
675.8 / 677.0	646 (0) [134]	657 (0) [153]	675 (0) [-]	OsF_2 antisym. str., a”
660.5 / 658.9 (0)	637 (0) [36]	652 (0) [50]	668 (0) [-]	OsF_2 sym. str., a’
607.4 (0.0)	581 (0) [66]	594 (0) [75]	614 (0) [-]	OsF’ sym. str., a’
		$NOsF_4$ (C_{4v}, $^2B_1$)		
- [g]	1140 (−36) [13]	1192 (−37) [13]	1145 (−36) [-]	NOs str., a_1
- [g]	664 (0) [25]	687 (0) [31]	706 (0) [-]	OsF_4 stretch, a_1
689.9 (0)	658 (0) [2 × 152]	674 (0) [2 × 176]	693 (0) [-]	OsF_4 stretch, e
- [h]	605 (0) [0]	617 (0) [0]	635 (0) [-]	OsF_4 stretch, b_2

[a] Neon matrix; matrix sites are separated by a slash. [b] Intensities in km mol^{-1} in square brackets. [c] M06-L/def2-QZVP: 785 a_1 (−11) [12], 703 e (0) [200], 617 a_1 (−1) [40]. [d] NEVPT2/aug-cc-pwCVTZ-DK; [f] ν(^{15}N–Os) in cm^{-1}, see text. [e] Band is likely hidden by the stronger antisymmetric F-Ru-F stretching mode (a’’). [g] Too weak or overlapped. [h] Not IR active.

Table S5. The experimental isotopic pattern of the N-Ru stretching band of $NRuF_3$ caused by the seven naturally occurring, stable ruthenium isotopes.

Isotopologue	ν(NRu), a'	ν(FRuF) antisym., a''	ν(RuF'), a'
$N^{96}RuF_3$	1109.57	673.32	637.93
$N^{98}RuF_3$	1108.25	*too weak*	*too weak*
$N^{99}RuF_3$	1107.46	670.80	636.83
$N^{100}RuF_3$	1106.83	669.96	636.43
$N^{101}RuF_3$	1105.97	669.12	636.05
$N^{102}RuF_3$	1105.40	668.48	635.84
$N^{104}RuF_3$	1104.10	666.94	635.16

Table 6. The experimental isotopic pattern of the N-Ru stretching band of $NRuF_4$ caused by the seven naturally occurring, stable ruthenium isotopes.

Isotopologue	ν(NRu), a'
$N^{96}RuF_4$	705.85
$N^{98}RuF_4$	703.73
$N^{99}RuF_4$	702.87
$N^{100}RuF_4$	701.89
$N^{101}RuF_4$	700.89
$N^{102}RuF_4$	700.01
$N^{104}RuF_4$	698.25

Table S7. Comparison of the experimental and calculated $^{96/104}$Ru isotopic ratios of the bands assigned to $NRuF_3$ and $NRuF_4$.

	Frequency [cm^{-1}] [a]	**$^{96/104}$Ru Isotopic Ratio**		
	Exp.	**Exp.**	**B3LYP**	**CCSD(T)**
$NRuF_3$				
ν(NRu), a’	1105.40	1.00495	1.00495	1.00497
ν(FRuF),antisym.a’’	668.48	1.00956	1.00940	1.00963
ν(RuF’),a’	635.84	1.00361	1.00414	1.00378
$NRuF_4$				
ν(NRu), a’	1098.53	- [b]	1.00509	1.00507
ν(NRu), a’	700.01	1.01088	1.01097	1.01093
Unknown Product	606.52	1.00289	-	-

[a] Band position of isotopologue containing the most abundant ruthenium isotope ^{102}Ru; [b] Intensity too low to safely assign the $NRu^{96}F_4$ band (see Figure S5)

Table S8. CCSD(T) diagnostics to estimate the presence of multi-reference character of NMF_3 (M = Fe, Ru, Os).

Compound	T_1	D_1	**%TAE**
$NFeF_3$ ($^3A_2$)	0.1013	0.4353	14.2
$NRuF_3$ (^{1}A’)	0.0356	0.1166	7.7
$NRuF_3$ (^{3}A’’)	0.0296	0.0922	7.8
$NOsF_3$ (^{1}A’)	0.0280	0.0915	6.8
$NOsF_3$ (^{3}A”)	0.0290	0.0839	6.6

Table S9. AIM charges, NPA charges, NLMO bond orders (totals by atom) and Wiberg bond indices (totals by atom) for all experimentally detected NMF_3 and NMF_4 species calculated at the DFT (M06-L for M = Fe and B3LYP for M = Ru, Os) levels of theory.

	$NFeF_3$ ($^3A_2$)		**$NRuF_3$ ($^1A_1$)**		**$NOsF_3$ ($^1A'$)**		**$NOsF_3$ ($^3A''$)**		**$NRuF_4$ ($^2B_2$)**		**$NOsF_4$ ($^2B_2$)**	
	N	**Fe**	**N**	**Ru**	**N**	**Os**	**N**	**Os**	**N**	**Ru**	**N**	**Os**
	M06-L		**B3LYP**									
AIM Charge	−0.25	1.90	−0.35	2.04	−0.49	2.21	−0.51	2.25	−0.25	2.38	−0.40	2.66
NPA Charge	0.05	1.41	−0.03	1.55	−0.21	1.72	−0.26	1.80	0.08	1.69	−0.11	1.99
NLMO B.O.	2.30	3.21	2.62	3.64	2.77	3.84	2.80	3.80	2.28	4.30	2.54	4.48
Wiberg B.I.	2.52	3.29	3.04	4.28	3.03	4.47	2.86	3.98	3.05	4.61	3.04	4.76

Table S10. Electronic energies (hartree) and energy differences (kJ mol^{-1}) of singlet and triplet $NRuF_3$ calculated at the ROHF/UCCSD(T) level of theory with basis sets up to quintuple zeta quality, as well as CBS extrapolations. The single point energies were calculated at the minima obtained at the CCSD(T)/aug-cc-pVTZ(-PP) levels.

Basis set	$NRuF_3$ (C_s, $^1A'$)			$NRuF_3$ (C_{3v}, $^3A_2$)			ΔE_{T-S}
	Reference E.	Correlation E.	Total Energy	Reference E.	Correlation E.	Total Energy	
aVDZ(-PP)	−446.504523	−1.181185	−447.685709	−446.507003	−1.181062	−447.688064	−6.2
aVTZ(-PP)	−446.600941	−1.422827	−448.023769	−446.602085	−1.420950	−448.023035	1.9
aQZ(-PP)	−446.627712	−1.506839	−448.134551	−446.628722	−1.504153	−448.132875	4.4
aV5Z(-PP)	−446.634844	−1.538137	−448.172981	−446.635786	−1.534972	−448.170758	5.8
CBS [a]	−446.634844	−1.570975	−448.205819	−446.635786	−1.567306	−448.203092	7.2
CBS [b]	−445.634844	−1.556720	−447.191564	−445.635786	−1.553102	−447.188889	7.0
apwCVDZ(−PP)	−446.511415	−1.500142	−448.011557	−446.513189	−1.501410	−448.014598	−8.0
apwCVTZ(−PP)	−446.603800	−1.818958	−448.422758	−446.604814	−1.818014	−448.422827	−0.2
apwCVQZ(−PP)	−446.628602	−1.928322	−448.556924	−446.629599	−1.926530	−448.556129	2.1
apwCV5Z(−PP)	−446.635065	−1.970985	−448.606050	−446.635995	−1.968682	−448.604677	3.6
CBS [a]	−446.635065	−2.015746	−448.650811	−446.635995	−2.012907	−448.648902	5.0
CBS [b]	−445.635065	−1.998272	−447.633337	−445.635995	−1.995455	−447.631450	5.0

[a] Two-point extrapolation of the QZ and 5Z CCSD(T) correlation energies via $E_n = E_{\mathrm{CBS}} + \frac{A}{(n+1)^3}$, where *n* is the cardinal number of the basis set (4 = QZ and 5 = 5Z) and *A* is a fitting parameter.[13b,45] [b] Exponential three point extrapolation of the TZ, QZ and 5Z CCSD(T) correlation energies via $E_n = E_{CBS} + Be^{-\alpha n}$, where *n* is the cardinal number of the basis set (3 = TZ, 4 = QZ and 5 = 5Z), and α and *B* are fitting parameters.[46]

Table S11. Electronic energies (hartree) and energy differences (kJ mol^{-1}) of singlet and triplet $NOsF_3$ calculated at the ROHF/ UCCSD(T) level of theory with basis sets up to quintuple zeta quality, as well as CBS extrapolations. The single point energies were calculated at the minima obtained at the CCSD(T)/aug−cc−pVTZ(−PP) level of theory.

Basis set	$NOsF_3$ (C_s, $^1A'$)			$NOsF_3$ (C_s, $^3A''$)			ΔE_{T-S}
	Reference E.	Correlation E.	Total Energy	Reference E.	Correlation E.	Total Energy	
aVDZ(−PP)	−442.857904	−1.147078	−444.004982	−442.871032	−1.137832	−444.008864	−10.2
aVTZ(−PP)	−442.957181	−1.384106	−444.341287	−442.969238	−1.373362	−444.342600	−3.4
aVQZ(−PP)	−442.983445	−1.466771	−444.450217	−442.995504	−1.455350	−444.450854	−1.7
aV5Z(−PP)	−442.990207	−1.497605	−444.487811	−443.002211	−1.485787	−444.487998	−0.5
CBS [a]	−442.990207	−1.529955	−444.520161	−443.002211	−1.517720	−444.519931	0.6
CBS [b]	−442.990207	−1.515947	−444.506153	−443.002211	−1.503757	−444.505968	0.5
awCVDZ(−PP)	−442.864299	−1.406781	−444.271080	−442.877117	−1.398780	−444.275898	−12.6
apwCVTZ(−PP)	−442.959193	−1.726200	−444.685394	−442.971236	−1.716295	−444.687530	−5.6
apwCVQZ(−PP)	−442.983945	−1.834221	−444.818166	−442.995976	−1.823596	−444.819572	−3.7
apwCV5Z(−PP)	−442.990330	−1.876415	−444.866746	−443.002320	−1.865356	−444.867676	−2.4
CBS [a]	−442.990330	−1.920685	−444.911016	−443.002320	−1.909169	−444.911490	−1.2
CBS [b]	−441.990330	−1.903463	−443.893793	−442.002320	−1.891963	−443.894284	−1.3

[a] Two-point extrapolation of the QZ and 5Z CCSD(T) correlation energies via $E_n = E_{\mathrm{CBS}} + \frac{A}{(n+1)^3}$, where *n* is the cardinal number of the basis set (4 = QZ and 5 = 5Z) and *A* is a fitting parameter.[13a,45]; [b] Exponential three point extrapolation of the TZ, QZ and 5Z CCSD(T) correlation energies via $E_n = E_{CBS} + Be^{-\alpha n}$, where *n* is the cardinal number of the basis set (3 = TZ, 4 = QZ and 5 = 5Z), and α and *B* are fitting parameters.[46]

Table S12. Total electronic energies (E_{el}) in hartree and electronic energy differences (ΔE_{el}) in kJ mol^{-1} of different points at the ^{1}A' and ^{3}A" energy potential surfaces (PES) of $NOsF_3$ obtained at the B3LYP/def2-QZVP and UCCSD(T)/cc-pVTZ(-PP) level of theory.

	B3LYP/def2-QZVP		**CCSD(T)/cc-pVTZ(-PP)**	
	E_{el} **[hartree]**	ΔE_{el} **[kJ mol^{-1}]**	E_{el} **[hartree]**	ΔE_{el} **[kJ mol^{-1}]**
^{1}A' Minimum	−445.014761	0	-444.559950	0
^{1}A' MECP	−445.009614	13.5	-444.569336	24.6
^{3}A" Minimum	−445.018544	0	-444.559951	0
^{3}A" MECP	−445.009649	23.4	-444.568806	23.2

Table S13. AIM charges, NPA charges, NLMO bond orders (totals by atom) and Wiberg bond indices (totals by atom) for NMF_2 species calculated the B3LYP (M = Ru, Os) and M06-L (M = Fe) levels of theory.

	$NFeF_2$ ($^2A_2$)		**$NRuF_2$ ($^2A_2$)**		**$NOsF_2$ ($^2A_2$)**	
	N	**Fe**	**N**	**Ru**	**N**	**Os**
AIM Charge	−0.35	1.53	−0.40	1.62	−0.50	1.72
NPA Charge	−0.03	1.10	−0.12	1.25	−0.22	1.28
NLMO B.O.	2.62	3.30	2.82	3.40	2.63	3.49
Wiberg B.I.	2.79	3.32	3.02	3.61	3.00	3.80

Table S14. Adiabatic Potential Energy Surfaces of $NFeF_3$ (Figure 6**a**) obtained at the SA-CASSCF(8,8)/NEVPT2/cc-pVTZ-DK,Fe=cc-pwCVTZ-DK level. RMN, RMF1, A1, RMF2, A2 and D1 are the MN bond length, MF' bond length, the NMF' bond angle, the MF bond length, the NMF angle and the F'MNF dihedral angle (see Figure 5). Energies in hartree, bond lengths in Å and angles in degree.

RMN	RMF1	A1	RMF2	A2	D1	a^1A'	b^1A'	c^1A'	a^1A''	b^1A''	a^3A'	b^3A'	a^3A''	b^3A''
1.51107	1.68807	96.60307	1.69638	113.74074	93.66276	-1626.076795	-1625.973598	-1625.975589	-1626.031556	-1626.001221	-1626.004367	-1625.976403	-1626.073821	-1626.024558
1.51269	1.69049	97.44400	1.69821	113.35754	95.54399	-1626.078618	-1625.978474	-1625.983043	-1626.036292	-1626.004008	-1626.008436	-1625.978687	-1626.079081	-1626.027246
1.51430	1.69291	98.28493	1.70003	112.97435	97.42522	-1626.079862	-1625.984452	-1625.988535	-1626.040546	-1626.006392	-1626.012018	-1625.980464	-1626.083914	-1626.029461
1.51592	1.69533	99.12586	1.70186	112.59116	99.30645	-1626.080560	-1625.991012	-1625.992605	-1626.044352	-1626.008383	-1626.015114	-1625.981835	-1626.088341	-1626.031225
1.51753	1.69775	99.96678	1.70368	112.20797	101.18768	-1626.080702	-1625.997867	-1625.995653	-1626.047761	-1626.009997	-1626.017722	-1625.982965	-1626.092401	-1626.032555
1.51915	1.70017	100.80771	1.70551	111.82478	103.06891	-1626.080297	-1626.004749	-1625.997961	-1626.050816	-1626.011264	-1626.019926	-1625.984398	-1626.096105	-1626.033523
1.52076	1.70259	101.64864	1.70733	111.44159	104.95015	-1626.079392	-1626.011629	-1625.999712	-1626.053544	-1626.012290	-1626.021798	-1625.987494	-1626.099465	-1626.034236
1.52237	1.70501	102.48956	1.70916	111.05840	106.83138	-1626.077985	-1626.018207	-1626.000773	-1626.055843	-1626.012819	-1626.023110	-1625.992245	-1626.102384	-1626.034436
1.52399	1.70742	103.33049	1.71099	110.67520	108.71261	-1626.076178	-1626.024287	-1626.001137	-1626.057719	-1626.012711	-1626.023783	-1625.996882	-1626.104874	-1626.034000
1.52560	1.70984	104.17142	1.71281	110.29201	110.59384	-1626.074017	-1626.029955	-1626.000939	-1626.059241	-1626.012092	-1626.023940	-1626.001113	-1626.106989	-1626.033062
1.52722	1.71226	105.01235	1.71464	109.90882	112.47507	-1626.071530	-1626.035239	-1626.000206	-1626.060441	-1626.011023	-1626.023614	-1626.004951	-1626.108748	-1626.031693
1.52883	1.71468	105.85327	1.71646	109.52563	114.35630	-1626.068803	-1626.040051	-1625.998972	-1626.061324	-1626.009548	-1626.022866	-1626.008361	-1626.110148	-1626.029937
1.53045	1.71710	106.69420	1.71829	109.14244	116.23754	-1626.066001	-1626.044234	-1625.997225	-1626.061897	-1626.007743	-1626.021783	-1626.011267	-1626.111187	-1626.027851
1.53206	1.71952	107.53513	1.72011	108.75925	118.11877	-1626.063495	-1626.047453	-1625.994885	-1626.062172	-1626.005836	-1626.020568	-1626.013504	-1626.111872	-1626.025615
1.53367	1.72194	108.37606	1.72194	108.37606	120.00000	-1626.063184	-1626.048127	-1625.993172	-1626.062202	-1626.005314	-1626.019965	-1626.014059	-1626.112008	-1626.025016
1.53180	1.72030	109.58665	1.71943	107.88987	121.21794	-1626.063184	-1626.048127	-1625.993172	-1626.062202	-1626.005314	-1626.019965	-1626.014059	-1626.112008	-1626.025016
1.52992	1.71866	110.79725	1.71692	107.40368	122.43588	-1626.064964	-1626.046198	-1625.994284	-1626.062023	-1626.006522	-1626.020447	-1626.012793	-1626.111608	-1626.026343
1.52804	1.71701	112.00784	1.71441	106.91749	123.65382	-1626.067020	-1626.043548	-1625.995043	-1626.061621	-1626.007799	-1626.020925	-1626.011076	-1626.110977	-1626.027648
1.52617	1.71537	113.21843	1.71190	106.43130	124.87176	-1626.069094	-1626.040372	-1625.995496	-1626.060971	-1626.008905	-1626.021288	-1626.008945	-1626.110096	-1626.028748
1.52429	1.71373	114.42903	1.70939	105.94511	126.08970	-1626.071045	-1626.036766	-1625.995654	-1626.060051	-1626.009757	-1626.021450	-1626.006437	-1626.108939	-1626.029581
1.52241	1.71209	115.63962	1.70688	105.45892	127.30764	-1626.072790	-1626.032777	-1625.995507	-1626.058841	-1626.010306	-1626.021357	-1626.003568	-1626.107486	-1626.030108
1.52054	1.71045	116.85022	1.70437	104.97273	128.52558	-1626.074269	-1626.028424	-1625.995036	-1626.057315	-1626.010518	-1626.020968	-1626.000342	-1626.105713	-1626.030297
1.51866	1.70881	118.06081	1.70186	104.48654	129.74352	-1626.075427	-1626.023713	-1625.994221	-1626.055449	-1626.010353	-1626.020251	-1625.996756	-1626.103592	-1626.030111
1.51678	1.70717	119.27141	1.69936	104.00035	130.96146	-1626.076212	-1626.018620	-1625.993024	-1626.053208	-1626.009782	-1626.019170	-1625.992793	-1626.101090	-1626.029515
1.51491	1.70552	120.48200	1.69685	103.51416	132.17940	-1626.076600	-1626.013096	-1625.991389	-1626.050558	-1626.008762	-1626.017676	-1625.988424	-1626.098169	-1626.028465
1.51303	1.70388	121.69259	1.69434	103.02797	133.39734	-1626.076552	-1626.007069	-1625.989272	-1626.047435	-1626.007221	-1626.015744	-1625.983661	-1626.094758	-1626.026914
1.51115	1.70224	122.90319	1.69183	102.54178	134.61528	-1626.076028	-1626.000483	-1625.986583	-1626.043795	-1626.005066	-1626.013258	-1625.978619	-1626.090828	-1626.024733
1.50928	1.70060	124.11378	1.68932	102.05560	135.83322	-1626.074946	-1625.993227	-1625.983227	-1626.039529	-1626.002198	-1626.010153	-1625.973712	-1626.086257	-1626.021843

1.50740	1.69896	125.32438	1.68681	101.56941	137.05116	-1626.073190	-1625.985329	-1625.979147	-1626.034567	-1625.998621	-1626.006411	-1625.969433	-1626.080964	-1626.018246

Table S15. Adiabatic Potential Energy Surfaces of $NRuF_3$ (Figure 6**b**) obtained at the SA-CASSCF(8,8)/NEVPT2/cc-pVTZ-DK level. RMN, RMF1, A1, RMF2, A2 and D1 are the RuN bond length, the RuF' bond length, the NRuF' bond angle, the RuF bond length, the NRuF angle and the F'RuNF dihedral angle (see Figure 5). Energies in hartree, bond lengths in Å and angles in degree.

RMN	RMF1	A1	RMF2	A2	D1	a^1A'	b^1A'	a^1A''	a^3A'	b^3A'	a^3A''	b^3A''	c^3A''
1.59151	1.85257	95.41620	1.86341	115.28640	88.32920	-4882.060830	-4881.919104	-4882.001768	-4881.946690	-4881.904183	-4882.025083	-4881.978223	-4881.898661
1.59184	1.85406	96.74090	1.86412	115.19180	90.59140	-4882.063281	-4881.927828	-4882.007362	-4881.950836	-4881.907225	-4882.030515	-4881.980059	-4881.902092
1.59217	1.85554	98.06560	1.86483	115.09720	92.85360	-4882.064930	-4881.936563	-4882.012431	-4881.954416	-4881.910018	-4882.035459	-4881.981343	-4881.904791
1.59250	1.85703	99.39030	1.86554	115.00260	95.11580	-4882.065785	-4881.945321	-4882.017006	-4881.957554	-4881.913016	-4882.039932	-4881.982242	-4881.906766
1.59283	1.85851	100.71500	1.86625	114.90800	97.37800	-4882.065948	-4881.954229	-4882.021143	-4881.960331	-4881.917505	-4882.043993	-4881.982894	-4881.908147
1.59316	1.86000	102.03970	1.86696	114.81340	99.64020	-4882.065243	-4881.962909	-4882.024801	-4881.962711	-4881.923836	-4882.047585	-4881.983073	-4881.909153
1.59349	1.86148	103.36440	1.86767	114.71880	101.90240	-4882.063576	-4881.971538	-4882.027830	-4881.965039	-4881.930240	-4882.050568	-4881.982740	-4881.912829
1.59382	1.86297	104.68910	1.86838	114.62420	104.16460	-4882.061164	-4881.979752	-4882.030308	-4881.965973	-4881.935116	-4882.053056	-4881.981220	-4881.919763
1.59415	1.86445	106.01380	1.86909	114.52960	106.42680	-4882.058350	-4881.987697	-4882.032477	-4881.966045	-4881.939294	-4882.055282	-4881.979006	-4881.926101
1.59448	1.86594	107.33850	1.86981	114.43500	108.68900	-4882.055075	-4881.995371	-4882.034292	-4881.965532	-4881.943044	-4882.057184	-4881.976239	-4881.932024
1.59481	1.86742	108.66320	1.87052	114.34040	110.95120	-4882.051400	-4882.002705	-4882.035754	-4881.964493	-4881.946352	-4882.058757	-4881.972942	-4881.937513
1.59514	1.86891	109.98790	1.87123	114.24580	113.21340	-4882.047434	-4882.009588	-4882.036883	-4881.962960	-4881.949154	-4882.060016	-4881.969112	-4881.942530
1.59547	1.87039	111.31260	1.87194	114.15120	115.47560	-4882.043341	-4882.015751	-4882.037643	-4881.961051	-4881.951376	-4882.060916	-4881.964789	-4881.947065
1.59580	1.87188	112.63730	1.87265	114.05660	117.73780	-4882.039674	-4882.020575	-4882.038027	-4881.958945	-4881.952788	-4882.061446	-4881.960020	-4881.950950
1.59613	*1.87336*	*113.96200*	*1.87336*	*113.96200*	*120.00000*	*-4882.038031*	*-4882.022576*	*-4882.038031*	*-4881.957291*	*-4881.952738*	*-4882.061597*	*-4881.956156*	*-4881.952738*
1.59616	1.87272	115.15450	1.87203	113.00220	121.52860	-4882.039341	-4882.021286	-4882.037853	-4881.958248	-4881.953192	-4882.061513	-4881.959073	-4881.951226
1.59619	1.87209	116.34700	1.87071	112.04240	123.05720	-4882.042154	-4882.017919	-4882.037346	-4881.959443	-4881.952792	-4882.061118	-4881.962961	-4881.948019
1.59622	1.87145	117.53950	1.86938	111.08260	124.58580	-4882.045400	-4882.013381	-4882.036498	-4881.960665	-4881.951713	-4882.060398	-4881.966539	-4881.944360
1.59625	1.87082	118.73200	1.86805	110.12280	126.11440	-4882.048579	-4882.008109	-4882.035288	-4881.961729	-4881.950112	-4882.059325	-4881.969743	-4881.940369
1.59629	1.87018	119.92450	1.86673	109.16300	127.64300	-4882.051534	-4882.002324	-4882.033737	-4881.962509	-4881.948018	-4882.057921	-4881.972504	-4881.936048
1.59632	1.86954	121.11700	1.86540	108.20320	129.17160	-4882.054152	-4881.996096	-4882.031811	-4881.962954	-4881.945474	-4882.056146	-4881.974817	-4881.931403
1.59635	1.86891	122.30950	1.86407	107.24340	130.70020	-4882.056359	-4881.989462	-4882.029484	-4881.963027	-4881.942479	-4882.053972	-4881.976643	-4881.926432
1.59638	1.86827	123.50200	1.86274	106.28360	132.22880	-4882.058091	-4881.982418	-4882.026722	-4881.962686	-4881.939021	-4882.051360	-4881.977949	-4881.921111
1.59641	1.86764	124.69450	1.86142	105.32380	133.75740	-4882.059291	-4881.974942	-4882.023485	-4881.961883	-4881.935066	-4882.048268	-4881.978682	-4881.915395
1.59644	1.86700	125.88700	1.86009	104.36400	135.28600	-4882.059890	-4881.967004	-4882.019724	-4881.960558	-4881.930556	-4882.044647	-4881.978771	-4881.909206
1.59647	1.86636	127.07950	1.85876	103.40420	136.81460	-4882.060206	-4881.958638	-4882.015695	-4881.956846	-4881.924397	-4882.040850	-4881.977388	-4881.901885

1.59650	1.86573	128.27200	1.85744	102.44440	138.34320	-4882.059239	-4881.949526	-4882.010592	-4881.954053	-4881.918519	-4882.035860	-4881.975800	-4881.899549
1.59653	1.86509	129.46450	1.85611	101.48460	139.87180	-4882.057316	-4881.939663	-4882.004643	-4881.950406	-4881.911835	-4882.030006	-4881.973208	-4881.896354
1.59656	1.86446	130.65700	1.85478	100.52480	141.40040	-4882.054242	-4881.928833	-4881.997654	-4881.945699	-4881.904182	-4882.023089	-4881.969400	-4881.892112

Table S16. Adiabatic Potential Energy Surfaces of $NOsF_3$ (Figure 6**c**) obtained at the SA-CASSCF(8,8)/NEVPT2/cc-pVTZ-DK level. RMN, RMF1, A1, RMF2, A2 and D1 are the OsN bond length, the OsF' bond length, the NOsF' bond angle, the OsF bond length, the NOsF angle and the F'OsNF dihedral angle (see Figure 5). Energies in hartree, bond lengths in Å and angles in degree.

RMN	RMF1	A1	RMF2	A2	D1	a^1A'	b^1A'	a^1A''	a^3A'	b^3A'	a^3A''	b^3A''	c^3A''
1.62159	1.86334	96.09113	1.88474	116.01434	87.62533	-17592.580260	-17592.449170	-17592.529650	-17592.449780	-17592.417240	-17592.554670	-17592.486310	-17592.413990
1.62198	1.86548	97.45957	1.88536	115.95969	89.93780	-17592.582700	-17592.457310	-17592.534790	-17592.453820	-17592.420870	-17592.559420	-17592.488040	-17592.417530
1.62237	1.86763	98.82800	1.88597	115.90504	92.25028	-17592.584250	-17592.465260	-17592.539280	-17592.457280	-17592.424210	-17592.563530	-17592.489150	-17592.420110
1.62276	1.86977	100.19644	1.88659	115.85039	94.56276	-17592.585000	-17592.473110	-17592.543190	-17592.460220	-17592.427650	-17592.567070	-17592.489740	-17592.421870
1.62315	1.87192	101.56487	1.88721	115.79574	96.87523	-17592.584910	-17592.480770	-17592.546470	-17592.462620	-17592.431470	-17592.570030	-17592.489750	-17592.422830
1.62354	1.87406	102.93331	1.88782	115.74108	99.18771	-17592.584080	-17592.488190	-17592.549220	-17592.464530	-17592.435580	-17592.572480	-17592.489130	-17592.423240
1.62393	1.87621	104.30174	1.88844	115.68643	101.50019	-17592.582430	-17592.495450	-17592.551460	-17592.465920	-17592.439490	-17592.574480	-17592.487830	-17592.423430
1.62432	1.87835	105.67018	1.88905	115.63178	103.81266	-17592.579870	-17592.502660	-17592.553130	-17592.467470	-17592.443470	-17592.575970	-17592.486110	-17592.426950
1.62471	1.88050	107.03862	1.88967	115.57713	106.12514	-17592.576830	-17592.509450	-17592.554340	-17592.467540	-17592.446370	-17592.577080	-17592.483350	-17592.431900
1.62510	1.88264	108.40705	1.89029	115.52248	108.43762	-17592.573390	-17592.516010	-17592.555250	-17592.466890	-17592.448770	-17592.577950	-17592.479940	-17592.436490
1.62548	1.88479	109.77549	1.89090	115.46783	110.75009	-17592.569640	-17592.522400	-17592.555930	-17592.465800	-17592.450890	-17592.578670	-17592.476070	-17592.440890
1.62587	1.88693	111.14392	1.89152	115.41318	113.06257	-17592.565580	-17592.528480	-17592.556340	-17592.464240	-17592.452620	-17592.579180	-17592.471640	-17592.445000
1.62626	1.88908	112.51236	1.89213	115.35853	115.37505	-17592.561460	-17592.534090	-17592.556540	-17592.462330	-17592.453950	-17592.579550	-17592.466750	-17592.448830
1.62665	1.89122	113.88079	1.89275	115.30388	117.68752	-17592.557830	-17592.538600	-17592.556500	-17592.460230	-17592.454630	-17592.579730	-17592.461340	-17592.452290
1.62704	1.89337	115.24923	1.89337	115.24923	120.00000	-17592.556225	-17592.540465	-17592.556225	-17592.458417	-17592.454196	-17592.579724	-17592.456442	-17592.454196
1.62701	1.89019	115.49010	1.89204	114.22360	121.90130	-17592.557870	-17592.539180	-17592.556030	-17592.460830	-17592.456170	-17592.579760	-17592.461280	-17592.453320
1.62699	1.88702	115.73098	1.89072	113.19798	123.80260	-17592.561240	-17592.535720	-17592.555580	-17592.463620	-17592.457110	-17592.579600	-17592.466790	-17592.450920
1.62696	1.88384	115.97186	1.88939	112.17236	125.70390	-17592.565200	-17592.530960	-17592.554810	-17592.466440	-17592.457210	-17592.579160	-17592.471930	-17592.448000
1.62694	1.88067	116.21274	1.88807	111.14674	127.60520	-17592.569270	-17592.525430	-17592.553770	-17592.469040	-17592.456690	-17592.578470	-17592.476700	-17592.444620
1.62691	1.87749	116.45361	1.88674	110.12111	129.50650	-17592.573230	-17592.519290	-17592.552400	-17592.471300	-17592.455610	-17592.577490	-17592.481060	-17592.440770
1.62688	1.87432	116.69449	1.88542	109.09549	131.40780	-17592.576930	-17592.512540	-17592.550640	-17592.473060	-17592.453910	-17592.576130	-17592.484920	-17592.436360
1.62686	1.87114	116.93537	1.88409	108.06987	133.30910	-17592.580230	-17592.505170	-17592.548400	-17592.474250	-17592.451530	-17592.574280	-17592.488190	-17592.431350
1.62683	1.86797	117.17625	1.88277	107.04425	135.21040	-17592.582950	-17592.497110	-17592.545540	-17592.474700	-17592.448370	-17592.571810	-17592.490690	-17592.425630
1.62681	1.86479	117.41712	1.88144	106.01862	137.11170	-17592.584940	-17592.488290	-17592.541950	-17592.474270	-17592.444290	-17592.568570	-17592.492270	-17592.419080

1.62678	1.86162	117.65800	1.88012	104.99300	139.01300	-17592.586340	-17592.478320	-17592.537570	-17592.471120	-17592.438100	-17592.564610	-17592.492080	-17592.414940
1.62675	1.85845	117.89888	1.87880	103.96738	140.91430	-17592.585880	-17592.466980	-17592.531570	-17592.467980	-17592.431460	-17592.558900	-17592.490900	-17592.412790
1.62673	1.85527	118.13975	1.87747	102.94175	142.81560	-17592.583560	-17592.453830	-17592.523750	-17592.462960	-17592.423070	-17592.551350	-17592.487710	-17592.408990
1.62670	1.85210	118.38063	1.87615	101.91613	144.71690	-17592.578580	-17592.438120	-17592.513360	-17592.455300	-17592.412390	-17592.541150	-17592.481690	-17592.402700
1.62668	1.84892	118.62151	1.87482	100.89051	146.61820	-17592.570020	-17592.418830	-17592.499410	-17592.444100	-17592.399110	-17592.527350	-17592.471860	-17592.392960

Table S17. Adiabatic Potential Energy Surfaces of $NOsF_3$ (Figure 6**d**) obtained at the SA-CASSCF(8,8)/NEVPT2/cc-pVTZ-DK level. RMN, RMF1, A1, RMF2, A2 and D1 are the OsN bond length, the OsF' bond length, the NOsF' bond angle, the OsF bond length, the NOsF angle and the F'OsNF dihedral angle (see Figure 5). Energies in hartree, bond lengths in Å and angles in degree.

RMN	RMF1	A1	RMF2	A2	D1	a^1A'	b^1A'	a^1A''	a^3A'	b^3A'	a^3A''	b^3A''	c^3A''
1.64110	1.89256	126.92771	1.86221	101.49391	93.35660	-17592.559350	-17592.525640	-17592.559190	-17592.471240	-17592.438640	-17592.583180	-17592.468440	-17592.450060
1.64009	1.89262	126.09353	1.86443	102.47643	95.25970	-17592.561810	-17592.527380	-17592.561130	-17592.473220	-17592.439580	-17592.584840	-17592.470890	-17592.451570
1.63909	1.89267	125.25935	1.86666	103.45895	97.16280	-17592.563550	-17592.528950	-17592.562500	-17592.474700	-17592.440770	-17592.585940	-17592.472820	-17592.453000
1.63808	1.89273	124.42518	1.86888	104.44148	99.06590	-17592.564670	-17592.530360	-17592.563340	-17592.475760	-17592.443380	-17592.586520	-17592.474360	-17592.454430
1.63708	1.89279	123.59100	1.87111	105.42400	100.96900	-17592.565210	-17592.531570	-17592.563670	-17592.476250	-17592.446500	-17592.586620	-17592.475240	-17592.455550
1.63608	1.89285	122.75682	1.87334	106.40652	102.87210	-17592.565150	-17592.532530	-17592.563490	-17592.476020	-17592.448600	-17592.586220	-17592.475280	-17592.456190
1.63507	1.89291	121.92265	1.87556	107.38905	104.77520	-17592.564620	-17592.533390	-17592.562930	-17592.475230	-17592.450090	-17592.585470	-17592.474640	-17592.456530
1.63407	1.89296	121.08847	1.87779	108.37157	106.67830	-17592.563790	-17592.534170	-17592.562140	-17592.474020	-17592.451170	-17592.584540	-17592.473470	-17592.456610
1.63306	1.89302	120.25429	1.88001	109.35409	108.58140	-17592.562710	-17592.534890	-17592.561130	-17592.472380	-17592.451980	-17592.583460	-17592.471800	-17592.456480
1.63206	1.89308	119.42011	1.88224	110.33661	110.48450	-17592.561490	-17592.535780	-17592.560100	-17592.470460	-17592.452730	-17592.582440	-17592.469800	-17592.456310
1.63106	1.89314	118.58594	1.88446	111.31914	112.38760	-17592.560100	-17592.536780	-17592.559060	-17592.468220	-17592.453370	-17592.581480	-17592.467410	-17592.456080
1.63005	1.89319	117.75176	1.88669	112.30166	114.29070	-17592.558720	-17592.537980	-17592.558160	-17592.465780	-17592.453990	-17592.580750	-17592.464760	-17592.455880
1.62905	1.89325	116.91758	1.88891	113.28418	116.19380	-17592.557410	-17592.539170	-17592.557360	-17592.463140	-17592.454480	-17592.580200	-17592.461850	-17592.455650
1.62804	1.89331	116.08340	1.89114	114.26670	118.09690	-17592.556500	-17592.540170	-17592.556760	-17592.460550	-17592.454770	-17592.579910	-17592.458850	-17592.455360
1.62704	1.89337	115.24923	1.89337	115.24923	120.00000	-17592.556225	-17592.540465	-17592.556225	-17592.458417	-17592.454196	-17592.579724	-17592.456442	-17592.454196
1.62701	1.89019	115.49010	1.89204	114.22360	121.90130	-17592.557870	-17592.539180	-17592.556030	-17592.460830	-17592.456170	-17592.579760	-17592.461280	-17592.453320
1.62699	1.88702	115.73098	1.89072	113.19798	123.80260	-17592.561240	-17592.535720	-17592.555580	-17592.463620	-17592.457110	-17592.579600	-17592.466790	-17592.450920
1.62696	1.88384	115.97186	1.88939	112.17236	125.70390	-17592.565200	-17592.530960	-17592.554810	-17592.466440	-17592.457210	-17592.579160	-17592.471930	-17592.448000
1.62694	1.88067	116.21274	1.88807	111.14674	127.60520	-17592.569270	-17592.525430	-17592.553770	-17592.469040	-17592.456690	-17592.578470	-17592.476700	-17592.444620
1.62691	1.87749	116.45361	1.88674	110.12111	129.50650	-17592.573230	-17592.519290	-17592.552400	-17592.471300	-17592.455610	-17592.577490	-17592.481060	-17592.440770
1.62688	1.87432	116.69449	1.88542	109.09549	131.40780	-17592.576930	-17592.512540	-17592.550640	-17592.473060	-17592.453910	-17592.576130	-17592.484920	-17592.436360
1.62686	1.87114	116.93537	1.88409	108.06987	133.30910	-17592.580230	-17592.505170	-17592.548400	-17592.474250	-17592.451530	-17592.574280	-17592.488190	-17592.431350

1.62683	1.86797	117.17625	1.88277	107.04425	135.21040	-17592.582950	-17592.497110	-17592.545540	-17592.474700	-17592.448370	-17592.571810	-17592.490690	-17592.425630
1.62681	1.86479	117.41712	1.88144	106.01862	137.11170	-17592.584940	-17592.488290	-17592.541950	-17592.474270	-17592.444290	-17592.568570	-17592.492270	-17592.419080
1.62678	1.86162	117.65800	1.88012	104.99300	139.01300	-17592.586340	-17592.478320	-17592.537570	-17592.471120	-17592.438100	-17592.564610	-17592.492080	-17592.414940
1.62675	1.85845	117.89888	1.87880	103.96738	140.91430	-17592.585880	-17592.466980	-17592.531570	-17592.467980	-17592.431460	-17592.558900	-17592.490900	-17592.412790
1.62673	1.85527	118.13975	1.87747	102.94175	142.81560	-17592.583560	-17592.453830	-17592.523750	-17592.462960	-17592.423070	-17592.551350	-17592.487710	-17592.408990
1.62670	1.85210	118.38063	1.87615	101.91613	144.71690	-17592.578580	-17592.438120	-17592.513360	-17592.455300	-17592.412390	-17592.541150	-17592.481690	-17592.402700
1.62668	1.84892	118.62151	1.87482	100.89051	146.61820	-17592.570020	-17592.418830	-17592.499410	-17592.444100	-17592.399110	-17592.527350	-17592.471860	-17592.392960

Calculated molecular structures and vibrational data

The following table list computed z-matrices (structures), total energies, and vibrational data of optimized structures in C_s point group symmetry (unless stated otherwise) and with positive HOMO-LUMO (closed shell) or SOMO-LUMO (open shell) gap.

F_2NFeF ($^3A'$)	
B3LYP/def2-QZVP	
Cartesian coordinates	5 Energy = -1617.885680869 N 0.0200174 -0.7334605 0.0000000 F -0.9471905 -1.7059422 0.0000000 F 1.1888999 -1.4511922 0.0000000 Fe -0.0918882 1.0591772 0.0000000 F -0.1698386 2.8314177 0.0000000
Vibrational data (^{14}N)	# mode symmetry wave number IR intensity selection rules # cm**(-1) km/mol IR RAMAN 7 a" 29.43 15.41477 YES YES 8 a' 96.55 15.17501 YES YES 9 a' 210.30 18.55117 YES YES 10 a" 255.91 5.75702 YES YES 11 a' 329.10 0.32272 YES YES 12 a' 565.22 1.26244 YES YES 13 a' 673.12 164.84817 YES YES 14 a' 874.71 155.17964 YES YES 15 a' 1034.82 301.48996 YES YES

BP86/def2-QZVP	
Cartesian coordinates	5 Energy = -1618.346313239 N 0.0373682 -0.6538728 0.0000000 F -0.9620967 -1.6760250 0.0000000 F 1.1954484 -1.4730200 0.0000000 Fe -0.0814740 1.0256217 0.0000000 F -0.1892459 2.7772961 0.0000000
Vibrational data (^{14}N)	# mode symmetry wave number IR intensity selection rules # cm**(-1) km/mol IR RAMAN 7 a" 37.00 12.39328 YES YES 8 a' 95.16 4.31188 YES YES 9 a' 275.14 3.66558 YES YES 10 a' 366.42 6.90198 YES YES 11 a" 376.58 6.09699 YES YES 12 a' 424.33 218.11955 YES YES 13 a' 547.90 6.99519 YES YES 14 a' 682.11 290.25040 YES YES 15 a' 841.43 184.03013 YES YES
M06-L/def2-QZVP	
Cartesian coordinates	5 Energy = -1617.979179046 N 0.0337354 -0.6779314 0.0000000 F -0.9400297 -1.6687692 0.0000000 F 1.1742336 -1.4749600 0.0000000 Fe -0.0719128 1.0349806 0.0000000 F -0.1960266 2.7866800 0.0000000
Vibrational data (^{14}N)	# mode symmetry wave number IR intensity selection rules # cm**(-1) km/mol IR RAMAN 7 a' 108.20 7.66625 YES YES 8 a" 195.66 15.13882 YES YES

	9 a' 296.83 8.38855 YES YES 10 a' 360.44 0.92347 YES YES 11 a" 380.05 6.25535 YES YES 12 a' 531.21 209.24993 YES YES 13 a' 583.00 10.87019 YES YES 14 a' 700.12 232.26580 YES YES 15 a' 906.00 387.39380 YES YES
$FNFeF_2$ (^{3}A")	
B3LYP/def2-QZVP	
Cartesian coordinates	5 Energy = -1617.975573816 Fe 0.6712147 0.2301833 0.0000000 F 0.9771787 0.5558377 1.6952085 F 0.9771787 0.5558377 -1.6952085 N -0.7181742 -0.9790599 0.0000000 F -1.9073979 -0.3627989 0.0000000
Vibrational data (^{14}N)	# mode symmetry wave number IR intensity selection rules # cm**(-1) km/mol IR RAMAN 7 a" 73.65 0.03279 YES YES 8 a' 139.35 26.98295 YES YES 9 a' 147.12 24.98256 YES YES 10 a' 217.52 3.56907 YES YES 11 a" 223.66 0.34654 YES YES 12 a' 432.33 13.07446 YES YES 13 a' 614.25 67.29753 YES YES 14 a" 743.72 216.77241 YES YES 15 a' 1024.90 271.91027 YES YES
BP86/def2-QZVP	
Cartesian coordinates	5 Energy = -1618.440612378

	Fe 0.5963808 0.0784963 0.0000000 F 1.0303946 0.6221026 1.5915390 F 1.0303946 0.6221026 -1.5915390 N -0.6884254 -0.9300658 0.0000000 F -1.9687445 -0.3926356 0.0000000
Vibrational data (^{14}N)	# mode symmetry wave number IR intensity selection rules # cm**(-1) km/mol IR RAMAN 7 a" 107.16 0.30397 YES YES 8 a' 126.35 17.17554 YES YES 9 a' 140.31 14.06378 YES YES 10 a' 265.84 0.42271 YES YES 11 a" 329.58 0.01683 YES YES 12 a' 611.04 20.89920 YES YES 13 a' 696.69 158.89399 YES YES 14 a" 742.40 152.63765 YES YES 15 a' 841.16 191.76773 YES YES
M06-L/def2-QZVP	
Cartesian coordinates	5 Energy = -1618.080219914 N -0.6009009 -1.0148392 0.0000000 F 0.3518498 -1.9608345 0.0000000 Fe -0.1143908 0.6270698 0.0000000 F 0.1817210 1.1743019 -1.6278403 F 0.1817210 1.1743019 1.6278403
Vibrational data (^{14}N)	# mode symmetry wave number IR intensity selection rules # cm**(-1) km/mol IR RAMAN 7 a" 90.71 0.17636 YES YES 8 a' 128.27 13.60551 YES YES 9 a' 147.87 21.23656 YES YES 10 a' 274.73 4.08887 YES YES 11 a" 289.45 0.34049 YES YES

	12 a' 512.70 9.27683 YES YES 13 a' 651.82 73.46579 YES YES 14 a" 747.45 187.87762 YES YES 15 a' 959.46 328.98704 YES YES
Vibrational data (^{15}N)	# mode symmetry wave number IR intensity selection rules # cm**(-1) km/mol IR RAMAN 7 a" 90.64 0.17226 YES YES 8 a' 128.13 13.57629 YES YES 9 a' 147.84 21.22452 YES YES 10 a' 272.85 4.03667 YES YES 11 a" 282.25 0.35791 YES YES 12 a' 498.93 8.32778 YES YES 13 a' 651.02 74.65331 YES YES 14 a" 747.44 187.86737 YES YES 15 a' 941.70 313.72487 YES YES
$NFeF_3$ (C_{3v} – $^3A_2$)	
B3LYP/def2-QZVP	
Cartesian coordinates	5 Energy = -1617.976610363 Fe -0.0000000 0.0000000 0.0079618 N 0.0000000 0.0000000 -1.6302797 F 0.8342270 -1.4449235 0.5388982 F 0.8342270 1.4449235 0.5388982 F -1.6684539 0.0000000 0.5388982
Vibrational data (^{14}N)	# mode symmetry wave number IR intensity selection rules # cm**(-1) km/mol IR RAMAN 7 e 155.22 5.27661 YES YES 8 e 155.22 5.27661 YES YES 9 a1 187.18 8.83064 YES YES 10 e 232.67 3.91819 YES YES 11 e 232.67 3.91819 YES YES

	12 a1 421.35 21.22831 YES YES 13 a1 682.58 33.50537 YES YES 14 e 701.25 146.02441 YES YES 15 e 701.25 146.02441 YES YES
Vibrational data (^{15}N)	# mode symmetry wave number IR intensity selection rules # cm**(-1) km/mol IR RAMAN 7 e 154.46 4.98055 YES YES 8 e 154.46 4.98055 YES YES 9 a1 187.15 8.85413 YES YES 10 e 229.23 4.26499 YES YES 11 e 229.23 4.26499 YES YES 12 a1 409.09 19.60704 YES YES 13 a1 682.11 34.23770 YES YES 14 e 701.25 146.02183 YES YES 15 e 701.25 146.02183 YES YES
ROB3LYP/def2-QZVP (calculation in C_s using Molpro)	
Cartesian coordinates	5 RKS-SCF000/DEF2-QZVP ENERGY=-1617.96164679 N 0.0038072789 -1.5899360016 0.0000000000 Fe 0.0008517711 -0.1103621721 0.0000000000 F 1.6106905567 0.5217013431 0.0000000000 F -0.8080562228 0.5168697998 -1.3940348323 F -0.8080562228 0.5168697998 1.3940348323
Vibrational data (^{14}N)	1 A 2 A 3 A 4 A 5 A Wavenumbers [cm-1] 174.99 175.46 246.80 326.86 327.00 Intensities [km/mol] 3.79 3.73 7.88 1.40 1.37 Intensities [relative] 3.03 2.98 6.30 1.12 1.09 6 A 7 A 8 A 9 A Wavenumbers [cm-1] 679.42 715.22 715.76 1191.56 Intensities [km/mol] 51.67 124.61 124.98 51.54

	Intensities [relative] 41.34 99.70 100.00 41.24
BP86/def2-QZVP	
Cartesian coordinates	5 Energy = -1618.471358935 Fe -0.0000000 0.0000000 -0.0870506 N 0.0000000 0.0000000 -1.5977653 F 0.8079015 -1.3993265 0.5597309 F 0.8079015 1.3993265 0.5597309 F -1.6158030 0.0000000 0.5597309
Vibrational data (^{14}N)	# mode symmetry wave number IR intensity selection rules # cm**(-1) km/mol IR RAMAN 7 e 167.39 2.87179 YES YES 8 e 167.39 2.87179 YES YES 9 a1 239.69 5.49977 YES YES 10 e 309.72 1.28113 YES YES 11 e 309.72 1.28113 YES YES 12 a1 650.45 39.90483 YES YES 13 e 691.28 100.10245 YES YES 14 e 691.28 100.10245 YES YES 15 a1 1096.45 33.93383 YES YES
Vibrational data (^{15}N)	# mode symmetry wave number IR intensity selection rules # cm**(-1) km/mol IR RAMAN 7 e 167.13 2.80366 YES YES 8 e 167.13 2.80366 YES YES 9 a1 239.10 5.46806 YES YES 10 e 304.02 1.39198 YES YES 11 e 304.02 1.39198 YES YES 12 a1 649.45 39.11997 YES YES 13 e 691.27 100.10346 YES YES 14 e 691.27 100.10346 YES YES 15 a1 1067.95 34.07242 YES YES

M06-L/def2-QZVP	
Cartesian coordinates	5 Energy = -1618.108613779 N -0.0000000 0.0000000 -1.6162454 Fe 0.0000000 0.0000000 -0.0709558 F -0.8100550 1.4030564 0.5625015 F -0.8100550 -1.4030564 0.5625015 F 1.6201100 0.0000000 0.5625015
Vibrational data (^{14}N)	# mode symmetry wave number IR intensity selection rules # cm**(-1) km/mol IR RAMAN 7 e 167.17 3.24683 YES YES 8 e 167.17 3.24683 YES YES 9 a1 226.92 5.48559 YES YES 10 e 281.36 3.86380 YES YES 11 e 281.36 3.86380 YES YES 12 a1 617.34 42.84699 YES YES 13 e 703.25 126.64097 YES YES 14 e 703.25 126.64097 YES YES 15 a1 784.68 11.78418 YES YES
Vibrational data (^{15}N)	# mode symmetry wave number IR intensity selection rules # cm**(-1) km/mol IR RAMAN 7 e 166.73 3.09705 YES YES 8 e 166.73 3.09705 YES YES 9 a1 226.58 5.49940 YES YES 10 e 276.50 4.10189 YES YES 11 e 276.50 4.10189 YES YES 12 a1 608.24 39.09826 YES YES 13 e 703.25 126.64091 YES YES 14 e 703.25 126.64091 YES YES 15 a1 773.68 15.13882 YES YES
CCSD(T)/aug-cc-pVTZ (calculation in C_s)	

Cartesian coordinates	5 UCCSD(T)/AUG-CC-PVTZ ENERGY=-1616.58884135 N -0.0000000000 -1.6558196996 0.0000000000 Fe -0.0000000000 -0.0441039939 0.0000000000 F 1.6861214269 0.4501368796 0.0000000000 F -0.8430607134 0.4501368796 -1.4602239896 F -0.8430607134 0.4501368796 1.4602239896
Vibrational data (^{14}N)	1 A` 2 A`` 3 A` 4 A`` 5 A` Wavenumbers [cm-1] 87.62 132.56 184.09 225.79 231.05 Intensities [km/mol] 0.00 0.00 0.00 0.00 0.00 Intensities [relative] 0.00 0.00 0.00 0.00 0.00  6 A` 7 A`` 8 A` 9 A` Wavenumbers [cm-1] 537.56 718.94 720.08 757.29 Intensities [km/mol] 0.00 0.00 0.00 0.00 Intensities [relative] 0.00 0.00 0.00 0.00
Vibrational data (^{15}N)	1 A` 2 A`` 3 A` 4 A`` 5 A` Wavenumbers [cm-1] 87.66 132.40 183.78 221.65 226.62 Intensities [km/mol] 0.00 0.00 0.00 0.00 0.00 Intensities [relative] 0.00 0.00 0.00 0.00 0.00  6 A` 7 A`` 8 A` 9 A` Wavenumbers [cm-1] 528.75 718.93 720.03 747.74 Intensities [km/mol] 0.00 0.00 0.00 0.00 Intensities [relative] 0.00 0.00 0.00 0.00
CCSD(T)/aug-cc-pVTZ(Fe: aug-cc-pVTZ-PP) (calculation in C_s)	
Cartesian coordinates	5 UCCSD(T)/USERDEF ENERGY=-1625.76907210 Fe 0.0000327714 0.0000000000 0.0052274647 N 0.0000103441 0.0000000000 -1.5776279214 F 0.8343780343 -1.4450891256 0.5222495883

	F 0.8343780343 1.4450891256 0.5222495883 F -1.6687991842 0.0000000000 0.5222780802
Vibrational data (^{14}N)	1 A 2 A 3 A 4 A 5 A Wavenumbers [cm-1] 60.63 67.35 185.20 242.61 253.84 Intensities [km/mol] 0.00 0.00 0.00 0.00 0.00 Intensities [relative] 0.00 0.00 0.00 0.00 0.00 6 A 7 A 8 A 9 A Wavenumbers [cm-1] 563.67 751.03 752.58 791.12 Intensities [km/mol] 0.00 0.00 0.00 0.00 Intensities [relative] 0.00 0.00 0.00 0.00
Vibrational data (^{15}N)	1 A 2 A 3 A 4 A 5 A Wavenumbers [cm-1] 61.02 67.00 185.01 238.71 249.60 Intensities [km/mol] 0.00 0.00 0.00 0.00 0.00 Intensities [relative] 0.00 0.00 0.00 0.00 0.00 6 A 7 A 8 A 9 A Wavenumbers [cm-1] 555.79 751.01 752.58 779.51 Intensities [km/mol] 0.00 0.00 0.00 0.00 Intensities [relative] 0.00 0.00 0.00 0.00
NEVPT2/aug-cc-pVTZ-DK(Fe: aug-cc-pwCVTZ-DK)	
Cartesian coordinates	5 NEVPT2/AUG-CC-PVTZ-DK,FE=AUG-CC-PWCVTZ-DK ENERGY=-1626.14489052 N -0.0000000000 -1.5990266515 0.0000000000 Fe -0.0000000000 -0.0653517671 0.0000000000 F 1.6341336229 0.4774937965 -0.0000000000 F -0.8170668115 0.4774937965 -1.4152012306 F -0.8170668115 0.4774937965 1.4152012306
Vibrational data (^{14}N)	1 A`` 2 A` 3 A` 4 A` 5 A`` Wavenumbers [cm-1] 185.48 198.28 235.04 287.16 288.62 Intensities [km/mol] 0.00 0.00 0.00 0.00 0.00

	Intensities [relative]	0.00	0.00	0.00	0.00	0.00
		6 A`	7 A`	8 A``	9 A`	
	Wavenumbers [cm-1]	689.00	735.27	737.02	1028.10	
	Intensities [km/mol]	0.00	0.00	0.00	0.00	
	Intensities [relative]	0.00	0.00	0.00	0.00	
Vibrational data (^{15}N)		1 A``	2 A`	3 A`	4 A`	5 A``
	Wavenumbers [cm-1]	184.89	197.82	234.44	282.06	283.63
	Intensities [km/mol]	0.00	0.00	0.00	0.00	0.00
	Intensities [relative]	0.00	0.00	0.00	0.00	0.00
		6 A`	7 A`	8 A``	9 A`	
	Wavenumbers [cm-1]	686.96	735.27	737.02	1002.48	
	Intensities [km/mol]	0.00	0.00	0.00	0.00	
	Intensities [relative]	0.00	0.00	0.00	0.00	
$NFeF_3$ (^{1}A') (Minimum)						
BP86/def2-QZVP						
Cartesian coordinates	Energy = -1618.444955695					
	Fe -0.1689715 -0.1012646 0.0000000					
	N 0.0640009 -1.5823645 0.0000000					
	F -0.6719125 0.5632119 -1.5170175					
	F -0.6719125 0.5632119 1.5170175					
	F 1.4487958 0.5572052 0.0000000					
Vibrational data (^{14}N)	# mode	symmetry	wave number cm**(-1)	IR intensity km/mol	selection rules IR	RAMAN
	7	a"	139.05	10.76696	YES	YES
	8	a'	176.29	2.38009	YES	YES
	9	a"	243.03	0.92703	YES	YES
	10	a'	252.96	5.65554	YES	YES
	11	a'	341.25	3.41039	YES	YES
	12	a'	658.86	36.50823	YES	YES

	13 a' 681.41 49.59544 YES YES 14 a" 716.89 138.83798 YES YES 15 a' 1140.00 36.98015 YES YES
NEVPT2/cc-pVTZ-DK(Fe: cc-pwCVTZ-DK)	
Cartesian coordinates	5 NEVPT2/CC-PVTZ-DK,FE=CC-PWCVTZ-DK ENERGY=-1625.64312761 N 0.0000000000 1.5197704505 -0.4497517400 Fe 0.0000000000 0.0305775786 -0.1575755234 F 0.0000000000 0.0409493994 1.5408424945 F -1.5405046256 -0.6556641550 -0.3679087035 F 1.5405046256 -0.6556641550 -0.3679087035
$NFeF_3$ (^{1}A') (Saddle Point)	
BP86/def2-QZVP	
Cartesian coordinates	5 Energy = -1618.385851291 Fe 0.1370322 -0.0946389 0.0000000 N -0.0030579 -1.5891218 0.0000000 F 1.6890360 0.6580319 0.0000000 F -0.9115051 0.5128644 -1.2485916 F -0.9115051 0.5128644 1.2485916
Vibrational data (^{14}N)	# mode symmetry wave number IR intensity selection rules # cm**(-1) km/mol IR RAMAN 1 a" -137.76 0.00000 YES YES 8 a' 186.96 2.88662 YES YES 9 a" 231.33 2.45155 YES YES 10 a' 264.67 3.86482 YES YES 11 a' 345.09 0.44466 YES YES 12 a' 654.67 37.76467 YES YES 13 a" 659.70 70.04001 YES YES 14 a' 723.86 96.82317 YES YES 15 a' 1137.00 38.14481 YES YES

NEVPT2/aug-cc-pVTZ-DK(Fe: aug-cc-pwCVTZ-DK)	
Cartesian coordinates	5 NEVPT2/AUG-CC-PVTZ-DK,FE=AUG-CC-PWCVTZ-DK ENERGY=-1625.67617024 N 0.0000000000 1.5680654701 -0.2682192113 Fe 0.0000000000 0.0965028169 0.0915728716 F 0.0000000000 -0.3948210436 1.7247955065 F -1.2226253765 -0.5517856743 -0.8903622078 F 1.2226253765 -0.5517856743 -0.8903622078
Vibrational data (^{14}N)	1 A 2 A 3 A 4 A 5 A Wavenumbers [cm-1] 203.81 257.26 283.08 357.88 709.22 Intensities [km/mol] 0.00 0.00 0.00 0.00 0.00 Intensities [relative] 0.00 0.00 0.00 0.00 0.00 6 A 7 A 8 A Wavenumbers [cm-1] 750.53 802.85 1075.06 Intensities [km/mol] 0.00 0.00 0.00 Intensities [relative] 0.00 0.00 0.00 Normal Modes of imaginary frequencies 1 Wavenumbers [cm-1] 184.60 Intensities [km/mol] 0.00 Intensities [relative] 0.00
Vibrational data (^{15}N)	1 A 2 A 3 A 4 A 5 A Wavenumbers [cm-1] 202.78 253.36 282.35 352.12 707.97 Intensities [km/mol] 0.00 0.00 0.00 0.00 0.00 Intensities [relative] 0.00 0.00 0.00 0.00 0.00 6 A 7 A 8 A Wavenumbers [cm-1] 750.48 802.84 1047.17

	Intensities [km/mol] 0.00 0.00 0.00 Intensities [relative] 0.00 0.00 0.00 1 Wavenumbers [cm-1] 183.99 Intensities [km/mol] 0.00 Intensities [relative] 0.00
$NFeF_2$ ($^2A_2$ – C_{2v})	
BP86/def2-QZVP	
Cartesian coordinates	4 Energy = -1518.570495693 Fe 0.0000000 0.0000000 -0.0226156 N 0.0000000 0.0000000 -1.5257077 F -1.5299908 0.0000000 0.7741617 F 1.5299908 0.0000000 0.7741617
Vibrational data (^{14}N)	# mode symmetry wave number IR intensity selection rules # cm**(-1) km/mol IR RAMAN 7 b2 182.27 15.07020 YES YES 8 a1 184.10 6.20329 YES YES 9 b1 288.27 0.77438 YES YES 10 a1 654.78 46.58282 YES YES 11 b1 751.39 126.02097 YES YES 12 a1 1104.72 48.10863 YES YES
$NFeF_2$ ($^4A''$)	
B3LYP/def2-QZVP	
Cartesian coordinates	4 Energy = -1518.119228568 Fe 0.0278021 0.0773987 0.0000000 N -0.5077336 -1.4284634 0.0000000 F 0.2399658 0.6755324 1.6257462

	F 0.2399658 0.6755324 -1.6257462
Vibrational data (^{14}N)	# mode symmetry wave number IR intensity selection rules # cm**(-1) km/mol IR RAMAN 7 a' 145.26 46.55205 YES YES 8 a' 176.76 14.75617 YES YES 9 a" 268.15 0.39399 YES YES 10 a' 628.29 36.09440 YES YES 11 a' 756.21 21.54315 YES YES 12 a" 763.68 179.24321 YES YES
BP86/def2-QZVP	
Cartesian coordinates	4 Energy = -1518.550298159 Fe 0.0166550 0.0535941 0.0000000 N -0.5042037 -1.4207936 0.0000000 F 0.2437743 0.6835998 1.6045511 F 0.2437743 0.6835998 -1.6045511
Vibrational data (^{14}N)	# mode symmetry wave number IR intensity selection rules # cm**(-1) km/mol IR RAMAN 7 a' 124.87 33.26064 YES YES 8 a' 193.76 6.56351 YES YES 9 a" 295.52 0.14397 YES YES 10 a' 637.14 36.05705 YES YES 11 a" 757.36 139.60363 YES YES 12 a' 976.46 24.15930 YES YES
M06-L/def2-QZVP	
Cartesian coordinates	4 Energy = -1518.218305422 Fe 0.0210806 0.0597000 0.0000000 N -0.5082336 -1.4302536 0.0000000 F 0.2435765 0.6852768 1.6070787 F 0.2435765 0.6852768 -1.6070787

Vibrational data (^{14}N)	# mode symmetry wave number IR intensity selection rules # cm**(-1) km/mol IR RAMAN 7 a' 154.58 39.31281 YES YES 8 a' 182.44 10.64684 YES YES 9 a" 283.39 0.59237 YES YES 10 a' 644.96 38.30042 YES YES 11 a" 773.87 161.72457 YES YES 12 a' 859.04 23.34863 YES YES
NFeF (^{1}A')	
B3LYP/def2-QZVP	
Cartesian coordinates	3 Energy = -1418.196942249 N -0.8352737 1.2834060 0.0000000 Fe -0.2283230 -0.0402701 0.0000000 F 1.0635968 -1.2431359 0.0000000
Vibrational data (^{14}N)	# mode symmetry wave number IR intensity selection rules # cm**(-1) km/mol IR RAMAN 7 a' 110.26 36.90356 YES YES 8 a' 659.63 125.43469 YES YES 9 a' 1255.90 147.67327 YES YES
BP86/def2-QZVP	
Cartesian coordinates	3 Energy = -1418.614447922 N -0.7194815 1.3410679 0.0000000 Fe -0.3383297 -0.1457525 0.0000000 F 1.0578112 -1.1953155 0.0000000
Vibrational data (^{14}N)	# mode symmetry wave number IR intensity selection rules # cm**(-1) km/mol IR RAMAN 7 a' 166.18 10.02727 YES YES 8 a' 672.08 81.59539 YES YES

	9 a' 1023.03 91.37623 YES YES
M06-L/def2-QZVP	
Cartesian coordinates	3 Energy = -1418.264492520 N -0.6880505 1.2722872 0.0000000 Fe -0.3869861 -0.1672201 0.0000000 F 1.0750366 -1.1050671 0.0000000
Vibrational data (^{14}N)	# mode symmetry wave number IR intensity selection rules # cm**(-1) km/mol IR RAMAN 7 a' 155.21 14.64147 YES YES 8 a' 679.16 108.90657 YES YES 9 a' 1200.36 92.81648 YES YES
$NRuF_3$ (^{1}A')	
B3LYP/def2-QZVP	
Cartesian coordinates	5 Energy = -449.2125490913 Ru -0.2295315 -0.1671942 0.0000000 N 0.2078405 -1.6762571 0.0000000 F 1.4156439 0.7112763 0.0000000 F -0.6969764 0.5660875 -1.6557313 F -0.6969764 0.5660875 1.6557313
Vibrational data (^{14}N)	# mode symmetry wave number IR intensity selection rules # cm**(-1) km/mol IR RAMAN 7 a" 140.48 11.58363 YES YES 8 a' 145.40 4.18558 YES YES 9 a" 221.42 1.28794 YES YES 10 a' 224.40 7.85554 YES YES 11 a' 326.12 6.61481 YES YES 12 a' 633.58 57.94256 YES YES 13 a" 660.55 170.88815 YES YES

	14 a' 669.35 53.63524 YES YES 15 a' 1201.63 42.63381 YES YES
Vibrational data (^{15}N)	# mode symmetry wave number IR intensity selection rules # cm**(-1) km/mol IR RAMAN 7 a" 140.06 11.68921 YES YES 8 a' 145.22 4.09724 YES YES 9 a" 217.00 1.12343 YES YES 10 a' 224.23 7.81067 YES YES 11 a' 319.83 6.73314 YES YES 12 a' 633.48 57.78115 YES YES 13 a" 660.55 170.86323 YES YES 14 a' 669.27 53.47856 YES YES 15 a' 1166.20 41.31606 YES YES
BP86/def2-QZVP	
Cartesian coordinates	5 Energy = -449.5409092607 Ru -0.2254464 -0.1681867 0.0000000 N 0.2076329 -1.6993337 0.0000000 F 1.4202437 0.7209890 0.0000000 F -0.7012151 0.5732657 -1.6574811 F -0.7012151 0.5732657 1.6574811
Vibrational data (^{14}N)	# mode symmetry wave number IR intensity selection rules # cm**(-1) km/mol IR RAMAN 7 a" 115.45 12.37316 YES YES 8 a' 140.86 2.87881 YES YES 9 a" 210.51 1.49515 YES YES 10 a' 218.62 6.01410 YES YES 11 a' 315.87 5.48997 YES YES 12 a' 617.82 48.43595 YES YES 13 a" 640.58 149.89386 YES YES 14 a' 651.14 45.50603 YES YES

	15 a' 1150.27 40.07358 YES YES
Vibrational data (^{15}N)	# mode symmetry wave number IR intensity selection rules # cm**(-1) km/mol IR RAMAN 7 a" 115.12 12.43546 YES YES 8 a' 140.69 2.81783 YES YES 9 a" 206.32 1.32536 YES YES 10 a' 218.45 5.98200 YES YES 11 a' 309.78 5.54414 YES YES 12 a' 617.70 48.26582 YES YES 13 a" 640.58 149.87678 YES YES 14 a' 651.07 45.37272 YES YES 15 a' 1116.38 38.76958 YES YES
CCSD(T)/aug-cc-pVTZ(-PP)	
Cartesian coordinates	5 UCCSD(T)/USERDEF ENERGY=-448.02376908 Ru -0.2482196139 -0.1415726171 0.0000000000 N 0.2058519177 -1.6683109472 0.0000000000 F 1.4036142992 0.7101998411 0.0000000000 F -0.6806233015 0.5498418616 -1.6786455388 F -0.6806233015 0.5498418616 1.6786455388
Vibrational data (^{14}N)	1 A 2 A 3 A 4 A 5 A Wavenumbers [cm-1] 153.51 158.33 225.86 226.88 321.89 Intensities [km/mol] 0.00 0.00 0.00 0.00 0.00 Intensities [relative] 0.00 0.00 0.00 0.00 0.00 6 A 7 A 8 A 9 A Wavenumbers [cm-1] 648.82 677.96 681.64 1084.72 Intensities [km/mol] 0.00 0.00 0.00 0.00 Intensities [relative] 0.00 0.00 0.00 0.00
Vibrational data (^{15}N)	1 A 2 A 3 A 4 A 5 A

	Wavenumbers [cm-1] 153.34 157.57 222.51 225.67 315.86 Intensities [km/mol] 0.00 0.00 0.00 0.00 0.00 Intensities [relative] 0.00 0.00 0.00 0.00 0.00 6 A 7 A 8 A 9 A Wavenumbers [cm-1] 648.71 677.96 681.56 1052.62 Intensities [km/mol] 0.00 0.00 0.00 0.00 Intensities [relative] 0.00 0.00 0.00 0.00
$NRuF_3$ (^{1}A') (Saddle point)	
B3LYP/def2-QZVP	
Cartesian coordinates	5 Energy = -449.2092804041 Ru 0.1926203 -0.1308375 0.0000000 N 0.0261138 -1.6957358 0.0000000 F 1.8046906 0.8160869 0.0000000 F -1.0117123 0.5052432 -1.2757559 F -1.0117123 0.5052432 1.2757559
Vibrational data (^{14}N)	# mode symmetry wave number IR intensity selection rules # cm**(-1) km/mol IR RAMAN 1 a" -136.27 0.00000 YES YES 8 a' 158.95 6.85409 YES YES 9 a" 193.35 1.11396 YES YES 10 a' 243.31 3.40732 YES YES 11 a' 334.22 1.79481 YES YES 12 a' 638.29 97.80838 YES YES 13 a" 640.84 77.73013 YES YES 14 a' 683.23 91.14722 YES YES 15 a' 1193.73 47.60703 YES YES
BP86/def2-QZVP	
Cartesian coordinates	5

	Energy = -449.5385900192 Ru 0.1889815 -0.1344266 0.0000000 N -0.0290101 -1.7134782 0.0000000 F 1.8479076 0.7343642 0.0000000 F -1.0039395 0.5567703 -1.2679319 F -1.0039395 0.5567703 1.2679319
Vibrational data (^{14}N)	# mode symmetry wave number IR intensity selection rules # cm**(-1) km/mol IR RAMAN 1 a" -113.31 0.00000 YES YES 8 a' 151.50 5.18453 YES YES 9 a" 186.13 1.62067 YES YES 10 a' 240.19 2.30781 YES YES 11 a' 324.04 1.57113 YES YES 12 a' 622.14 74.33507 YES YES 13 a" 623.64 66.46453 YES YES 14 a' 665.90 82.85495 YES YES 15 a' 1141.27 42.70175 YES YES
CCSD(T)/aug-cc-pVTZ(-PP)	
Cartesian coordinates	5 UCCSD(T)/AUG-CC-PVTZ,RU=AUG-CC-PVTZ-PP ENERGY=-448.01978832 Ru 0.1989302016 -0.1071433142 0.0000000000 N 0.0200330139 -1.6935334021 0.0000000000 F 1.8246345469 0.8108776158 0.0000000000 F -1.0217988312 0.4948995503 -1.2677897058 F -1.0217988312 0.4948995503 1.2677897058
Vibrational data (^{14}N)	1 A 2 A 3 A 4 A 5 A Wavenumbers [cm-1] 157.02 194.48 245.22 324.61 648.05 Intensities [km/mol] 0.00 0.00 0.00 0.00 0.00 Intensities [relative] 0.00 0.00 0.00 0.00 0.00 6 A 7 A 8 A

	Wavenumbers [cm-1] 657.45 695.12 1070.31 Intensities [km/mol] 0.00 0.00 0.00 Intensities [relative] 0.00 0.00 0.00 1 Wavenumbers [cm-1] 137.00 Intensities [km/mol] 0.00 Intensities [relative] 0.00
Vibrational data (^{15}N)	1 A 2 A 3 A 4 A 5 A Wavenumbers [cm-1] 156.65 191.66 244.55 318.53 647.86 Intensities [km/mol] 0.00 0.00 0.00 0.00 0.00 Intensities [relative] 0.00 0.00 0.00 0.00 0.00 6 A 7 A 8 A Wavenumbers [cm-1] 657.43 695.09 1038.47 Intensities [km/mol] 0.00 0.00 0.00 Intensities [relative] 0.00 0.00 0.00 1 Wavenumbers [cm-1] 136.16 Intensities [km/mol] 0.00 Intensities [relative] 0.00
$NRuF_3$ ($^3A_2$ – C_{3v})	
B3LYP/def2-QZVP	
Cartesian coordinates	5 Energy = -449.2162041256 Ru 0.0000000 0.0000000 -0.1583439 N -0.0000000 0.0000000 -1.7354498 F -1.7027133 0.0000000 0.6320504 F 0.8513567 -1.4745930 0.6320504 F 0.8513567 1.4745930 0.6320504

Vibrational data (^{14}N)	# mode symmetry wave number IR intensity selection rules # cm**(-1) km/mol IR RAMAN 7 e 115.55 3.84713 YES YES 8 e 115.55 3.84713 YES YES 9 a1 195.70 8.77212 YES YES 10 e 282.64 3.45947 YES YES 11 e 282.64 3.45947 YES YES 12 e 627.89 113.45195 YES YES 13 e 627.89 113.45195 YES YES 14 a1 641.71 72.39758 YES YES 15 a1 1186.13 57.91788 YES YES
Vibrational data (^{15}N)	# mode symmetry wave number IR intensity selection rules # cm**(-1) km/mol IR RAMAN 7 e 115.45 3.78791 YES YES 8 e 115.45 3.78791 YES YES 9 a1 195.49 8.74429 YES YES 10 e 276.80 3.57756 YES YES 11 e 276.80 3.57756 YES YES 12 e 627.88 113.42613 YES YES 13 e 627.88 113.42613 YES YES 14 a1 641.54 71.98906 YES YES 15 a1 1151.02 56.04822 YES YES
BP86/def2-QZVP	
Cartesian coordinates	5 Energy = -449.5464924977 Ru 0.0000000 0.0000000 -0.1597160 N 0.0000000 0.0000000 -1.7574356 F -1.7057368 0.0000000 0.6398363 F 0.8528684 -1.4772114 0.6398363 F 0.8528684 1.4772114 0.6398363
Vibrational data (^{14}N)	# mode symmetry wave number IR intensity selection rules

	# cm**(-1) km/mol IR RAMAN 7 e 102.92 3.14908 YES YES 8 e 102.92 3.14908 YES YES 9 a1 190.87 6.58499 YES YES 10 e 274.09 2.42345 YES YES 11 e 274.09 2.42345 YES YES 12 e 612.41 92.78843 YES YES 13 e 612.41 92.78843 YES YES 14 a1 623.13 57.24195 YES YES 15 a1 1131.95 51.81268 YES YES
Vibrational data (^{15}N)	# mode symmetry wave number IR intensity selection rules # cm**(-1) km/mol IR RAMAN 7 e 102.84 3.10901 YES YES 8 e 102.84 3.10901 YES YES 9 a1 190.66 6.56295 YES YES 10 e 268.43 2.50503 YES YES 11 e 268.43 2.50503 YES YES 12 e 612.40 92.76469 YES YES 13 e 612.40 92.76469 YES YES 14 a1 622.96 56.88692 YES YES 15 a1 1098.43 50.06846 YES YES
CCSD(T)/aug-cc-pVTZ(-PP) (calculation in C_s)	
Cartesian coordinates	5 UCCSD(T)/USERDEF ENERGY=-448.02302842 Ru 0.0000056843 0.0000000000 -0.1368111874 N 0.0000083347 0.0000000000 -1.7329376335 F -1.7119195925 0.0000000000 0.6240451861 F 0.8559527867 -1.4825466742 0.6240304674 F 0.8559527867 1.4825466742 0.6240304674
Vibrational data (^{14}N)	1 A 2 A 3 A 4 A 5 A Wavenumbers [cm-1] 95.39 95.46 183.05 264.88 267.59

	Intensities [km/mol]	0.00	0.00	0.00	0.00	0.00
	Intensities [relative]	0.00	0.00	0.00	0.00	0.00
		6 A	7 A	8 A	9 A	
	Wavenumbers [cm-1]	638.89	639.04	650.91	1121.62	
	Intensities [km/mol]	0.00	0.00	0.00	0.00	
	Intensities [relative]	0.00	0.00	0.00	0.00	
Vibrational data (^{15}N)		1 A	2 A	3 A	4 A	5 A
	Wavenumbers [cm-1]	95.26	95.36	182.88	259.60	262.24
	Intensities [km/mol]	0.00	0.00	0.00	0.00	0.00
	Intensities [relative]	0.00	0.00	0.00	0.00	0.00
		6 A	7 A	8 A	9 A	
	Wavenumbers [cm-1]	638.89	639.03	650.65	1088.43	
	Intensities [km/mol]	0.00	0.00	0.00	0.00	
	Intensities [relative]	0.00	0.00	0.00	0.00	
$FNRuF_2$ (^{3}A")						
B3LYP/def2-QZVP						
Cartesian coordinates	5 Energy = -449.1573313462 Ru -0.4310211 0.4631061 0.0000000 N 0.0458104 -1.1766224 0.0000000 F 1.4275960 -1.4284082 0.0000000 F -0.5211927 1.0709622 -1.7581990 F -0.5211927 1.0709622 1.7581990					
Vibrational data (^{14}N)	# mode symmetry wave number IR intensity selection rules # cm**(-1) km/mol IR RAMAN 7 a" 115.51 0.96486 YES YES 8 a' 132.78 15.96700 YES YES 9 a' 149.10 7.02535 YES YES 10 a' 250.27 0.22400 YES YES					

	11 a" 336.67 0.04722 YES YES 12 a' 614.84 70.22821 YES YES 13 a" 674.82 197.22465 YES YES 14 a' 722.98 197.44424 YES YES 15 a' 857.38 107.19311 YES YES
Vibrational data (^{15}N)	# mode symmetry wave number IR intensity selection rules # cm**(-1) km/mol IR RAMAN 7 a" 115.50 0.96403 YES YES 8 a' 132.72 15.93472 YES YES 9 a' 148.93 7.05612 YES YES 10 a' 247.82 0.22187 YES YES 11 a" 327.78 0.03526 YES YES 12 a' 614.58 70.42724 YES YES 13 a" 674.77 197.23201 YES YES 14 a' 711.24 184.78323 YES YES 15 a' 833.26 107.86564 YES YES
BP86/def2-QZVP	
Cartesian coordinates	5 Energy = -449.4844274026 Ru -0.4264655 0.4724047 0.0000000 N 0.0267719 -1.1687116 0.0000000 F 1.4542388 -1.4447396 0.0000000 F -0.5272726 1.0705233 -1.7612453 F -0.5272726 1.0705233 1.7612453
Vibrational data (^{14}N)	# mode symmetry wave number IR intensity selection rules # cm**(-1) km/mol IR RAMAN 7 a" 115.38 0.79904 YES YES 8 a' 129.02 11.53677 YES YES 9 a' 150.83 4.98091 YES YES 10 a' 228.62 0.53805 YES YES 11 a" 332.38 0.17070 YES YES

	12 a' 607.72 150.98231 YES YES 13 a' 620.36 189.35179 YES YES 14 a" 669.89 165.83574 YES YES 15 a' 833.66 18.85258 YES YES
F_2NRuF (^3A")	
B3LYP/def2-QZVP	
Cartesian coordinates	5 Energy = -449.0673348158 N 0.6062182 0.4784034 0.0000000 F 1.4938959 0.3814864 1.0732974 F 1.4938959 0.3814864 -1.0732974 Ru -1.1285816 0.0390172 0.0000000 F -2.4654284 -1.2803935 0.0000000
Vibrational data (^{14}N)	# mode symmetry wave number IR intensity selection rules # cm**(-1) km/mol IR RAMAN 7 a' 71.79 9.50790 YES YES 8 a" 130.98 3.59864 YES YES 9 a" 273.92 2.10363 YES YES 10 a' 352.34 10.41625 YES YES 11 a' 468.62 1.17255 YES YES 12 a' 590.89 6.35660 YES YES 13 a' 627.83 165.07653 YES YES 14 a" 720.57 170.25053 YES YES 15 a' 937.89 348.98867 YES YES
BP86/def2-QZVP	
Cartesian coordinates	5 Energy = -449.3864616213 N 0.5871947 0.4382405 0.0000000 F 1.5243100 0.4232248 1.0886925 F 1.5243100 0.4232248 -1.0886925

	Ru -1.1010054 -0.0354701 0.0000000 F -2.5348091 -1.2492200 0.0000000
Vibrational data (^{14}N)	# mode symmetry wave number IR intensity selection rules # cm**(-1) km/mol IR RAMAN 7 a' 64.81 7.04519 YES YES 8 a" 120.26 2.53828 YES YES 9 a" 287.67 0.47676 YES YES 10 a' 362.44 10.22412 YES YES 11 a' 462.12 0.30631 YES YES 12 a" 471.55 198.75532 YES YES 13 a' 560.04 22.35746 YES YES 14 a' 626.23 187.74773 YES YES 15 a' 888.59 369.83161 YES YES
$NRuF_2$ ($^2A_1$ – C_{2v})	
B3LYP/def2-QZVP	
Cartesian coordinates	4 Energy = -349.3592709467 Ru 0.0000000 0.0000000 -0.1130509 F -1.5983451 0.0000000 0.8968725 F 1.5983451 0.0000000 0.8968725 N 0.0000000 0.0000000 -1.6806942
Vibrational data (^{14}N)	# mode symmetry wave number IR intensity selection rules # cm**(-1) km/mol IR RAMAN 7 a1 150.84 8.35183 YES YES 8 b2 217.85 21.92131 YES YES 9 b1 226.33 6.66585 YES YES 10 a1 620.25 80.24791 YES YES 11 b1 633.64 155.17322 YES YES 12 a1 1199.95 70.91294 YES YES
Vibrational data (^{15}N)	# mode symmetry wave number IR intensity selection rules # cm**(-1) km/mol IR RAMAN

	7	a1	150.73	8.33534	YES	YES
	8	b2	215.25	22.06547	YES	YES
	9	b1	221.21	6.55719	YES	YES
	10	a1	620.09	79.84818	YES	YES
	11	b1	633.64	155.13306	YES	YES
	12	a1	1164.42	68.31747	YES	YES
BP86def2-QZVP						
Cartesian coordinates	4 Energy = -349.6429345337 Ru 0.0000000 0.0000000 -0.0421047 F -1.6500875 0.0000000 0.8370439 F 1.6500875 0.0000000 0.8370439 N 0.0000000 0.0000000 -1.6319831					
Vibrational data (^{14}N)	# mode	symmetry	wave number cm**(-1)	IR intensity km/mol	selection rules IR	RAMAN
	7	b2	140.34	10.07492	YES	YES
	8	a1	140.63	6.59108	YES	YES
	9	b1	257.58	2.09602	YES	YES
	10	a1	609.43	56.61426	YES	YES
	11	b1	657.86	118.56348	YES	YES
	12	a1	1150.82	44.61683	YES	YES
Vibrational data (^{15}N)	# mode	symmetry	wave number cm**(-1)	IR intensity km/mol	selection rules IR	RAMAN
	7	b2	138.93	10.15924	YES	YES
	8	a1	140.52	6.57738	YES	YES
	9	b1	251.74	2.06585	YES	YES
	10	a1	609.36	56.42520	YES	YES
	11	b1	657.86	118.53145	YES	YES
	12	a1	1116.64	42.83396	YES	YES
NRuF (^{1}A')						

B3LYP/def2-QZVP	
Cartesian coordinates	3 Energy = -249.4681749998 N -0.7636745 1.4649454 0.0000000 Ru -0.2472823 -0.0038843 0.0000000 F 1.0109568 -1.4610611 0.0000000
Vibrational data (^{14}N)	# mode symmetry wave number IR intensity selection rules # cm**(-1) km/mol IR RAMAN 7 a' 111.36 24.92755 YES YES 8 a' 592.14 139.29947 YES YES 9 a' 1225.59 106.87720 YES YES
Vibrational data (^{15}N)	# mode symmetry wave number IR intensity selection rules # cm**(-1) km/mol IR RAMAN 7 a' 109.42 24.87606 YES YES 8 a' 591.96 138.74045 YES YES 9 a' 1189.16 102.52694 YES YES
BP86/def2-QZVP	
Cartesian coordinates	3 Energy = -249.6962748053 N -0.7416205 1.4724700 0.0000000 Ru -0.2775501 -0.0310340 0.0000000 F 1.0191706 -1.4414360 0.0000000
Vibrational data (^{14}N)	# mode symmetry wave number IR intensity selection rules # cm**(-1) km/mol IR RAMAN 7 a' 119.54 21.68419 YES YES 8 a' 591.60 121.27984 YES YES 9 a' 1180.20 93.30420 YES YES
Vibrational data (^{15}N)	# mode symmetry wave number IR intensity selection rules # cm**(-1) km/mol IR RAMAN 7 a' 117.46 21.59550 YES YES

64

	8 a' 591.43 120.75909 YES YES 9 a' 1145.15 89.53202 YES YES
$NRuF_4$ ($^2B_2$ – C_{4v})	
B3LYP/def2-QZVP	
Cartesian coordinates	6 Energy = -549.0738622897 N 0.0000000 0.0000000 1.6292002 Ru -0.0000000 0.0000000 0.0483234 F 1.2672066 1.2672066 -0.4193785 F 1.2672066 -1.2672066 -0.4193785 F -1.2672066 1.2672066 -0.4193785 F -1.2672066 -1.2672066 -0.4193785
Vibrational data (^{14}N)	# mode symmetry wave number IR intensity selection rules # cm**(-1) km/mol IR RAMAN 7 b2 122.87 0.00000 NO YES 8 e 253.21 7.53124 YES YES 9 e 253.21 7.53124 YES YES 10 a1 263.84 7.62219 YES YES 11 b1 304.78 0.00000 NO YES 12 e 340.05 2.61182 YES YES 13 e 340.05 2.61182 YES YES 14 b2 587.60 0.00000 NO YES 15 a1 669.52 26.83520 YES YES 16 e 694.19 196.38844 YES YES 17 e 694.19 196.38844 YES YES 18 a1 1175.13 14.54667 YES YES
Vibrational data (^{15}N)	# mode symmetry wave number IR intensity selection rules # cm**(-1) km/mol IR RAMAN 7 b2 122.87 0.00000 NO YES 8 e 252.22 7.19231 YES YES 9 e 252.22 7.19231 YES YES

	10	a1	263.40	7.58592	YES	YES
	11	b1	304.78	0.00000	NO	YES
	12	e	333.31	2.97490	YES	YES
	13	e	333.31	2.97490	YES	YES
	14	b2	587.60	0.00000	NO	YES
	15	a1	669.41	26.70163	YES	YES
	16	e	694.19	196.38607	YES	YES
	17	e	694.19	196.38607	YES	YES
	18	a1	1140.62	14.26550	YES	YES
BP86/def2-QZVP						
Cartesian coordinates	6 Energy = -549.4590996103 N 0.0000000 0.0000000 1.6539447 Ru 0.0000000 0.0000000 0.0516735 F 1.2720273 1.2720273 -0.4264021 F 1.2720273 -1.2720273 -0.4264021 F -1.2720273 1.2720273 -0.4264021 F -1.2720273 -1.2720273 -0.4264021					
Vibrational data (^{14}N)	# mode	symmetry	wave number cm**(-1)	IR intensity km/mol	selection rules IR	 RAMAN
	7	b2	122.62	0.00000	NO	YES
	8	e	248.84	5.37346	YES	YES
	9	e	248.84	5.37346	YES	YES
	10	a1	259.75	5.50449	YES	YES
	11	b1	296.81	0.00000	NO	YES
	12	e	332.36	2.55471	YES	YES
	13	e	332.36	2.55471	YES	YES
	14	b2	576.15	0.00000	NO	YES
	15	a1	644.78	21.65410	YES	YES
	16	e	675.41	161.85084	YES	YES
	17	e	675.41	161.85084	YES	YES

	18 a1 1125.73 16.00755 YES YES
Vibrational data (^{15}N)	# mode symmetry wave number IR intensity selection rules # cm**(-1) km/mol IR RAMAN 7 b2 122.62 0.00000 NO YES 8 e 247.73 5.08819 YES YES 9 e 247.73 5.08819 YES YES 10 a1 259.31 5.47530 YES YES 11 b1 296.81 0.00000 NO YES 12 e 325.99 2.85933 YES YES 13 e 325.99 2.85933 YES YES 14 b2 576.15 0.00000 NO YES 15 a1 644.68 21.53607 YES YES 16 e 675.40 161.84468 YES YES 17 e 675.40 161.84468 YES YES 18 a1 1092.65 15.59090 YES YES
CCSD(T)/aug-cc-pVTZ(-PP) (Calculation in C_{2v})	
Cartesian coordinates	6 UCCSD(T)/AUG-CC-PVTZ,RU=AUG-CC-PVTZ-PP ENERGY=-547.76517712 N 0.0000000000 -0.0000000000 -1.6602280654 Ru 0.0000000000 -0.0000000000 -0.0536568805 F 1.7941816843 0.0000000000 0.3773661575 F 0.0000000000 1.7941816843 0.3773661575 F 0.0000000000 -1.7941816843 0.3773661575 F -1.7941816843 0.0000000000 0.3773661575
Vibrational data (^{14}N)	1 A1 2 B2 3 B1 4 A1 5 A2 Wavenumbers [cm-1] 112.61 248.28 248.28 254.69 296.69 Intensities [km/mol] 0.00 0.00 0.00 0.00 0.00 Intensities [relative] 0.00 0.00 0.00 0.00 0.00 6 B1 7 B2 8 A1 9 A1 10 B1 Wavenumbers [cm-1] 325.44 325.44 597.59 680.82 710.95

	Intensities [km/mol]	0.00	0.00	0.00	0.00	0.00
	Intensities [relative]	0.00	0.00	0.00	0.00	0.00
		11 B2	12 A1			
	Wavenumbers [cm-1]	710.95	1082.23			
	Intensities [km/mol]	0.00	0.00			
	Intensities [relative]	0.00	0.00			
Vibrational data (^{15}N)		1 A1	2 B2	3 B1	4 A1	5 A2
	Wavenumbers [cm-1]	112.61	247.21	247.21	254.28	296.69
	Intensities [km/mol]	0.00	0.00	0.00	0.00	0.00
	Intensities [relative]	0.00	0.00	0.00	0.00	0.00
		6 B1	7 B2	8 A1	9 A1	10 B1
	Wavenumbers [cm-1]	319.13	319.13	597.59	680.66	710.95
	Intensities [km/mol]	0.00	0.00	0.00	0.00	0.00
	Intensities [relative]	0.00	0.00	0.00	0.00	0.00
		11 B2	12 A1			
	Wavenumbers [cm-1]	710.95	1050.30			
	Intensities [km/mol]	0.00	0.00			
	Intensities [relative]	0.00	0.00			
$NOsF_3$ (^{1}A')						
B3LYP/def2-QZVP						
Cartesian coordinates	5 Energy = -445.0147611427 Os 0.2118695 -0.0804130 0.0000000 N 0.0469604 -1.6903823 0.0000000 F 1.9374225 0.6457335 0.0000000 F -1.0981262 0.5625309 -1.2042000 F -1.0981262 0.5625309 1.2042000					

Vibrational data (^{14}N)	# mode symmetry wave number IR intensity selection rules # cm**(-1) km/mol IR RAMAN 7 a" 94.77 8.70859 YES YES 8 a' 157.51 6.34168 YES YES 9 a" 160.81 4.22783 YES YES 10 a' 288.31 0.56612 YES YES 11 a' 337.45 2.25736 YES YES 12 a" 629.21 59.32085 YES YES 13 a' 647.17 75.32060 YES YES 14 a' 671.00 93.68788 YES YES 15 a' 1195.66 28.31092 YES YES
Vibrational data (^{15}N)	# mode symmetry wave number IR intensity selection rules # cm**(-1) km/mol IR RAMAN 7 a" 94.48 8.83694 YES YES 8 a' 157.28 6.28614 YES YES 9 a" 158.01 3.95685 YES YES 10 a' 286.64 0.48555 YES YES 11 a' 331.46 2.35944 YES YES 12 a" 629.21 59.31508 YES YES 13 a' 647.12 75.41929 YES YES 14 a' 670.97 93.51862 YES YES 15 a' 1158.16 26.83453 YES YES
BP86/def2-QZVP	
Cartesian coordinates	5 Energy = -445.3601994103 Os 0.2150175 -0.0647964 0.0000000 N 0.0695934 -1.6932890 0.0000000 F 1.9547202 0.6231321 0.0000000 F -1.1196656 0.5674766 -1.1923435 F -1.1196656 0.5674766 1.1923435
Vibrational data (^{14}N)	# mode symmetry wave number IR intensity selection rules

	# cm**(-1) km/mol IR RAMAN 7 a" 112.01 2.37649 YES YES 8 a" 155.22 5.56160 YES YES 9 a' 159.91 4.14987 YES YES 10 a' 293.90 0.15989 YES YES 11 a' 333.82 1.69314 YES YES 12 a" 609.15 51.02886 YES YES 13 a' 637.49 44.75508 YES YES 14 a' 657.02 98.08169 YES YES 15 a' 1147.52 23.00545 YES YES
Vibrational data (^{15}N)	# mode symmetry wave number IR intensity selection rules # cm**(-1) km/mol IR RAMAN 7 a" 111.99 2.41526 YES YES 8 a" 152.14 5.40744 YES YES 9 a' 159.70 4.11446 YES YES 10 a' 291.39 0.12015 YES YES 11 a' 328.76 1.73281 YES YES 12 a" 609.15 51.01597 YES YES 13 a' 637.46 44.82327 YES YES 14 a' 656.97 97.95313 YES YES 15 a' 1111.53 21.78340 YES YES
M06-L/def2-QZVP	
Cartesian coordinates	5 Energy = -445.1765263734 Os 0.2145163 -0.0798466 0.0000000 N 0.0565914 -1.6873005 0.0000000 F 1.9441265 0.6368152 0.0000000 F -1.1076171 0.5651660 -1.1920648 F -1.1076171 0.5651660 1.1920648
Vibrational data (^{14}N)	# mode symmetry wave number IR intensity selection rules # cm**(-1) km/mol IR RAMAN

	7	a"	100.00	6.01765	YES	YES
	8	a'	155.50	5.99784	YES	YES
	9	a"	159.38	4.77145	YES	YES
	10	a'	293.35	0.39749	YES	YES
	11	a'	340.07	2.23387	YES	YES
	12	a"	619.62	59.45138	YES	YES
	13	a'	645.31	61.07871	YES	YES
	14	a'	664.75	105.02581	YES	YES
	15	a'	1181.99	31.64593	YES	YES
CCSD(T)/aug-cc-pVTZ(-PP)						
Cartesian coordinates	5					
	UCCSD(T)/USERDEF ENERGY=-444.34128605					
	Os	0.2133133067	-0.0635978523	0.0000000000		
	N	0.0512604172	-1.6822834377	0.0000000000		
	F	1.9400930901	0.6320088256	0.0000000000		
	F	-1.1023334070	0.5569362323	-1.1911669081		
	F	-1.1023334070	0.5569362323	1.1911669081		
Vibrational data (^{14}N)		1 A	2 A	3 A	4 A	5 A
	Wavenumbers [cm-1]	112.70	166.65	168.27	301.10	344.93
	Intensities [km/mol]	0.00	0.00	0.00	0.00	0.00
	Intensities [relative]	0.00	0.00	0.00	0.00	0.00
		6 A	7 A	8 A	9 A	
	Wavenumbers [cm-1]	651.65	664.02	688.84	1152.17	
	Intensities [km/mol]	0.00	0.00	0.00	0.00	
	Intensities [relative]	0.00	0.00	0.00	0.00	
Vibrational data (^{15}N)		1 A	2 A	3 A	4 A	5 A
	Wavenumbers [cm-1]	112.07	163.73	168.05	297.61	340.65
	Intensities [km/mol]	0.00	0.00	0.00	0.00	0.00
	Intensities [relative]	0.00	0.00	0.00	0.00	0.00

	6 A 7 A 8 A 9 A Wavenumbers [cm-1] 651.65 663.97 688.82 1115.88 Intensities [km/mol] 0.00 0.00 0.00 0.00 Intensities [relative] 0.00 0.00 0.00 0.00
$NOsF_3$ (^{1}A') (Saddle point)	
BP86/def2-QZVP	
Cartesian coordinates	Energy = -445.3553333122 Os -0.2507953 -0.1540708 0.0000000 N 0.1022617 -1.7472001 0.0000000 F 1.4637138 0.6406218 0.0000000 F -0.6575901 0.6303245 -1.6883909 F -0.6575901 0.6303245 1.6883909
Vibrational data (^{14}N)	# mode symmetry wave number IR intensity selection rules # cm**(-1) km/mol IR RAMAN 1 a" -129.53 0.00000 YES YES 8 a' 135.96 2.06117 YES YES 9 a" 201.33 3.07315 YES YES 10 a' 207.33 5.44236 YES YES 11 a' 300.99 5.27951 YES YES 12 a" 609.17 148.33817 YES YES 13 a' 621.49 42.30664 YES YES 14 a' 652.62 42.12874 YES YES 15 a' 1154.60 31.18101 YES YES
B3LYP/def2-QZVP	
Cartesian coordinates	Energy = -445.0120434426 Os -0.2421890 -0.1723479 0.0000000 N 0.2159030 -1.7216683 0.0000000 F 1.4148021 0.7269237 0.0000000 F -0.6942581 0.5835462 -1.6829258 F -0.6942581 0.5835462 1.6829258

Vibrational data (^{14}N)	7 a" -100.05 0.00000 YES YES 8 a' 139.78 3.13320 YES YES 9 a" 208.92 3.21573 YES YES 10 a' 212.48 7.24448 YES YES 11 a' 309.71 6.69390 YES YES 12 a" 626.19 163.79036 YES YES 13 a' 635.76 49.07285 YES YES 14 a' 668.62 51.00883 YES YES 15 a' 1201.15 34.46664 YES YES
CCSD(T)/aug-cc-pVTZ(-PP)	
Cartesian coordinates	UCCSD(T)/AUG-CC-PVTZ,OS=AUG-CC-PVTZ-PP ENERGY=-444.33811776 N 0.0000000000 -1.3511107882 -1.0090462066 Os 0.0000000000 -0.1134113509 0.0407080910 F 0.0000000000 1.3622588249 -1.1131922331 F -1.6888413563 0.3846297047 0.7247873218 F 1.6888413563 0.3846297047 0.7247873218
$NOsF_3$ (^{3}A")	
B3LYP/def2-QZVP	
Cartesian coordinates	5 Energy = -445.0185439098 Os 0.1752333 -0.0877040 0.0000000 N 0.2353676 -1.7152545 0.0000000 F 0.5222079 0.4522222 1.7690544 F 0.5222079 0.4522222 -1.7690544 F -1.4550167 0.8985142 0.0000000
Vibrational data (^{14}N)	# mode symmetry wave number IR intensity selection rules # cm**(-1) km/mol IR RAMAN 7 a' 121.68 2.86186 YES YES 8 a" 211.12 3.47256 YES YES 9 a' 216.97 6.47895 YES YES 10 a' 238.88 5.17383 YES YES

	11 a" 310.07 2.06572 YES YES 12 a' 594.21 74.59639 YES YES 13 a' 651.66 49.64608 YES YES 14 a" 657.25 152.55974 YES YES 15 a' 1166.29 31.11246 YES YES
Vibrational data (^{15}N)	# mode symmetry wave number IR intensity selection rules # cm**(-1) km/mol IR RAMAN 7 a' 121.54 2.78571 YES YES 8 a" 211.11 3.45139 YES YES 9 a' 216.65 6.49066 YES YES 10 a' 234.53 5.28788 YES YES 11 a" 302.52 2.09521 YES YES 12 a' 594.21 74.58419 YES YES 13 a' 651.66 49.61697 YES YES 14 a" 657.24 152.52776 YES YES 15 a' 1129.68 29.51928 YES YES
BP86/def2-QZVP	
Cartesian coordinates	5 Energy = -445.3658941028 Os 0.1866027 -0.0820812 0.0000000 N 0.2450010 -1.7255596 0.0000000 F 0.5084003 0.4482530 1.7808904 F 0.5084003 0.4482530 -1.7808904 F -1.4484044 0.9111347 0.0000000
Vibrational data (^{14}N)	# mode symmetry wave number IR intensity selection rules # cm**(-1) km/mol IR RAMAN 7 a' 126.25 1.76509 YES YES 8 a" 209.42 2.65201 YES YES 9 a' 215.15 4.56824 YES YES 10 a' 231.58 3.37872 YES YES 11 a" 305.16 1.41612 YES YES

	12 a' 580.58 66.22472 YES YES 13 a' 636.82 36.43085 YES YES 14 a" 646.36 134.21937 YES YES 15 a' 1123.96 26.74544 YES YES
Vibrational data (^{15}N)	# mode symmetry wave number IR intensity selection rules # cm**(-1) km/mol IR RAMAN 7 a' 126.09 1.71050 YES YES 8 a" 209.41 2.63670 YES YES 9 a' 214.73 4.54806 YES YES 10 a' 227.52 3.49313 YES YES 11 a" 297.75 1.43473 YES YES 12 a' 580.58 66.21191 YES YES 13 a' 636.81 36.40334 YES YES 14 a" 646.35 134.19472 YES YES 15 a' 1088.69 25.37391 YES YES
M06-L/def2-QZVP	
Cartesian coordinates	5 Energy = -445.1809264953 Os 0.1778569 -0.0953509 0.0000000 N 0.2392572 -1.7201596 0.0000000 F 0.5167217 0.4557327 1.7693005 F 0.5167217 0.4557327 -1.7693005 F -1.4505574 0.9040451 0.0000000
Vibrational data (^{14}N)	# mode symmetry wave number IR intensity selection rules # cm**(-1) km/mol IR RAMAN 7 a' 121.82 2.74791 YES YES 8 a" 210.42 3.48920 YES YES 9 a' 217.48 5.82187 YES YES 10 a' 241.72 4.56685 YES YES 11 a" 308.95 2.18357 YES YES 12 a' 586.67 75.10479 YES YES

	13 a' 642.62 47.16880 YES YES 14 a" 649.20 149.83021 YES YES 15 a' 1156.15 35.21212 YES YES
CCSD(T)/aug-cc-pVTZ(-PP)	
Cartesian coordinates	5 UCCSD(T)/USERDEF ENERGY=-444.34259854 Os 0.1812594542 -0.0736561393 0.0000000000 N 0.2488686836 -1.7093349032 0.0000000000 F 0.5036103700 0.4377248947 1.7707750462 F 0.5036103700 0.4377248947 -1.7707750462 F -1.4373488777 0.9075413532 0.0000000000
Vibrational data (^{14}N)	1 A 2 A 3 A 4 A 5 A Wavenumbers [cm-1] 125.96 216.50 219.56 234.60 306.28 Intensities [km/mol] 0.00 0.00 0.00 0.00 0.00 Intensities [relative] 0.00 0.00 0.00 0.00 0.00 6 A 7 A 8 A 9 A Wavenumbers [cm-1] 614.29 667.96 674.85 1130.27 Intensities [km/mol] 0.00 0.00 0.00 0.00 Intensities [relative] 0.00 0.00 0.00 0.00
Vibrational data (^{15}N)	1 A 2 A 3 A 4 A 5 A Wavenumbers [cm-1] 125.78 216.49 219.03 230.65 298.80 Intensities [km/mol] 0.00 0.00 0.00 0.00 0.00 Intensities [relative] 0.00 0.00 0.00 0.00 0.00 6 A 7 A 8 A 9 A Wavenumbers [cm-1] 614.28 667.95 674.85 1094.66 Intensities [km/mol] 0.00 0.00 0.00 0.00 Intensities [relative] 0.00 0.00 0.00 0.00
$NOsF_3$ (MECP)	

B3LYP/def2-QZVP (ORCA)	
Cartesian coordinates	5 Coordinates from ORCA-job MECP N 0.13198978036287 0.00000526875099 -0.00575459635524 Os 0.04917238912738 0.00001354020650 1.61364554078717 F 1.71184455120966 -0.00002338926068 2.50530705438433 F -1.20445929676235 1.28424962439923 2.24264876284551 F -1.20442742393756 -1.28424504409605 2.24266923833822
UHF-UCCSD(T)/cc-pVTZ(-PP) (ORCA)	
Cartesian coordinates	5 Coordinates from ORCA-job MECP N 0.15480699413023 0.00007522168397 -0.00683259186786 Os 0.02655123263285 0.00016243535483 1.61155399004442 F 1.68159726368437 -0.00028342202728 2.49138947348428 F -1.18961672184577 1.29534592125077 2.25107131342794 F -1.18921876860169 -1.29530015626229 2.25133381491120
$NOsF_2$ ($^2A_2$ – C_{2v})	
B3LYP/def2-QZVP	
Cartesian coordinates	4 Energy = -345.1647128739 Os 0.0000000 0.0000000 0.0356313 N 0.0000000 0.0000000 -1.5815500 F -1.7176708 0.0000000 0.7729593 F 1.7176708 0.0000000 0.7729593
Vibrational data (^{14}N)	# mode symmetry wave number IR intensity selection rules # cm**(-1) km/mol IR RAMAN 7 a1 163.60 3.84836 YES YES 8 b2 187.24 6.72869 YES YES 9 b1 278.30 2.05675 YES YES 10 a1 654.30 47.50580 YES YES

	11 b1 674.71 138.66862 YES YES 12 a1 1200.12 28.52014 YES YES
Vibrational data (^{15}N)	# mode symmetry wave number IR intensity selection rules # cm**(-1) km/mol IR RAMAN 7 a1 163.55 3.84302 YES YES 8 b2 185.48 6.73376 YES YES 9 b1 271.59 2.00318 YES YES 10 a1 654.30 47.50381 YES YES 11 b1 674.68 138.59675 YES YES 12 a1 1162.49 26.90051 YES YES
BP86/def2-QZVP	
Cartesian coordinates	4 Energy = -345.4642229991 Os 0.0000000 0.0000000 0.0478155 N 0.0000000 0.0000000 -1.5830297 F -1.7256455 0.0000000 0.7676071 F 1.7256455 0.0000000 0.7676071
Vibrational data (^{14}N)	# mode symmetry wave number IR intensity selection rules # cm**(-1) km/mol IR RAMAN 7 a1 163.96 2.18989 YES YES 8 b2 182.37 3.90329 YES YES 9 b1 272.81 1.32351 YES YES 10 a1 649.62 37.51229 YES YES 11 b1 666.18 123.61120 YES YES 12 a1 1163.02 22.46874 YES YES
Vibrational data (^{15}N)	# mode symmetry wave number IR intensity selection rules # cm**(-1) km/mol IR RAMAN 7 a1 163.90 2.18644 YES YES 8 b2 180.72 3.89814 YES YES 9 b1 266.26 1.28252 YES YES 10 a1 649.62 37.50428 YES YES

	11 b1 666.17 123.56246 YES YES 12 a1 1126.56 21.19565 YES YES
NOsF (^{1}A')	
B3LYP/def2-QZVP	
Cartesian coordinates	3 Energy = -245.2177683460 Os 0.6196501 0.1325370 0.0000000 N -0.3723913 1.3957486 0.0000000 F -0.2472497 -1.5280737 0.0000000
Vibrational data (^{14}N)	# mode symmetry wave number IR intensity selection rules # cm**(-1) km/mol IR RAMAN 7 a' 216.43 0.10046 YES YES 8 a' 631.23 119.38082 YES YES 9 a' 1213.91 30.43792 YES YES
BP86/def2-QZVP	
Cartesian coordinates	3 Energy = -245.4741075501 Os 0.6327018 0.1269969 0.0000000 N -0.3809407 1.3900265 0.0000000 F -0.2517520 -1.5168115 0.0000000
Vibrational data (^{14}N)	# mode symmetry wave number IR intensity selection rules # cm**(-1) km/mol IR RAMAN 7 a' 235.06 0.65575 YES YES 8 a' 641.07 92.50010 YES YES 9 a' 1175.54 22.81104 YES YES
$NOsF_4$ ($^2B_2$ – C_{4v})	
B3LYP/def2-QZVP	
Cartesian coordinates	6 Energy = -544.9144073546

	N 0.0000000 0.0000000 1.6700056 Os 0.0000000 0.0000000 0.0489409 F 1.2796581 1.2796581 -0.4297366 F 1.2796581 -1.2796581 -0.4297366 F -1.2796581 1.2796581 -0.4297366 F -1.2796581 -1.2796581 -0.4297366
Vibrational data (^{14}N)	# mode symmetry wave number IR intensity selection rules # cm**(-1) km/mol IR RAMAN 7 b2 134.10 0.00000 NO YES 8 a1 243.58 6.63961 YES YES 9 e 249.79 7.27783 YES YES 10 e 249.79 7.27783 YES YES 11 b1 286.20 0.00000 NO YES 12 e 329.56 3.51230 YES YES 13 e 329.56 3.51230 YES YES 14 b2 617.24 0.00000 NO YES 15 e 674.32 176.38993 YES YES 16 e 674.32 176.38993 YES YES 17 a1 686.84 30.78787 YES YES 18 a1 1192.42 13.28492 YES YES
Vibrational data (^{15}N)	# mode symmetry wave number IR intensity selection rules # cm**(-1) km/mol IR RAMAN 7 b2 134.10 0.00000 NO YES 8 a1 243.41 6.62360 YES YES 9 e 249.23 6.98264 YES YES 10 e 249.23 6.98264 YES YES 11 b1 286.20 0.00000 NO YES 12 e 322.21 3.83251 YES YES 13 e 322.21 3.83251 YES YES 14 b2 617.24 0.00000 NO YES 15 e 674.32 176.37856 YES YES

	16 e 674.32 176.37856 YES YES 17 a1 686.83 30.74941 YES YES 18 a1 1155.11 12.72822 YES YES
BP86/def2-QZVP	
Cartesian coordinates	6 Energy = -545.3097556915 N 0.0000000 0.0000000 1.6877557 Os 0.0000000 0.0000000 0.0483698 F 1.2848923 1.2848923 -0.4340314 F 1.2848923 -1.2848923 -0.4340314 F -1.2848923 1.2848923 -0.4340314 F -1.2848923 -1.2848923 -0.4340314
Vibrational data (^{14}N)	# mode symmetry wave number IR intensity selection rules # cm**(-1) km/mol IR RAMAN 7 b2 132.82 0.00000 NO YES 8 a1 238.77 4.67881 YES YES 9 e 244.56 5.50861 YES YES 10 e 244.56 5.50861 YES YES 11 b1 276.83 0.00000 NO YES 12 e 320.81 3.08158 YES YES 13 e 320.81 3.08158 YES YES 14 b2 605.23 0.00000 NO YES 15 e 658.05 152.20696 YES YES 16 e 658.05 152.20696 YES YES 17 a1 664.36 24.75087 YES YES 18 a1 1140.46 12.94366 YES YES
Vibrational data (^{15}N)	# mode symmetry wave number IR intensity selection rules # cm**(-1) km/mol IR RAMAN 7 b2 132.82 0.00000 NO YES 8 a1 238.61 4.66642 YES YES 9 e 243.96 5.26204 YES YES

	10	e	243.96	5.26204	YES	YES
	11	b1	276.83	0.00000	NO	YES
	12	e	313.74	3.33965	YES	YES
	13	e	313.74	3.33965	YES	YES
	14	b2	605.23	0.00000	NO	YES
	15	e	658.05	152.19752	YES	YES
	16	e	658.05	152.19752	YES	YES
	17	a1	664.35	24.72035	YES	YES
	18	a1	1104.76	12.35962	YES	YES
CCSD(T)/aug-cc-pVTZ(-PP)						
Cartesian coordinates	6					
	UCCSD(T)/AUG-CC-PVTZ,OS=AUG-CC-PVTZ-PP ENERGY=-544.12920372					
	N	-0.0000000000	-0.0000000000	-1.6729194364		
	Os	-0.0000000000	-0.0000000000	-0.0422087884		
	F	1.8021400214	0.0000000000	0.4139846943		
	F	0.0000000000	1.8021400214	0.4139846943		
	F	0.0000000000	-1.8021400214	0.4139846943		
	F	-1.8021400214	0.0000000000	0.4139846943		
Vibrational data (^{14}N)		1 A1	2 A1	3 B1	4 B2	5 A2
	Wavenumbers [cm-1]	136.22	241.61	249.87	249.87	283.34
	Intensities [km/mol]	0.00	0.00	0.00	0.00	0.00
	Intensities [relative]	0.00	0.00	0.00	0.00	0.00
		6 B2	7 B1	8 A1	9 B1	10 B2
	Wavenumbers [cm-1]	323.23	323.23	635.02	693.20	693.20
	Intensities [km/mol]	0.00	0.00	0.00	0.00	0.00
	Intensities [relative]	0.00	0.00	0.00	0.00	0.00
		11 A1	12 A1			
	Wavenumbers [cm-1]	705.63	1145.42			
	Intensities [km/mol]	0.00	0.00			

	Intensities [relative]	0.00	0.00			
Vibrational data (^{15}N)		1 A1	2 A1	3 B1	4 B2	5 A2
	Wavenumbers [cm-1]	136.22	241.45	249.21	249.21	283.34
	Intensities [km/mol]	0.00	0.00	0.00	0.00	0.00
	Intensities [relative]	0.00	0.00	0.00	0.00	0.00
		6 B2	7 B1	8 A1	9 B1	10 B2
	Wavenumbers [cm-1]	316.15	316.15	635.02	693.20	693.20
	Intensities [km/mol]	0.00	0.00	0.00	0.00	0.00
	Intensities [relative]	0.00	0.00	0.00	0.00	0.00
		11 A1	12 A1			
	Wavenumbers [cm-1]	705.60	1109.43			
	Intensities [km/mol]	0.00	0.00			
	Intensities [relative]	0.00	0.00			

Supporting Information References

[1] T. Stüker, T. Hohmann, H. Beckers, S. Riedel, *Angew. Chem. Int. Ed.* **2020**, *59*, 23174–23179.

[2] TURBOMOLE GmbH, *TURBOMOLE V7.3*: a development of University of Karlsruhe and Forschungszentrum Karlsruhe GmbH, **2018**.

[3] a) A. D. Becke, *Phys. Rev. A* **1988**, *38*, 3098–3100; b) J. P. Perdew, *Phys. Rev. B* **1986**, *33*, 8822–8824;

[4] Y. Zhao, D. G. Truhlar, *Theor. Chem. Acc.* **2008**, *120*, 215–241.

[5] a) A. D. Becke, *J. Chem. Phys.* **1993**, *98*, 5648–5652; b) C. Lee, W. Yang, R. G. Parr, *Phys. Rev. B* **1988**, *37*, 785–789; c) P. J. Stephens, F. J. Devlin, C. F. Chabalowski, M. J. Frisch, *J. Phys. Chem.* **1994**, *98*, 11623–11627; d) S. H. Vosko, L. Wilk, M. Nusair, *Can. J. Phys.* **1980**, *58*, 1200–1211;

[6] a) F. Weigend, F. Furche, R. Ahlrichs, *J. Chem. Phys.* **2003**, *119*, 12753–12762; b) F. Weigend, R. Ahlrichs, *Phys. Chem. Chem. Phys.* **2005**, *7*, 3297–3305;

[7] D. Andrae, U. Huermann, M. Dolg, H. Stoll, H. Preu, *Theor. Chim. Acta* **1990**, *77*, 123–141.

[8] P. J. Knowles, C. Hampel, H.-J. Werner, *J. Chem. Phys.* **1993**, *99*, 5219–5227.

[9] H.-J. Werner, P. J. Knowles, G. Knizia, F. R. Manby, M. Schütz, P. Celani, W. Györffy, D. Kats, T. Korona, R. Lindh, A. Mitrushenkov, G. Rauhut, K. R. Shamasundar, T. B. Adler, R. D. Amos, S. J. Bennie, A. Bernhardsson, A. Berning, D. L. Cooper, M. J. O. Deegan, A. J. Dobbyn, F. Eckert, E. Goll, C. Hampel, A. Hesselmann, G. Hetzer, T. Hrenar, G. Jansen, C. Köppl, S. J. R. Lee,

Y. Liu, A. W. Lloyd, Q. Ma, R. A. Mata, A. J. May, S. J. McNicholas, W. Meyer, T. F. Miller III, M. E. Mura, A. Nicklass, D. P. O'Neill, P. Palmieri, D. Peng, K. Pflüger, R. Pitzer, M. Reiher, T. Shiozaki, H. Stoll, A. J. Stone, R. Tarroni, T. Thorsteinsson, M. Wang, M. Welborn, *MOLPRO, version 2019.2, a package of ab initio programs*.

[10] a) P. J. Knowles, H.-J. Werner, *Chem. Phys. Lett.* **1985**, *115*, 259–267; b) D. A. Kreplin, P. J. Knowles, H.-J. Werner, *The Journal of chemical physics* **2019**, *150*, 194106; c) H.-J. Werner, P. J. Knowles, *J. Chem. Phys.* **1985**, *82*, 5053–5063;

[11] a) C. Angeli, R. Cimiraglia, S. Evangelisti, T. Leininger, J.-P. Malrieu, *J. Chem. Phys.* **2001**, *114*, 10252–10264; b) C. Angeli, R. Cimiraglia, J.-P. Malrieu, *J. Chem. Phys.* **2002**, *117*, 9138–9153; c) C. Angeli, M. Pastore, R. Cimiraglia, *Theor Chem Acc* **2007**, *117*, 743–754;

[12] a) N. B. Balabanov, K. A. Peterson, *J. Chem. Phys.* **2005**, *123*, 64107; b) R. A. Kendall, T. H. Dunning, R. J. Harrison, *J. Chem. Phys.* **1992**, *96*, 6796–6806; c) T. H. Dunning, *J. Chem. Phys.* **1989**, *90*, 1007–1023;

[13] a) D. Figgen, K. A. Peterson, M. Dolg, H. Stoll, *J. Chem. Phys.* **2009**, *130*, 164108; b) K. A. Peterson, D. Figgen, M. Dolg, H. Stoll, *J. Chem. Phys.* **2007**, *126*, 124101;

[14] A. Wolf, M. Reiher, B. A. Hess, *J. Chem. Phys.* **2002**, *117*, 9215–9226.

[15] W. Jiang, N. J. DeYonker, A. K. Wilson, *J. Chem. Theory Comput.* **2012**, *8*, 460–468.

[16] J. Wang, S. Manivasagam, A. K. Wilson, *J. Chem. Theory Comput.* **2015**, *11*, 5865–5872.

[17] a) F. Neese, *WIREs Comput. Mol. Sci.* **2012**, *2*, 73–78; b) F. Neese, *WIREs Comput. Mol. Sci.* **2017**, *2*, e1327; c) J. N. Harvey, M. Aschi, H. Schwarz, W. Koch, *Theor Chem Acc* **1998**, *99*, 95–99;

[18] R. F. W. Bader, *Atoms in Molecules: A Quantum Theory;* Clarendon Press, **1994**.

[19] T. Lu, F. Chen, *J. Comput. Chem.* **2012**, *33*, 580–592.

[20] A. E. Reed, Schleyer, Paul v. R, *J. Am. Chem. Soc.* **1990**, *112*, 1434–1445.

[21] K. B. Wiberg, *Tetrahedron* **1968**, *24*, 1083–1096.

[22] E. D. Glendening, J. K. Badenhoop, A. E. Reed, J. E. Carpenter, J. A. Bohmann, C. M. Morales, P. Karafiloglou, C. R. Landis, F. Weinhold, *NBO 7.0;* Theoretical Chemistry Institute, University of Wisconsin, Madison, WI, **2018**.

[23] W. Humphrey, A. Dalke, K. Schulten, *Journal of Molecular Graphics* **1996**, *14*, 33-8, 27-8.

[24] X. Wang, L. Andrews, R. Lindh, V. Veryazov, B. O. Roos, *J. Phys. Chem. A* **2008**, *112*, 8030–8037.

[25] C. Vogel, F. W. Heinemann, J. Sutter, C. Anthon, K. Meyer, *Angew. Chem. Int. Ed.* **2008**, *47*, 2681–2684.

[26] T. Schlöder, T. Vent-Schmidt, S. Riedel, *Angew. Chem. Int. Ed.* **2012**, *51*, 12063–12067.

[27] A. K. Brisdon, E. G. Hope, J. H. Holloway, W. Levason, J. S. Ogden, *J. Fluorine Chem.* **1993**, *64*, 117–123.

[28] M. R. Sundberg, R. Ponec, *Inorg. Chim. Acta FIELD Full Journal Title:Inorganica Chimica Acta* **2006**, *359*, 899–906.

[29] M. Kaupp, *J. Comput. Chem.* **2007**, *28*, 320–325.

[30] B. O. Roos, A. C. Borin, L. Gagliardi, *Angew. Chem. Int. Ed.* **2007**, *46*, 1469–1472.

[31] J. J. Scepaniak, C. S. Vogel, M. M. Khusniyarov, F. W. Heinemann, K. Meyer, J. M. Smith, *Science* **2011**, *331*, 1049–1052.

[32] J. F. Berry, E. Bill, E. Bothe, S. D. George, B. Mienert, F. Neese, K. Wieghardt, *Science* **2006**, *312*, 1937–1941.

[33] a) M. E. Jacox, *J. Phys. Chem. Ref. Data* **1998**, *27*, 115–393; b) D. E. Milligan, M. E. Jacox, *J. Chem. Phys.* **1964**, *40*, 2461–2466;

[34] a) G. Sabenya, L. Lázaro, I. Gamba, V. Martin-Diaconescu, E. Andris, T. Weyhermüller, F. Neese, J. Roithova, E. Bill, J. Lloret-Fillol, M. Costas, *J. Am. Chem. Soc.* **2017**, *139*, 9168–9177; b) E. Andris, R. Navrátil, J. Jašík, G. Sabenya, M. Costas, M. Srnec, J. Roithová, *Chemistry – A European Journal* **2018**, *24*, 5078–5081;

[35] a) T. A. Betley, J. C. Peters, *J. Am. Chem. Soc.* **2004**, *126*, 6252–6254; b) J.-U. Rohde, T. A. Betley, T. A. Jackson, C. T. Saouma, J. C. Peters, Que, Lawrence, Jr, *Inorganic Chemistry (Washington, DC, United States)* **2007**, *46*, 5720–5726;

[36] L. Bucinsky, M. Breza, W.-T. Lee, A. K. Hickey, D. A. Dickie, I. Nieto, J. A. DeGayner, T. D. Harris, K. Meyer, J. Krzystek, A. Ozarowski, J. Nehrkorn, A. Schnegg, K. Holldack, R. H. Herber, J. Telser, J. M. Smith, *Inorg. Chem.* **2017**, *56*, 4752–4769.

[37] J. J. Scepaniak, M. D. Fulton, R. P. Bontchev, E. N. Duesler, M. L. Kirk, J. M. Smith, *J. Am. Chem. Soc.* **2008**, *130*, 10515–10517.

[38] M. Keilwerth, L. Grunwald, W. Mao, F. W. Heinemann, J. Sutter, E. Bill, K. Meyer, *J. Am. Chem. Soc.* **2021**, *143*, 1458–1465.

[39] W. D. Wagner, K. Nakamoto, *J. Am. Chem. Soc.* **1989**, *111*, 1590–1598.

[40] a) J. W. Buchler, C. Dreher, K. L. Lay, *Z. Naturforsch, B: Chem. Sci.* **1982**, *37*, 1155–1162; b) J. W. Buchler, C. Dreher, K.-L. Lay, A. Raap, K. Gersonde, *Inorg. Chem.* **1983**, *22*, 879–884; c) C. Campochiaro, J. A. Hofmann, D. F. Bocian, *Inorg. Chem.* **1985**, *24*, 449–450;

[41] J. T. Groves, T. Takahashi, W. M. Butler, *Inorg. Chem.* **1983**, *22*, 884–887.

[42] H.-X. Wang, L. Wu, B. Zheng, L. Du, W.-P. To, C.-H. Ko, D. L. Phillips, C.-M. Che, *Angewandte Chemie International Edition* **2020**.

[43] a) T. Petrenko, S. DeBeer George, N. Aliaga-Alcalde, E. Bill, B. Mienert, Y. Xiao, Y. Guo, W. Sturhahn, S. P. Cramer, K. Wieghardt, F. Neese, *J. Am. Chem. Soc.* **2007**, *129*, 11053–11060; b) N. Aliaga-Alcalde, S. DeBeer George, B. Mienert, E. Bill, K. Wieghardt, F. Neese, *Angew. Chem. Int. Ed.* **2005**, *44*, 2908–2912;

[44] N. B. Thompson, M. T. Green, J. C. Peters, *J. Am. Chem. Soc.* **2017**, *139*, 15312–15315.

[45] a) A. Halkier, T. Helgaker, P. Jorgensen, W. Klopper, H. Koch, J. Olsen, A. K. Wilson, *Chem. Phys. Lett.* **1998**, *286*, 243–252; b) T. Helgaker, W. Klopper, H. Koch, J. Noga, *J. Chem. Phys.* **1997**, *106*, 9639–9646;

[46] A. Halkier, T. Helgaker, P. Jørgensen, W. Klopper, J. Olsen, *Chem. Phys. Lett.* **1999**, *302*, 437–446.

A.2 Fluoro Nitrenoid Complexes $FN{=}MF_2$ (M = Co, Rh, Ir): Electronic Structure Dichotomy and Formation of Nitrido Fluorides $N{\equiv}MF_3$

Angewandte Chemie
Eine Zeitschrift der Gesellschaft Deutscher Chemiker

Supporting Information

Fluoro Nitrenoid Complexes $FN{=}MF_2$ (M = Co, Rh, Ir): Electronic Structure Dichotomy and Formation of Nitrido Fluorides $N{\equiv}MF_3$

*Tony Stüker, Thomas Hohmann, Helmut Beckers, and Sebastian Riedel**

ange_202010950_sm_miscellaneous_information.pdf

Contents

Contents 1
Experimental and Computational Details 1
Detailed Assignments 2
Synthesis of $^{15}NF_3$ 4
Supporting Figures 6
Supporting Tables 13
Detailed Computational Results 15
Supporting Information References 34

Experimental and Computational Details

Computational Details

Density functional theory (DFT) calculations were performed using the TURBOMOLE 7.0.1 program package[1] employing the GGA and hybrid exchange-correlation density functionals BP86[2] and B3LYP[3] with the polarized quadruple-ξ basis set def2-QZVP[4] which applies the Stuttgart-Dresden effective core potential for rhodium and iridium[5]. The Coupled Cluster Single Double and perturbative Triple excitations (CCSD(T)) calculations were carried out in the spin unrestricted ROHF-UCCSD(T) open-shell coupled cluster formalism using default frozen core settings as implemented in the Molpro 2019 software package.[6] The same software was used for all Complete Active Space Self Consistent Field (CASSCF) and Complete Active Space Perturbation Theory Second Order (CASPT2) calculations. Unless stated otherwise, all CCSD(T) calculations were combined with the augmented triple-ξ basis sets aug-cc-pVTZ for nitrogen and fluorine, and aug-cc-pVTZ-PP for rhodium and iridium.[7–9] CASPT2 calculations for $FNRhF_2$ and $FNCoF_2$ were carried out with relativistic corrections using the second order Douglas-Kroll-Hess Hamiltonian combined with the Dunning's correlation consistent polarized triple-ξ basis sets cc-pVTZ-DK[7,8,10]. The active space for the state-specific complete active-space (SS-CASSCF) reference wavefunction was chosen to consist of the M-N σ and π binding and anti-binding and the metal centered d-type molecular orbitals formed by the 2p(N), 3d(Co) and 4d(Rh) atomic orbitals, yielding 9 electrons in 7 molecular orbitals (9,7) for $FNCoF_2$ and $FNRhF_2$. Single point SS-CASSCF calculations carried out for $NRhF_3$ and $NIrF_3$ consisted of an active space of of 9 electrons in 8 orbitals covering the M-N three bonding, three antibonding and the singly and doubly occupied metal centered molecular orbitals. The lowest 9 molecular orbitals for $FNCoF_2$/$NCoF_3$ and the lowest 18 molecular orbitals for $FNRhF_2$/$NRhF_3$ were frozen in the subsequent CASPT2 dynamic

correlation treatment. Harmonic vibrational frequency calculations were carried out for optimized structures analytically (BP86, B3LYP) or numerically (CCSD(T) and CASPT2).Matrix-isolation Experiments

$^{14}NF_3$ and $^{15}NF_3$ (vide infra) were premixed with neon or argon (both 99.999 %, Linde) in a stainless-steel cylinder. The mixing vessel was connected to a stainless-steel vacuum line connected to a self-made matrix chamber by a stainless-steel capillary. The gas mixture was then co-deposited for 100 min with laser-ablated cobalt, rhodium or iridium atoms onto a CsI window (argon matrices) or onto a gold plated copper mirror (neon matrices) and cooled to 4 K by using a closed-cycle helium cryostat (Sumitomo Heavy Industries, RDK–205D) inside the vacuum chamber. For the laser-ablation, the 1064 nm fundamental of a Nd:YAG laser (Continuum, Minilite II, 10 Hz repetition rate, 35–50 mJ pulse^{-1}) was focused onto a rotating iridium metal target through a hole in the cold window. Infrared spectra were recorded on a Bruker Vertex 70 spectrometer purged with dry air (argon matrices) or a Bruker Vertex 80v with evacuated optical path (neon matrices) at 0.5 cm^{-1} resolution in the region 4000–430 cm^{-1} by using a liquid-nitrogen-cooled mercury cadmium telluride (MCT) detector. The matrix samples were irradiated by a mercury arc streetlamp (Osram HQL 250) with the outer globe removed.

Detailed Assignments

Laser-ablated iridium, rhodium and cobalt atoms were reacted with $^{14}NF_3$ and $^{15}NF_3$ in a 1:1000 excess of neon or argon and deposited on a gold-plated copper mirror cooled to 5 and 12 K, respectively. The IR spectra in excess neon are shown in Figures 2–4 for iridium, rhodium and cobalt. The complementary argon spectra for iridium and rhodium are shown in Figures S1-S3. By comparing spectra of the reaction products of one metal with those of another metal, the metal dependent bands were identified. Further simplification was achieved by neglecting bands belonging to MF_n obtained by recording complementary spectra of metal fluorine reaction products under the same conditions. It is worth pointing out that the IR spectra obtained in neon are generally of better quality in terms of intensity and line broadening. This is because neon is being considered the least interacting and most inert cryogenic matrix available.[11]

$FNCoF_2$

After co-depositing laser-ablated Co and NF_3 diluted in Ne, the IR spectra shown in Figure S11 and S12 were recorded. The 1100–725 cm^{-1} region in Figure S11 contains two bands. A weak band at 1056.8 cm^{-1} which exhibits an $^{14/15}N$ isotopic shift of −21.4 cm^{-1} and at 751.7 cm^{-1} without isotopic shift. In the spectral region of 725–525 cm^{-1} shown in Figure S12 two bands with an isotopic shift are located at 629.6 and 586.1 cm^{-1} with isotopic shifts of −3.5 and −12.1 cm^{-1}, respectively. The isotopic shift of the band at 1056.8 cm^{-1} is considereably less than expected for a terminal bond nitrogen atom and consistent with an assignment to to the F-N stretching mode of $FNCoF_2$. The remaining bands at 751.7, 629.6 and 586.1 cm^{-1} are assigned to the antisymmetric F-Co-F, symmetric F-Co-F and to the N-Co stretching mode. Attempts to use single reference correlation methods to calculate the geometry and frequencies of this species failed. They did not converge (CCSD(T)), or did not yield qualitatively

consistent results (B3LYP and BP86). To account for the strong non-dynamical correlation, CASSCF(9,7) with subsquent CASPT2 dynamical correlation treatment was employed. The values calculated at the CASPT2/cc-pVTZ-DK level of theory are in good agreement with the experiment (Table 1). The assignment of $FNCoF_2$ is further supported by the fact that the lowest energy structural isomer based on the reaction enthalpies summarized in Table S1.

$NRhF_3$

The IR spectra obtained after co-depositing evaporated rhodium and diluted NF_3 in neon shown in Figures S13 and S14 contain three bands with significant isotopic shifts. The position of the band at 1116.1 cm^{-1} (Figure 3, **A**) and the isotopic shift of −33 cm^{-1} are indicative for a terminally bond nitrogen with a triple bond. This band, as well as three additional bands in the M-F stretching region were assigned to $NRhF_3$. The bands located at 626.2 and 622.8 cm^{-1} loose intensity upon broadband irradiation and annealing to 12 K with their initially weaker matrix sites at 624.8 and 622.2 cm^{-1} gaining intensity. These bands were assigned to the antisymmetric and symmetric F-Rh-F stretching mode, respectively. The last band is located at 542.5 cm^{-1} shows a small isotopic shift of −0.5 cm^{-1} and was assigned to the Rh-F' stretching mode. The assignments are supported by quantum chemical calculations, which yield 1087 (1113), 625 (603), 618 (601) and 581 (562) cm^{-1} at the BP86 (B3LYP) levels of theory. The calculated isotopic shift of the N-Rh stretching mode is −32 (−33) at the BP86 (B3LYP) level of theory, respectively, and in very good agreement with the experimentally observed values in neon and in argon (both −33 cm^{-1}). The small observed isotopic shift of −0.4 (−0.5) cm^{-1} of the Rh-F' stretching mode observed in neon (argon) was not predicted by both DFT methods but is also observed in $NIrF_3$ as well. Unfortunately, calculations at the CCSD(T) level of theory yield two imaginary frequencies probably caused by a low-laying excited electronic state which interferes with the calculation of displaced steps during the numerical hessian calculation where the symmetry is lowered to C_1. However, the structure obtained at the B3LYP level of theory is very close to the one obtained at the CCSD(T) level (Figures 5 and S5) and the good match of the B3LYP results for $NIrF_3$ with the experimental values suggest a good performance of B3LYP for the NMF_3 species.

$FNRhF_2$

The two remaining bands with significant isotopic shifts of −18.9 and −18.0 cm^{-1} (labeled **B** and **C** in Figure S13) centered at 872.6 and 761.4 cm^{-1} are indicative for absorptions of two modes exhibiting significant displacements of a nitrogen atom which is not terminally bonded. The assignment to the two modes involving the F-N-Rh moiety of $FNRhF_2$ suggests itself, however, while quantum chemical calculations at the DFT BP86 (B3LYP) level of theory yield acceptable band positions of 850 (935) and 721 (786) cm^{-1}, the isotopic shifts of −24 (−24) and −12 (−16) cm^{-1} do not match the observed ones. More sophisticated calculations at the CCSD(T) (CASPT2) levels of theory yield isotopic shifts of −16 (−19) and −19 (−20) (Table S5) which are in better agreement with the observed values. However, the deviations between the calculated and observed band positions at 899 (981) and 720 (756) cm^{-1} indicates the presence of vibronic coupling effects which are not taken into account in the harmonic approximation. The band centered at 872.6 cm^{-1} was assigned to the F-N stretching mode, while the band at 761.4 cm^{-1} was assigned to the N-Rh stretching mode. Along with vibrations related to the F-

N-Rh moiety, the bands belonging to the antisymmetric and symmetric F-Rh-F stretching modes were assigned to bands at 638.6 and 596.7 cm^{-1} (labeled **A** and **D** in Figure S14) in an overall very good agreement with the calculated values summarized in Table 1. The antisymmetric F-N-Rh stretching mode could not be identified in the corresponding argon spectrum. Additional bands are much weaker. They are tentatively assigned in Figures S1 and S2 and summarized in Table 1. The presence of both species, $NRhF_3$ and $FNRhF_2$, is reasonably justified considering the small energy difference of 7 [12] kJ mol^{-1} calculated at the B3LYP [CCSD(T)] level of theory (see Table S1 and Figure 1).

$NIrF_3$

After depositing iridium and NF_3 diluted in neon, bands immune to annealing and broadband irradiation centered at 1150.4, 659.8, 651.6, 648.9 and 562.1 cm^{-1} shown in Figure S15 were singled out and assigned to $NIrF_3$ with a point group symmetry of C_s. The position of the band centered at 1150.4 cm^{-1} (Figure S15, **A**), the isotopic shift of −36 cm^{-1} and the $^{14/15}N$ isotopic ratio of 1.0323 are indicative for a vibration of a strongly bond single nitrogen atom attached to a heavy element. Theoretical calculations support the assignment to the Ir≡N stretching mode, with calculated isotopic shifts of −35, −36, and −36 and $^{14/15}N$ isotopic ratios of 1.0325, 1.0325 and 1.0326 obtained the BP86/def2-QZVP, B3LYP/def2-QZVP and ROHF-UCCSD(T)/aug-cc-pVTZ(-PP) levels of theory, respectively. However, the absolute values of 1121, 1158 and 1126 cm^{-1} (BP86, B3LYP and CCSD(T)) deviate by −29, 8 and −24 cm^{-1}, respectively. The assignment of the absorption at 659.8 cm^{-1} (Figure S15, **B**) to the symmetric F-Ir-F stretching mode is backed by calculated values of 618, 635 and 653 cm^{-1} (BP86, B3LYP and CCSD(T)). Isotopic shifts were not observed and were calculated to be 0 for the $^{14/15}N$ substituted isotopologue. The more intense antisymmetric F-Ir-F stretching mode and its matrix site are located at 651.6 and 648.9 cm^{-1} (Figure S15, **C**) and do not show any matrix shift either. The calculated values of 618, 634, and 650 cm^{-1} (BP86, B3LYP, CCSD(T)) confirm the proximity of the symmetric and antisymmetric F-Ir-F stretching frequencies. Finally, the band showing a very small isotopic shift of −0.2 cm^{-1} centered at 562.1 cm^{-1} (Figure S15, **D**) was assigned to the F'-Ir stretching mode involving the fluorine atom residing the mirror plane of the molecule. The IR spectra obtained in argon (Figure S3) are not as comprehensive as in neon. The Ir-N stretching mode and the F'-Ir stretching mode were tentatively assigned to very weak bands centered at 1144.6 and 560.1 cm^{-1}, respectively. The bands belonging to the symmetric and antisymmetric F-Ir-F stretching modes are probably overlapped by the bands belonging to the strong and broad symmetric deformation mode of NF_3 and its matrix sites.

Synthesis of $^{15}NF_3$

The synthesis of $^{15}NF_3$ was carried out in an electric discharge cell described by Ruff and Menzel[12] following the procedure described by Maya[13]. A 1:4 mixture of $^{15}N_2$ and F_2 was slowly allowed to enter an electric discharge cell submerged in liquid nitrogen (LN_2) shown in Figure S9. The electronic discharge arc was generated by a current of 7.0 kV, while the flow was adjusted to maintain a constant pressure of 30–35 mbar inside the reactor. After 1.5 h a volume of 113 mL of the $^{15}N_2/F_2$ mixture was admitted to the reactor. The condensed, crude reaction product at the bottom of the reactor was

recondensed into a glass cylinder. The volatile gas phase of the LN2 cooled crude phase contained F_2 (identified through the presence of SiF_4). To remove all remaining F_2 from the crude product, the glass cylinder was cooled using a N_2 slurry and pumping off all volatile components for 5 min at 10^{-3} mbar. The purification process was followed by gas phase IR spectra shown in Figure S0. The purified product did not show any IR active impurities in a matrix-isolation spectrum in 99.9 % excess neon shown in Figure S4. In addition to the assignments by Allan et al.[14], six more combination- and overtone bands were identified and listed in Table S2. The overall yield was 73 % with respect to $^{15}N_2$, significantly higher than the reported yield of 30 % $^{14}NF_3$.[13]

Supporting Figures

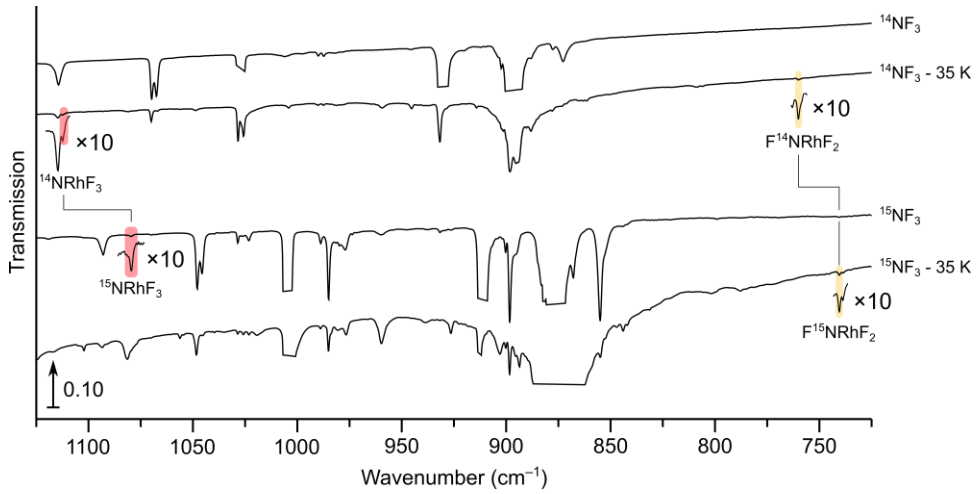

Figure S1. Infrared transmission spectra in the 1125–725 cm^{-1} region of laser ablated rhodium co-deposited with 0.5 % $^{14}NF_3$ and $^{15}NF_3$ diluted in argon and treated according to the labels.

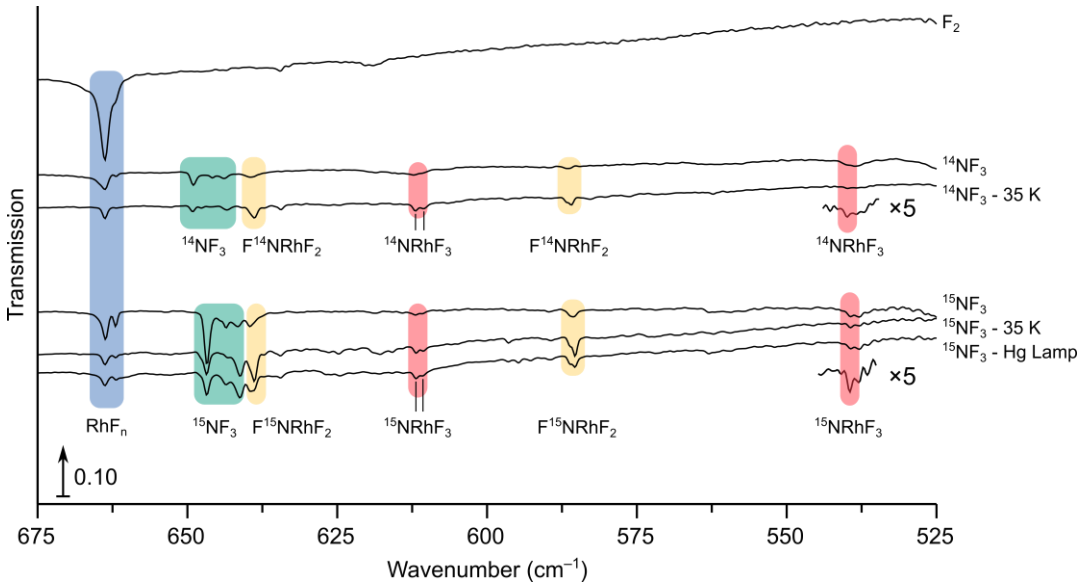

Figure S2. Infrared transmission spectra in the 675–525 cm^{-1} region of laser ablated rhodium co-deposited with 0.5 % of F_2, $^{14}NF_3$ and $^{15}NF_3$ diluted in argon and treated according to the labels.

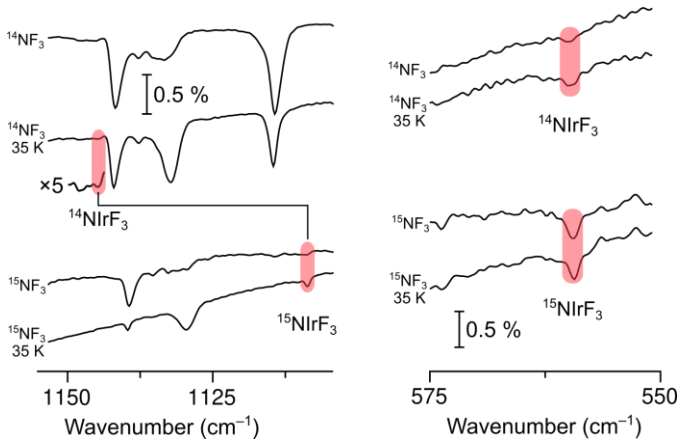

Figure S3. Infrared transmission spectra in the 1155–1100 and 575–550 cm^{-1} regions of laser ablated iridium co-deposited with 0.5 % $^{14}NF_3$ and $^{15}NF_3$ diluted in argon and treated according to the labels.

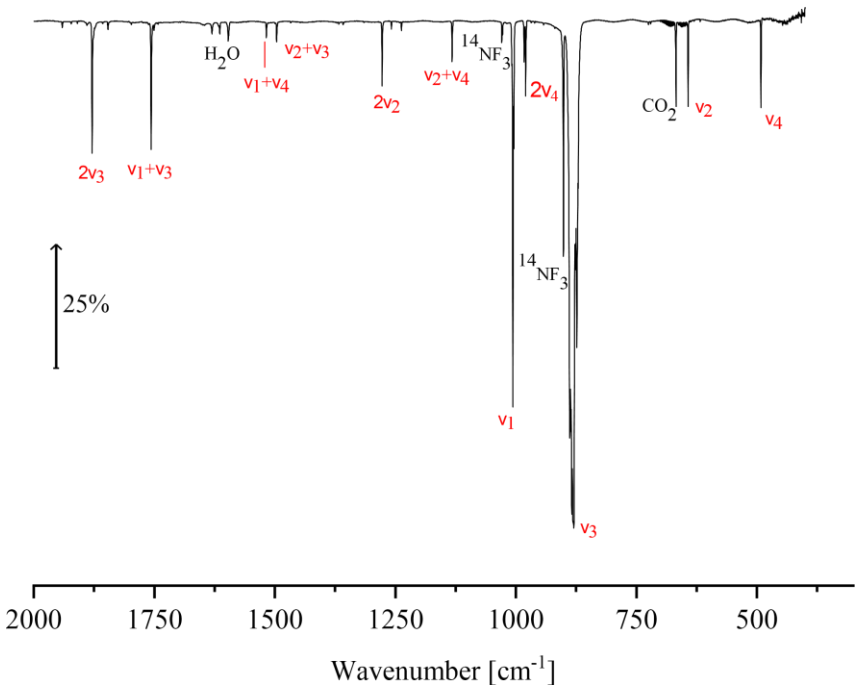

Figure S4. IR spectrum of $^{15}NF_3$ in excess neon (0.1%) at 4.2 K.

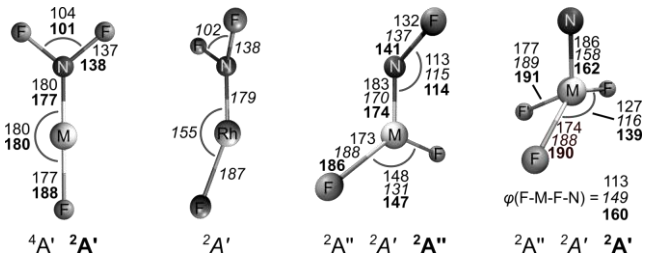

Figure S5. Molecular structures and electronic ground state symbols calculated at the B3LYP level of theory. Bond lengths in pm and angles in degree (φ denotes the dihedral angle of F-M-F-N). Values for M = Co (normal), Rh (italic) and Ir (bold).

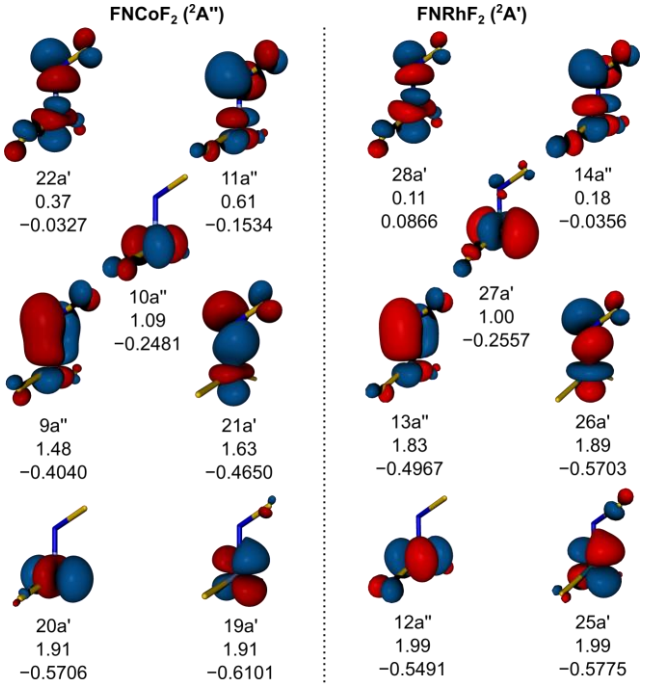

Figure S6. Natural frontier molecular orbitals (isovalue 0.05 a.u.) of $FNCoF_2$ (left) and $FNRhF_2$ (right) calculated at the CASSCF(9,7)/cc-pVTZ-DK level of theory, including irreps, occupation numbers and orbital energies.

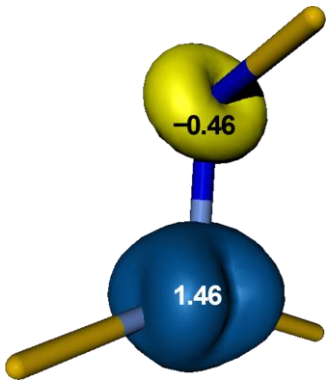

Figure S7. Spin density plot (isovalue 0.03 a.u.) of $FNCoF_2$ calculated at the CASSCF(9,7)/cc-pVTZ-DK level of theory.

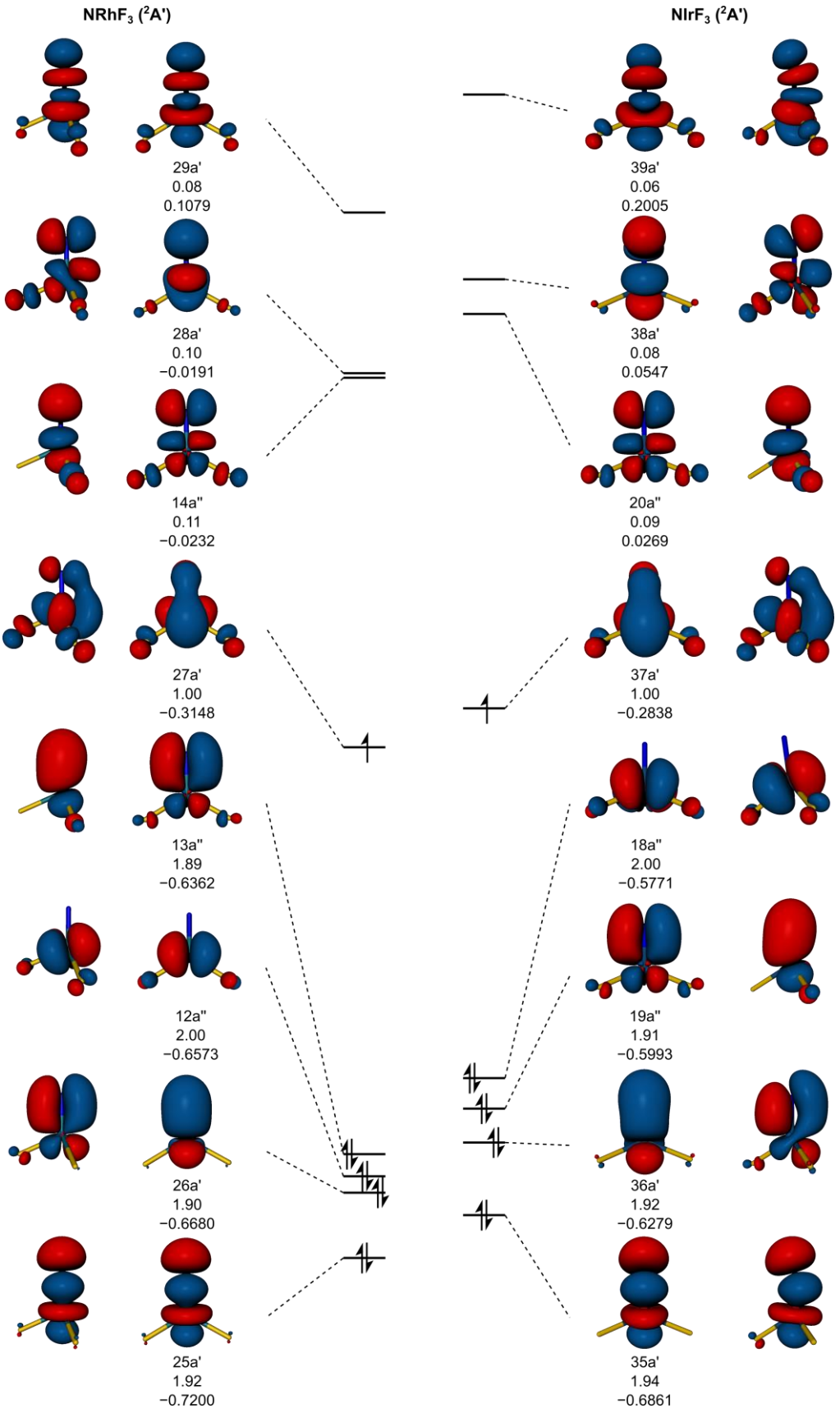

Figure S8. MO diagram of the active space natural molecular orbitals, irreproducible representations, occupation numbers and orbital energies of $NRhF_3$ (left) and $NIrF_3$ (right) calculated at the CASSCF(9,8)/cc-pVTZ-DK level of theory at the B3LYP/def2-QZVP optimized ground state structures.

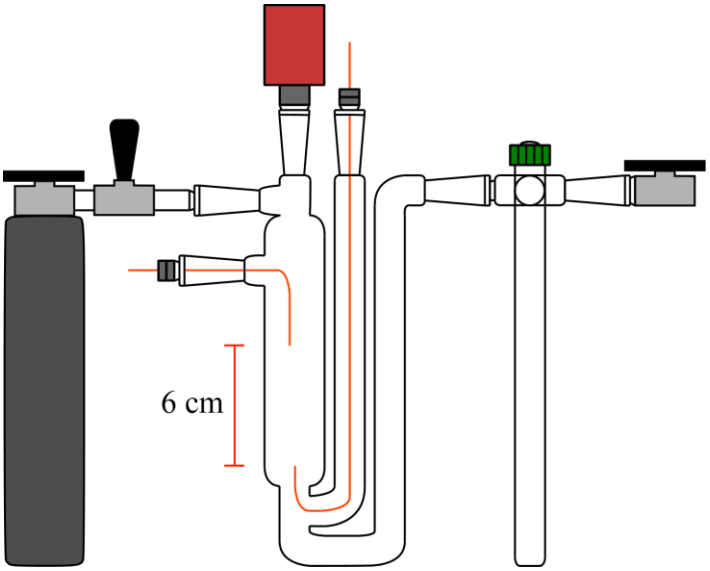

Figure S9. Electric discharge cell attached with a stainless-steel cylinder containing premixed $^{15}N_2$ and F_2 (left) and a dried glass for the final product (right).

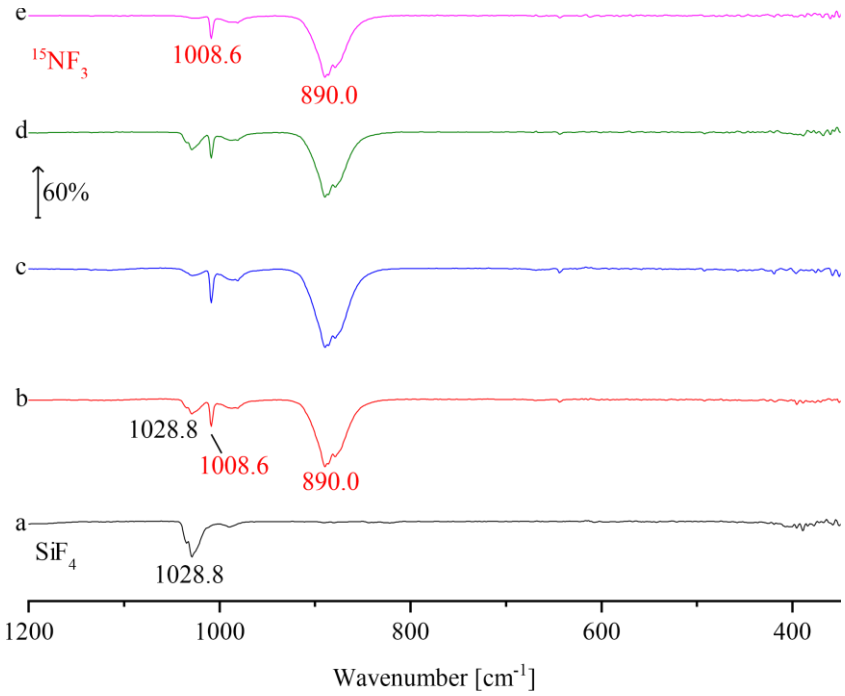

Figure S10. Gas phase IR spectra of the most volatile components of crude product during the purification process of $^{15}NF_3$ by gradually reducing the pressure to 10^{-3} mbar (e).

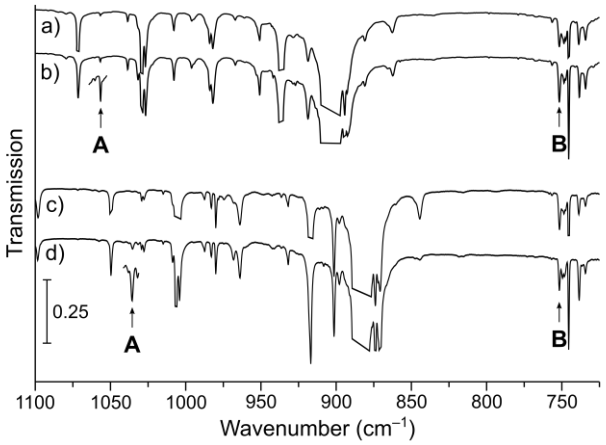

Figure S11. Infrared transmission spectra in the 1100–725 cm^{-1} region after co-depositing laser-ablated cobalt atoms with 0.1 % $^{14}NF_3$ (a), with $^{14}NF_3$ after annealing to 10 K (b) as well as with $^{15}NF_3$ (c), with subsequent annealing to 10 K (d). The absorption bands belonging to the F-N stretching mode and antisymmetric F-Co-F stretching mode are labeled **A** and **B**, respectively.

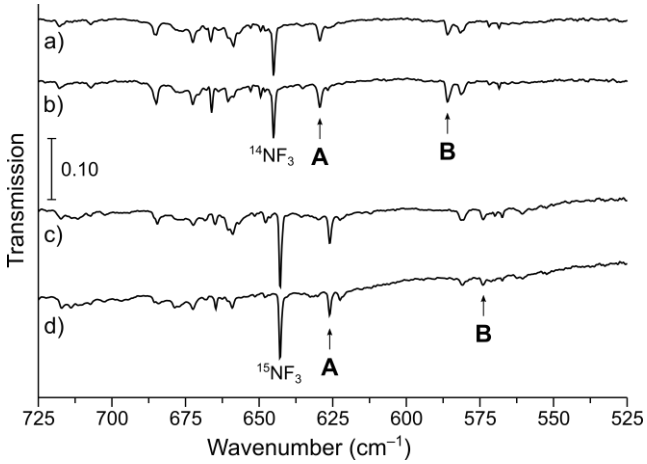

Figure S12. Infrared transmission spectra in the 725–525 cm^{-1} region after co-depositing laser-ablated cobalt atoms with 0.1 % $^{14}NF_3$ (a), with $^{14}NF_3$ after annealing to 10 K (b) as well as with $^{15}NF_3$ (c), with subsequent annealing to 10 K (d). The absorption bands belonging to the symmetric F-Co-F stretching mode and Co-N stretching mode are labeled **A** and **B**, respectively.

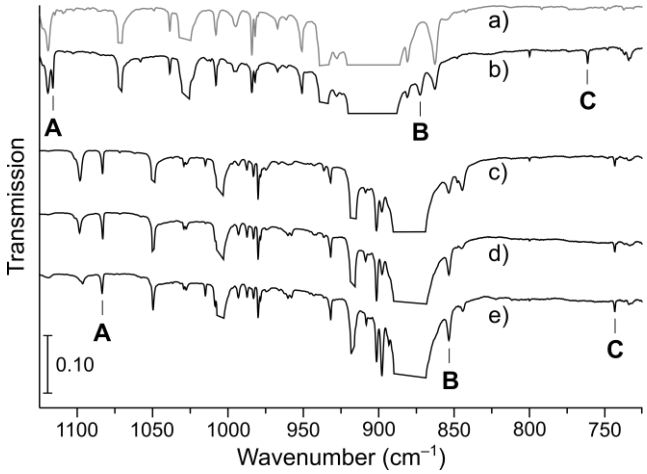

Figure S13. Infrared transmission spectra in the 1125–725 cm^{-1} region after co-depositing laser-ablated iridium atoms with 0.1 % $^{14}NF_3$ (a), co-depositing rhodium with $^{14}NF_3$ (b) as well as $^{15}NF_3$ (c), with subsequent full-arc photolysis (d) and annealing to 12 K (e). The absorption bands belonging to the N-Rh stretching mode of $NRhF_3$, Rh-N-F stretching mode and to the symmetric Rh-N-F stretching mode are labeled **A**, **B** and **C**. For the sake of clearity, some very strong NF_3 absorption bands were cropped.

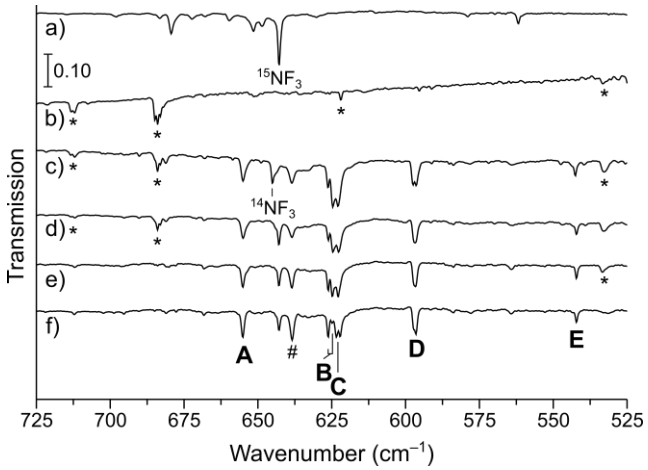

Figure S14. Infrared transmission spectra in the 725–525 cm^{-1} region after co-depositing laser-ablated iridium atoms with 0.1 % $^{15}NF_3$ (a), co-depositing rhodium with 0.1 % F_2 (b), with 0.1 % $^{14}NF_3$ (c), with 0.1 % $^{15}NF_3$ (d), after full arc photolysis (e) and annealing to 12 K (f). The absorption bands belonging to the antisymmetric and symmetric F-Rh-F stretching mode of $FNRhF_2$ are labeled with **A** and **D**. The absorption bands stemming from the antisymmetric and symmetric F-Rh-F stretching, as well as the F'-Rh stretching mode of $NRhF_3$ are labeled with **B**, **C** and **E**, respectively. Bands marked with asterisks are assigned to rhodium fluorides.

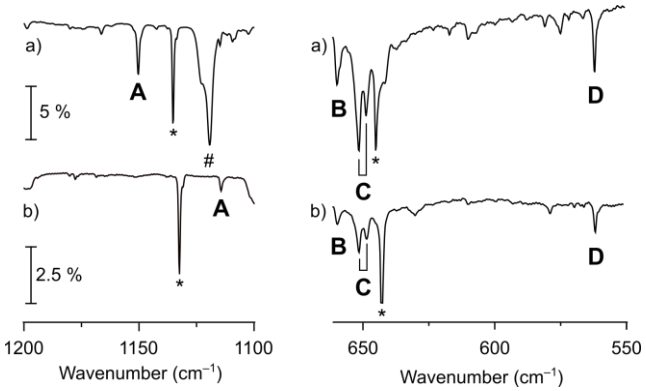

Figure S15. Infrared transmission spectra in the 1200–1100 cm^{-1} (left) and 660–550 cm^{-1} (right) region from co-deposition of laser-ablated iridium atoms with 0.1 % $^{14}NF_3$ (a) and 0.1 % $^{15}NF_3$ in neon. Bands highlighted. Labels **A**, **B, C** and **D** denote the absorption bands of $NIrF_3$. Namely, the Ir-N stretching mode, the symmetric F-Ir-F stretching mode, the antisymmetric F-Ir-F stretching mode and the Ir-F' stretching mode, respectively. Labels ***** and # denote absorptions bands from NF_3 and NF, respectively.

Supporting Tables

Table S1. Reaction enthalpies at $T = 0$ for reactions of formation and selected decomposition reactions obtained at the B3LYP and BP86 level of theory. All complexes in *C*s point group symmetry, unless stated otherwise.

Reaction		ΔH^0 [kJ mol^{-1}]	
		B3LYP	**BP86**
Co + NF_3 ($^1A_1$)	→ F_2NCoF ($^4A_2$ – C_{2v})	−470	−441
F_2NCoF ($^4A_2$ – C_{2v})	→ $FNCoF_2$ ($^2A''$)	−92	−158
$FNCoF_2$ ($^2A''$)	→ $NCoF_3$ ($^2A''$)	77	47
$FNCoF_2$ ($^2A''$)	→ $NCoF_2$ ($^1A_1$ – C_{2v}) + F	331	290
$FNCoF_2$ ($^2A''$)	→ $NCoF_2$ ($^3B_1$ – C_{2v}) + F	311	315
$FNCoF_2$ ($^2A''$)	→ $NCoF_2$ ($^1A_1$ – C_{2v}) + ½ F_2	258	187
$FNCoF_2$ ($^2A''$)	→ $NCoF_2$ ($^3B_1$ – C_{2v}) + ½ F_2	238	212
$FNCoF_2$ ($^2A''$)	→ NCoF ($^4A''$) + F_2	522	533
$FNCoF_2$ ($^2A''$)	→ NCoF ($^2A'$) + F_2	522	493
Rh + NF_3 ($^1A_1$)	→ F_2NRhF ($^2A'$)	−356	−413
F_2NRhF ($^2A'$)	→ $FNRhF_2$ ($^2A'$)	−136	−155
$FNRhF_2$ ($^2A'$)	→ $NRhF_3$ ($^2A'$) [a]	−7	−26
$NRhF_3$ ($^2A'$)	→ $NRhF_2$ ($^1A_1$ – C_{2v}) + F	168	221
$NRhF_3$ ($^2A'$)	→ $NRhF_2$ ($^1A_1$ – C_{2v}) + ½ F	95	118
$NRhF_3$ ($^2A'$)	→ NRhF ($^2A'$) + F_2	386	423
Ir + NF_3 ($^1A_1$)	→ F_2NIrF ($^2A'$)	−460	−509
F_2NIrF ($^2A'$)	→ $FNIrF_2$ ($^2A''$)	−186	−201
$FNIrF_2$ ($^2A''$)	→ $NIrF_3$ ($^2A'$) [b]	−81	−77
$NIrF_3$ ($^2A'$)	→ $NIrF_2$ ($^1A_1$) + F	197	240
$NIrF_3$ ($^2A'$)	→ $NIrF_2$ ($^1A_1$) + ½ F	248	274
$NIrF_3$ ($^2A'$)	→ NIrF ($^2A'$) + F_2	444	468

[a]: CCSD(T) at B3LYP minimum: ΔH^0 = −12 kJ mol^{-1}; [b]: CCSD(T) at B3LYP minimum: ΔH^0 = −98 kJ mol^{-1}

Table S2. Assignments of IR absorptions of 0.1 % $^{15}NF_3$ isolated in solid neon (Figure S2).

Assignment	Frequency [cm^{-1}]	Intensity*	Isotopic Shift [cm^{-1}]	Lit.[14]
$\nu_1 + \nu_3$	1879.1	m		-
$2\nu_3$	1756.7	m		-
$\nu_2 + \nu_3$	1517.5	w		-
$\nu_1 + \nu_4$	1496.3	w		-
$2\nu_2$	1277.4	m		-
$\nu_2 + \nu_4$	1132.3	m		-
ν_1	1006.2	s	–22.9	1008.9
$2\nu_4$	979.7	m		981.9
ν_3	879.9	vs	–21.5	886.3
ν_2	642.7	m		644.8
ν_4	491.6	m		492.0

Table S3. Selected structural parameters calculated at various levels of theory for $FNMNF_2$ (M = Co, Rh) species. Bond lengths in pm, angles in degrees.

	r(FN)		r(NM)		r(MF)		a(FNM)		a(FMF)	
Method	**$FNCoF_2$**	**$FNRhF_2$**	**$FNCoF_2$**	**$FNRhF_2$**	**$FNCoF_2$**	**$FNRhF_2$**	**$FNCoF_2$**	**$FNRhF_2$**	**$FNCoF_2$**	**$FNRhF_2$**
CASPT2	131	135	177	174	171	186	113	113	148	135
B3LYP	132	137	183	170	173	188	113	115	148	131
BP86 [a)]	138	142	162	172	172	186/191	115	117	133	131

[a]: BP86 converged to a structure with C_1 point group symmetry for $FNRhF_2$.

Table S4. Weights of the main configurations of the electronic ground states of $FNCoF_2$ (^{2}A'', Cs) and $FNRhF_2$ (^{2}A', C_s) obtained at the CASSCF(9,7)/cc-pVTZ-DK level of theory.

Configuration[a)]	Weight [%]
$FNCoF_2$ (^{2}A'', C_s)	
$\sigma^2\ \pi^2\ \delta^1\ \pi^{*0}\ \sigma^{*0}$	48
$\sigma^2\ \pi^0\ \delta^1\ \pi^{*2}\ \sigma^{*0}$	10
$\sigma^2\ \pi^1\ \delta^1\ \pi^{*1}\ \sigma^{*2}$	6
$\sigma^0\ \pi^2\ \delta^1\ \pi^{*0}\ \sigma^{*2}$	5
$\sigma^0\ \pi^0\ \delta^1\ \pi^{*2}\ \sigma^{*2}$	4
$FNRhF_2$ (^{2}A', C_s)	
$\sigma^2\ \pi^2\ \delta^1\ \pi^{*0}\ \sigma^{*0}$	81
$\sigma^2\ \pi^0\ \delta^1\ \pi^{*2}\ \sigma^{*0}$	5

[a] Approximate local symmetries are used for an ostensive description the frontier molecular orbitals along the M-N bond axis. σ, π, δ, σ*, π* and δ* correspond to 21a', 9a'', 10a'', 11a'' and 22a' ($FNCoF_2$) and 26a', 13a'', 27a', 14a'' and 28a' ($FNRhF_2$) (see Figure S6).

Table S5. Comparison of infrared band positions (cm^{-1}) and isotopic shifts (cm^{-1}, in parenthesis) of $FNRhF_2$ ($^2A'$ - C_s) observed in solid neon with values calculated using CCSD(T) with different basis set qualities, and CASPT2.

Assignment	Neon	cc-pVDZ(-PP)[a)]	aug-cc-pVTZ(-PP)[a)]	cc-pVTZ-DK[b)]	CASPT2
F-N str. [a']	872.6 (−18.9)	893 (−16)	872 (−16)	899 (−17)	981 (−19)
N-Rh str. [a']	761.4 (−18.0)	536 (−15)	707 (−19)	720 (−18)	756 (−20)
antisym. F-Rh-F str. [a'']	655.1 (0)	665 (0)	652 (0)	663 (0)	672 (0)
sym. F-Rh-F str. [a']	596.7 (0)	620 (−2)	580 (−2)	603 (−2)	623 (−0.5)

[a]: RHF/UCCSD(T) using ECP28MDF. [b]: RHF/UCCSD(T) using DKH2 relativistic approximation.

Detailed Computational Results

All structures in C_s point group symmetry (unless stated otherwise) and with positive HOMO-LUMO or SOMO-LUMO gap.

$NCoF_3$

$NCoF_3$ ($^2A''$)

UB3LYP/def2-QZVP

Cartesian coordinates

```
5
Energy = -1736.977510164
Co   -0.0824265    0.1971398    0.0000000
N     0.0349649   -1.6577570    0.0000000
F    -0.8083289    0.4847773   -1.5498606
F    -0.8083289    0.4847773    1.5498606
F     1.6641194    0.4910626    0.0000000
```

Vibrational data (^{14}N)

```
#  mode     symmetry     wave number   IR intensity    selection rules
#                          cm**(-1)       km/mol         IR     RAMAN
     7        a"            59.35        30.72704       YES     YES
     8        a'           105.26         1.24646       YES     YES
     9        a"           167.56         1.25348       YES     YES
    10        a'           172.03        11.22983       YES     YES
    11        a'           178.97        23.98249       YES     YES
    12        a'           350.87        14.14127       YES     YES
    13        a'           641.89        16.50932       YES     YES
    14        a'           669.44       116.12893       YES     YES
    15        a"           681.27       219.92593       YES     YES

zero point VIBRATIONAL energy  :      0.0068952  Hartree
```

UBP86/def2-QZVP

Cartesian coordinates

```
5
Energy = -1737.485783464
Co    0.0728443   -0.1192190    0.0000000
N    -0.0208896   -1.6287334    0.0000000
F    -0.8502485    0.5715962   -1.3132437
F    -0.8502485    0.5715962    1.3132437
F     1.6485423    0.6047601    0.0000000
```

Vibrational data (^{14}N)

```
#  mode     symmetry     wave number   IR intensity    selection rules
#                          cm**(-1)       km/mol         IR     RAMAN
     1        a"           -84.40         0.00000       YES     YES
     2                     -0.00         0.00000        -       -
     3                     -0.00         0.00000        -       -
     4                      0.00         0.00000        -       -
     5                      0.00         0.00000        -       -
     6                      0.00         0.00000        -       -
     7                      0.00         0.00000        -       -
     8        a'           155.54         2.71508       YES     YES
     9        a"           194.10         2.25560       YES     YES
    10        a'           232.19         5.74052       YES     YES
    11        a'           305.27         0.33614       YES     YES
    12        a'           632.77        35.06050       YES     YES
    13        a"           633.32        70.40555       YES     YES
    14        a'           673.32        82.23947       YES     YES
    15        a'          1064.23        38.95532       YES     YES

zero point VIBRATIONAL energy  :      0.0088637  Hartree
```

$NCoF_3$ ($^2A'$)

UB3LYP/def2-QZVP

Cartesian coordinates

```
5
Energy = -1736.964585276
Co   -0.1036774    0.0986648    0.0000000
N    -0.0159914   -1.6090243    0.0000000
F    -0.7092819    0.4651010   -1.5717060
F    -0.7092819    0.4651010    1.5717060
F     1.5382325    0.5801575    0.0000000
```

Vibrational data (^{14}N)

#	mode	symmetry	wave number cm**(-1)	IR intensity km/mol	selection rules IR	RAMAN
	7	a"	136.23	3.27842	YES	YES
	8	a'	146.67	7.70575	YES	YES
	9	a'	186.57	15.49275	YES	YES
	10	a"	202.06	0.30524	YES	YES
	11	a'	214.74	7.02491	YES	YES
	12	a'	445.19	7.28441	YES	YES
	13	a'	648.89	25.69070	YES	YES
	14	a'	711.12	78.98532	YES	YES
	15	a"	730.09	154.14645	YES	YES

zero point VIBRATIONAL energy : 0.0077949 Hartree

UBP86/def2-QZVP

Cartesian coordinates

```
5
Energy = -1737.485954003
Co   -0.0826662   -0.1198141    0.0000000
N     0.0413591   -1.6272030    0.0000000
F    -0.7391524    0.5790938   -1.4494765
F    -0.7391524    0.5790938    1.4494765
F     1.5196121    0.5888295    0.0000000
```

Vibrational data (^{14}N)

#	mode	symmetry	wave number cm**(-1)	IR intensity km/mol	selection rules IR	RAMAN
	7	a"	96.35	14.57294	YES	YES
	8	a'	135.96	2.70331	YES	YES
	9	a"	208.18	1.48976	YES	YES
	10	a'	233.29	6.05019	YES	YES
	11	a'	301.59	1.36632	YES	YES
	12	a'	633.56	35.02780	YES	YES
	13	a'	643.95	55.50206	YES	YES
	14	a"	665.89	99.37128	YES	YES
	15	a'	1063.94	40.79076	YES	YES

zero point VIBRATIONAL energy : 0.0090733 Hartree

Vibrational data (^{15}N)

#	mode	symmetry	wave number cm**(-1)	IR intensity km/mol	selection rules IR	RAMAN
	7	a"	96.16	14.66095	YES	YES
	8	a'	135.79	2.64381	YES	YES
	9	a"	204.32	1.40225	YES	YES
	10	a'	232.82	6.01191	YES	YES
	11	a'	296.11	1.48385	YES	YES
	12	a'	632.86	34.36728	YES	YES
	13	a'	643.94	55.51619	YES	YES
	14	a"	665.87	99.40245	YES	YES
	15	a'	1035.35	40.36567	YES	YES

zero point VIBRATIONAL energy : 0.0089833 Hartree

$NCoF_3$ (^{4}A')

UB3LYP/def2-QZVP

Cartesian coordinates

```
5
Energy = -1736.959281210
Co   -0.0580699    0.0719537    0.0000000
N     0.0662034   -1.5643483    0.0000000
F    -0.8334018    0.5109545   -1.4886131
F    -0.8334018    0.5109545    1.4886131
F     1.6586701    0.4704857    0.0000000
```

Vibrational data (^{14}N)

#	mode	symmetry	wave number cm**(-1)	IR intensity km/mol	selection rules IR	RAMAN
	7	a"	131.43	20.84005	YES	YES
	8	a'	160.01	6.70559	YES	YES
	9	a'	200.18	9.67781	YES	YES
	10	a"	206.95	4.28889	YES	YES
	11	a'	219.46	6.78440	YES	YES
	12	a'	582.80	13.89695	YES	YES
	13	a"	652.65	181.26272	YES	YES
	14	a'	655.46	24.57878	YES	YES
	15	a'	671.43	96.45802	YES	YES

zero point VIBRATIONAL energy : 0.0079288 Hartree

UBP86/def2-QZVP

Cartesian coordinates

```
5
Energy = -1737.472854233
Co   -0.0434505    0.0123310    0.0000000
N     0.1221596   -1.5603138    0.0000000
F    -0.8764964    0.5539332   -1.4272844
F    -0.8764964    0.5539332    1.4272844
F     1.6742837    0.4401164    0.0000000
```

Vibrational data (^{14}N)

#	mode	symmetry	wave number cm**(-1)	IR intensity km/mol	selection rules IR	RAMAN
	7	a"	118.94	1.18366	YES	YES
	8	a'	162.37	4.68961	YES	YES
	9	a'	208.98	5.47374	YES	YES
	10	a"	237.30	9.10538	YES	YES
	11	a'	257.04	1.46665	YES	YES
	12	a'	609.22	23.16261	YES	YES
	13	a"	619.81	110.15532	YES	YES
	14	a'	644.64	73.47093	YES	YES
	15	a'	943.64	2.85718	YES	YES

zero point VIBRATIONAL energy : 0.0086615 Hartree

$FNCoF_2$

$FNCoF_2$ ($^2A'$)

UB3LYP/def2-QZVP

Cartesian coordinates

```
5
Energy = -1737.006373197
Co     0.6679205     0.1377497     0.0000000
F      0.9992619     0.6113960     1.6590249
F      0.9992619     0.6113960    -1.6590249
N     -0.7514116    -0.9950999     0.0000000
F     -1.9150327    -0.3654418     0.0000000
```

Vibrational data (^{14}N)

```
#  mode     symmetry     wave number   IR intensity    selection rules
#                          cm**(-1)       km/mol         IR     RAMAN
     7        a"            73.82         0.07915       YES     YES
     8        a'           116.38        23.64476       YES     YES
     9        a'           140.74        29.53924       YES     YES
    10        a'           214.91         5.37310       YES     YES
    11        a"           233.25         0.00917       YES     YES
    12        a'           435.21        13.13023       YES     YES
    13        a'           613.69        67.59420       YES     YES
    14        a"           723.27       166.39989       YES     YES
    15        a'          1079.89       291.07245       YES     YES

zero point VIBRATIONAL energy  :      0.0082724  Hartree
```

Vibrational data (^{15}N)

```
#  mode     symmetry     wave number   IR intensity    selection rules
#                          cm**(-1)       km/mol         IR     RAMAN
     7        a"            73.79         0.07699       YES     YES
     8        a'           116.31        23.60588       YES     YES
     9        a'           140.71        29.54361       YES     YES
    10        a'           213.80         5.30993       YES     YES
    11        a"           227.47         0.01604       YES     YES
    12        a'           422.53        12.00386       YES     YES
    13        a'           613.49        68.33462       YES     YES
    14        a"           723.26       166.40925       YES     YES
    15        a'          1059.92       277.78702       YES     YES

zero point VIBRATIONAL energy  :      0.0081815  Hartree
```

UBP86/def2-QZVP

Cartesian coordinates

```
5
Energy = -1737.500231984
Co     0.5467649     0.0561976     0.0000000
F      1.0761863     0.6485766     1.5474194
F      1.0761863     0.6485766    -1.5474194
N     -0.7185615    -0.9438777     0.0000000
F     -1.9805759    -0.4094731     0.0000000
```

Vibrational data (^{14}N)

```
#  mode     symmetry     wave number   IR intensity    selection rules
#                          cm**(-1)       km/mol         IR     RAMAN
     7        a"           112.51         0.43116       YES     YES
     8        a'           138.65         7.71356       YES     YES
     9        a'           166.08        17.58136       YES     YES
    10        a'           276.60         1.94540       YES     YES
    11        a"           351.05         1.14144       YES     YES
    12        a'           616.31        36.43540       YES     YES
    13        a"           722.19       100.77692       YES     YES
    14        a'           741.09       122.74231       YES     YES
    15        a'           932.95       170.49928       YES     YES

zero point VIBRATIONAL energy  :      0.0092435  Hartree
```

Vibrational data (^{15}N)

```
#  mode     symmetry     wave number   IR intensity    selection rules
#                          cm**(-1)       km/mol         IR     RAMAN
     7        a"           112.49         0.42856       YES     YES
     8        a'           138.37         7.69169       YES     YES
     9        a'           166.04        17.55108       YES     YES
    10        a'           274.06         1.94428       YES     YES
    11        a"           342.20         1.00243       YES     YES
    12        a'           613.18        32.56996       YES     YES
    13        a"           722.09       100.89330       YES     YES
    14        a'           729.61       121.56463       YES     YES
    15        a'           911.38       165.26980       YES     YES

zero point VIBRATIONAL energy  :      0.0091341  Hartree
```

CASPT2/cc-pVTZ-DK

Cartesian coordinates

```
    5
 RS2C/USERDEF  ENERGY=-1746.62362045
 N          -0.5955943213       -1.2875004164       -0.0000000000
 F           0.3679036402       -2.1752735487       -0.0000000000
 Co         -0.0886500391        0.3767507245       -0.0000000000
 F           0.1730977030        0.9779040322        1.6014094830
 F           0.1730977030        0.9779040322       -1.6014094830
```

Vibrational data (^{14}N)

```
Vibration        Wavenumber
   Nr             [1/cm]
   1               76.66
   2              140.92
   3              169.96
   4              235.12
   5              286.35
   6              636.09
   7              673.16
   8              756.86
   9             1165.69

Zero point energy:  0.00943348 [H]     2070.41 [1/CM]       24.77 [KJ/MOL]
```

Vibrational data (^{15}N)	Vibration Wavenumber Nr [1/cm] 1 76.52 2 140.76 3 169.89 4 229.59 5 284.29 6 622.31 7 670.29 8 756.86 9 1142.42 Zero point energy: 0.00932434 [H] 2046.46 [1/CM] 24.48 [KJ/MOL]
$FNCoF_2$ ($^2A''$)	
UB3LYP/def2-QZVP	
Cartesian coordinates	5 Energy = -1737.008529542 Co 0.6578907 0.2282534 0.0000000 F 0.9933517 0.5639077 1.6648322 F 0.9933517 0.5639077 -1.6648322 N -0.7297857 -0.9699712 0.0000000 F -1.9148085 -0.3860975 0.0000000
Vibrational data (^{14}N)	# mode symmetry wave number IR intensity selection rules # cm**(-1) km/mol IR RAMAN 7 a" 86.22 0.00738 YES YES 8 a' 136.01 21.15162 YES YES 9 a' 156.35 16.81925 YES YES 10 a' 229.94 6.05818 YES YES 11 a" 242.76 0.04905 YES YES 12 a' 441.58 11.52011 YES YES 13 a' 610.87 60.15444 YES YES 14 a" 763.84 170.91208 YES YES 15 a' 1079.65 293.27012 YES YES zero point VIBRATIONAL energy : 0.0085368 Hartree
Vibrational data (^{15}N)	# mode symmetry wave number IR intensity selection rules # cm**(-1) km/mol IR RAMAN 7 a" 86.19 0.00688 YES YES 8 a' 135.87 21.13980 YES YES 9 a' 156.31 16.78193 YES YES 10 a' 228.82 6.05007 YES YES 11 a" 236.72 0.05756 YES YES 12 a' 428.68 10.54890 YES YES 13 a' 610.80 60.60073 YES YES 14 a" 763.84 170.91249 YES YES 15 a' 1059.62 279.81559 YES YES zero point VIBRATIONAL energy : 0.0084448 Hartree
UBP86/def2-QZVP	
Cartesian coordinates	5 Energy = -1737.504066547 Co 0.5575227 0.1057569 0.0000000 F 1.0263887 0.6095572 1.5790247 F 1.0263887 0.6095572 -1.5790247 N -0.6776175 -0.9507779 0.0000000 F -1.9326826 -0.3740934 0.0000000
Vibrational data (^{14}N)	# mode symmetry wave number IR intensity selection rules # cm**(-1) km/mol IR RAMAN 7 a" 98.33 0.01475 YES YES 8 a' 145.38 10.86359 YES YES 9 a' 155.70 7.50066 YES YES 10 a" 293.08 0.59630 YES YES 11 a' 309.92 1.36285 YES YES 12 a' 626.80 62.87264 YES YES 13 a" 731.64 122.80177 YES YES 14 a' 764.99 36.78948 YES YES 15 a' 869.57 220.12138 YES YES zero point VIBRATIONAL energy : 0.0091022 Hartree
Vibrational data (^{15}N)	# mode symmetry wave number IR intensity selection rules # cm**(-1) km/mol IR RAMAN 7 a" 98.19 0.01322 YES YES 8 a' 145.37 10.83214 YES YES 9 a' 155.53 7.52429 YES YES 10 a" 286.02 0.60140 YES YES 11 a' 307.58 1.30870 YES YES 12 a' 625.63 61.79012 YES YES 13 a" 731.64 122.80493 YES YES 14 a' 747.66 33.35537 YES YES 15 a' 850.86 214.20949 YES YES zero point VIBRATIONAL energy : 0.0089953 Hartree
CASPT2/cc-pVTZ-DK	
Cartesian coordinates	5 RS2C/USERDEF ENERGY=-1746.62921561 N -0.6242290885 -1.2490400345 -0.0000000000 F 0.3476754071 -2.1288914983 -0.0000000000 Co -0.0513718917 0.4289961249 -0.0000000000 F 0.1359488491 0.8595025921 1.6401541026 F 0.1359488491 0.8595025921 -1.6401541026
Vibrational data (^{14}N)	Vibration Wavenumber Nr [1/cm] 1 131.49 2 157.58

	3 182.22 4 298.34 5 393.72 6 605.28 7 650.95 8 859.03 9 1151.77 Zero point energy: 0.01009317 [H] 2215.19 [1/CM] 26.50 [KJ/MOL]
Vibrational data (^{15}N)	Vibration Wavenumber Nr [1/cm] 1 131.48 2 157.43 3 182.15 4 296.62 5 383.87 6 589.22 7 650.15 8 858.73 9 1129.33 Zero point energy: 0.00997606 [H] 2189.49 [1/CM] 26.19 [KJ/MOL]
$FNCoF_2$ (^{4}A'')	
UB3LYP/def2-QZVP	
Cartesian Coordinates	5 Energy = -1736.990866197 Co 0.5683084 0.2635693 0.0000000 F 1.3053751 0.6112250 1.5383805 F 1.3053751 0.6112250 -1.5383805 N -0.9991972 -0.4730433 0.0000000 F -2.1798615 -1.0129759 0.0000000
Vibrational data (^{14}N)	# mode symmetry wave number IR intensity selection rules # cm**(-1) km/mol IR RAMAN 1 a" -117.18 0.00000 YES YES 2 -0.00 0.00000 - - 3 -0.00 0.00000 - - 4 0.00 0.00000 - - 5 0.00 0.00000 - - 6 0.00 0.00000 - - 7 0.00 0.00000 - - 8 a' 55.22 2.36818 YES YES 9 a' 153.03 10.11935 YES YES 10 a" 192.11 4.02763 YES YES 11 a' 203.07 22.47860 YES YES 12 a' 409.09 1.29660 YES YES 13 a' 657.68 102.21115 YES YES 14 a" 712.90 154.54927 YES YES 15 a' 1265.61 378.12091 YES YES
UBP86/def2-QZVP	
Cartesian coordinates	5 Energy = -1737.478861591 Co 0.5189827 0.2408345 0.0000000 F 1.3212532 0.6175159 1.4943089 F 1.3212532 0.6175159 -1.4943089 N -0.9813842 -0.4592354 0.0000000 F -2.1801049 -1.0166309 0.0000000
Vibrational data (^{14}N)	# mode symmetry wave number IR intensity selection rules # cm**(-1) km/mol IR RAMAN 1 a" -100.01 0.00000 YES YES 2 -0.00 0.00000 - - 3 -0.00 0.00000 - - 4 -0.00 0.00000 - - 5 -0.00 0.00000 - - 6 -0.00 0.00000 - - 7 -0.00 0.00000 - - 8 a' 107.66 2.89045 YES YES 9 a' 165.12 3.70206 YES YES 10 a' 187.24 12.16159 YES YES 11 a" 249.71 2.68147 YES YES 12 a' 504.88 1.45047 YES YES 13 a' 658.70 113.48983 YES YES 14 a" 699.55 99.92836 YES YES 15 a' 1203.90 335.32383 YES YES zero point VIBRATIONAL energy : 0.0086041 Hartree

F_2NCoF

F_2NCoF (^{2}A')	
UB3LYP/def2-QZVP	
Cartesian coordinates	5 Energy = -1736.956358175 N 0.5926403 0.4164280 0.0000000 F 1.4009083 0.6604467 1.0728089 F 1.4009083 0.6604467 -1.0728089 Co -1.0109650 -0.3199323 0.0000000 F -2.3834919 -1.4173891 0.0000000
Vibrational data (^{14}N)	# mode symmetry wave number IR intensity selection rules # cm**(-1) km/mol IR RAMAN 7 a' 57.91 12.09354 YES YES 8 a" 106.98 11.78200 YES YES 9 a" 236.73 7.17646 YES YES 10 a' 270.78 3.10322 YES YES

	11 a' 332.51 1.31858 YES YES 12 a' 572.20 1.74459 YES YES 13 a' 680.93 160.22754 YES YES 14 a" 897.33 158.22600 YES YES 15 a' 1067.13 324.70384 YES YES zero point VIBRATIONAL energy : 0.0096196 Hartree
UBP86/def2-QZVP	
Cartesian coordinates	5 Energy = -1737.441345404 N 0.5433949 0.3888218 0.0000000 F 1.3880715 0.6644346 1.0837875 F 1.3880715 0.6644346 -1.0837875 Co -0.9582474 -0.3449221 0.0000000 F -2.3612905 -1.3727688 0.0000000
Vibrational data (^{14}N)	# mode symmetry wave number IR intensity selection rules # cm**(-1) km/mol IR RAMAN 7 a' 38.63 7.48164 YES YES 8 a" 107.45 7.64337 YES YES 9 a" 266.90 3.49066 YES YES 10 a' 356.08 1.89152 YES YES 11 a' 411.32 0.09485 YES YES 12 a' 554.74 1.27295 YES YES 13 a" 643.20 183.28885 YES YES 14 a' 696.29 171.80163 YES YES 15 a' 925.22 249.92458 YES YES zero point VIBRATIONAL energy : 0.0091123 Hartree
F_2NCoF ($^4B_2$ – C_{2v})	
UBP86/def2-QZVP	
Cartesian coordinates	5 Energy = -1737.443567762 N 0.0000000 0.0000000 0.7169257 F -1.0945571 0.0000000 1.5788056 F 1.0945571 0.0000000 1.5788056 Co 0.0000000 0.0000000 -1.0562770 F 0.0000000 0.0000000 -2.8182599
Vibrational data (^{14}N)	# mode symmetry wave number IR intensity selection rules # cm**(-1) km/mol IR RAMAN 7 b2 9.39 0.07651 YES YES 8 b1 85.90 13.31764 YES YES 9 b2 95.98 21.88961 YES YES 10 b1 207.10 8.88776 YES YES 11 a1 339.54 1.25675 YES YES 12 a1 554.21 0.72027 YES YES 13 a1 674.19 168.59633 YES YES 14 b1 789.70 145.89988 YES YES 15 a1 1031.08 200.60030 YES YES zero point VIBRATIONAL energy : 0.0086276 Hartree
Vibrational data (^{15}N)	# mode symmetry wave number IR intensity selection rules # cm**(-1) km/mol IR RAMAN 7 b2 9.16 0.07616 YES YES 8 b1 85.84 13.27865 YES YES 9 b2 95.65 21.71159 YES YES 10 b1 205.38 8.74926 YES YES 11 a1 339.16 1.20669 YES YES 12 a1 551.87 0.95444 YES YES 13 a1 674.19 168.68674 YES YES 14 b1 774.20 141.39183 YES YES 15 a1 1005.54 190.19853 YES YES zero point VIBRATIONAL energy : 0.0085226 Hartree
UB3LYP/def2-QZVP	
Cartesian coordinates	5 Energy = -1736.974544782 N 0.0000000 0.0000000 0.7359383 F -1.0853741 0.0000000 1.5786927 F 1.0853741 0.0000000 1.5786927 Co 0.0000000 0.0000000 -1.0621840 F 0.0000000 0.0000000 -2.8311397
Vibrational data (^{14}N)	# mode symmetry wave number IR intensity selection rules # cm**(-1) km/mol IR RAMAN 7 b2 72.71 13.05138 YES YES 8 b1 91.72 14.98879 YES YES 9 b2 152.08 18.35703 YES YES 10 b1 214.09 13.11832 YES YES 11 a1 338.79 1.63549 YES YES 12 a1 572.29 0.25407 YES YES 13 a1 675.97 196.91217 YES YES 14 b1 919.99 133.07714 YES YES 15 a1 1125.56 165.37073 YES YES zero point VIBRATIONAL energy : 0.0094844

$NCoF_2$

$NCoF_2$ ($^1A_1$ – C_{2v})	
UBP86/def2-QZVP	
Cartesian coordinates	4 Energy = -1637.617920216

	Co 0.0000000 0.0000000 -0.0620052 N 0.0000000 0.0000000 -1.5539271 F -1.4841339 0.0000000 0.8079661 F 1.4841339 0.0000000 0.8079661
Vibrational data (^{14}N)	# mode symmetry wave number IR intensity selection rules # cm**(-1) km/mol IR RAMAN 7 a1 183.16 4.87774 YES YES 8 b2 234.94 9.57772 YES YES 9 b1 254.82 3.08114 YES YES 10 a1 657.26 39.09898 YES YES 11 b1 713.48 114.63394 YES YES 12 a1 1128.26 55.50316 YES YES zero point VIBRATIONAL energy : 0.0072262 Hartree
Vibrational data (^{15}N)	# mode symmetry wave number IR intensity selection rules # cm**(-1) km/mol IR RAMAN 1 0.00 0.00000 - - 2 0.00 0.00000 - - 3 0.00 0.00000 - - 4 0.00 0.00000 - - 5 0.00 0.00000 - - 6 0.00 0.00000 - - 7 a1 182.90 4.85836 YES YES 8 b2 232.90 9.71167 YES YES 9 b1 249.53 3.06102 YES YES 10 a1 656.46 38.36220 YES YES 11 b1 713.48 114.64223 YES YES 12 a1 1098.04 54.55861 YES YES zero point VIBRATIONAL energy : 0.0071382 Hartree
UB3LYP/def2-QZVP	
Cartesian coordinates	4 Energy = -1637.139673305 Co 0.0000000 0.0000000 -0.0616639 N 0.0000000 0.0000000 -1.5272705 F -1.4889224 0.0000000 0.7944672 F 1.4889224 0.0000000 0.7944672
Vibrational data (^{14}N)	# mode symmetry wave number IR intensity selection rules # cm**(-1) km/mol IR RAMAN 1 0.00 0.00000 - - 2 0.00 0.00000 - - 3 0.00 0.00000 - - 4 0.00 0.00000 - - 5 0.00 0.00000 - - 6 0.00 0.00000 - - 7 a1 181.39 8.12707 YES YES 8 b2 232.95 16.51720 YES YES 9 b1 264.48 3.08692 YES YES 10 a1 668.86 54.81777 YES YES 11 b1 727.50 133.84664 YES YES 12 a1 1179.98 70.54244 YES YES zero point VIBRATIONAL energy : 0.0074158 Hartree
$NCoF_2$ ($^3B_1$ – C_{2v})	
UBP86/def2-QZVP	
Cartesian coordinates	4 Energy = -1637.569854742 Co 0.0000000 0.0000000 0.2451546 N 0.0000000 0.0000000 -1.4260783 F -1.7047621 0.0000000 0.5904619 F 1.7047621 0.0000000 0.5904619
Vibrational data (^{14}N)	# mode symmetry wave number IR intensity selection rules # cm**(-1) km/mol IR RAMAN 1 0.00 0.00000 - - 2 0.00 0.00000 - - 3 0.00 0.00000 - - 4 0.00 0.00000 - - 5 0.00 0.00000 - - 6 0.00 0.00000 - - 7 b2 78.71 33.70119 YES YES 8 b1 165.97 1.41811 YES YES 9 a1 215.60 7.81754 YES YES 10 a1 609.15 11.31088 YES YES 11 b1 726.88 148.64000 YES YES 12 a1 752.47 0.03273 YES YES zero point VIBRATIONAL energy : 0.0058065 Hartree
UB3LYP/def2-QZVP	
Cartesian coordinates	4 Energy = -1637.126142293 Co 0.0000000 0.0000000 0.2955723 N 0.0000000 0.0000000 -1.4283857 F -1.7157838 0.0000000 0.5664067 F 1.7157838 0.0000000 0.5664067
Vibrational data (^{14}N)	# mode symmetry wave number IR intensity selection rules # cm**(-1) km/mol IR RAMAN 1 -0.00 0.00000 - - 2 -0.00 0.00000 - - 3 0.00 0.00000 - - 4 0.00 0.00000 - - 5 0.00 0.00000 - - 6 0.00 0.00000 - - 7 b2 136.15 42.68995 YES YES 8 a1 216.95 15.36504 YES YES

	9 b1 238.75 0.00124 YES YES 10 a1 605.58 7.60221 YES YES 11 a1 630.09 9.20571 YES YES 12 b1 761.68 197.35444 YES YES zero point VIBRATIONAL energy : 0.0058986 Hartree

NCoF

NCoF (^{4}A'')	
UBP86/def2-QZVP	
Cartesian coordinates	3 Energy = -1537.671464455 N -0.5836409 1.3722074 0.0000000 Co -0.4340743 -0.2015633 0.0000000 F 1.0177152 -1.1706441 0.0000000
Vibrational data (^{14}N)	# mode symmetry wave number IR intensity selection rules # cm**(-1) km/mol IR RAMAN 7 a' 181.46 12.10371 YES YES 8 a' 662.42 71.72647 YES YES 9 a' 958.49 31.08107 YES YES
UB3LYP/def2-QZVP	
Cartesian coordinates	3 Energy = -1537.265567115 N -0.6525997 1.4077269 0.0000000 Co -0.3679524 -0.1641616 0.0000000 F 1.0205521 -1.2435654 0.0000000
Vibrational data (^{14}N)	# mode symmetry wave number IR intensity selection rules # cm**(-1) km/mol IR RAMAN 7 a' 116.84 15.25455 YES YES 8 a' 640.59 72.16031 YES YES 9 a' 810.79 75.69130 YES YES
NCoF (^{2}A')	
UBP86/def2-QZVP	
Cartesian coordinates	3 Energy = -1537.685782498 N -0.7454242 1.3667106 0.0000000 Co -0.2224294 -0.0588210 0.0000000 F 0.9678536 -1.3078896 0.0000000
Vibrational data (^{14}N)	# mode symmetry wave number IR intensity selection rules # cm**(-1) km/mol IR RAMAN 7 a' 90.06 11.49674 YES YES 8 a' 676.20 71.13325 YES YES 9 a' 1105.40 75.13259 YES YES zero point VIBRATIONAL energy : 0.0042639 Hartree
Vibrational data (^{15}N)	# mode symmetry wave number IR intensity selection rules # cm**(-1) km/mol IR RAMAN 7 a' 88.77 11.46668 YES YES 8 a' 674.58 69.55188 YES YES 9 a' 1076.83 74.61935 YES YES zero point VIBRATIONAL energy : 0.0041922 Hartree
UB3LYP/def2-QZVP	
Cartesian coordinates	3 Energy = -1537.264970174 N -0.8763492 1.3887076 0.0000000 Co -0.0511842 0.0281166 0.0000000 F 0.9275334 -1.4168241 0.0000000
Vibrational data (^{14}N)	# mode symmetry wave number IR intensity selection rules # cm**(-1) km/mol IR RAMAN 7 a' 38.02 21.48325 YES YES 8 a' 517.29 25.44988 YES YES 9 a' 736.70 96.38469 YES YES

$NRhF_3$

$NRhF_3$ (^{2}A')	
UBP86/def2-QZVP	
Cartesian coordinates	5 Energy = -465.1250025960 Rh -0.1399902 -0.2138791 0.0000000 N 0.0078043 -1.8047678 0.0000000 F -0.6911719 0.6472559 -1.5902650 F -0.6911719 0.6472559 1.5902650 F 1.5145297 0.7241294 0.0000000
Vibrational data (^{14}N)	# mode symmetry wave number IR intensity selection rules # cm**(-1) km/mol IR RAMAN 7 a' 74.38 2.82222 YES YES 8 a" 134.80 7.74304 YES YES 9 a" 190.37 2.35006 YES YES 10 a' 203.77 5.17666 YES YES 11 a' 273.94 3.15410 YES YES 12 a' 562.25 45.29625 YES YES 13 a' 600.82 48.34327 YES YES 14 a" 603.09 95.77682 YES YES 15 a' 1087.45 47.68040 YES YES zero point VIBRATIONAL energy : 0.0084996 Hartree

Vibrational data (^{15}N)

```
#  mode     symmetry     wave number   IR intensity    selection rules
#                          cm**(-1)       km/mol         IR     RAMAN
     7        a'             74.31        2.76875       YES     YES
     8        a"            134.54        7.90728       YES     YES
     9        a"            186.46        2.18950       YES     YES
    10        a'            203.49        5.15530       YES     YES
    11        a'            268.77        3.29529       YES     YES
    12        a'            562.25       45.28897       YES     YES
    13        a'            600.65       48.02650       YES     YES
    14        a"            603.09       95.79221       YES     YES
    15        a'           1055.07       46.03235       YES     YES

zero point VIBRATIONAL energy  :      0.0084033
```

UB3LYP/def2-QZVP

Cartesian coordinates

```
5
Energy = -464.7836586566
Rh   -0.1500554   -0.2026445    0.0000000
N     0.0043903   -1.7724057    0.0000000
F    -0.6774970    0.6284580   -1.6036316
F    -0.6774970    0.6284580    1.6036316
F     1.5006592    0.7181285    0.0000000
```

Vibrational data (^{14}N)

```
#  mode     symmetry     wave number   IR intensity    selection rules
#                          cm**(-1)       km/mol         IR     RAMAN
     7        a'             70.20        4.72915       YES     YES
     8        a"            156.24        6.00424       YES     YES
     9        a"            204.81        2.24836       YES     YES
    10        a'            208.73        7.06775       YES     YES
    11        a'            285.54        3.95289       YES     YES
    12        a'            580.83       52.32699       YES     YES
    13        a'            618.29       62.99995       YES     YES
    14        a"            625.07      117.90314       YES     YES
    15        a'           1112.98       54.55496       YES     YES

zero point VIBRATIONAL energy  :      0.0087998  Hartree
```

Vibrational data (^{15}N)

```
#  mode     symmetry     wave number   IR intensity    selection rules
#                          cm**(-1)       km/mol         IR     RAMAN
     7        a'             70.13        4.65449       YES     YES
     8        a"            156.06        6.16298       YES     YES
     9        a"            200.43        2.14226       YES     YES
    10        a'            208.43        7.04629       YES     YES
    11        a'            280.16        4.14645       YES     YES
    12        a'            580.82       52.31848       YES     YES
    13        a'            618.20       62.72236       YES     YES
    14        a"            625.06      117.91473       YES     YES
    15        a'           1079.69       52.49527       YES     YES

zero point VIBRATIONAL energy  :      0.0087003  Hartree
```

RHF-UCCSD(T)/aug-cc-pVTZ(-PP)

Cartesian coordinates

```
    5
 UCCSD(T)/USERDEF  ENERGY=-463.54661547
 Rh        -0.1626075169       -0.1814607136        0.0000000000
 N          0.0004540618       -1.7626120982        0.0000000000
 F         -0.6644731875        0.6129142971       -1.6177711634
 F         -0.6644731875        0.6129142971        1.6177711634
 F          1.4910998299        0.7182385177        0.0000000000

T1 diagnostic:  0.02947583
D1 diagnostic:  0.10755742
```

Vibrational data (^{14}N)

```
 Imaginary Vibration  Wavenumber
        Nr             [1/cm]
        1              152.69
        2              110.90

     Vibration        Wavenumber
        Nr             [1/cm]
        1              145.51
        2              168.60
        3              249.35
        4              584.46
        5              621.21
        6              631.19
        7             1164.02
```

$NRhF_3$ ($^4A''$)

UBP86/def2-QZVP

Cartesian coordinates

```
5
Energy = -465.0835381244
Rh   -0.0548919    0.0013453    0.0000000
N     0.1942306   -1.6599282    0.0000000
F    -0.9892941    0.6312355   -1.5152511
F    -0.9892941    0.6312355    1.5152511
F     1.8392496    0.3961062    0.0000000
```

Vibrational data (^{14}N)

```
#  mode     symmetry     wave number   IR intensity    selection rules
#                          cm**(-1)       km/mol         IR     RAMAN
     1        a"            -42.14        0.00000       YES     YES
     2                      -0.00        0.00000         -       -
     3                      -0.00        0.00000         -       -
     4                      -0.00        0.00000         -       -
     5                       0.00        0.00000         -       -
     6                       0.00        0.00000         -       -
     7                       0.00        0.00000         -       -
     8        a'            106.89        6.01975       YES     YES
     9        a'            168.83        6.67762       YES     YES
    10        a"            195.58        8.48916       YES     YES
    11        a'            253.77        1.06099       YES     YES
```

	12 a' 540.55 47.44788 YES YES 13 a" 558.62 92.27919 YES YES 14 a' 588.48 55.34010 YES YES 15 a' 928.98 1.92571 YES YES zero point VIBRATIONAL energy : 0.0076130 Hartree

$FNRhF_2$

$FNRhF_2$ ($^2A''$)	
UBP86/def2-QZVP	
Cartesian coordinates	5 Energy = -465.1135362013 F 1.2093482 -0.1828113 -1.7446750 Rh 0.5438307 -0.2701357 0.0000000 F 1.2093482 -0.1828113 1.7446750 N -1.1745684 -0.3187857 0.0000000 F -1.7879586 0.9545439 0.0000000
Vibrational data (^{14}N)	# mode symmetry wave number IR intensity selection rules # cm**(-1) km/mol IR RAMAN 7 a' 109.43 8.69355 YES YES 8 a" 110.74 0.60271 YES YES 9 a' 129.61 4.17406 YES YES 10 a' 317.66 1.58379 YES YES 11 a" 373.02 2.45020 YES YES 12 a' 578.57 61.58791 YES YES 13 a" 656.82 106.57691 YES YES 14 a' 763.07 235.82196 YES YES 15 a' 827.30 38.51876 YES YES zero point VIBRATIONAL energy : 0.0088079 Hartree
UB3LYP/def2-QZVP	
Cartesian coordinates	5 Energy = -464.7768766063 F 1.1953393 -0.1775565 -1.7473860 Rh 0.5427375 -0.2711853 0.0000000 F 1.1953393 -0.1775565 1.7473860 N -1.1749425 -0.3106740 0.0000000 F -1.7584735 0.9369722 0.0000000
Vibrational data (^{14}N)	# mode symmetry wave number IR intensity selection rules # cm**(-1) km/mol IR RAMAN 7 a' 110.16 13.26459 YES YES 8 a" 110.88 0.69375 YES YES 9 a' 124.88 6.46848 YES YES 10 a' 330.89 1.27957 YES YES 11 a" 337.68 0.02412 YES YES 12 a' 587.83 78.88401 YES YES 13 a" 659.78 152.91911 YES YES 14 a' 795.82 9.95449 YES YES 15 a' 886.49 264.48171 YES YES zero point VIBRATIONAL energy : 0.0089860 Hartree
CASPT2/cc-pVTZ-DK	
Cartesian coordinates	5 RS2C/USERDEF ENERGY=-5135.12197299 N -0.6219245232 -1.3512409434 -0.0000000000 F 0.3762961477 -2.2540436222 -0.0000000000 Rh -0.0422721273 0.3294831759 -0.0000000000 F 0.1593917812 0.8287964603 -1.7516517214 F 0.1593917812 0.8287964603 1.7516517214
Vibrational data (^{14}N)	Vibration Wavenumber Nr [1/cm] 1 114.73 2 136.62 3 155.89 4 320.76 5 326.00 6 636.92 7 694.11 8 712.50 9 996.73 Zero point energy: 0.00932740 [H] 2047.13 [1/CM] 24.49 [KJ/MOL]
Vibrational data (^{154}N)	Vibration Wavenumber Nr [1/cm] 1 114.77 2 136.61 3 155.82 4 312.71 5 323.90 6 636.84 7 673.42 8 712.50 9 977.73 Zero point energy: 0.00921362 [H] 2022.16 [1/CM] 24.19 [KJ/MOL]
RHF-UCCSD(T)/aug-cc-pVTZ-DK	
Single Point B3LYP minimum	5 Energy = -5134.90671671 F 1.1953393 -0.1775565 -1.7473860 Rh 0.5427375 -0.2711853 0.0000000 F 1.1953393 -0.1775565 1.7473860

	N -1.1749425 -0.3106740 0.0000000 F -1.7584735 0.9369722 0.0000000 T1 diagnostic: 0.04675588 D1 diagnostic: 0.19468227
$FNRhF_2$ ($^2A'$)	
UBP86/def2-QZVP	
Cartesian coordinates	5 Energy = -465.1145214309 F 1.2825350 -0.1937175 -1.7110184 Rh 0.4961048 -0.2778330 0.0000000 F 1.2825350 -0.1937175 1.7110184 N -1.2055324 -0.2895846 0.0000000 F -1.8556423 0.9548526 0.0000000
Vibrational data (^{14}N)	1 a" -119.10 0.00000 YES YES 2 -0.00 0.00000 - - 3 -0.00 0.00000 - - 4 -0.00 0.00000 - - 5 0.00 0.00000 - - 6 0.00 0.00000 - - 7 0.00 0.00000 - - 8 a" 124.41 1.00971 YES YES 9 a' 127.16 5.75679 YES YES 10 a' 165.55 10.60533 YES YES 11 a' 266.21 1.06385 YES YES 12 a' 584.86 58.81893 YES YES 13 a" 609.97 172.40545 YES YES 14 a' 731.07 190.87034 YES YES 15 a' 858.79 94.31362 YES YES
UB3LYP/def2-QZVP	
Cartesian coordinates	5 Energy = -464.7812237473 F 1.2674668 -0.1891948 -1.7123441 Rh 0.4887109 -0.2713834 0.0000000 F 1.2674668 -0.1891948 1.7123441 N -1.2087954 -0.2920414 0.0000000 F -1.8148491 0.9418144 0.0000000 T1 diagnostic: 0.04315135 D1 diagnostic: 0.16672494
Vibrational data (^{14}N)	# mode symmetry wave number IR intensity selection rules # cm**(-1) km/mol IR RAMAN 7 a" 117.14 0.66171 YES YES 8 a' 129.09 7.48470 YES YES 9 a' 171.62 14.97100 YES YES 10 a' 281.89 1.18747 YES YES 11 a" 294.87 0.16733 YES YES 12 a' 594.11 74.92821 YES YES 13 a" 640.70 149.71552 YES YES 14 a' 785.94 117.42896 YES YES 15 a' 934.66 168.23779 YES YES zero point VIBRATIONAL energy : 0.0089988 Hartree
Vibrational data (^{15}N)	# mode symmetry wave number IR intensity selection rules # cm**(-1) km/mol IR RAMAN 7 a" 117.13 0.66421 YES YES 8 a' 129.00 7.48213 YES YES 9 a' 171.60 14.95100 YES YES 10 a' 279.40 1.16820 YES YES 11 a" 287.11 0.17883 YES YES 12 a' 593.84 74.60447 YES YES 13 a" 640.70 149.71199 YES YES 14 a' 769.65 106.05722 YES YES 15 a' 910.93 169.00734 YES YES zero point VIBRATIONAL energy : 0.0088834 Hartree
CASPT2/cc-pVTZ-DK	
Cartesian coordinates	5 RS2C/USERDEF ENERGY=-5135.12094042 N -0.6099844490 1.3826515997 0.0000000000 F 0.3963720782 2.2821553746 0.0000000000 Rh -0.0647784664 -0.2659677470 0.0000000000 F 0.2021089135 -0.9304505669 1.7215153928 F 0.2021089135 -0.9304505669 -1.7215153928
Vibrational data (^{14}N)	Vibration Wavenumber Nr [1/cm] 1 124.60 2 148.57 3 185.64 4 289.99 5 301.71 6 635.04 7 679.56 8 748.29 9 990.67 Zero point energy: 0.00934974 [H] 2052.03 [1/CM] 24.55 [KJ/MOL]
Vibrational data (^{154}N)	Vibration Wavenumber Nr [1/cm] 1 124.62 2 148.45 3 185.63 4 287.89 5 293.95

	6 634.26 7 679.56 8 728.37 9 970.94 Zero point energy: 0.00923494 [H] 2026.84 [1/CM] 24.25 [KJ/MOL]
RHF-UCCSD(T)/cc-pVTZ-DK	
Cartesian coordinates	5 UCCSD(T)/USERDEF ENERGY=-5134.86624986 F 1.2106200830 -0.1851219494 -1.7475105656 Rh 0.5314767484 -0.2567589344 0.0000000000 F 1.2106200830 -0.1851219494 1.7475105656 N -1.1866524395 -0.3073004114 0.0000000000 F -1.7660644751 0.9343032447 0.0000000000 T1 diagnostic: 0.04315135 D1 diagnostic: 0.16672494
Vibrational data (^{14}N)	Vibration Wavenumber Nr [1/cm] 1 90.45 2 108.67 3 169.77 4 272.41 5 287.29 6 602.96 7 662.87 8 719.53 9 898.79 Zero point energy: 0.00868606 [H] 1906.37 [1/CM] 22.81 [KJ/MOL]
Vibrational data (^{154}N)	Vibration Wavenumber Nr [1/cm] 1 90.45 2 108.62 3 169.80 4 270.40 5 280.16 6 600.69 7 662.87 8 701.23 9 882.21 Zero point energy: 0.00858055 [H] 1883.21 [1/CM] 22.53 [KJ/MOL]
RHF-UCCSD(T)/cc-pVDZ(-PP)	
Cartesian coordinates	5 UCCSD(T)/CC-PVDZ,RH=CC-PVDZ-PP ENERGY=-463.07033821 F 1.1836841447 -0.1842461586 -1.7928084951 Rh 0.5747187837 -0.2510917318 0.0000000000 F 1.1836841447 -0.1842461586 1.7928084951 N -1.1912103992 -0.3145890842 0.0000000000 F -1.7508766739 0.9341731330 0.0000000000 T1 diagnostic: 0.05885526 D1 diagnostic: 0.22377600
Vibrational data (^{14}N)	Vibration Wavenumber Nr [1/cm] 1 109.99 2 134.28 3 173.29 4 260.62 5 272.49 6 536.08 7 619.70 8 665.37 9 893.32 Zero point energy: 0.00834982 [H] 1832.57 [1/CM] 21.92 [KJ/MOL]
Vibrational data (^{154}N)	Vibration Wavenumber Nr [1/cm] 1 109.99 2 134.25 3 173.26 4 253.74 5 270.58 6 521.43 7 617.56 8 665.37 9 877.43 Zero point energy: 0.00825518 [H] 1811.80 [1/CM] 21.67 [KJ/MOL]
RHF-UCCSD(T)/aug-cc-pVTZ(-PP)	
Cartesian coordinates	5 UCCSD(T)/USERDEF ENERGY=-463.54228861 F 1.2115020377 -0.1841600603 -1.7527667348 Rh 0.5314205692 -0.2581662671 0.0000000000 F 1.2115020377 -0.1841600603 1.7527667348 N -1.1889856678 -0.3103822366 0.0000000000 F -1.7654389767 0.9368686242 0.0000000000 T1 diagnostic: 0.04360507 D1 diagnostic: 0.17099709
Vibrational data (^{14}N)	Vibration Wavenumber Nr [1/cm] 1 78.78 2 95.02

	3 168.39 4 262.09 5 265.80 6 580.11 7 651.95 8 706.60 9 872.03 Zero point energy: 0.00838543 [H] 1840.39 [1/CM] 22.02 [KJ/MOL]
Vibrational data (^{154}N)	Vibration Wavenumber Nr [1/cm] 1 78.78 2 94.94 3 168.48 4 258.75 5 260.15 6 578.23 7 651.95 8 688.00 9 855.90 Zero point energy: 0.00828155 [H] 1817.59 [1/CM] 21.74 [KJ/MOL]
RHF-UCCSD(T)/aug-cc-pVTZ-DK	
Single Point B3LYP minimum	5 Energy = -5134.91139993 F 1.2674668 -0.1891948 -1.7123441 Rh 0.4887109 -0.2713834 0.0000000 F 1.2674668 -0.1891948 1.7123441 N -1.2087954 -0.2920414 0.0000000 F -1.8148491 0.9418144 0.0000000 T1 diagnostic: 0.03825013 D1 diagnostic: 0.14250080
FNRhF$_2$ (A – C_1)	
UBP86/def2-QZVP	
Cartesian coordinates	5 Energy = -465.1145302452 F 1.0202200 0.2598587 -1.8593214 Rh 0.5556683 -0.1178206 -0.0714266 F 1.5061252 0.1304750 1.5334495 N -1.0571361 -0.6364492 0.1021351 F -2.0248775 0.3639361 0.2951633
Vibrational data (^{14}N)	# mode symmetry wave number IR intensity selection rules # cm**(-1) km/mol IR RAMAN 7 a 90.02 18.12589 YES YES 8 a 111.53 0.86345 YES YES 9 a 158.16 10.01637 YES YES 10 a 235.15 8.54492 YES YES 11 a 269.03 0.93638 YES YES 12 a 571.54 100.83765 YES YES 13 a 625.06 132.41313 YES YES 14 a 720.69 180.95561 YES YES 15 a 849.70 102.69768 YES YES zero point VIBRATIONAL energy : 0.0082717 Hartree
Vibrational data (^{15}N)	# mode symmetry wave number IR intensity selection rules # cm**(-1) km/mol IR RAMAN 7 a 89.68 18.06742 YES YES 8 a 111.52 0.86782 YES YES 9 a 158.00 9.94902 YES YES 10 a 229.96 7.86173 YES YES 11 a 266.49 0.92703 YES YES 12 a 571.29 102.12900 YES YES 13 a 624.94 132.31129 YES YES 14 a 708.34 167.64499 YES YES 15 a 825.39 103.43826 YES YES zero point VIBRATIONAL energy : 0.0081686 Hartree

F_2NRhF

F_2NRhF ($^2A'$)	
UBP86/def2-QZVP	
Cartesian coordinates	5 Energy = -465.0566951810 F 1.5409517 -0.4970374 -1.0826662 N 0.6764619 -0.2045102 0.0000000 F 1.5409517 -0.4970374 1.0826662 Rh -0.9861563 0.3283025 0.0000000 F -2.7722090 0.8702825 0.0000000
Vibrational data (^{14}N)	# mode symmetry wave number IR intensity selection rules # cm**(-1) km/mol IR RAMAN 7 a' 23.69 4.39584 YES YES 8 a" 118.66 3.41477 YES YES 9 a" 323.01 5.22785 YES YES 10 a' 372.01 4.99836 YES YES 11 a' 414.95 0.89419 YES YES 12 a' 563.25 7.48285 YES YES 13 a" 571.26 198.80152 YES YES 14 a' 634.83 196.57650 YES YES 15 a' 924.64 361.91707 YES YES

UB3LYPdef2-QZVP	
Cartesian coordinates	5 Energy = -464.7299697738 F 1.5044702 -0.2919310 -1.0703948 N 0.6479047 -0.4643889 0.0000000 F 1.5044702 -0.2919310 1.0703948 Rh -1.0891582 -0.0518959 0.0000000 F -2.5676868 1.1001468 0.0000000
Vibrational data (^{14}N)	# mode symmetry wave number IR intensity selection rules # cm**(-1) km/mol IR RAMAN 1 -0.00 0.00000 - - 2 0.00 0.00000 - - 3 0.00 0.00000 - - 4 0.00 0.00000 - - 5 0.00 0.00000 - - 6 0.00 0.00000 - - 7 a' 48.51 9.15165 YES YES 8 a" 139.18 4.21222 YES YES 9 a" 281.26 2.39126 YES YES 10 a' 318.72 5.69616 YES YES 11 a' 458.11 1.45833 YES YES 12 a' 588.23 14.55817 YES YES 13 a' 634.79 146.07276 YES YES 14 a" 792.39 172.82747 YES YES 15 a' 983.32 307.94240 YES YES zero point VIBRATIONAL energy : 0.0096697 Hartree
F_2NRhF (^{4}A'')	
UBP86/def2-QZVP	
Cartesian coordinates	5 Energy = -465.0310830718 F 1.5733523 -0.4355884 -1.0972268 N 0.7068371 -0.4270292 0.0000000 F 1.5733523 -0.4355884 1.0972268 Rh -1.0089743 0.4034544 0.0000000 F -2.8445674 0.8947516 0.0000000
Vibrational data (^{14}N)	# mode symmetry wave number IR intensity selection rules # cm**(-1) km/mol IR RAMAN 7 a" 61.29 6.86247 YES YES 8 a' 90.91 5.67979 YES YES 9 a" 203.17 0.88544 YES YES 10 a' 218.02 2.06314 YES YES 11 a' 383.43 6.76419 YES YES 12 a' 542.70 0.85805 YES YES 13 a' 584.75 136.32565 YES YES 14 a" 770.28 157.31923 YES YES 15 a' 945.19 292.04257 YES YES
UB3LYPdef2-QZVP	
Cartesian coordinates	5 Energy = -464.7201593610 F 1.5674191 -0.5307839 -1.0784020 N 0.8100069 -0.1566487 0.0000000 F 1.5674191 -0.5307839 1.0784020 Rh -1.0708510 0.2893872 0.0000000 F -2.8739941 0.9288292 0.0000000
Vibrational data (^{14}N)	# mode symmetry wave number IR intensity selection rules # cm**(-1) km/mol IR RAMAN 1 -0.00 0.00000 - - 2 -0.00 0.00000 - - 3 0.00 0.00000 - - 4 0.00 0.00000 - - 5 0.00 0.00000 - - 6 0.00 0.00000 - - 7 a' 70.84 9.37160 YES YES 8 a" 83.74 10.26102 YES YES 9 a' 147.11 9.84852 YES YES 10 a" 225.25 2.40465 YES YES 11 a' 318.93 2.21753 YES YES 12 a' 574.41 35.77246 YES YES 13 a' 590.97 139.32738 YES YES 14 a" 904.27 150.70686 YES YES 15 a' 1056.89 339.36366 YES YES zero point VIBRATIONAL energy : 0.0090498 Hartree

$NRhF_2$

$NRhF_2$ ($^1A_1$ – C_{2v})	
UBP86/def2-QZVP	
Cartesian coordinates	4 Energy = -365.2652448926 Rh 0.0000000 0.0000000 -0.1613503 F -1.5182963 0.0000000 0.9499143 F 1.5182963 0.0000000 0.9499143 N 0.0000000 0.0000000 -1.7384783
Vibrational data (^{14}N)	# mode symmetry wave number IR intensity selection rules # cm**(-1) km/mol IR RAMAN 7 a1 146.33 5.98316 YES YES 8 b2 214.22 7.30914 YES YES 9 b1 219.44 7.86756 YES YES 10 a1 607.55 64.43561 YES YES

	11 b1 610.72 103.94588 YES YES 12 a1 1151.79 63.63990 YES YES zero point VIBRATIONAL energy : 0.0067207 Hartree
UB3LYPdef2-QZVP	
Cartesian coordinates	4 Energy = -364.9758642536 Rh 0.0000000 0.0000000 -0.1711984 F -1.5116457 0.0000000 0.9486391 F 1.5116457 0.0000000 0.9486391 N 0.0000000 0.0000000 -1.7260796
Vibrational data (^{14}N)	# mode symmetry wave number IR intensity selection rules # cm**(-1) km/mol IR RAMAN 7 a1 147.87 8.62397 YES YES 8 b2 213.90 11.57977 YES YES 9 b1 227.09 8.90820 YES YES 10 a1 617.33 83.19454 YES YES 11 b1 618.22 118.42241 YES YES 12 a1 1203.78 72.08579 YES YES zero point VIBRATIONAL energy : 0.0068987 Hartree
Vibrational data (^{15}N)	# mode symmetry wave number IR intensity selection rules # cm**(-1) km/mol IR RAMAN 7 a1 147.79 8.61047 YES YES 8 b2 211.03 11.99796 YES YES 9 b1 222.01 8.83313 YES YES 10 a1 617.15 82.76296 YES YES 11 b1 618.21 118.48273 YES YES 12 a1 1167.96 69.46966 YES YES zero point VIBRATIONAL energy : 0.0068987 Hartree
$NRhF_2$ ($^3B_2$ – C_{2v})	
Cartesian coordinates	4 Energy = -364.9364956873 Rh 0.0000000 0.0000000 0.0235522 F -1.7210864 0.0000000 0.7969246 F 1.7210864 0.0000000 0.7969246 N 0.0000000 0.0000000 -1.6174013
Vibrational data (^{14}N)	# mode symmetry wave number IR intensity selection rules # cm**(-1) km/mol IR RAMAN 7 a1 150.64 7.73951 YES YES 8 b2 202.01 20.84999 YES YES 9 b1 239.76 0.88301 YES YES 10 a1 600.19 48.90509 YES YES 11 b1 644.82 147.22990 YES YES 12 a1 1003.49 11.33293 YES YES

NRhF

NRhF (^{2}A')	
UBP86/def2-QZVP	
Cartesian coordinates	3 Energy = -265.3338973032 N -0.7620554 1.4838931 0.0000000 Rh -0.2364461 -0.0344348 0.0000000 F 0.9985015 -1.4494583 0.0000000
Vibrational data (^{14}N)	# mode symmetry wave number IR intensity selection rules # cm**(-1) km/mol IR RAMAN 7 a' 113.83 4.42255 YES YES 8 a' 622.31 89.31311 YES YES 9 a' 1096.97 60.63485 YES YES zero point VIBRATIONAL energy : 0.0041762 Hartree
UB3LYPdef2-QZVP	
Cartesian coordinates	3 Energy = -265.0930282922 N -0.7500161 1.4758311 0.0000000 Rh -0.2509060 -0.0347037 0.0000000 F 1.0009221 -1.4411274 0.0000000
Vibrational data (^{14}N)	# mode symmetry wave number IR intensity selection rules # cm**(-1) km/mol IR RAMAN 7 a' 126.13 7.32084 YES YES 8 a' 623.80 108.50390 YES YES 9 a' 1135.18 65.45220 YES YES zero point VIBRATIONAL energy : 0.0042946 Hartree
Vibrational data (^{15}N)	

$NIrF_3$

$NIrF_3$ (^{2}A')	
UB3LYP/def2-QZVP	
Cartesian coordinates	5 Energy = -458.6101089774 Ir -0.2324947 -0.1416380 0.0000000 N -0.1698665 -1.7575368 0.0000000 F -0.4683487 0.4787989 -1.7781147 F -0.4683487 0.4787989 1.7781147 F 1.3390586 0.9415771 0.0000000

	zero point VIBRATIONAL energy : 0.0092347 Hartree
Vibrational data (^{14}N)	# mode symmetry wave number IR intensity selection rules # cm**(-1) km/mol IR RAMAN 7 a' 115.60 1.61921 YES YES 8 a" 187.23 13.05511 YES YES 9 a' 227.00 5.07407 YES YES 10 a" 247.11 1.37580 YES YES 11 a' 268.86 4.27204 YES YES 12 a' 580.67 39.55680 YES YES 13 a" 634.01 146.61325 YES YES 14 a' 635.39 43.32419 YES YES 15 a' 1157.70 23.41349 YES YES zero point VIBRATIONAL energy : 0.0092347 Hartree
Vibrational data (^{15}N)	# mode symmetry wave number IR intensity selection rules # cm**(-1) km/mol IR RAMAN 7 a' 115.32 1.52961 YES YES 8 a" 185.96 13.25430 YES YES 9 a' 225.79 5.20238 YES YES 10 a" 242.70 0.98143 YES YES 11 a' 265.34 4.35970 YES YES 12 a' 580.67 39.55760 YES YES 13 a" 633.98 146.72396 YES YES 14 a' 635.38 43.29869 YES YES 15 a' 1121.27 22.22143 YES YES zero point VIBRATIONAL energy : 0.0091273 Hartree
UBP86/def2-QZVP	
Cartesian coordinates	5 Energy = -458.9683328816 Ir -0.2304637 -0.1459280 0.0000000 N -0.1743213 -1.7784011 0.0000000 F -0.4696134 0.4863221 -1.7797658 F -0.4696134 0.4863221 1.7797658 F 1.3440118 0.9516849 0.0000000 zero point VIBRATIONAL energy : 0.0089030 Hartree
Vibrational data (^{14}N)	# mode symmetry wave number IR intensity selection rules # cm**(-1) km/mol IR RAMAN 7 a' 113.14 1.09749 YES YES 8 a" 153.14 17.48524 YES YES 9 a' 223.02 3.49021 YES YES 10 a" 239.18 1.28440 YES YES 11 a' 260.10 2.87107 YES YES 12 a' 562.40 36.37451 YES YES 13 a" 617.91 131.95565 YES YES 14 a' 618.39 34.26185 YES YES 15 a' 1120.69 22.44945 YES YES zero point VIBRATIONAL energy : 0.0089030 Hartree
Vibrational data (^{15}N)	# mode symmetry wave number IR intensity selection rules # cm**(-1) km/mol IR RAMAN 7 a' 112.87 1.03787 YES YES 8 a" 151.96 17.49906 YES YES 9 a' 221.73 3.57017 YES YES 10 a" 235.14 0.94908 YES YES 11 a' 256.82 2.93944 YES YES 12 a' 562.39 36.37347 YES YES 13 a" 617.88 132.10253 YES YES 14 a' 618.37 34.22088 YES YES 15 a' 1085.44 21.33025 YES YES zero point VIBRATIONAL energy : 0.0089030 Hartree
RHF-UCCSD(T)/aug-cc-pVTZ(-PP)	
Cartesian coordinates	5 UCCSD(T)/USERDEF ENERGY=-457.86466570 Ir -0.2391045032 -0.1211980871 0.0000000000 N -0.1850065394 -1.7432729342 0.0000000000 F -0.4473897992 0.4561078126 -1.7831466137 F -0.4473897992 0.4561078126 1.7831466137 F 1.3188906412 0.9522553961 0.0000000000 T1 diagnostic: 0.02898143 D1 diagnostic: 0.10115151
Vibrational data (^{14}N)	Vibration Wavenumber Nr [1/cm] 1 104.89 2 179.90 3 225.03 4 240.28 5 269.34 6 607.25 7 650.22 8 652.63 9 1126.20 Zero point energy: 0.00923966 [H] 2027.87 [1/CM] 24.26 [KJ/MOL]
Vibrational data (^{15}N)	Vibration Wavenumber Nr [1/cm] 1 104.55 2 178.91 3 223.49 4 235.91 5 266.43 6 607.25

	7 650.20 8 652.60 9 1090.65 Zero point energy: 0.00913544 [H] 2005.00 [1/CM] 23.99 [KJ/MOL]

$FNIrF_2$

$FNIrF_2$ ($^2A'$)	
UB3LYP/def2-QZVP	
Cartesian coordinates	5 Energy = -458.5706094499 F 1.3049440 -0.2086339 -1.7143579 Ir 0.5089844 -0.2782058 0.0000000 F 1.3049440 -0.2086339 1.7143579 N -1.1997081 -0.2449976 0.0000000 F -1.9191644 0.9404713 0.0000000
Vibrational data (^{14}N)	# mode symmetry wave number IR intensity selection rul # cm**(-1) km/mol IR RAMA 7 a' 109.96 8.56509 YES YES 8 a" 120.72 0.04914 YES YES 9 a' 169.48 7.65746 YES YES 10 a' 288.55 1.29362 YES YES 11 a" 420.39 48.32981 YES YES 12 a' 623.28 45.70357 YES YES 13 a' 703.06 215.95348 YES YES 14 a" 741.67 21.54040 YES YES 15 a' 961.67 124.18477 YES YES zero point VIBRATIONAL energy : 0.0094288 Hartree
Vibrational data (^{15}N)	# mode symmetry wave number IR intensity selection rules # cm**(-1) km/mol IR RAMAN 7 a' 109.82 8.55889 YES YES 8 a" 120.71 0.04946 YES YES 9 a' 169.40 7.64199 YES YES 10 a' 285.57 1.34575 YES YES 11 a" 410.25 45.29440 YES YES 12 a' 623.08 44.12064 YES YES 13 a' 691.43 205.56301 YES YES 14 a" 739.31 23.11765 YES YES 15 a' 933.63 122.89715 YES YES zero point VIBRATIONAL energy : 0.0094288 Hartree
UBP86/def2-QZVP	
Cartesian coordinates	5 Energy = -458.9269467684 F 1.3324608 -0.2155969 -1.7032235 Ir 0.5071831 -0.2869029 0.0000000 F 1.3324608 -0.2155969 1.7032235 N -1.1989080 -0.2344858 0.0000000 F -1.9731967 0.9525824 0.0000000
Vibrational data (^{14}N)	# mode symmetry wave number IR intensity selection rules # cm**(-1) km/mol IR RAMAN 7 a' 106.68 6.01777 YES YES 8 a" 112.60 0.09537 YES YES 9 a' 162.30 4.93230 YES YES 10 a' 294.81 0.47866 YES YES 11 a" 338.94 8.65496 YES YES 12 a' 614.35 27.14428 YES YES 13 a' 641.54 272.92351 YES YES 14 a" 658.52 68.49828 YES YES 15 a' 903.35 83.94606 YES YES zero point VIBRATIONAL energy : 0.0087325 Hartree
$FNIrF_2$ ($^2A''$)	
UBP86/def2-QZVP	
Cartesian coordinates	5 Energy = -458.9390808806 F 1.1447808 -0.1935728 -1.7853805 Ir 0.6156118 -0.2355852 0.0000000 F 1.1447808 -0.1935728 1.7853805 N -1.1214705 -0.3346896 0.0000000 F -1.7837028 0.9574204 0.0000000
Vibrational data (^{14}N)	# mode symmetry wave number IR intensity selection rules # cm**(-1) km/mol IR RAMAN 1 -0.00 0.00000 - - 2 -0.00 0.00000 - - 3 -0.00 0.00000 - - 4 0.00 0.00000 - - 5 0.00 0.00000 - - 6 0.00 0.00000 - - 7 a" 106.72 0.37770 YES YES 8 a' 154.44 2.49710 YES YES 9 a' 168.09 0.94280 YES YES 10 a" 304.06 0.36940 YES YES 11 a' 327.56 3.58129 YES YES 12 a' 632.47 89.63256 YES YES 13 a" 666.97 128.03929 YES YES 14 a' 679.53 222.48041 YES YES 15 a' 867.79 22.71469 YES YES zero point VIBRATIONAL energy : 0.0089023 Hartree

Vibrational data (^{15}N)	# mode symmetry wave number IR intensity selection rules # cm**(-1) km/mol IR RAMAN 7 a" 106.69 0.37653 YES YES 8 a' 154.44 2.49700 YES YES 9 a' 168.05 0.94304 YES YES 10 a" 295.95 0.35557 YES YES 11 a' 325.46 3.15544 YES YES 12 a' 631.39 111.49350 YES YES 13 a" 666.97 128.04743 YES YES 14 a' 667.30 192.48109 YES YES 15 a' 840.89 19.45455 YES YES zero point VIBRATIONAL energy : 0.0087872 Hartree
UB3LYP/def2-QZVP	
Cartesian coordinates	5 Energy = -458.5794076515 F 1.1400249 -0.1903900 -1.7820358 Ir 0.6090333 -0.2350006 0.0000000 F 1.1400249 -0.1903900 1.7820358 N -1.1286061 -0.3226483 0.0000000 F -1.7604770 0.9384289 0.0000000
Vibrational data (^{14}N)	# mode symmetry wave number IR intensity selection rules # cm**(-1) km/mol IR RAMAN 7 a" 109.31 0.37819 YES YES 8 a' 157.91 4.68500 YES YES 9 a' 168.71 1.50875 YES YES 10 a" 302.70 0.76878 YES YES 11 a' 346.28 2.34988 YES YES 12 a' 641.66 73.34058 YES YES 13 a" 675.11 155.12460 YES YES 14 a' 779.10 224.13031 YES YES 15 a' 880.82 45.04697 YES YES zero point VIBRATIONAL energy : 0.0092530 Hartree
Vibrational data (^{15}N)	# mode symmetry wave number IR intensity selection rules # cm**(-1) km/mol IR RAMAN 7 a" 109.28 0.37624 YES YES 8 a' 157.91 4.68528 YES YES 9 a' 168.67 1.50972 YES YES 10 a" 294.62 0.74311 YES YES 11 a' 343.92 2.07110 YES YES 12 a' 641.37 76.11434 YES YES 13 a" 675.10 155.14057 YES YES 14 a' 765.03 213.65419 YES YES 15 a' 852.96 41.60832 YES YES zero point VIBRATIONAL energy : 0.0091328 Hartree
ROHF-UCCSD(T)/aug-cc-pVTZ(-PP)	
Single Point B3LYP minimum	5 Energy = -457.82700748 F 1.1400249 -0.1903900 -1.7820358 Ir 0.6090333 -0.2350006 0.0000000 F 1.1400249 -0.1903900 1.7820358 N -1.1286061 -0.3226483 0.0000000 F -1.7604770 0.9384289 0.0000000 T1 diagnostic: 0.03488436 D1 diagnostic: 0.13687633

F_2NIrF

F_2NIrF (^{2}A')	
UBP86/def2-QZVP	
Cartesian coordinates	5 Energy = -458.8629945639 F 1.5482979 -0.4917268 -1.0791222 N 0.6755083 -0.2168063 0.0000000 F 1.5482979 -0.4917268 1.0791222 Ir -0.9922915 0.3134368 0.0000000 F -2.7798124 0.8868231 0.0000000
Vibrational data (^{14}N)	# mode symmetry wave number IR intensity selection rules # cm**(-1) km/mol IR RAMAN 7 a' 61.67 1.77356 YES YES 8 a" 112.23 2.42212 YES YES 9 a" 307.81 0.00019 YES YES 10 a' 376.03 12.13799 YES YES 11 a" 553.69 177.98760 YES YES 12 a' 562.80 1.43913 YES YES 13 a' 584.97 35.49821 YES YES 14 a' 647.62 134.52596 YES YES 15 a' 990.44 413.55337 YES YES zero point VIBRATIONAL energy : 0.0095621 Hartree
UB3LYP/def2-QZVP	
Cartesian coordinates	5 Energy = -458.5097621591 F 1.5344514 -0.4909063 -1.0645917 N 0.6949504 -0.2219223 0.0000000 F 1.5344514 -0.4909063 1.0645917 Ir -0.9873562 0.3162936 0.0000000 F -2.7764969 0.8874415 0.0000000

Vibrational data (^{14}N)	# mode symmetry wave number IR intensity selection rules # cm**(-1) km/mol IR RAMAN 7 a' 50.96 2.62706 YES YES 8 a" 124.94 3.95268 YES YES 9 a" 323.40 0.42925 YES YES 10 a' 385.43 10.19836 YES YES 11 a' 561.60 1.00217 YES YES 12 a' 623.95 11.67796 YES YES 13 a' 652.35 155.26240 YES YES 14 a" 751.42 162.06913 YES YES 15 a' 1036.12 376.49589 YES YES zero point VIBRATIONAL energy : 0.0102749 Hartree
F_2NIrF ($^4A''$)	
UBP86/def2-QZVP	
Cartesian coordinates	5 Energy = -458.8266783106 F 1.5089255 -0.5623194 -1.1060538 N 0.8217645 0.0091915 0.0000000 F 1.5089255 -0.5623194 1.1060538 Ir -1.0371870 0.1922373 0.0000000 F -2.8024284 0.9232099 0.0000000
Vibrational data (^{14}N)	# mode symmetry wave number IR intensity selection rules # cm**(-1) km/mol IR RAMAN 7 a' 78.74 4.11158 YES YES 8 a" 80.02 3.72134 YES YES 9 a" 194.24 0.18452 YES YES 10 a' 233.53 0.04359 YES YES 11 a' 449.06 2.58740 YES YES 12 a' 559.11 58.96818 YES YES 13 a' 595.52 74.70332 YES YES 14 a" 658.07 150.16710 YES YES 15 a' 853.08 331.16844 YES YES
UB3LYP/def2-QZVP	
Cartesian coordinates	5 Energy = -458.4779953696 F 1.4948764 -0.6022118 -1.0835070 N 0.8885042 -0.0334061 0.0000000 F 1.4948764 -0.6022118 1.0835070 Ir -1.0191132 0.4341641 0.0000000 F -2.8591438 0.8036657 0.0000000
Vibrational data (^{14}N)	# mode symmetry wave number IR intensity selection rules # cm**(-1) km/mol IR RAMAN 7 a' 83.93 3.99938 YES YES 8 a" 114.99 1.62177 YES YES 9 a' 246.08 0.69189 YES YES 10 a' 406.78 11.29014 YES YES 11 a" 407.88 9.33163 YES YES 12 a' 584.56 5.02530 YES YES 13 a' 650.39 130.64898 YES YES 14 a" 1001.55 292.75634 YES YES 15 a' 1084.75 267.05364 YES YES

$NIrF_2$

$NIrF_2$ ($^1A_1$)	
UBP86/def2-QZVP	
Cartesian coordinates	4 Energy = -359.1012494309 Ir 0.0000000 0.0000000 -0.0765255 N 0.0000000 0.0000000 -1.6908691 F -1.6251573 0.0000000 0.8836950 F 1.6251573 0.0000000 0.8836950
Vibrational data (^{14}N)	# mode symmetry wave number IR intensity selection rules # cm**(-1) km/mol IR RAMAN 7 a1 143.42 3.05471 YES YES 8 b1 211.05 5.54659 YES YES 9 b2 236.94 2.33622 YES YES 10 b1 628.70 105.81544 YES YES 11 a1 629.74 51.28666 YES YES 12 a1 1179.79 30.05040 YES YES zero point VIBRATIONAL energy : 0.0069020 Hartree
UB3LYP/def2-QZVP	
Cartesian coordinates	4 Energy = -358.7910333724 Ir 0.0000000 0.0000000 -0.0819104 N 0.0000000 0.0000000 -1.6803279 F -1.6217495 0.0000000 0.8811169 F 1.6217495 0.0000000 0.8811169
Vibrational data (^{14}N)	# mode symmetry wave number IR intensity selection rules # cm**(-1) km/mol IR RAMAN 7 a1 143.75 4.98222 YES YES 8 b1 216.38 6.47647 YES YES 9 b2 240.74 4.53107 YES YES 10 a1 636.19 62.85175 YES YES 11 b1 638.94 116.16148 YES YES 12 a1 1223.85 34.92929 YES YES zero point VIBRATIONAL energy : 0.0070620 Hartree

NIrF

NIrF (^{2}A')	
UBP86/def2-QZVP	
Cartesian coordinates	3 Energy = -259.1595662934 Ir -0.1550380 0.0071461 0.0000000 N -1.0118928 -1.3789176 0.0000000 F 1.1669308 1.3717715 0.0000000
Vibrational data (^{14}N)	# mode symmetry wave number IR intensity selection rules # cm**(-1) km/mol IR RAMAN 7 a' 45.92 4.48934 YES YES 8 a' 622.32 102.29311 YES YES 9 a' 1151.56 45.60841 YES YES zero point VIBRATIONAL energy : 0.0041458 Hartree
UB3LYP/def2-QZVP	
Cartesian coordinates	3 Energy = -258.8968248209 Ir -0.0672616 -0.0673564 0.0000000 N -1.0635023 -1.3434876 0.0000000 F 1.1307639 1.4108441 0.0000000
Vibrational data (^{14}N)	# mode symmetry wave number IR intensity selection rules # cm**(-1) km/mol IR RAMAN 7 a' 31.03 6.01178 YES YES 8 a' 629.62 124.10892 YES YES 9 a' 1184.57 50.37776 YES YES

Supporting Information References

[1] TURBOMOLE GmbH, *TURBOMOLE V7.0.1*, **2015**.

[2] a) A. D. Becke, *Phys. Rev. A* **1988**, *38*, 3098; b) J. P. Perdew, *Phys. Rev. B* **1986**, *33*, 8822.

[3] a) S. H. Vosko, L. Wilk, M. Nusair, *Can. J. Phys.* **1980**, *58*, 1200; b) C. Lee, W. Yang, R. G. Parr, *Phys. Rev. B* **1988**, *37*, 785; c) A. D. Becke, *J. Chem. Phys.* **1993**, *98*, 5648; d) P. J. Stephens, F. J. Devlin, C. F. Chabalowski, M. J. Frisch, *J. Phys. Chem.* **1994**, *98*, 11623.

[4] a) F. Weigend, F. Furche, R. Ahlrichs, *J. Chem. Phys.* **2003**, *119*, 12753; b) F. Weigend, R. Ahlrichs, *Phys. Chem. Chem. Phys.* **2005**, *7*, 3297.

[5] D. Andrae, U. Huermann, M. Dolg, H. Stoll, H. Preu, *Theor. Chim. Acta* **1990**, *77*, 123.

[6] H.-J. Werner, P. J. Knowles, G. Knizia, F. R. Manby, M. Schütz, P. Celani, W. Györffy, D. Kats, T. Korona, R. Lindh, A. Mitrushenkov, G. Rauhut, K. R. Shamasundar, T. B. Adler, R. D. Amos, S. J. Bennie, A. Bernhardsson, A. Berning, D. L. Cooper, M. J. O. Deegan, A. J. Dobbyn, F. Eckert, E. Goll, C. Hampel, A. Hesselmann, G. Hetzer, T. Hrenar, G. Jansen, C. Köppl, S. J. R. Lee, Y. Liu, A. W. Lloyd, Q. Ma, R. A. Mata, A. J. May, S. J. McNicholas, W. Meyer, T. F. Miller III, M. E. Mura, A. Nicklass, D. P. O'Neill, P. Palmieri, D. Peng, K. Pflüger, R. Pitzer, M. Reiher, T. Shiozaki, H. Stoll, A. J. Stone, R. Tarroni, T. Thorsteinsson, M. Wang, M. Welborn, *MOLPRO, version 2019.2, a package of ab initio programs*.

[7] K. A. Peterson, D. Figgen, M. Dolg, H. Stoll, *J. Chem. Phys.* **2007**, *126*, 124101.

[8] D. Figgen, K. A. Peterson, M. Dolg, H. Stoll, *J. Chem. Phys.* **2009**, *130*, 164108.

[9] R. A. Kendall, T. H. Dunning, R. J. Harrison, *J. Chem. Phys.* **1992**, *96*, 6796.

[10] a) T. H. Dunning, *J. Chem. Phys.* **1989**, *90*, 1007; b) W. A. de Jong, R. J. Harrison, D. A. Dixon, *J. Chem. Phys.* **2001**, *114*, 48; c) N. B. Balabanov, K. A. Peterson, *J. Chem. Phys.* **2005**, *123*, 64107.

[11] O. M. Wilkin, N. Harris, J. F. Rooms, E. L. Dixon, A. J. Bridgeman, N. A. Young, *J. Phys. Chem. A* **2018**, *122*, 1994.

[12] O. Ruff, W. Menzel, *Z. Anorg. Allg. Chem.* **1934**, *217*, 85.

[13] W. Maya, *Inorg. Chem.* **1964**, *3*, 1063.

[14] A. Allan, J.L. Duncan, J.H. Holloway, D.C. McKean, *J. Mol. Spectrosc.* **1969**, *31*, 368.

A.3 A Cornucopia of Iridium Nitrogen Compounds Produced from Laser-Ablated Iridium Atoms and Dinitrogen

Chemistry–A European Journal

Supporting Information

A Cornucopia of Iridium Nitrogen Compounds Produced from Laser-Ablated Iridium Atoms and Dinitrogen

Tony Stüker, Helmut Beckers, and Sebastian Riedel*[a]

A Cornucopia of Iridium Nitrogen Compounds Produced from Laser-Ablated Iridium Atoms and Dinitrogen

Table of Contents

Table of Contents 1

Supplemental Tables 3

Supplemental Figures 5

Supplemental computational results 10

BP86/def2-QZVP 10

BP86/ZORA-def2-TZVPP(N)/SARC-ZORA-TZVPP(Ir) 17

M06-L/ZORA-def2-TZVPP(N)/SARC-ZORA-TZVPP(Ir) 18

CCSD(T)/aug-cc-pVTZ(-PP) 19

References 22

Supplemental Tables

Table S1. Low-energy electronic state configuration (sorted by increasing energy) and vibrational frequencies (in cm^{-1}) of selected nitrogen containing molecules.

Molecule	Point Group	Electronic state and HOMOs		ΔE	Vibrational frequencies (Intensities) [Symmetry] $\tilde{\nu}^c$
N_2	$D_{\infty h}$	$^1\Sigma^+$	$(1\sigma_g^2\ 1\sigma_u^2\ 1\pi_g^4\ 2\sigma_g^2)$		2348 (0) [σ_g]
N_3		$^2\Pi_g$	$(1\pi_u^4\ 3\sigma_u^2\ 4\sigma_g^2\ 1\pi_g^4)$	0	479 (9) [π_u], 1716 (142) [σ_u]
N_3^-		$^1\Sigma_g^+$	$(1\pi_u^4\ 3\sigma_u^2\ 4\sigma_g^2\ 1\pi_g^4)$	−263	2042 (894) [σ_u]
IrN	$C_{\infty v}$	$^1\Sigma$	$(5\sigma^2\ 2\pi^4\ 1\delta^4\ 6\sigma^2)$	0	1209 (36) [σ] *1195 (38) [σ]*
	$C_{\infty v}$	$^3\Pi$	$(2\pi^4\ 1\delta^4\ 6\sigma^1\ 3\pi^1)$	+95	1039 (15) [σ]
$Ir(N)_2$	C_{2v}	$^2B_1$	$(2b_1^2\ 6a_1^2\ 5b_2^2\ 7a_1^2\ 3b_1^1)$	0	869 (41) [b_2]
	C_{2v}	$^2B_2$	$(2b_1^2\ 6a_1^2\ 7a_1^2\ 5b_2^1\ 3b_1^2)$	+103	1119 (595) [b_2]
		$^2A_1$	$(2b_1^2\ 6a_1^2\ 5b_2^2\ 7a_1^1\ 3b_1^2)$	+111	1005 (3) [b_2], 990 (1) [a_1]
		$^4A_2$	$(6a_1^2\ 7a_1^2\ 5b_2^1\ 3b_1^1\ 8a_1^1)$	+59	958 (11) [a_1], 466 (595) [b_2]
$Ir(N)_3$	D_{3h}	$^1A_1'$			968 (0) [a1'], 770 (2 × 0.7) [e']
IrN_2	$C_{\infty v}$	$^2\Delta$	$(7\sigma^2\ 3\pi^4\ 1\delta^3\ 8\sigma^2)$	0	382 (3) [π], 382 (3) [π], 584 (10) [σ^+], 2119 (283) [σ^+] *377 (3) [π], 377 (3) [π], 549 (29) [σ^+], 2140 (463) [σ^+]*
	C_s	$^4A'$	$(4a''^2\ 11a'^1\ 12a'^1\ 13a'^1)$	+104	143 (20) [a'] 332 (0) [a'], 2119 (312) [a']
$Ir(N_2)^-$	$C_{\infty v}$	$^1\Sigma^+$	$(7\sigma^2\ 3\pi^4\ 1\delta^4\ 8\sigma^2)$	−182	429 (3) [π], 429 (3) [π], 654 (5) [σ^+], 1955 (675) [σ^+] *434 (3) [π], 434 (3) [π], 648 (12)* [σ^+], *1963 (1018)* [σ^+]
$Ir(N_2)^+$	$C_{\infty v}$	$^3\Delta$	$(7\sigma^2\ 3\pi^4\ 1\delta^3\ 8\sigma^1)$	+848	341 (1) [π], 341 (1) [π], 488 (15), 2212 (48) *313 (1) [π], 313 (1) [π], 401 (14) [σ^+], 2286 (24) [σ^+]*
$Ir(N_2)_2$	$D_{\infty h}$	$^2\Delta_g$	$(2\pi_g^4\ 7\sigma_g^2\ 1\delta_g^3)$	0	439 (99), 2149 (1001)
	$D_{\infty h}$	$^4\Pi_u$	$(2\pi_g^4\ 1\delta_g^2\ 7\sigma_g^2\ 2\pi_u^1)$	+246	276 (30), 1964 (1793)
$[Ir(N_2)_2]^+$	$D_{\infty h}$	$^3\Delta_g$	$(2\pi_g^4\ 7\sigma_g^2\ 1\delta_g^2)$	+846	383 (48) [σ_u], 2269 (173) [σ_u]
	$D_{\infty h}$	$^1\Sigma_g^+$	$(2\pi_g^4\ 7\sigma_g^2\ 1\delta_g^2)$	+866	383 (48) [σ_u], 2239 (174) [σ_u]
	$D_{\infty h}$	$^1\Sigma_g^+$	$(2\pi_g^4\ 7\sigma_g^0\ 1\delta_g^4)$	+944	379 (46) [σ_u], 2209 (211) [σ_u]
$[Ir(N_2)_2]^-$	C_{2v}	$^1A_1$	$((2a_2^2\ 8b_1^2)\ 9a_1^2\ (3b_2^2\ 10a_1^2))$	−224	486 (69) [b_1], 1988 (1926) [b_1], 2052 (38) [a_1]
$Ir(N_3)$	C_s	$^3A''$	$(13a''^2\ 4a''^2\ 14a'^2\ 15a''^1\ 5a''^1)$		2020 (407) [a'], 1153 (53) [a']
IrNNIr	$D_{\infty h}$	$^3\Sigma_u^+$	$6\sigma_g^2\ 2\pi_u^4\ 1\delta_g^3\ 1\delta_u^3$		2081 (0) [σ_g], 781 (162) [σ_u] *2103 (0) [σ_g], 729 (361) [σ_u]*
$NIr(N_2)$	C_s	$^1A'$			2110 (388) [a'], 1085 (27) [a']
IrIrN	C_s	$^2A'$	$(13a'^2\ 14a'^2\ 5a''^2\ 6a''^2\ 15a'^1)$		1054 (60) [a']

[c]Selected vibrational absorptions with intensities greater than 0 and wavenumbers in observable range. See detailed computational results for all data.

Table**Table S2.** Overview of IR bands (in cm^{-1}) of dinitrogen complexes of the platinum group metals obtained in solid argon matrices.

Metal	$M(^{14}N_2)$	$M(^{15}N_2)$	$\Delta\nu_{N_2}$ c)	$M(^{14}N_2)_2$	$M(^{15}N_2)_2$	$\Delta\nu_{N_2}$ c)	$M(^{14}N_2)_2^-$	$M(^{15}N_2)_2^-$	$\Delta\nu_{N_2}$ c)
Ru[1]	2034.6	1967.1	293	2077.6	2008.6	250			
Rh[2]	2153.3	2081.7	175	2185.9	2112.8	142	1958.9	1893.4	369
Pd[3]	2213.0	2138.7	115	2234.0	2159.5	94			
Os[1]	2044.2	1976.2	283	2083.2	2013.9	245			
Ir	2087.6	2018.2	240	2144.7	2073.7	183	1956.4[a]	1890.3[a]	371[a]
Pt[4]	2168.5	2096.2	159	2195.4	2122.2	133	1862.5[b]	1803.5[b]	465[b]

[a] Recorded in neon matrix. [b] Recorded in pure dinitrogen matrix. [c] Red shift relative to uncoordinated N_2.

Table S3. NPA- and QTAIM results, bond lengths of selected iridium nitrogen molecules obtained by analyzing the BP86/def2-QZVP wavefunctions..

Property		NN	$(NH_2)_2$	Ir(NN')	$Ir(NN')_2$	IrNNIr	$Ir(N_2)^+$	$Ir(N_2)_2^-$	IrN	$Ir(N)_2$	$Ir(N)_3$
Bond length	Ir-N	-	-	179	190	180	187	185	160	170	176
	N-N	110	144	113	112	115	112	114	-	-	-
QTAIM Charge	Ir	-	-	0.227	1.611	0.227	0.954	–0.018	0.278	0.896	1.250
	N	0.000	-0.667	–0.264	–0.499	–0.227	–0.191	–0.154	–0.278	–0.448	–0.417[a]
	N'	-	-	0.037	–0.307	-	0.237	–0.337	-	-	-
AIM ρ_b	Ir-N	-	-	0.209	0.111	0.205	0.171	0.178	0.378	0.290	0.260
	N-N	0.700	0.298	0.622	0.592	0.579	0.648	0.613	-	-	
NPA Charge	Ir	-	-	0.069	0.087	0.087	0.926	–0.46	–0.032	0.588	0.847
	N	0.000	-0.678	-0.032	–0.070	–0.087	–0.122	–0.08	0.032	–0.294	–0.282
	N'	-	-	-0.037	0.027		0.196	–0.19	-	-	-
NPA B.O	Ir-N	-	-	0.65	0.38/0.43	0.62	0.50	0.55	2.82	2.06	1.74[a]
	N-N	3.01	1.02	2.56	2.64	2.51	2.55	2.61	-	-	

[a]Averaged values.

Table S4. Absolute and relative energies of the two lowest electronic states of all irreproducible representation of doublet, quartet, and sextet spin states of molecular iridium dinitride $Ir(N)_2$.

	Doublet		Quartet		Sextet	
Irrep.	*E* (hartree)	ΔE (kJ mol^{-1})	*E* (hartree)	ΔE (kJ mol^{-1})	*E* (hartree)	ΔE (kJ mol^{-1})
A_1	–212.5839098	50	–212.5115669	240	–212.5067341	252
A_1	–212.5572517	120	–212.4780023	328	–212.4098773	507
B_1	–212.6029061	0	–212.5594627	114	–212.4358756	439
B_1	–212.5285217	195	–212.5050720	257	–212.4212219	477
B_2	–212.5565516	122	–212.5285079	195	–212.4148392	494
B_2	–212.5190630	220	–212.5074391	251	–212.3828112	578
A_2	–212.5479788	144	–212.5709677	84	–212.4102628	506
A_2	–212.5377015	171	–212.4960646	281	–212.3931535	551

Supplemental Figures

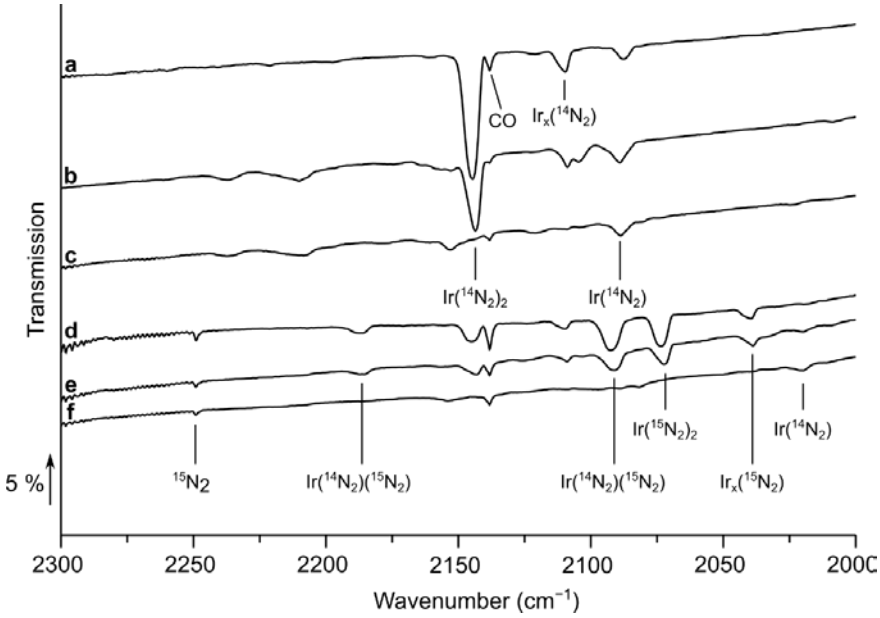

Figure S1. Infrared transmission spectra in the 2000–2350 cm^{-1} region of the reaction products of laser-ablated iridium atoms with 10 % $^{14}N_2$ (**a**, **b** and **c**) or a 1:1 mixture of $^{14}N_2$ and $^{15}N_2$ (**d**, **e** and **f**). Spectrum **a** and **d** were recorded after 90 min deposition, **b** and **e** after annealing to 25 K, and **c** and **f** were taken after irradiation with an LED light of 455 nm wavelength for 10 min.

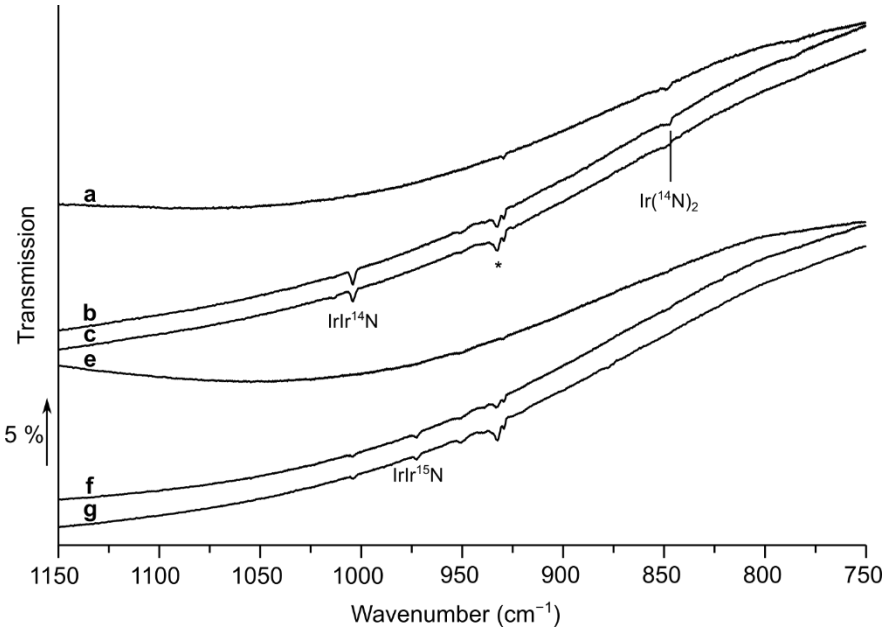

Figure S2. Infrared transmission spectra in the 750–1150 cm^{-1} region of the reaction products of laser-ablated iridium atoms with 10 % $^{14}N_2$ (**a**, **b** and **c**) or a 1:1 mixture of $^{14}N_2$ and $^{15}N_2$ (**d**, **e** and **f**). Spectrum **a** and **d** were recorded after 90 min deposition, **b** and **e** after annealing to 25 K, and **c** and **f** were taken after irradiation with an LED light of 455 nm wavelength for 10 min. Signal group highlighted with the asterisk belongs to nitrogen-less impurities which do not exhibit an isotopic shift.

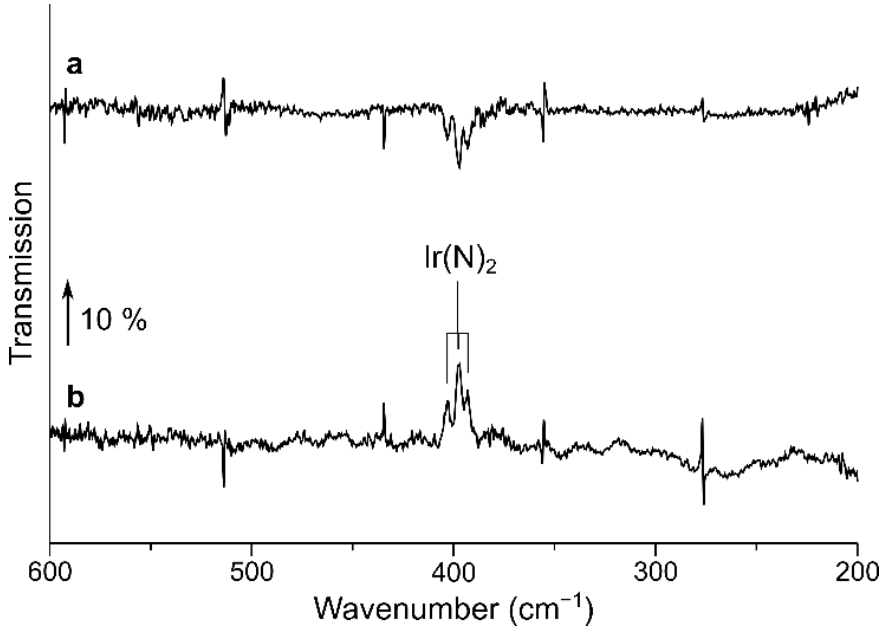

Figure S3. Infrared transmission spectrum in the 200–600 cm^{-1} region of the reaction products of laser-ablated iridium atoms with 10 % of a 1:1 mixture of $^{14}N_2$ and $^{15}N_2$ diluted in neon. Spectrum **a** was taken after 90 min of deposition, difference spectrum **b** was recorded after irradiating the matrix with LED light of 455 nm wavelength for 10 min.

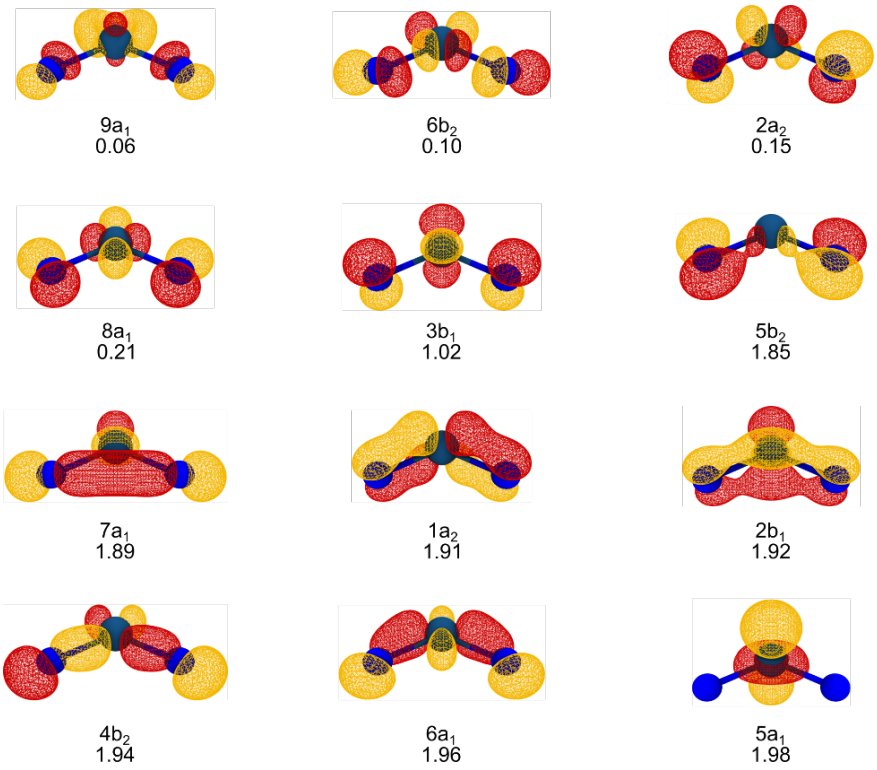

Figure S4. Valence natural molecular orbitals with an isosurface value of 0.04 $Å^{-1}$ at the CASSCF(15,12)/cc-pVTZ(-PP) level of theory with occupation numbers and orbital wavefunction symmetry.

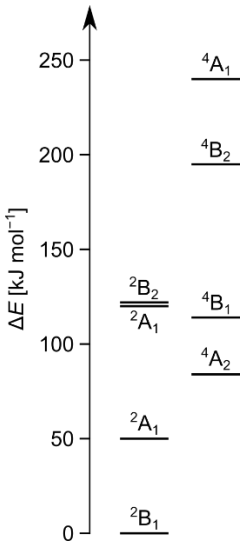

Figure S5. The four lowest electronic doublet and quartet states of $Ir(N)_2$ calculated using SA-CASSCF(15,12)/cc-pVTZ at the minimum geometry obtained at the BP86/def2-QZVP level of theory.

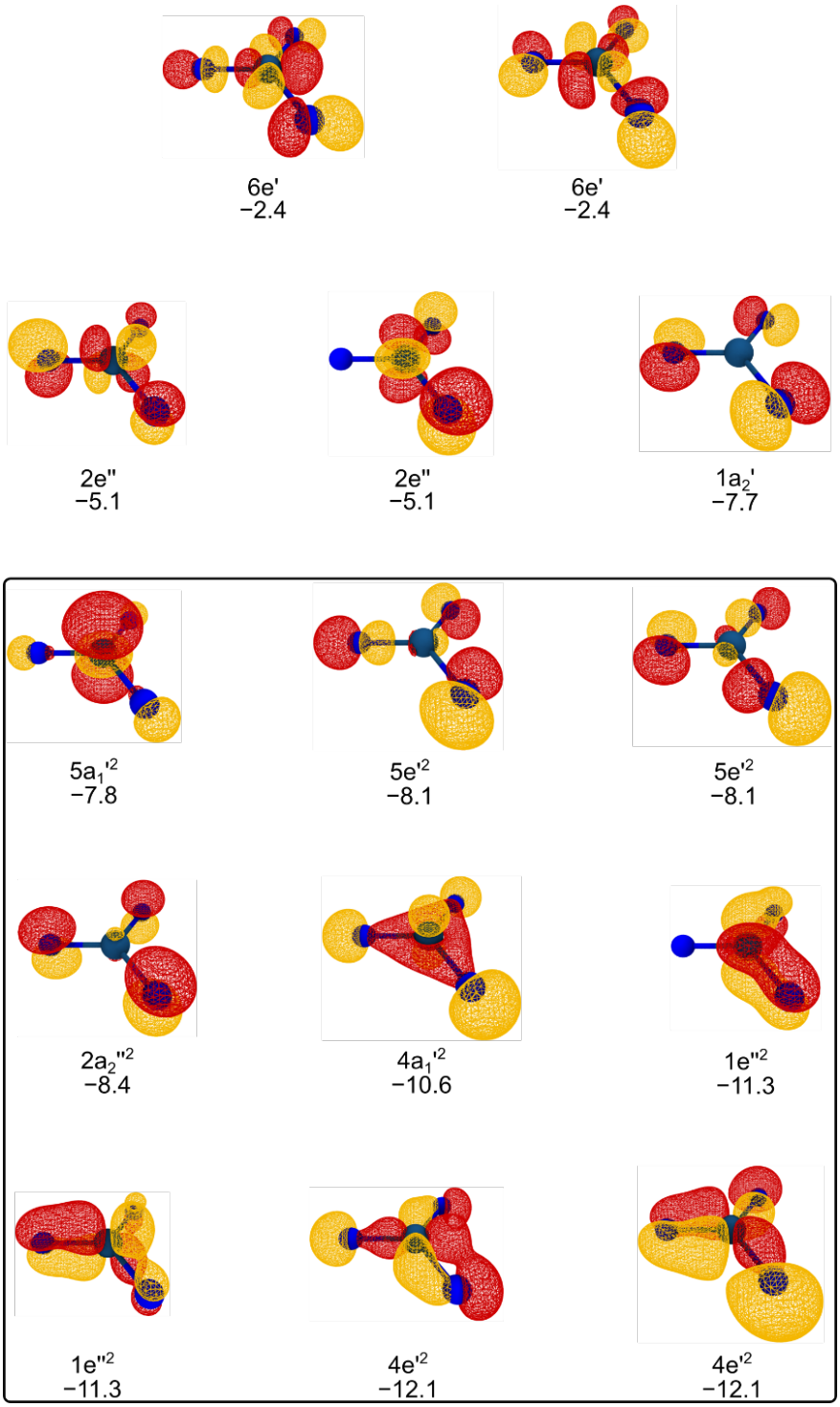

Figure 6. Molecular orbitals arising from the 5d(Ir) and 2p(N) atomic orbitals of $Ir(N)_3$ calculated at the R-BP86/ZORA-def2-TZVPP(N)/SARC-ZORA-TZVPP(Ir) level of theory with corresponding symmetries and energies (eV). Occupation numbers of orbitals inside the box 2, outside 0.

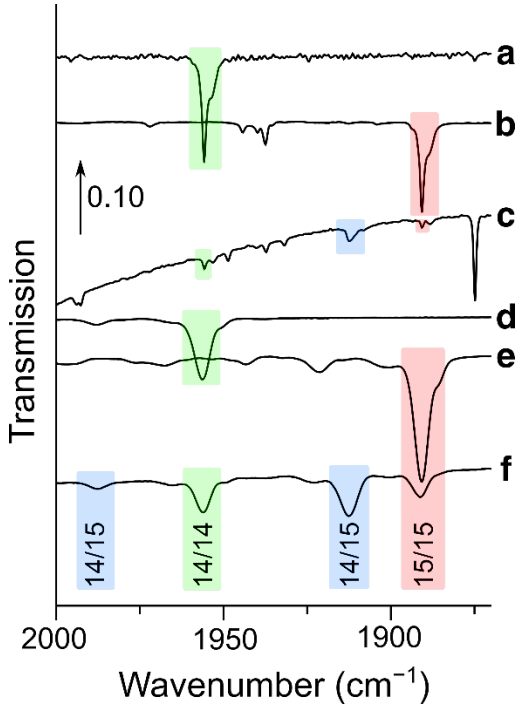

Figure S7. Infrared transmission spectrum of $Ir(N_2)^-$ in the 1870–2000 cm^{-1} region obtained by reacting laser-ablated iridium atoms with neat $^{14}N_2$ (**a**), neat $^{15}N_2$ (**b**), a neat 1:1 mixture of $^{14}N_2$ and $^{15}N_2$ (**c**), 10 % of $^{14}N_2$ in Ne (**d**), 10 % of $^{15}N_2$ in Ne (**e**) and 10 % of a 1:1 mixture of $^{14}N_2$ and $^{15}N_2$ in Ne (**f**). Trace **c** is enhanced by a factor of 6. The highlighted bands are assigned to the isotopologues $Ir(^{14}N)_2(^{14}N_2)$ (green), $Ir(^{14}N)_2(^{15}N_2)$ (blue), and $Ir(^{15}N)_2(^{15}N_2)$ (red).

Supplemental computational results

The vibrational data were calculated with the mass of the most abundant isotope, unless indicated otherwise. Vibrational modes with wavenumbers equal to zero (rotations and translations) are omitted. Point groups and electronic states given here are the ones used in the calculations. The electronic energy is given in hartree, x y z coordinates in Angstroem. Unless otherwise indicated, all BP86 and M06-L DFT calculations were carried out using the unrestricted Kohn-Sham (UKS) formalism.

BP86/def2-QZVP

N_2 (D_{6h}, $^1A_{1g}$) RKS

```
Energy = -109.5871592871
N     0.0000000    0.0000000    0.5508504
N     0.0000000    0.0000000   -0.5508504

14N2
#  mode     symmetry     wave number   IR intensity    selection rules
#                          cm**(-1)        km/mol         IR     RAMAN
     6        a1g          2347.76         0.00000       NO      YES

14N15N (1A1)
#                          cm**(-1)        km/mol         IR     RAMAN
     6        a1           2308.70         0.00000       YES     YES

15N2
#  mode     symmetry     wave number   IR intensity    selection rules
#                          cm**(-1)        km/mol         IR     RAMAN
     6        a1g          2268.70         0.00000       NO      YES
```

N_3 (D_{6h}, $^2B_{3g}$)

```
Energy = -164.2411958613
N     0.0000000    0.0000000    1.1852937
N     0.0000000    0.0000000    0.0000000
N     0.0000000    0.0000000   -1.1852937

14N3
#  mode     symmetry     wave number   IR intensity    selection rules
#                          cm**(-1)        km/mol         IR     RAMAN
     6        b2u           478.69         9.06192       YES     NO
     7        b3u           583.88         1.25736       YES     NO
     8        ag           1318.96         0.00000       NO      YES
     9        b1u          1716.01       141.84904       YES     NO
```

N_3^- (D_{6h}, $^1A_{1g}$) RKS

```
Energy = -164.3423630893
N     0.0000000    0.0000000    1.1914452
N     0.0000000    0.0000000   -0.0000000
N     0.0000000    0.0000000   -1.1914452

14N3-
#  mode     symmetry     wave number   IR intensity    selection rules
#                          cm**(-1)        km/mol         IR     RAMAN
     6        e1u           630.52         1.45779       YES     NO
     7        e1u           630.52         1.45779       YES     NO
     8        a1g          1296.02         0.00000       NO      YES
     9        a2u          2042.07       893.58204       YES     NO

15N3-
#  mode     symmetry     wave number   IR intensity    selection rules
#                          cm**(-1)        km/mol         IR     RAMAN
     6        e1u           609.28         1.36125       YES     NO
     7        e1u           609.28         1.36125       YES     NO
     8        a1g          1252.37         0.00000       NO      YES
     9        a2u          1973.30       834.40904       YES     NO

14N15N15N- (C6v, 1A1)
#  mode     symmetry     wave number   IR intensity    selection rules
#                          cm**(-1)        km/mol         IR     RAMAN
     6        e1            612.87         1.56487       YES     YES
     7        e1            612.87         1.56487       YES     YES
     8        a1           1273.95         0.07689       YES     YES
     9        a1           1985.20       848.71210       YES     YES
```

$^{15}N^{14}N^{14}N^{-}$ (C_{6v}, $^{1}A_1$)

# mode	symmetry	wave number cm**(-1)	IR intensity km/mol	selection rules IR	RAMAN
6	e1	627.03	1.26587	YES	YES
7	e1	627.03	1.26587	YES	YES
8	a1	1273.98	0.05871	YES	YES
9	a1	2031.02	879.19016	YES	YES

IrN (C_{6v}, $^{1}A_1$)

```
Energy = -159.2161562580
Ir    0.0000000    0.0000000   -0.7990476
N     0.0000000    0.0000000    0.7990476
```

$Ir^{14}N$

# mode	symmetry	wave number cm**(-1)	IR intensity km/mol	selection rules IR	RAMAN
6	a1	1208.95	36.14598	YES	YES

$Ir^{15}N$

# mode	symmetry	wave number cm**(-1)	IR intensity km/mol	selection rules IR	RAMAN
6	a1	1171.04	33.91496	YES	YES

$Ir(N)_2$ (C_{2v}, $^{2}B_1$)

```
Energy = -213.9559837886
N     1.4123939    0.0000000    0.3160590
Ir    0.0000000    0.0000000   -0.6321178
N    -1.4123939    0.0000000    0.3160590
```

$Ir(^{14}N)_2$

# mode	symmetry	wave number cm**(-1)	IR intensity km/mol	selection rules IR	RAMAN
7	a1	392.69	0.02446	YES	YES
8	b1	868.62	41.44662	YES	YES
9	a1	1027.06	1.51089	YES	YES

$Ir(^{15}N)_2$

# mode	symmetry	wave number cm**(-1)	IR intensity km/mol	selection rules IR	RAMAN
7	a1	380.51	0.02324	YES	YES
8	b1	842.08	39.04173	YES	YES
9	a1	994.21	1.41392	YES	YES

$Ir(^{15}N)(^{14}N)$ (C_s, A'')

# mode	symmetry	wave number cm**(-1)	IR intensity km/mol	selection rules IR	RAMAN
7	a'	387.40	0.03082	YES	YES
8	a'	852.88	39.69499	YES	YES
9	a'	1011.80	1.91496	YES	YES

$Ir(N)_2$ (C_{2v}, $^{2}B_2$)

```
Energy = -213.9168489215
N     1.4829328    0.0000000    0.2901401
Ir    0.0000000    0.0000000   -0.5802799
N    -1.4829328    0.0000000    0.2901401
```

# mode	symmetry	wave number cm**(-1)	IR intensity km/mol	selection rules IR	RAMAN
7	a1	276.66	0.58989	YES	YES
8	a1	983.51	6.92432	YES	YES
9	b1	1119.44	595.71207	YES	YES

$Ir(N)_2$ (C_{2v}, $^{2}A_1$)

```
Energy = -213.9140155669
N     1.4875439    0.0000000    0.2814508
Ir    0.0000000    0.0000000   -0.5629013
N    -1.4875439    0.0000000    0.2814508
```

# mode	symmetry	wave number cm**(-1)	IR intensity km/mol	selection rules IR	RAMAN
7	a1	346.49	0.80753	YES	YES
8	a1	990.22	1.15859	YES	YES
9	b1	1004.94	3.37700	YES	YES

$Ir(N)_2$ (C_{2v}, $^4A_2$)

```
Energy = -213.9321859773
N     1.5245185    0.0000000    0.2729119
Ir    0.0000000    0.0000000   -0.5458234
N    -1.5245185    0.0000000    0.2729119

#  mode     symmetry     wave number   IR intensity    selection rules
#                          cm**(-1)        km/mol         IR     RAMAN
     7        a1            254.36         1.92459       YES     YES
     8        b1            466.21        33.49477       YES     YES
     9        a1            957.58        11.11216       YES     YES
```

$Ir(N)_3$ (D_{3h}, $^1A_1$')

```
Energy = -268.6541880303
Ir    0.0000000    0.0000000    0.0000000
N     0.8805308   -1.5251241    0.0000000
N     0.8805308    1.5251241    0.0000000
N    -1.7610616    0.0000000    0.0000000

#  mode     symmetry     wave number   IR intensity    selection rules
#                          cm**(-1)        km/mol         IR     RAMAN
     7        a2"           134.71         0.98897       YES      NO
     8        e'            185.11         0.61870       YES     YES
     9        e'            185.11         0.61870       YES     YES
    10        e'            770.49         0.69120       YES     YES
    11        e'            770.49         0.69120       YES     YES
    12        a1'           968.10         0.00000       NO      YES
```

$Ir(N_2)$ (C_{6v}, $^2A_2$)

```
Energy = -214.0303648898
Ir    0.0000000    0.0000000   -1.5731627
N     0.0000000    0.0000000    0.2208581
N     0.0000000    0.0000000    1.3523046

Ir(14N2)
#  mode     symmetry     wave number   IR intensity    selection rules
#                          cm**(-1)        km/mol         IR     RAMAN
     6        b1            381.97         2.82388       YES     YES
     7        b2            381.97         2.82388       YES     YES
     8        a1            584.12         9.63272       YES     YES
     9        a1           2119.09       282.87333       YES     YES

Ir(15N2)
#  mode     symmetry     wave number   IR intensity    selection rules
#                          cm**(-1)        km/mol         IR     RAMAN
     6        b2            368.85         2.63819       YES     YES
     7        b2            368.85         2.63819       YES     YES
     8        a1            566.85         9.07778       YES     YES
     9        a1           2047.34       264.17935       YES     YES
```

$Ir(N_2)$ (C_s, ^4A')

```
Energy = -213.9887166667
N    -0.1306671   -0.3041779    0.0000000
N     0.1114863   -1.4013518    0.0000000
Ir    0.0191808    1.7055297    0.0000000

#  mode     symmetry     wave number   IR intensity    selection rules
#                          cm**(-1)        km/mol         IR     RAMAN
     7        a'            142.43        19.57173       YES     YES
     8        a'            332.09         0.12137       YES     YES
     9        a'           2118.96       311.72410       YES     YES
```

$Ir(N_2)^-$ (C_{2v}, $^1A_1$)

```
Energy = -214.0996310483
```

```
Ir    0.0000000    0.0000000   -1.5443968
N     0.0000000    0.0000000    0.1926815
N     0.0000000    0.0000000    1.3517153
```

$Ir(^{14}N_2)^-$

# mode	symmetry	wave number cm**(-1)	IR intensity km/mol	selection rules IR	RAMAN
6	b1	429.13	2.65017	YES	YES
7	b2	429.13	2.65017	YES	YES
8	a1	653.87	5.31846	YES	YES
9	a1	1954.76	675.12711	YES	YES

$Ir(^{15}N_2)^-$

# mode	symmetry	wave number cm**(-1)	IR intensity km/mol	selection rules IR	RAMAN
6	b2	414.80	2.43853	YES	YES
7	b2	414.80	2.43853	YES	YES
8	a1	634.68	5.21638	YES	YES
9	a1	1888.98	630.72998	YES	YES

$Ir(N_2)^+$ (C_s, $^4A'$)

```
Energy = -213.7070345445
Ir    0.0000000    0.0000000   -1.6178553
N     0.0000000    0.0000000    0.2509589
N     0.0000000    0.0000000    1.3668964
```

$Ir(^{14}N_2)^+$

# mode	symmetry	wave number cm**(-1)	IR intensity km/mol	selection rules IR	RAMAN
6	b2	341.18	0.90551	YES	YES
7	b2	341.18	0.90551	YES	YES
8	a1	487.91	15.23200	YES	YES
9	a1	2211.96	48.49148	YES	YES

$Ir(^{15}N_2)^+$

# mode	symmetry	wave number cm**(-1)	IR intensity km/mol	selection rules IR	RAMAN
6	b2	329.77	0.86805	YES	YES
7	b2	329.77	0.86805	YES	YES
8	a1	473.60	13.99107	YES	YES
9	a1	2137.47	45.27682	YES	YES

$Ir(N_2)_2$ (D_{2h}, ^2A_g)

```
Energy = -323.6864664802
Ir    0.0000000    0.0000000    0.0000000
N     0.0000000    0.0000000    1.8991645
N     0.0000000    0.0000000    3.0198683
N     0.0000000    0.0000000   -1.8991645
N     0.0000000    0.0000000   -3.0198683
```

$Ir(^{14}N_2)_2$

# mode	symmetry	wave number cm**(-1)	IR intensity km/mol	selection rules IR	RAMAN
6	b3u	75.49	0.27235	YES	NO
7	b2u	75.50	0.27235	YES	NO
8	b3g	326.53	0.00000	NO	YES
9	b2g	326.54	0.00000	NO	YES
10	b1u	439.41	99.53577	YES	NO
11	b3u	463.30	0.03105	YES	NO
12	b2u	463.35	0.03085	YES	NO
13	ag	490.52	0.00000	NO	YES
14	b1u	2148.81	1001.24580	YES	NO
15	ag	2200.37	0.00000	NO	YES

$Ir(^{15}N_2)_2$

# mode	symmetry	wave number cm**(-1)	IR intensity km/mol	selection rules IR	RAMAN
6	b3u	73.42	0.25760	YES	NO
7	b2u	73.43	0.25760	YES	NO
8	b3g	315.54	0.00000	NO	YES
9	b2g	315.55	0.00000	NO	YES
10	b1u	428.00	94.43042	YES	NO
11	b3u	448.36	0.03018	YES	NO
12	b2u	448.40	0.03000	YES	NO
13	ag	474.00	0.00000	NO	YES
14	b1u	2076.44	934.98223	YES	NO
15	ag	2126.27	0.00000	NO	YES

$Ir(^{15}N_2)(^{14}N_2)$ (C_{2v}, $^2A_1$)

# mode	symmetry	wave number cm**(-1)	IR intensity km/mol	selection rules IR	RAMAN
6	b1	74.46	0.26496	YES	YES

7	b2	74.47	0.26495	YES	YES
8	b2	320.74	0.00010	YES	YES
9	b1	320.75	0.00010	YES	YES
10	a1	432.74	94.71981	YES	YES
11	b1	456.14	0.03053	YES	YES
12	b2	456.18	0.03034	YES	YES
13	a1	483.23	2.26519	YES	YES
14	a1	2093.45	745.54068	YES	YES
15	a1	2182.49	222.57143	YES	YES

$Ir(N_2)_2$ (D_{2h}, $^4B_{2u}$)

```
Energy = -323.5917128454
Ir     0.0000000    0.0000000    0.0000000
N      0.0000000    0.0000000    1.9197455
N      0.0000000    0.0000000    3.0595303
N      0.0000000    0.0000000   -1.9197455
N      0.0000000    0.0000000   -3.0595303
```

# mode	symmetry	wave number cm**(-1)	IR intensity km/mol	selection rules IR	RAMAN
6	b2u	87.71	2.25204	YES	NO
7	b3u	95.54	1.80407	YES	NO
8	b3u	276.08	29.91069	YES	NO
9	b3g	315.71	0.00000	NO	YES
10	b2g	368.99	0.00000	NO	YES
11	b1u	443.80	0.04404	YES	NO
12	ag	475.61	0.00000	NO	YES
13	b2u	493.01	0.12332	YES	NO
14	b1u	1963.81	1793.21471	YES	NO
15	ag	2055.51	0.00000	NO	YES

$Ir(N_2)_2^+$ (D_{2h}, ^3A_g)

```
Energy = -323.3643926816
Ir     0.0000000    0.0000000    0.0000000
N      0.0000000    0.0000000    1.9555958
N      0.0000000    0.0000000    3.0659497
N      0.0000000    0.0000000   -1.9555958
N      0.0000000    0.0000000   -3.0659497
```

# mode	symmetry	wave number cm**(-1)	IR intensity km/mol	selection rules IR	RAMAN
6	b2u	85.52	0.10171	YES	NO
7	b3u	85.52	0.10171	YES	NO
8	b2g	304.51	0.00000	NO	YES
9	b3g	304.51	0.00000	NO	YES
10	b1u	383.06	48.38707	YES	NO
11	ag	430.73	0.00000	NO	YES
12	b2u	470.20	0.61928	YES	NO
13	b3u	470.20	0.61928	YES	NO
14	b1u	2242.64	173.28622	YES	NO
15	ag	2269.64	0.00000	NO	YES

$Ir(N_2)_2^+$ (D_{2h}, ^1A_g)

```
Energy = -323.3568461762
Ir     0.0000000    0.0000000    0.0000000
N      0.0000000    0.0000000    1.9524098
N      0.0000000    0.0000000    3.0630648
N      0.0000000    0.0000000   -1.9524098
N      0.0000000    0.0000000   -3.0630648
```

# mode	symmetry	wave number cm**(-1)	IR intensity km/mol	selection rules IR	RAMAN
6	b2u	85.75	0.09727	YES	NO
7	b3u	85.75	0.09727	YES	NO
8	b2g	307.75	0.00000	NO	YES
9	b3g	307.75	0.00000	NO	YES
10	b1u	382.67	47.66188	YES	NO
11	ag	434.27	0.00000	NO	YES
12	b3u	477.52	0.71588	YES	NO
13	b2u	477.52	0.71589	YES	NO
14	b1u	2239.14	173.80930	YES	NO
15	ag	2265.58	0.00000	NO	YES

$Ir(N_2)_2^+$ (D_{2h}, ^1A_g)

```
Energy = -323.3272925494
Ir     0.0000000    0.0000000    0.0000000
N      0.0000000    0.0000000    1.9378028
N      0.0000000    0.0000000    3.0506974
N      0.0000000    0.0000000   -1.9378028
```

```
N     0.0000000    0.0000000   -3.0506974

#  mode     symmetry     wave number   IR intensity    selection rules
#                          cm**(-1)        km/mol         IR     RAMAN
     6        e1u            84.33         0.02829       YES     NO
     7        e1u            84.33         0.02829       YES     NO
     8        e1g           318.71         0.00000       NO      YES
     9        e1g           318.71         0.00000       NO      YES
    10        a2u           378.50        46.34882       YES     NO
    11        a1g           451.74         0.00000       NO      YES
    12        e1u           507.55         0.81635       YES     NO
    13        e1u           507.55         0.81635       YES     NO
    14        a2u          2209.40       211.08150       YES     NO
    15        a1g          2244.15         0.00000       NO      YES
```

$Ir(N_2)_2^-$ ($C_{2v,}$ $^1A_1$)

```
Energy = -323.7712152965
N    -1.8251145    0.0000000    0.0646127
N    -2.9215603    0.0000000   -0.2597363
Ir    0.0000000    0.0000000    0.3902468
N     1.8251145    0.0000000    0.0646127
N     2.9215603    0.0000000   -0.2597363

Ir(14N2)2-
#  mode     symmetry     wave number   IR intensity    selection rules
#                          cm**(-1)        km/mol         IR     RAMAN
     7        a1             68.16         3.24006       YES     YES
     8        a2            353.25         0.00000       NO      YES
     9        b1            362.69         0.05866       YES     YES
    10        b2            441.59         0.96035       YES     YES
    11        b1            486.15        68.36593       YES     YES
    12        a1            493.22         3.16098       YES     YES
    13        a1            547.61         0.55652       YES     YES
    14        b1           1988.14      1926.19429       YES     YES
    15        a1           2051.53        37.69070       YES     YES

Ir(15N2)2-
#  mode     symmetry     wave number   IR intensity    selection rules
#                          cm**(-1)        km/mol         IR     RAMAN
     7        a1             66.27         2.89115       YES     YES
     8        a2            341.36         0.00000       NO      YES
     9        b1            350.48         0.05370       YES     YES
    10        b2            427.15         0.88392       YES     YES
    11        b1            473.41        65.70096       YES     YES
    12        a1            477.44         2.91609       YES     YES
    13        a1            529.19         0.51669       YES     YES
    14        b1           1921.19      1798.87534       YES     YES
    15        a1           1982.44        35.20007       YES     YES

Ir(15N2)(14N2)- (Cs, 1A')
#  mode     symmetry     wave number   IR intensity    selection rules
#                          cm**(-1)        km/mol         IR     RAMAN
     7        a              67.22         3.06527       YES     YES
     8        a             346.81         0.00387       YES     YES
     9        a             356.22         0.06184       YES     YES
    10        a             434.86         0.91828       YES     YES
    11        a             478.08        59.35779       YES     YES
    12        a             486.49         9.59787       YES     YES
    13        a             539.32         1.65117       YES     YES
    14        a            1939.72      1541.85010       YES     YES
    15        a            2031.93       357.12640       YES     YES
```

$Ir(N_3)$ ($C_{s,}$ $^3A''$)

```
Energy = -268.7297430506
Ir   -0.8727706    1.8857263    0.0000000
N    -0.7277581    0.0225820    0.0000000
N     0.3642280   -0.5803123    0.0000000
N     1.2363008   -1.3279960    0.0000000

#  mode     symmetry     wave number   IR intensity    selection rules
#                          cm**(-1)        km/mol         IR     RAMAN
     7        a'            143.79         3.56380       YES     YES
     8        a'            430.61         3.54809       YES     YES
     9        a"            443.15         1.37139       YES     YES
    10        a'            671.92         5.10472       YES     YES
    11        a'           1152.81        53.23297       YES     YES
    12        a'           2019.81       407.41122       YES     YES
```

IrNNIr ($D_{2h,}$ $^3B_{1u}$)

```
Energy = -318.4719683227
```

```
Ir    0.0000000    0.0000000   -2.3766401
N     0.0000000    0.0000000   -0.5754674
N     0.0000000    0.0000000    0.5754674
Ir    0.0000000    0.0000000    2.3766401
```

$Ir^{14}N^{14}NIr$

# mode	symmetry	wave number cm**(-1)	IR intensity km/mol	selection rules IR	RAMAN
6	b2u	111.33	6.24364	YES	NO
7	b3u	111.33	6.24364	YES	NO
8	ag	203.20	0.00000	NO	YES
9	b3g	256.80	0.00000	NO	YES
10	b2g	256.80	0.00000	NO	YES
11	b1u	781.81	161.57713	YES	NO
12	ag	2080.71	0.00000	NO	YES

$Ir^{15}N^{15}NIr$

# mode	symmetry	wave number cm**(-1)	IR intensity km/mol	selection rules IR	RAMAN
6	b2u	107.84	5.85827	YES	NO
7	b3u	107.84	5.85827	YES	NO
8	ag	203.20	0.00000	NO	YES
9	b3g	248.19	0.00000	NO	YES
10	b2g	248.19	0.00000	NO	YES
11	b1u	757.29	151.60420	YES	NO
12	ag	2010.69	0.00000	NO	YES

$Ir^{14}N^{15}NIr$ (C_{2v}, $^3A_1$)

# mode	symmetry	wave number cm**(-1)	IR intensity km/mol	selection rules IR	RAMAN
6	b2	109.52	6.04099	YES	YES
7	b1	109.52	6.04099	YES	YES
8	a1	203.20	0.00000	YES	YES
9	b2	252.57	0.00997	YES	YES
10	b1	252.57	0.00997	YES	YES
11	a1	769.16	156.35928	YES	YES
12	a1	2046.18	0.23139	YES	YES

NIr(N_2) (C_s, ^{1}A')

```
Energy = -268.8194957881
Ir   -1.0046934   -0.4350909    0.0000000
N    -0.6944564   -2.0561243    0.0000000
N     0.3500444    0.9867359    0.0000000
N     1.3491054    1.5044794    0.0000000
```

$^{14}NIr(^{14}N_2)$

# mode	symmetry	wave number cm**(-1)	IR intensity km/mol	selection rules IR	RAMAN
7	a'	146.66	7.90813	YES	YES
8	a"	310.09	1.70767	YES	YES
9	a'	342.87	4.01490	YES	YES
10	a'	417.83	3.83047	YES	YES
11	a'	1084.86	27.23003	YES	YES
12	a'	2109.59	388.12093	YES	YES

$^{15}NIr(^{14}N_2)$

# mode	symmetry	wave number cm**(-1)	IR intensity km/mol	selection rules IR	RAMAN
7	a'	143.44	7.46759	YES	YES
8	a"	309.89	1.73449	YES	YES
9	a'	342.83	3.96068	YES	YES
10	a'	416.59	4.05497	YES	YES
11	a'	1050.80	25.53628	YES	YES
12	a'	2109.57	388.23032	YES	YES

IrIrN (C_s, ^{2}A')

```
Energy = -263.7144182651
Ir   -0.5963376    1.8879672    0.0000000
Ir   -0.3190028   -0.3927475    0.0000000
N     0.9153404   -1.4952197    0.0000000
```

$IrIr^{14}N$

# mode	symmetry	wave number cm**(-1)	IR intensity km/mol	selection rules IR	RAMAN
7	a'	105.80	5.85343	YES	YES
8	a'	221.76	0.95737	YES	YES
9	a'	1054.29	60.02501	YES	YES

$IrIr^{15}N$

# mode	symmetry	wave number cm**(-1)	IR intensity km/mol	selection rules IR	RAMAN
7	a'	102.86	5.46297	YES	YES

```
     8        a'           221.66         0.95186       YES     YES
     9        a'          1021.00        56.40977       YES     YES
```

BP86/ZORA-def2-TZVPP(N)/SARC-ZORA-TZVPP(Ir)

Ir(N)$_2$ (C_1, ^{2}A)

```
Energy = -18527.459076532468
Ir  -0.00000005284280      0.00000000000000     -0.63128496123684
N   -1.41022715939508      0.00000000000000      0.31564266296423
N    1.41022721223788      0.00000000000000      0.31564269827261

 Mode    freq (cm**-1)   T**2         TX         TY         TZ
-----------------------------------------------------------------------
   6:       392.86    0.015350  ( -0.000000   0.000000  -0.123897)
   7:       878.80   37.913039  ( -6.157356  -0.000000   0.000007)
   8:      1035.26    1.480248  ( -0.000023   0.000000   1.216654)
```

Ir(N)$_2$ TS (C_1, ^{2}A)

```
Energy = -18527.365959366154
Ir  -0.03866148720625      0.00000000000000     -1.00023248877844
N   -0.97294630786287      0.00000000000000      0.47158165101008
N    1.01160779506913      0.00000000000000      0.52865183776837

 Mode    freq (cm**-1)   T**2         TX         TY         TZ
-----------------------------------------------------------------------
   6:      -736.33    ***imaginary mode***
   7:       431.17    0.674613  ( -0.407012  -0.000001  -0.713410)
   8:       908.13    1.997347  (  0.615350  -0.000000  -1.272278)
```

Ir(N)$_2$ TS (C_1, ^{4}A)

```
Energy = -18527.361054029960
Ir   0.03301036678652      0.00000000000000     -1.00750169971361
N   -0.98054236764465      0.00000000000000      0.47425130571116
N    0.94753200085812      0.00000000000000      0.53325139400246

 Mode    freq (cm**-1)   T**2         TX         TY         TZ
-----------------------------------------------------------------------
   6:     -2308.50    ***imaginary mode***
   7:       367.41    1.577166  (  1.255181   0.034555   0.022207)
   8:       893.08    2.833148  ( -0.033693  -0.348179   1.646446)
```

Ir(N$_2$) (C_1, ^{2}A)

```
Energy = -18527.508956688940
Ir  -0.00000000066953     -0.00000000031987     -1.56484112101323
N   0.00000000133903      0.00000000063987      0.21341197152127
N   -0.00000000066950     -0.00000000031999      1.35142914949195

 Mode    freq (cm**-1)   T**2         TX         TY         TZ
-----------------------------------------------------------------------
   5:       392.74    1.514507  (  0.548736   1.101542  -0.000000)
   6:       392.74    1.514508  (  1.101542  -0.548737   0.000000)
   7:       602.92   11.393393  (  0.000000   0.000000  -3.375410)
   8:      2074.84  327.932089  ( -0.000000  -0.000000  18.108895)
```

Ir(N)$_3$ (C_1, ^{1}A) RKS

```
Energy = -18582.208568531445
N       0.877993      1.520731     -0.000000
Ir     -0.000001      0.000000      0.000000
N       0.877993     -1.520731     -0.000000
N      -1.755985      0.000000     -0.000000

 Mode    freq (cm**-1)   T**2         TX         TY         TZ
-----------------------------------------------------------------------
   6:       142.84    0.795457  (  0.000000   0.000000   0.891884)
   7:       189.97    0.508095  ( -0.712808   0.000045  -0.000000)
   8:       190.14    0.507954  (  0.000045   0.712709  -0.000000)
   9:       788.71    0.688991  (  0.830055   0.000374  -0.000000)
  10:       788.72    0.688937  ( -0.000374   0.830022  -0.000000)
  11:       976.94    0.000000  (  0.000059   0.000000   0.000000)
```

Ir(N)$_3$ (C_1, ^{1}A)

```
Energy = -18582.208568533388
N       0.877996      1.520736      0.000000
Ir     -0.000002      0.000000     -0.000000
```

```
N       0.877996     -1.520736      0.000000
N      -1.755990      0.000000      0.000000

 Mode    freq (cm**-1)   T**2         TX          TY          TZ
-------------------------------------------------------------------
   6:       142.86    0.795777  ( -0.000000   0.000000  -0.892063)
   7:       189.98    0.508199  (  0.712881   0.000024   0.000000)
   8:       190.15    0.507974  ( -0.000029   0.712723  -0.000000)
   9:       788.70    0.689450  (  0.830266  -0.010414  -0.000000)
  10:       788.70    0.689159  (  0.010430   0.830091  -0.000000)
  11:       976.93    0.000000  (  0.000075  -0.000010   0.000000)
```

Ir(N)$_3$ TS (C$_1$, ^{1}A) RKS

```
Energy = -18582.191698412571
N    0.98504117841954      1.70618191713348     -0.01726953128539
Ir   0.13626371759078      0.23596137442520     -0.00256235402343
N    0.41847717313611     -1.53641771301031      0.00986257570181
N   -1.53978106914643     -0.40572557854836      0.00996930960701

 Mode    freq (cm**-1)   T**2         TX          TY          TZ
-------------------------------------------------------------------
   6:      -315.28    ***imaginary mode***
   7:       123.26    1.381596  ( -0.001127  -0.010960  -1.175362)
   8:       189.88    5.598902  ( -2.049855   1.181945  -0.002140)
   9:       799.34    0.086670  ( -0.255809   0.145710   0.000010)
  10:       857.65   28.574006  (  2.672182   4.629386  -0.047255)
  11:      1000.79   14.419617  ( -1.898642  -3.288417   0.032987)
```

Ir(N)$_3$ TS (C$_1$, ^{3}A)

```
Energy = -18582.165316776885
N   0.89916651760164      1.62753405912247      0.20507888528382
Ir  0.23407666406960      0.21539804792815     -0.48693024802453
N   0.32738784340781     -1.41585703748299      0.16654561326475
N   -1.46063002507905     -0.42707506956763      0.11530574947595

 Mode    freq (cm**-1)   T**2         TX          TY          TZ
-------------------------------------------------------------------
   6:      -689.42    ***imaginary mode***
   7:       213.83    3.072218  (  1.727321  -0.191056   0.228209)
   8:       246.22    9.319231  (  0.115990  -0.589404   2.993055)
   9:       587.63    4.374417  (  1.554629  -1.337964   0.409143)
  10:       865.97   20.637535  ( -0.849950  -4.308688  -1.162034)
  11:       972.20    8.060881  (  1.123561   2.607322   0.019021)
```

Ir(N)(N$_2$) (C$_1$, ^{3}A) RKS

```
Energy =
Ir  -0.99843601031668     -0.43465654378306      0.00001460729074
N   -0.69857605006467     -2.05566281879788     -0.00000414845203
N   0.35043497938319      0.98244325687028     -0.00002586909360
N   1.34657708099816      1.50787610571065      0.00001541025489

 Mode    freq (cm**-1)   T**2         TX          TY          TZ
-------------------------------------------------------------------
   6:       149.71    7.640629  (  2.542583   1.084390  -0.000051)
   7:       315.22    1.726735  (  0.000292   0.000128  -1.314053)
   8:       349.88    3.848438  (  1.712748   0.956521   0.000004)
   9:       422.49    4.003985  ( -1.792344  -0.889656   0.000145)
  10:      1095.70   25.572155  (  4.370009  -2.544636  -0.000227)
  11:      2109.71  378.724859  ( 14.037302  13.478836  -0.000371)
```

M06-L/ZORA-def2-TZVPP(N)/SARC-ZORA-TZVPP(Ir)

Ir(N)$_2$ (C$_1$, ^{2}A)

```
Energy = -18525.467056933678
Ir  -0.00000009045772      0.00000000000000     -0.62823498277550
N   -1.40069500576939      0.00000000000000      0.31411766236377
N    1.40069509622710      0.00000000000000      0.31411772041173

 Mode    freq (cm**-1)   T**2         TX          TY          TZ
-------------------------------------------------------------------
   6:       406.40    0.119210  (  0.005129  -0.000348  -0.345230)
   7:       875.66   48.032941  ( -6.930580  -0.000055   0.000232)
   8:      1058.48    3.434843  (  0.002007  -0.000050   1.853332)
```

Ir(N)$_2$ TS (C$_1$, ^{2}A)

```
Energy = -18525.372866912498
```

```
Ir  -0.05423592809509      0.00000000000000     -1.00715026943836
N   -0.95916993255531      0.00000000000000      0.46383141403110
N    1.01340586065041      0.00000000000000      0.54331985540728

 Mode    freq (cm**-1)   T**2         TX         TY         TZ
-----------------------------------------------------------------
   6:      -711.55    ***imaginary mode***
   7:       437.25    0.311448  (  0.545333   0.000038   0.118574)
   8:       911.08    4.595018  (  0.881119   0.000033  -1.954136)
```

Ir(N)$_3$ (C_1, ^{1}A) RKS

```
Energy = -18580.193789971730
N    0.87443135203633      1.51461844965352      0.00000094120495
Ir  -0.00003416411595     -0.00000030039386     -0.00000282342226
N    0.87443065827745     -1.51461784888252      0.00000094120706
N   -1.74882784619783     -0.00000030037713      0.00000094101025

 Mode    freq (cm**-1)   T**2         TX         TY         TZ
-----------------------------------------------------------------
   6:       126.46    1.535762  ( -0.010504   0.007064  -1.239194)
   7:       193.03    1.102940  ( -0.799239   0.681121   0.015210)
   8:       195.47    1.122133  ( -0.655602  -0.832056   0.001262)
   9:       773.87    0.054071  ( -0.232480   0.004928  -0.000142)
  10:       776.07    0.086261  ( -0.007649  -0.293597   0.001649)
  11:      1003.90    0.000467  ( -0.020525   0.006719   0.000341)
```

Ir(N)$_3$ TS (C_1, ^{1}A) RKS

```
Energy = -18580.178264754060
N   0.97490410868930      1.68881126151210     -0.01770995567920
Ir  0.13030719215327      0.22545450004475      0.00043654942375
N   0.44375596989281     -1.53243636509665      0.00856198738820
N   -1.54896627073538     -0.38182939646019      0.00871141886726

 Mode    freq (cm**-1)   T**2         TX         TY         TZ
-----------------------------------------------------------------
   6:      -306.08    ***imaginary mode***
   7:       105.94    2.400416  ( -0.082091  -0.019473  -1.547029)
   8:       184.62    8.962498  ( -2.605275   1.474798  -0.003351)
   9:       819.45    0.035455  ( -0.030187   0.185858  -0.000671)
  10:       869.51   38.409588  (  3.103273   5.364424  -0.047283)
  11:      1023.99   13.526293  ( -1.835324  -3.186866   0.041968)
```

CCSD(T)/aug-cc-pVTZ(-PP)

IrN (C_{2v}, $^1A_1$)

```
Energy = -158.596318228943
Ir         0.00000        0.00000        0.10821
N          0.00000        0.00000       -1.49116


                    Normal Coordinate Analysis
  ------------------------------------------------------------------
    Irreducible         Harmonic       Infrared        Type
   Representation       Frequency      Intensity
  ------------------------------------------------------------------
                       (cm-1)         (km/mol)
  ------------------------------------------------------------------
       SG+              1195.3928        37.7081       VIBRATION
  ------------------------------------------------------------------
```

Ir(N_2) (C_{2v}, $^2A_2$)

```
Energy = -213.296141642281
Ir     0.000000     0.000000     0.300969
 N     0.000000     0.000000    -1.511567
 N     0.000000     0.000000    -2.635797

Ir(14N2)
                    Normal Coordinate Analysis
  ------------------------------------------------------------------
    Irreducible         Harmonic       Infrared        Type
   Representation       Frequency      Intensity
  ------------------------------------------------------------------
                       (cm-1)         (km/mol)
  ------------------------------------------------------------------
        PI               377.1830         2.7636       VIBRATION
        PI               377.1830         2.7636       VIBRATION
       SG+               548.5365        29.0796       VIBRATION
       SG+              2140.2401       462.6555       VIBRATION
```

$Ir(^{15}N_2)$

Normal Coordinate Analysis

Irreducible Representation	Harmonic Frequency (cm-1)	Infrared Intensity (km/mol)	Type
PI	364.5371	2.5891	VIBRATION
PI	364.5371	2.5891	VIBRATION
SG+	532.5155	27.4014	VIBRATION
SG+	2067.8968	431.9740	VIBRATION

$Ir(N_2)^-$ (C_{2v}, $^1A_1$)

```
Energy = -213.357526833504
Ir     0.000000     0.000000    -0.294152
 N     0.000000     0.000000     1.449982
 N     0.000000     0.000000     2.603441
```

$Ir(^{14}N_2)^-$

Normal Coordinate Analysis

Irreducible Representation	Harmonic Frequency (cm-1)	Infrared Intensity (km/mol)	Type
PI	434.0213	3.3179	VIBRATION
PI	434.0213	3.3179	VIBRATION
SG+	648.4311	11.7478	VIBRATION
SG+	1962.7107	1017.9657	VIBRATION

$Ir(^{15}N_2)^-$

Normal Coordinate Analysis

Irreducible Representation	Harmonic Frequency (cm-1)	Infrared Intensity (km/mol)	Type
PI	419.4812	3.1143	VIBRATION
PI	419.4812	3.1143	VIBRATION
SG+	629.4805	11.0542	VIBRATION
SG+	1896.4047	950.5014	VIBRATION

$Ir(N_2)^+$ (C_{2v}, $^3A_1$)

```
Energy = -212.992689411640
Ir     0.000000     0.000000    -0.315136
 N     0.000000     0.000000     1.617291
 N     0.000000     0.000000     2.725297
```

$Ir(^{14}N_2)^+$

Normal Coordinate Analysis

Irreducible Representation	Harmonic Frequency (cm-1)	Infrared Intensity (km/mol)	Type
PI	313.1245	0.6018	VIBRATION
PI	313.1245	0.6018	VIBRATION
SG+	400.6114	14.3507	VIBRATION
SG+	2285.8884	23.5659	VIBRATION

$Ir(^{15}N_2)^+$

Normal Coordinate Analysis

Irreducible Representation	Harmonic Frequency (cm-1)	Infrared Intensity (km/mol)	Type
PI	302.6168	0.5625	VIBRATION
PI	302.6168	0.5625	VIBRATION
SG+	388.9122	13.5247	VIBRATION
SG+	2208.6143	22.0039	VIBRATION

IrNNIr ($D_{2h,}$ $^3B_{1u}$)

```
Energy = -317.213761825221
 N     0.000000     0.000000     0.569367
 N     0.000000     0.000000    -0.569367
Ir     0.000000     0.000000    -2.385426
Ir     0.000000     0.000000     2.385426
```

$Ir^{14}N^{14}NIr$

Normal Coordinate Analysis

Irreducible Representation	Harmonic Frequency (cm-1)	Infrared Intensity (km/mol)	Type
PIu	115.1277	5.7702	VIBRATION
PIu	115.1277	5.7702	VIBRATION
SGg+	194.6052	0.0000	VIBRATION
PIg	345.5060	0.0000	VIBRATION
PIg	345.5060	0.0000	VIBRATION
SGu-	729.1069	361.6940	VIBRATION
SGg+	2102.6390	0.0000	VIBRATION

$Ir^{15}N^{15}NIr$

Normal Coordinate Analysis

Irreducible Representation	Harmonic Frequency (cm-1)	Infrared Intensity (km/mol)	Type
PIu	111.5034	5.4126	VIBRATION
PIu	111.5034	5.4126	VIBRATION
SGg+	194.6019	0.0000	VIBRATION
PIg	333.8749	0.0000	VIBRATION
PIg	333.8749	0.0000	VIBRATION
SGu-	706.1538	339.2793	VIBRATION
SGg+	2031.5923	0.0000	VIBRATION

$Ir^{14}N^{15}NIr$ (C_{2v}, $^3A_1$)

Normal Coordinate Analysis

Irreducible Representation	Harmonic Frequency (cm-1)	Infrared Intensity (km/mol)	Type
PI	113.2602	5.5836	VIBRATION
PI	113.2602	5.5836	VIBRATION
SG+	194.6035	0.0000	VIBRATION
PI	339.7635	0.0077	VIBRATION
PI	339.7635	0.0077	VIBRATION
SG+	717.2738	349.9890	VIBRATION
SG+	2067.5765	0.4977	VIBRATION

References

[1] A. Citra, L. Andrews, *J. Phys. Chem. A* **2000**, *104*, 1152–1161.

[2] X. Wang, L. Andrews, *J. Phys. Chem. A* **2002**, *106*, 2457–2464.

[3] W. Klotzbuecher, G. A. Ozin, *J. Am. Chem. Soc.* **1975**, *97*, 2672–2675.

[4] A. Citra, X. Wang, W. D. Bare, L. Andrews, *J. Phys. Chem. A* **2001**, *105*, 7799–7811.